

# **The effect of in situ nanofibrillar structure on the foamability of PLA/Polyester/nanoclay nanocomposites**

Von der Fakultät für Ingenieurwissenschaften  
der Universität Bayreuth  
zur Erlangung der Würde einer  
Doktor-Ingenieurin (Dr.-Ing.)  
genehmigte Dissertation

von

*M.Sc. Mahboobeh Shahnooshi*

aus

*Esfahan, Iran*

Gutachter: Prof. Dr.-Ing. Volker Altstadt  
Dr. Azizeh Javadi

Diese Dissertation ist im Rahmen einer binationalen Promotion in Kooperation mit der Amirkabir University of Technology, Teheran (Iran) entstanden.

Tag der mündlichen Prüfung: 09. März 2021

Lehrstuhl für Polymere Werkstoffe

Universität Bayreuth

2023

---

## Kurzfassung

Ein gestiegenes Umweltbewusstsein unserer Gesellschaft und unsere zunehmende Abhängigkeit von Kunststoffen, tragen zur Entwicklung biologisch abbaubarer Polymere aus nachhaltigen Ressourcen bei. Damit verbunden sind neue Methoden zur Synthese, Modifizierung und Verarbeitung. Im Rahmen dieser Arbeit konnte die Herstellung von Polymilchsäure (PLA) Schäumen durch die Verbesserung des Kristallisationsverhaltens und der Schmelzeelastizität mittels in situ Fibrillierung deutlich verbessert werden. Um in situ Nanofibrillen (NFs) aus PBT an einer PLA-Matrix zu bilden, wurde PLA mit 1 bis 10 Gew.-% PBT schmelzgesponnen. Der Durchmesser und das Aspektverhältnis der PBT-NFs sind vergleichbar mit denen von mehrwandigen Kohlenstoffnanoröhrchen (MWCNTs). Die Elastizität der Matrix konnte (I) durch angepasste Verarbeitungsparameter und (II) durch den Zusatz von Nanopartikeln erhöht werden. Die Beobachtung ellipsoidaler PBT-Domänen, die sich entlang einer kurzen Düse orientieren, wurde auf eine niedrige Grenzflächenspannung zwischen den Mischungsbestandteilen zurückgeführt und erfüllte die schmelzrheologischen Kriterien für eine Fibrillierung in dem Scherfeld einer Spinnöse. Die Stabilität der verformten Tropfen unter Scher- und Dehnströmungen wurde durch den Vergleich der Tropfenaufbruchzeit und der Verweilzeit im Strömungsfeld untersucht. Die verformten Tröpfchen (Ellipsen) besitzen dabei eine stabile Grenzfläche und entstehen durch Abschnürung der Domänen im anschließenden Dehnströmungsfeld. Eine Fibrillierung der PBT-Domänen, durch das Schmelzspinnen von PLA/PBT/Nanopartikeln, konnte nicht erzielt werden. Die Lokalisierung von Nanopartikeln in der PLA-Matrix konnte durch eine speziell dafür entwickelte Dosiersequenz erreicht werden. Auf die Fibrillierung der PBT-Domänen hatte die erhöhte Elastizität der Matrix keinen Einfluss. Diese Beobachtung bestätigte die Dominanz eines als „*Pinch-off*“ bezeichneten Mechanismus, bei dem die Oberflächenspannung zwischen den Komponenten eine entscheidende Rolle spielt. Die Dispersion von Nanopartikeln reduzierte die Polarität der Matrix und die Wechselwirkungen mit den tröpfchenförmigen PBT Domänen.

Bei den in situ hergestellten isotropen nanofibrillären Verbundwerkstoffen (NFCs) wurde eine zufällig orientierte 2D-Nanohybrid-Shish-Kebab (NHSK)-Überstruktur festgestellt. Eine orthogonale Strukturierung von aus der Schmelze kristallisierten PLA-Nanodomänen wurde auf den PBT-NFs-Oberflächen beobachtet. Die Bildung der NHSK-Überstruktur in der ruhenden Polymerschmelze durch „*soft epitaxie*“ bot eine besondere Voraussetzung für die Bildung der Morphologie der kristallinen Phase. Um die mechanischen Eigenschaften der NFCs zu verbessern, sollte ein Temperaturbereich gefunden werden, in dem die Morphologie der kristallinen Phase während des Temperns als NHSK-Überstruktur erhalten bleibt. Bei NFs aus 1 Gew.-% PBT (NFC1) führte die Erhöhung der Tempertemperatur ( $T_{iso}$ ) von 100 °C auf 114 °C zu einer Vergrößerung der Länge der Kebab-Struktur und damit zu einer Verzahnung der benachbarten Überstrukturen. Durch eine weitere Erhöhung der Temperatur ( $T_{iso} > 117$  °C) konnte ein Übergang zu einer sphärolitischen Kristallmorphologie beobachtet werden. Ein ähnlicher Übergang von 2D-NHSK-Überstrukturen zu 3D-Sphärolithen wurde mit steigendem PBT-NF-Gehalt beobachtet. Die Beschreibung der Kinetik der Kristallitmorphologie, der Kristallisationsgeschwindigkeit und der Keimbildungsmechanismen in Abhängigkeit vom PBT-NF-Gehalt und der isothermen Temperatur erfolgte durch Anwendung des Avrami-Modells.

Die dynamisch-mechanische Thermoanalyse (DMTA) ergab, dass die erhöhte Kristallisationsrate und die Bildung einer NHSK-Überstruktur auf dem 3D-Nanofibrillennetzwerk die Temperaturbeständigkeit von PLA deutlich verbesserte. Den DMTA-Ergebnissen zufolge stieg die Gebrauchstemperatur von PLA von 60 °C auf etwa 120 °C. Die Ergebnisse der Zugversuche zeigten, dass das spröde Verhalten von PLA sowohl im amorphen als auch im kristallinen Zustand verbessert wurde. Im amorphen Zustand war der Zugmodul der NFCs vergleichbar mit dem von PLA, aber eine Erhöhung der Bruchdehnung um 220 % führte zu einer deutlichen Verbesserung der Zähigkeit ( $\cong 270$  %). Bei einem konstanten Kristallinitätsgrad von 20 % zeigte PLA ein sprödes Verhalten. Im Gegensatz dazu blieb das zähelastische Verhalten der NFCs erhalten, und eine Erhöhung des Elastizitätsmoduls aufgrund längerer verzahnter Kebabs führte zu einer verbesserten Zähigkeit ( $\cong 250$  %).

Scherrheologische Untersuchungen der NFCs zeigten, dass die PBT-NF's bei einem Nanofibrillengehalt von 0,7 Gew.-% in der Schmelze ein dreidimensionales Perkolationsnetzwerk bildeten. Dehnrheologische Untersuchungen bestätigten, dass das PBT-NF-Netzwerk das Verfestigungsverhalten der NFC-Proben bei allen untersuchten Zusammensetzungen signifikant erhöht. Der Kaltverfestigungsfaktor kann anhand der Abweichung vom Trouton-Gesetz bewertet werden. Dieser ist ein Maß für die Schmelzefestigkeit und damit indirekt für die Schäumbarkeit eines Polymerwerkstoffs. In Gegenwart von 1 Gew.-% PBT-NF's wurde der Verfestigungsfaktor um mehr als 2 Größenordnungen erhöht. Ähnliches Verfestigungsverhalten wurde auch bei PLA/PBT/Nanopartikel Proben beobachtet, was hauptsächlich auf die starken Wechselwirkungen zwischen den PLA-Ketten und den Nanopartikelplättchen zurückzuführen ist.

Die Schäumbarkeit von PLA und NFCs wurde in einem Batch-Schaumverfahren unter Verwendung von überkritischem CO<sub>2</sub> (scCO<sub>2</sub>) als physikalisches Treibmittel untersucht. Es wurden verschiedene Parameter bei Schäumen gewählt, um die Auswirkungen des Kristallinitätsgrads der Proben auf die resultierenden Schaumeigenschaften zu untersuchen. Die Schaummorphologie und -dichte wurden grundsätzlich durch den Kristallinitätsgrad und die Kristallmorphologie der NFCs, die durch den PBT-NF-Gehalt bestimmt wurde, kontrolliert. Die Schaumergebnisse wurden anhand der Ergebnisse der Hochdruck-Differential-Scanning-Kalorimetrie (HPDSC) und der morphologischen Beobachtungen der kristallinen Phase der Schäume interpretiert. Die HPDSC-Messungen ergaben, dass die Kristallinität der Proben bei hohem scCO<sub>2</sub>-Druck (140-180 bar) stark temperaturabhängig und weniger druckabhängig ist. Bei einer hohen Sättigungstemperatur (128 °C), die zu amorphen Proben führte, verringerte sich die Schaumdichte von 338 kg/m<sup>3</sup> für PLA auf 83 kg/m<sup>3</sup> für NFC1. Dabei wurden gerissene Zellwände und eine ungleichmäßige Zellmorphologie beobachtet. Bei einer niedrigeren Sättigungstemperatur (116 °C) wurden Dichten von 47 kg/m<sup>3</sup> mit einer geschlossenzelligen mikrozellulären Morphologie (durchschnittliche Zellgröße von 13 µm und Zelldichte von  $1,5 \times 10^9$  Zellen/cm<sup>3</sup>) erzielt. Die geschlossenzellige Struktur wurde auf die Integrität der amorphen Phase von PLA zurückgeführt, die durch die Einbettung der feinen NHSK-Überstrukturen in den Zellwänden gewährleistet wird. Eine Erhöhung des PBT-NF-Gehalts führte zu kleinen Blasen in den Schaumproben aufgrund der Bündelung von Nanofibrillen und einer fächerförmigen transkristallinen Struktur.

Durch Senkung der Sättigungstemperatur auf 108 °C wurden in der NFC1 Domäne ein höherer Kristallinitätsgrad und dickere NHSK-Überstrukturen erzielt, die die amorphe Phase stark

nukleierten. Die starke Keimbildung für die Bildung von Schaumzellen in der amorphen Phase führte zu nanozellulären offenzelligen Schäumen. Allerdings mit einer hohen Schaumdichte von  $446 \text{ kg/m}^3$ . Unter den gleichen Schäumbedingungen wurden geschlossenzellige nanozelluläre Schaumproben von NFC3-Proben mit einer ebenfalls hohen Dichte von  $612 \text{ kg/m}^3$  erhalten. Die Zugabe von Nanopartikeln in Verbindung mit den PBT-Domänen verbesserte die Dehnviskosität der PLA/PBT/Nanopartikel-Proben leicht. Beide Komponenten könnten als Zellnukleierungsmittel für die PLA-Matrix wirken. Verbesserungen der Schaumeigenschaften konnten nicht erzielt werden. Zellbruch und Koaleszenz traten aufgrund der geringen Deformierbarkeit der PBT-Domänen, der Gegenwart der Nanopartikelplättchen und der kristallinen Phase im erheblichen Maße auf. Dieser Vergleich unterstreicht, dass die Grenzfläche der beiden Blendkomponenten eine sehr wirksame Modifikation der Rheologie der Schmelze und eine Zellkeimbildung mit einer nanofibrillären Morphologie ermöglicht.

Schlüsselwörter: Poly(milchsäure); In situ nanofibrilläre Verbundwerkstoffe; Schaumstoffe; Polymerschäume, mikrozelluläre Schäume; Nanozelluläre Schäume; Nanohybrid Shish-Kebab-Überstruktur

---

## Short Summary

Environmental concerns and our increasing dependence on plastics have devoted many researchers' efforts to discover new methods of synthesizing, modifying and processing biodegradable polymers from sustainable resources. The foaming properties of poly(lactic acid) (PLA) were modified through improvements in its crystallization behavior and melt elasticity using in situ fibrillation. Melt-spinning of poly(lactic acid) (PLA)/poly(butylene terephthalate) (PBT) containing 1 to 10 wt% of PBT was implemented to develop in situ nanofibrils (NFs) of PBT in a PLA matrix with diameter and aspect ratio comparable to those of multi-wall carbon nanotubes (MWCNTs). For this purpose, increasing the matrix's elasticity was achieved using (I) adjusted processing parameters and (II) the addition of nanoclay. Observation of ellipsoidal PBT domains oriented along a short die was attributed to a low interfacial tension between the blend constituents and fulfilled melt rheological criteria for fibrillation in a simple shear flow. The stability of the deformed droplets under the shear and elongational flows was studied by comparing the droplet breakup time and residence time in each flow field. The deformed droplets (ellipses) with a robust interface underwent coalescence through pinch-off in the subsequent elongational flow field. However, the melt-spinning of PLA/PBT/nanoclay did not lead to fibrillation of PBT domains. Although the localization of nanoclay in the PLA matrix was accomplished using planned feeding sequences, the increased matrix elasticity did not improve the drawability of the PBT domains. This observation confirmed the pinch-off mechanism dominance in which the surface tension between the components has a critical role. The dispersion of nanoclay reduced the matrix polarity and the interactions with the PBT droplets.

In the fabricated isotropic in situ nanofibrillar composites (NFCs), a random oriented 2D nanohybrid shish-kebab (NHSK) superstructure was observed as a result of orthogonal patterning of melt crystallized PLA nanodomains on the PBT NFs surface. The establishment of the NHSK superstructure in quiescent bulk through the mechanism of geometric confinement (soft epitaxy) provided a particular condition for tailoring the crystalline phase morphology via annealing temperature. Finding a temperature window in which the crystalline phase morphology remains as NHSK superstructure was followed to determine the best annealing temperature to improve the mechanical properties of the NFCs. In 1 wt% PBT NFs (NFC1), increasing the isothermal temperature ( $T_{iso}$ ) from 100 °C up to 114 °C led to an increase in the kebabs' length, thus to an interlocking of the adjacent superstructures. A transition to a spherulitic crystal morphology was observed due to a further temperature increase ( $T_{iso} \geq 117$  °C). A similar transition from 2D NHSK superstructures to 3D spherulites was observed by increasing PBT NF content. The Avrami model was applicable for interpreting variations of crystallite morphology, crystallization rate, and nucleation mechanisms with PBT NF content and isotherm temperature.

Dynamic mechanical thermal analysis (DMTA) revealed that the promoted crystallization rate and formation of the NHSK superstructure on the 3D nanofibrillar network improved the PLA's heat resistance. According to the DMTA results, the application temperature of the PLA increased from 60 °C to about 120 °C. Tensile test results showed that the brittle behavior of PLA was modified in both amorphous and crystalline states. At the amorphous state, while the tensile modulus of NFCs was almost equal to that of PLA, a 220 % increase in elongation at break resulted in significant

toughness improvement ( $\cong 270\%$ ). At a constant degree of crystallinity (20%), PLA presented a brittle behavior. On the contrary, the plastic behavior of NFCs survived, and an increase in elastic modulus due to longer interlocked kebabs led to enhanced toughness ( $\cong 250\%$ ).

Shear rheological studies of the NFCs showed that the PBT NFs formed a rheologically percolated 3D network at a nanofibril content of 0.7 wt%. Elongational rheology investigations confirmed that the PBT NF network significantly increased the strain hardening behavior of NFC samples at all the studied compositions. The strain hardening factor can be evaluated based on a deviation from the Trouton Law, which has been known to represent the melt strength and, thereby, foamability. A strain-hardening factor of more than two orders of magnitude was observed in the presence of 1 wt% of NFs. The strain hardening behavior was also observed in PLA/PBT/nanoclay samples, mainly due to the proper interactions between the PLA chains and nanoclay platelets.

The foamability of PLA and NFCs was investigated in a batch foaming process using supercritical CO<sub>2</sub> gas (scCO<sub>2</sub>) as a physical blowing agent. Different foaming conditions were chosen to examine the effect of samples' degree of crystallinity. In each foaming condition, the degree of crystallinity and crystallite morphology of NFCs, which was governed by PBT NF content, controlled the foam morphology and density. The results from the foamed samples were interpreted regarding the high-pressure differential scanning calorimetry (HPDSC) results and morphological observations of the foams' crystalline phase. The HPDSC measurements revealed that at high scCO<sub>2</sub> pressure (140-180 bar), the crystallinity of the samples is highly temperature-dependent and less pressure-dependent. At a high saturation temperature (128 °C), which resulted in amorphous samples, although the foam density decreased from 338 kg/m<sup>3</sup> for PLA to 83 kg/m<sup>3</sup> for NFC1, ruptured cell walls and non-uniform cell morphology were obtained. At a lower saturation temperature (116 °C), super-light foams (density of 47 kg/m<sup>3</sup>) with closed-cell microcellular morphology (average cell-size of 13 μm, and cell density of  $1.5 \times 10^9$  cells/cm<sup>3</sup>) were achieved. The closed-cell structure was attributed to the integrity of the amorphous phase of PLA provided by the embedment of the fine NHSK superstructures in the cell walls. However, increasing the PBT NF content resulted in small bubbles in the foam samples due to nanofibrils bundling and a fan-shaped transcrystalline structure.

By decreasing the saturation temperature to 108 °C, a higher degree of crystallinity and thicker NHSK superstructures were formed in NFC1, which strongly nucleated the amorphous phase. Strong cell nucleation of the amorphous phase resulted in nanocellular open-cell foams with a foam density of 446 kg/m<sup>3</sup>. At the same foaming condition, closed-cell nanocellular foam samples of NFC3 samples with a high density of 612 kg/m<sup>3</sup> were obtained, indicating the crucial role of a fibrillar additive with the capability of tailoring the morphology of crystalline regions. The inclusion of nanoclay in association with PBT solid droplets slightly improved the elongational viscosity of the PLA/PBT/nanoclay samples. Both components could act as a cell-nucleating agent for the PLA matrix; however, noticeable improvements in foam properties were not achieved. Cell rupture and coalescence were significant due to the inflexibility of the PBT solid droplets, nanoclay platelets, and crystalline phase. This comparison emphasized that the two components' interface provided much effective rheological modification and cell nucleation in a nanofibrillar morphology.

Keywords: Poly (lactic acid); In situ nanofibrillar composites; Foam; Microcellular foams; Nanocellular foams; Nanohybrid shish-kebab superstructure

---

## Acknowledgment

Throughout the writing of this dissertation, I have received a great deal of support and assistance. I would first like to express special appreciation to my both supervisors Dr. Azizeh Javadi and Prof. Dr. -Ing. Volker Altstädt and, for their patience, motivation, enthusiasm, and immense knowledge. I gratefully appreciate all the efforts of Dr. Javadi to finalize the joint doctoral contract as a successful experience between the two universities. I would like to express my sincere gratitude to Prof. Altstädt for the continuous support of my Ph.D. study and research. Their insightful feedback pushed me to sharpen my thinking and brought my work to a higher level. Thanks to Prof. Dr. Andreas Greiner and Prof. Hossein Nazockdast whose vision and motivation have deeply inspired me, and it was a great privilege to work under their guidance.

I would like to acknowledge all the members of the Department of Polymer Engineering at the University of Bayreuth for all of the opportunities I was given to further my research. Especially, I want to name Tobias Standau and Christian Brütting for their patient support and expertise, which were invaluable in formulating the research questions and methodology. Indeed, I appreciate the time and energy Tobias Standau spent on the correction of my dissertation. I would also like to thank Dr. Reina Giesa, Dr. Tristan Kolb, Dr. Jacqueline Uhm, and Christoph Kalsen for their valuable guidance throughout my experiments. Thanks to Annika Pfaffenberger for capturing many SEM and TEM images and thanks to Sebastian Gröschel who helped me choose the right direction to complete the processing steps. I also thank Bärbel Heindl-Tenhunen and Kerstin Mosig who have always been there for administrative support.

I heartfully thank my former boss at Avand Plast Kerman, Mr. Seyed Saeed Zamanzadeh, for his motivation and support during my Ph.D. I also want to thank all the people who helped me by contributing their time and knowledge to my research during the past years. I could not have completed this dissertation without the support of Dr. Fereshteh Karkhaneh, Dr. Omid Yousefzadeh, Dr. Amir Rostami, Dr. Mohsen Masoomi, Mohammad Mahdi Foroughi, Reza Gheshlaghi, and Iesa Babalou who provided stimulating scientific discussions or practical assistance. Last but not least, I thank Razieh Kalkum and Johannes Kalkum for occasionally happy distractions to rest my mind outside of my research. It would have been tough to go through some days without communicating with some friends.

In the end, I would like to express my ultimate gratitude to my parents for their shining eyes when looking at me, their sympathetic ear, and for being always there for me. I want to apologize to them for their bitter smile that tries to hide nostalgia.

---

## **Dedicated to**

175 Iranian divers with their hands tied



---

# Table of Contents

<b>Kurzfassung</b> .....	<b>I</b>
<b>Short Summary</b> .....	<b>IV</b>
<b>Acknowledgment</b> .....	<b>VI</b>
<b>Dedicated to</b> .....	<b>VII</b>
<b>Table of Contents</b> .....	<b>VIII</b>
<b>Abbreviations</b> .....	<b>XI</b>
<b>Symbols</b> .....	<b>XIII</b>
<b>1 Introduction and Motivation</b> .....	<b>1</b>
<b>2 State of the Art</b> .....	<b>5</b>
2.1 The concept of polymer nanocomposites .....	5
2.2 In situ fibrillar composites .....	6
2.2.1 Highly oriented in situ fibrillar micro/nanocomposites .....	7
2.2.2 Isotropic in situ fibrillar micro/nanocomposites .....	9
2.3 Rheological studies .....	18
2.3.1 Melt rheological studies for in situ development of polymer fibrils .....	18
2.3.2 Melt rheological studies of isotropic M/NFCs .....	23
2.4 Crystallization phenomena .....	28
2.4.1 Shish-kebab structure and hybrid shish-kebab structure.....	28
2.4.2 Melt crystallization kinetics.....	35
2.5 Immiscible polymer blends containing nanoparticles .....	37
2.5.1 Thermodynamic parameters (wetting parameters).....	37
2.5.2 Kinetic parameters.....	38
2.5.3 Effect of feeding sequence .....	38
2.5.4 Effect of viscosity .....	39
2.6 Foaming basics.....	40
2.6.1 Nucleation.....	40
2.6.2 CO <sub>2</sub> sorption and diffusivity in polymers.....	40
2.6.3 Terminologies .....	41
2.7 PLA foaming .....	43
2.7.1 Degree of crystallinity and crystal morphology .....	43
2.7.2 Molecular architecture .....	44
2.7.3 D-lactide content.....	45

---

2.7.4	Blending and compounding .....	45
2.8	Foamability of isotropic in situ microfibrillar composites.....	47
<b>3</b>	<b>Goals and Approaches.....</b>	<b>52</b>
<b>4</b>	<b>Experimental.....</b>	<b>57</b>
4.1	Materials .....	57
4.2	Processing .....	59
4.2.1	PLA/PBT fibers and composites .....	59
4.2.2	PLA/PBT/nanoclay fibers and nanocomposites .....	64
4.3	Characterization.....	67
4.3.1	Solid-state nuclear magnetic resonance .....	67
4.3.2	Contact angle measurements .....	67
4.3.3	Rheological measurements .....	68
4.3.1	Polarized optical microscopy .....	71
4.3.2	Scanning electron microscopy .....	71
4.3.3	Transmission electron microscopy.....	72
4.3.4	Atomic force microscopy.....	72
4.3.5	Differential scanning calorimetry .....	73
4.3.6	Mechanical properties.....	76
4.3.7	Foaming experiments .....	77
<b>5</b>	<b>Results and Discussions .....</b>	<b>79</b>
5.1	Chemical and physical interactions between the two polyesters.....	79
5.1.1	Solid-state NMR spectra.....	79
5.1.2	Surface free energy and interfacial tension.....	81
5.2	Rheological rationalization of the nanofibrils PBT nanofibrils development .....	82
5.3	Mathematical model of the spinning line.....	88
5.4	Morphology development in the blends, fibers, and NFCs.....	93
5.4.1	Morphological observations of non-stretched PLA/PBT strands.....	93
5.4.2	Morphological observation on the surface of PLA/PBT fibers and in the NFCs	98
5.4.3	Morphological observation of PLA/PBT/nanoclay nanocomposites.....	103
5.5	PLA crystallization in the presence of PBT nanofibrils.....	105
5.5.1	Non-isothermal crystallization .....	105
5.5.2	Crystallite morphology of NFCs evolved from the quiescent melt.....	112
5.5.3	Isothermal melt crystallization kinetics .....	120
5.5.4	Cold crystallization investigations .....	127
5.6	Thermo-mechanical properties of crystalline NFCs .....	132

---

5.7	Mechanical reinforcement by nanofibrils and NHSK superstructures .....	134
5.8	Rheological behavior of nanocomposites .....	139
5.8.1	Shear rheology of NFCs .....	139
5.8.2	Elongational rheology of the nanocomposites .....	142
5.9	Foam results .....	146
<b>6</b>	<b>Summary</b> .....	<b>155</b>
<b>7</b>	<b>Outlook</b> .....	<b>158</b>
<b>8</b>	<b>Bibliography</b> .....	<b>159</b>
	<b>Curriculum vitae</b> .....	<b>176</b>
	<b>Publications</b> .....	<b>177</b>

---

## Abbreviations

AFM	Atomic force microscopy
ARES	Advanced Rheometric Expansion System
CNT	Carbon nanotube
DMTA	Dynamic mechanical thermal analysis
DSC	Differential scanning calorimetry
DWCNT	Double-wall carbon nanotube
EVF	Extensional Viscosity Fixture
GF	Glass fiber
GNS	Graphene nanosheet
GPC	Gel permeation chromatography
HFIP	Hexafluorisopropanol
HPMIM	High-pressure microcellular injection molding
MFC	Micro fibrillar composite
MFR	Melt flow rate
mPE	Metallocene catalyzed polyethylene
MWCNTs	Multi-wall carbon nanotubes
NFCs	Nano fibrillar composites
NF	Nanofibril
NHSK	Nanohybrid shish-kebab
NMR	Nuclear magnetic resonance
PPZn	Phenylphosphonic acid zinc salt
PA6	Polyamide 6
PA66	Polyamide 66
PBAT	Poly (butylene adipate-co-terephthalate)
PBS	Poly (butylene succinate)
PBSA	Poly [(butylene succinate)-co-adipate]
PBT	poly (butylene terephthalate)
PCL	Poly (caprolactone)
PDLA	Poly (D-lactic acid)
PECTFE	Poly (ethylene-co-chlorotrifluoroethylene)
PET	Poly (ethylene terephthalate)
PHBV	Polyhydroxybutyrate-valerate
PLA	Poly (lactic acid) or Polylactide
PLLA	Poly (L- lactic acid)
PMMA	Poly (methyl methacrylate)
POM	Polarized optical microscopy

---

PP	Polypropylene
PPC	Poly (propylene carbonate)
PPS	Polyphenylene sulfide
PS	Polystyrene
PTFE	Poly (tetrafluoro ethylene)
PTT	Poly (trimethylene terephthalate)
PVOH	Poly (vinyl alcohol)
PVDF	Polyvinylidene fluoride
$R_g$	Radius of gyration
RMIM	Regular microcellular injection molding
$RuO_4$	Ruthenium tetroxide
SP	sulfonated poly (ethylene terephthalate)
scCO <sub>2</sub>	Supercritical CO <sub>2</sub>
sc-CO <sub>2</sub> LTFP	Supercritical carbon dioxide low-temperature foaming process
SEM	Scanning electron microscopy
TEM	Transmission electron microscopy
TPU	Thermoplastic poly (ester)urethane
VER	Volume expansion ratio
WAXD	Wide-angle X-ray diffraction

## Symbols

$T_a$	Ambient temperature
$n$	Avrami exponent
$k_b$	Boltzmann constant
$t_b$	Breakup time
$Ca$	Capillary number
$N_0$	Cell density
$G^*$	Complex shear modulus
$R^2$	Correlation coefficient
$Ca_c$	Critical capillary number
$\dot{\gamma}_c$	Critical shear rate
$k$	Crystallization rate constant
$R_{die}$	Die diameter
$r_{die}$	Die radius
$\Omega$	Dimensionless distortion growth rate
$Re$	Dimensionless Reynolds number
$x$	Direction along the fibers
$u^d$	Dispersive components of surface free energy
$Dr$	Draw ratio
$R$	Droplet diameter
$G''$	Dynamic loss modulus (shear mode)
$G'$	Dynamic storage modulus (shear mode)
$E'$	Dynamic storage modulus (extension mode)
$\lambda''$	Elasticity ratio
$\epsilon_b$	Elongation at break
$t_{1/2,exp}$	Experimental crystallization half-time
$\alpha_f$	Final breakup amplitude
$\rho_{foam}$	Foam density
$l_f$	Freeze line
$T_f$	Freeze temperature
$\omega$	Angular frequency
$T_g$	Glass transition temperature
$C_p$	Heat capacity of PLA
$h$	Heat convection coefficient
$H_{cc}$	Heat of cold crystallization
$H_m$	Heat of fusion
$H_{m0}$	Heat of fusion for the 100 % crystalline PLA

---

$T_{HM}$	High melt temperature
$T_{LM}$	Low melt temperature
$t_0$	Induction time
$\alpha_i$	Initial breakup amplitude
$D_0$	Initial fibril diameter
$T_i$	Initial melt temperature
$X_m$	Instability wave number
$X_c$	Normalized degree of crystallinity
$X_g$	Fiber content at gel point
$\upsilon_{12}$	Interfacial tension
$T_{iso}$	Isothermal crystallization temperature
$M$	Magnification factor
$\eta_m$	Matrix viscosity
$\rho$	Melt density of PLA
$U_0$	Melt velocity at the die
$T_m(HC)$	Melting temperature of homocrystallites
$T_m(SC)$	Melting temperature of stereo-complex crystallites
$t_{1/2}$	Model crystallization half-time
$n$	Number of cells within the statistical area
$\upsilon_{nu}$	Nutation frequency
$\delta$	Phase angle
$\upsilon^p$	Polar components of surface free energy
$\upsilon^p/\upsilon^d$	Polarity ratio
$T_{process}$	Processing temperature
$n_p$	Power-law exponent
$r_x$	Radius of the fiber as a function of x
$\lambda'$	Ratio of the capillary to the critical capillary number ( $Ca/Ca_c$ )
$\rho_{rel}$	Relative foam density
$V_c$	Relative volumetric crystalline fraction
$t_{iso}$	Required time to complete the crystallization peak
$t_{re}$	Residence time
$\gamma$	Strain or amplitude
$\dot{\gamma}$	Shear rate
$l$	Spinning length
$A$	Statistical area in SEM micrographs
$\dot{\epsilon}$	Strain rate (extensional mode)
$\dot{\epsilon}_x$	Strain rate as a function of x (extensional mode)
$\sigma_{ij}$	Stress (shear or extensional type)
$U_s$	Stretching velocity (spool velocity)
$\chi$	Strain hardening factor

---

$T$	Temperature of the fiber
$K$	Temperature-dependent overall crystallization rate constant
$E$	Tensile modulus
$\sigma_{SD}$	Standard deviation
$\sigma_b$	Tensile strength
$\sigma_{E^+}$	Tensile stress growth function
$-dv/dT$	Thermal coefficients of the surface tension
$k_{air}$	Thermal conductivity of air
$t$	Time
$u_i$	Total surface free energy of polymer i
$\eta_E^+$	Transient extensional viscosity
$U_x$	Velocity of the fiber as a function of x and Dr
$\eta$ or $ \eta^* $	Complex Shear viscosity
$\eta_d$	Complex shear viscosity of dispersed component
$\eta_m$	Complex shear viscosity of matrix component
$\lambda$	Viscosity ratio
$Q_v$	Volumetric flow rate
$\phi$	Volumetric foam expansion ratio
$W_{AB}$	Wettability parameter
$W_i$	Weissenberg number



## 1 Introduction and Motivation

Environmental concerns and worldwide increasing dependence on plastic products have devoted many researchers' efforts to discover new methods for synthesizing, modifying, and processing biodegradable polymers from sustainable resources<sup>1</sup>. Poly (lactic acid) or Polylactide (PLA) is one of the most promising biodegradable, biocompatible polymers, owing to its mechanical property, thermoplastic processability, biological properties, and large-scale production. Lactic acid  $\text{HOCH}_2\text{CHCOOH}$  is a chiral molecule with two enantiomeric isomers, L- and D-lactic acid (**Figure 1-1**), differing in their effect on polarized light. The stereoregularity makes poly (L-lactic acid) crystalline. Fully amorphous PLA can be made by the inclusion of relatively high D content (>10 %), whereas highly crystalline PLA is obtained when the D content is low (<2 %) <sup>2,3</sup>.

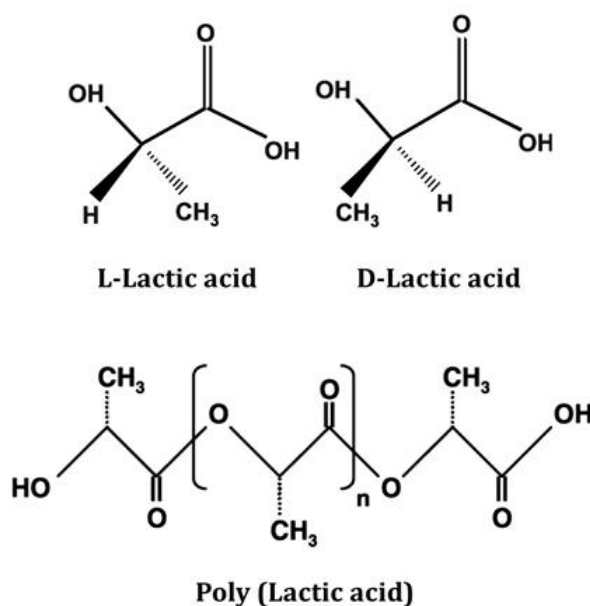


**Figure 1-1.** Chemical structure of optical isomers of lactic acid; and Poly (lactic acid) <sup>2</sup>.

PLA can be produced from oil derivatives or renewable resources like corn, potato, and sugar cane <sup>4</sup>. Ring-opening polymerization of lactide; or polycondensation of lactic acid monomers obtained from the fermentation of agricultural resources are the current synthesis methods of PLA <sup>5</sup>. In **Figure 1-2** a sketch of how the corn is transformed into PLA is shown. Additionally, the carbon footprint for every single step is given. The high amount of  $\text{CO}_2$  that is taken up during corn cultivation constitutes the green characteristics of PLA at the end. Considering other factors that also impact  $\text{CO}_2$  emissions, such as fertilizers, pesticides, and energy consumption, etc., the

manufacturer NatureWorks reported that the gross greenhouse emissions of PLA are compensated for down to 0.62 kg CO<sub>2</sub> equivalent per kilogram of the polymer <sup>6</sup>.

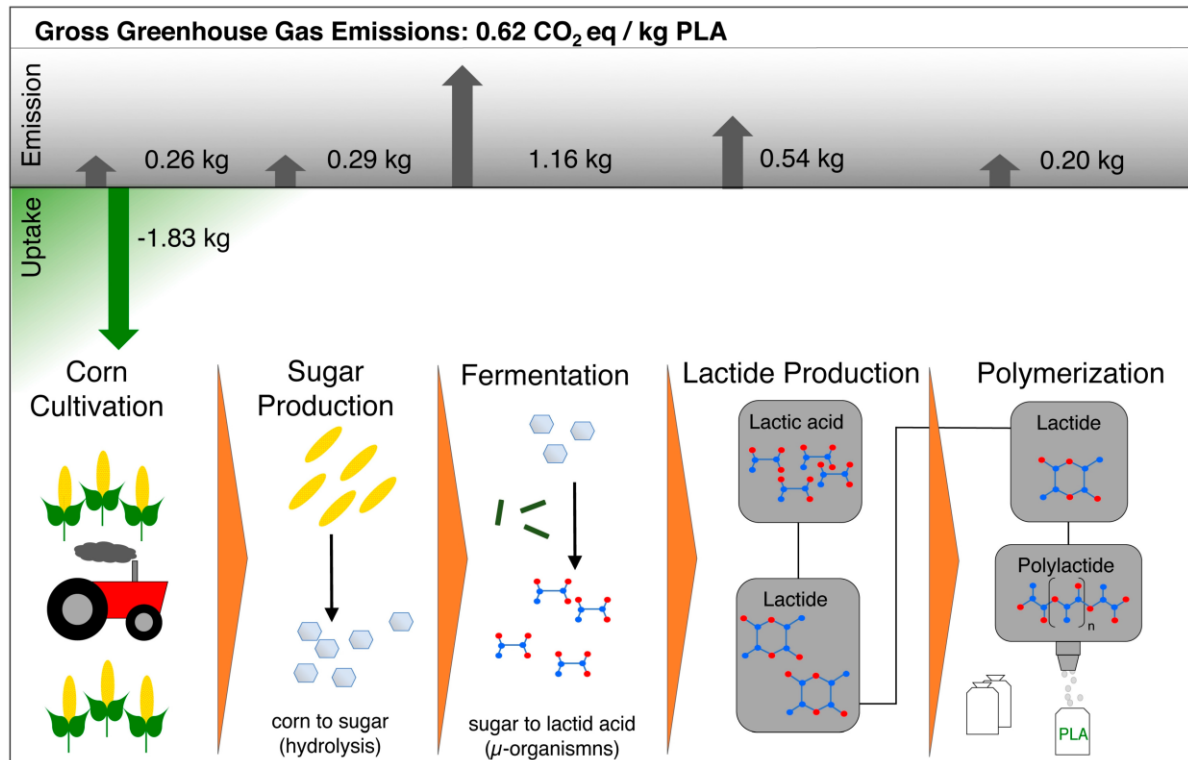


**Figure 1-2.** Steps of PLA production with greenhouse gas uptake and emissions for 1 kg of PLA <sup>3</sup>.

PLA characteristics like clarity, mechanical, thermal, and processing ability, compared to those of the traditional polymers such as polystyrene (PS), polypropylene (PP), and polyethylene (PE), have made scientists hopeful to come true the dream of an environmentally friendly alternative for oil derivative polymers <sup>7</sup>. Tissue engineering is one of the most important application domains since the degradation product, lactic acid, is metabolically innocuous <sup>8, 9</sup>. Different spinning methods can transform PLA into filaments, which can be used for subsequent fabrication of textile structures or used for implants and other surgical applications such as absorbable surgical sutures <sup>10, 11</sup>. Films are the second largest application area for PLA, for instance, transparent films for food contact <sup>12</sup>. PLA offers potential applications as commodity plastics, as in green packaging, as agricultural mulch films, and disposable materials <sup>13, 14</sup>. PLA burns with low smoke generation; it is ultraviolet resistant and easily dyeable <sup>14</sup>. Even though PLA prices decreased significantly below \$2000/ton over the last decade, the standard polymers are still lower priced, as

polystyrene, for example, can be purchased for less than \$1000/ton. Thus, PLA is not fully economically competitive compared to the fossil-based polymers<sup>3</sup>.

The development of polymeric foams started in the 1930s, with the first patented foam (1931) being macrocellular polystyrene foams (cell-size above 100  $\mu\text{m}$ )<sup>15</sup>. The principal motive behind this invention was to (i) reduce material density (save plastic) without compromising its properties, and (ii) decrease cost. Advancements in foam processing technology from the late 1980s to late 1990s led to the development of foams classified as fine-celled foams (cell-size between 10  $\mu\text{m}$  and 100  $\mu\text{m}$ ), microcellular foams (cell-size of  $\leq 10$   $\mu\text{m}$  and cell density of  $>10^9$  cells/ $\text{cm}^3$ ), and nanocellular foams (cell-size of  $\leq 1$   $\mu\text{m}$  and cell density of  $>10^{15}$  cells/ $\text{cm}^3$ ). These classifications, however, failed to specify the foam density range or expansion ratio. Furthermore, microcellular foams, compared to macrocellular foams at the same density, offered improved properties, particularly mechanically due to their smaller cell-sizes and cell-size uniformity<sup>16</sup>.

Primarily, Mooney et al. in 1996 conducted the use of high-pressure  $\text{CO}_2$  as a physical blowing agent to produce porous PLA foams through a static batch foaming to produce highly porous sponges for potential use in tissue engineering<sup>17</sup>. Since supercritical physical blowing agent does not remain in the foam as a toxic or harmful residue, the method received a great deal of attention. After the gas dissolved in the PLA, the foams were produced by rapid depressurization. Subsequently, due to the thermodynamic instability that was created, cell nucleation and cell growth occurred, and PLA foams with high porosity were produced. Nevertheless, foaming was a good idea for the weight reduction of relatively expensive PLA on the industrial scale. Therefore, another early approach was the foam extrusion of PLA/starch with the idea of industrializing a cost-effective cushioning material, which could be an alternative for expanded polystyrene<sup>18</sup>. Since then, a lot of research was done on the foaming of PLA and, in the last few years, PLA foams were even established commercially, such as thermoformed extrusion sheet foams from Sealed Air Corp. (Cryovac NatureTRAY™)<sup>19</sup>, and as bead foams from the companies Synbra Technology BV (BioFoam®)<sup>20</sup> and BASF SE (ecovio®EA)<sup>21</sup>.

PLA foam can be used in packing, automobile, construction, medicine, and other areas. In particular, PLA foams with a high expansion ratio can provide higher porosity, larger three-dimensional space, and specific surface area, making them have great application potential in insulation, adsorption, tissue engineering, drug release, and other areas. However, the low melt strength has been mentioned as the main neck for foaming processes of PLA in the literature, which leads to cell coalescence and cell rupture during cell growth. Moreover, its low melt strength causes gas loss during foam expansion, which results in severe shrinkage<sup>22</sup>. The linear,

short, and semi-rigid chains of PLA are known to cause poor performance during the elongational flow, which is highly demanded during bubble growth in the foaming process. Several strategies are summarized to enhance the foamability of PLA; these include (i) the introduction of chemical modifications, (ii) the addition of additives, and (iii) the enhancement of the slow crystallization kinetics<sup>23</sup>. The different methods for chemical modification of PLA include enhancing molecular weight, using chain extenders to increase molecular weight and/or introducing branched molecules, developing a cross-linked structure, modifying D-ratio, etc., have been reviewed by Standau et al.<sup>3</sup>. The effect of blending and compounding with different additives and nanoparticles has been reviewed by Nofar et al.<sup>23</sup>. However, due to the mentioned drawbacks of PLA, achieving a simple modification method, which can finally result in reproducible light-weight micro/nano cellular structures of PLA, is still under deep investigation.

A few researchers have recently investigated the approach of in situ microfibrillar composites (MFCs) to physically modify PLA's rheological behavior and its slow crystallization kinetics<sup>24, 25</sup>. The concept of converting polymer blends into in situ composites instead of adding fillers has been introduced to effectively improve the PLA foam specifications due to the cell nucleating effect of well-dispersed fibrils, enhanced melt strength, and crystallization rate<sup>24</sup>. By using a batch foaming process, the addition of the 3 wt% Polyamide 6 (PA6) microfibrils reduced the PLA foam's average cell-size from 70 to 23  $\mu\text{m}$ , while its cell density increased by a remarkable 2 orders of magnitude (from  $2.4 \times 10^6$  cells/ $\text{cm}^3$  to  $1.8 \times 10^8$  cells/ $\text{cm}^3$ )<sup>25</sup>. However, the effect of crystalline phase morphology on foaming was not reported.

Nevertheless, the effect of fibril diameter, which crucially affects the matrix viscoelastic behavior, crystallization morphology, and subsequently, the foam properties, has not been studied. Reducing the fibril diameters from micro-size to nano-size during morphology development is highly challenging. The generation of in situ fibrils is strongly influenced by processing parameters, dispersed phase composition, interactions between the components, and the rheological behavior of each component. Furthermore, deep insight into the foam morphology, fibrils emplacement in the cellular structure, and crystalline phase contribution under different foaming conditions and fibril contents have not been investigated. Accordingly, profound research on the development of nanofibrils that, on the one hand, thermodynamically tailor the arrangement of the PLA chains, and on the other hand, instruct a fine flexible network to modify the melt elasticity can enormously help to adjust the governing mechanisms in this method. The findings guide us in regulating conditions for the demanding foam properties, i.e., microcellular or nanocellular morphology, closed-cell or open-cell structure, and improved mechanical properties at low densities.

## 2 State of the Art

Over the last decade, great attempts were made to modify the processability, mechanical properties and foamability of PLA by its compounding with different kinds of nanoparticles <sup>26-28</sup>. In each study, apart from the improvement level, one or a combination of several mechanisms has been discussed, such as intense cell nucleation, crystallization kinetics enhancement, and melt strength modification. All of which stem from the very high aspect ratio of nanoparticles. In the following, the concept of adding nanoparticles to the matrix is overviewed, and then the proposed methodology in this thesis, which is to create nanofibers in situ, is explained in detail.

### 2.1 The concept of polymer nanocomposites

Nanomaterials are materials with morphological features on the nanoscale, and their special properties stem from their nanoscale dimensions. The European Commission offered a more precise definition: 50 % or more of the particles in the number size distribution is in size range of 1–100 nm <sup>29</sup>. A common characteristic feature of all nano-sized materials is the extremely increased ratio of surface area to volume. Discovery with a revolutionary effect in nanoscience was that of Iijima, who prepared carbon nanotubes (CNTs) <sup>30</sup>. It turned out that this all-carbon material is the ideal material ever created with the highest heat conductivity, highest electrical conductivity, the highest mechanical properties, etc., and thus attracted the attention of researchers from various fields, including polymer science and technology. For example, with tensile moduli in the terapascal range and lengths exceeding 10  $\mu\text{m}$  of carbon nanotubes, simple composite models predict order-of-magnitude enhancement in modulus at loadings less than 1 %. For this reason, a decade ago, it was believed that the most common polymer composites comprising about 30 % glass fibers would be replaced by the nanocomposites having only 2–5 % nano-sized filler as reinforcement! Unfortunately, this expectation turned out to be elusive <sup>31</sup>. The concept of polymer nanocomposites, i.e., the expectation that using 1–5 % of nanofiller instead of the common 30–40 %, failed for the following reasons: (i) poor dispersion, (ii) poor interfacial load transfer, (iii) process-related deficiencies, (iv) poor alignment, (v) poor load transfer to the interior of filler bundles, and (vi) the fractal nature of filler clusters <sup>32</sup>.

Nowadays, a relatively large number of nano-sized materials are available, and nevertheless, the preparation of true nanocomposites is not an easy task. The basic problem in manufacturing polymer nanocomposites is dispersing the reinforcing component to single nanoparticles in the

matrix material. Due to the inherent property of the nano-sized materials, namely, the extremely high specific surface, they tend to agglomerate. Thus their further dispersion in the matrix component is practically impossible. There is no convincing solution yet for the dispersion of the electrospun nanofiber webs and the control of the nanofiber orientation in the polymer matrix. Attempts to disperse single nanofibers from the nonwoven mats using ultrasound, kneaders, or high-speed stirrers have only been marginally successful. Very similar problems occurred in matrix reinforcement with carbon nanotubes and nanofilaments <sup>32</sup>.

## 2.2 In situ fibrillar composites

It has been established that the performance of an immiscible polymer blend not only depends on the physical characteristics of its components but also firmly on the phase interface and phase morphology, both of which are closely associated with the viscoelasticity of the polymer components and the flow histories during the manufacturing process <sup>33</sup>. For instance, the traditional approaches toward modifying the brittle behavior of PLA by formulating and associating with flexible biopolymers without specifically designed morphology were insufficient to realize the satisfactory combination of strength, stiffness, and ductility <sup>34, 35</sup>. Various flexible biopolymers, such as poly (butylene succinate) (PBS), poly[(butylene succinate)-co-adipate] (PBSA), and poly (butylene-adipate terephthalate)(PBAT), have been introduced into PLA to enhance the ductility and impact resistance, only to find limited promotion of ductility and impact toughness but greatly reduce strength and stiffness <sup>36-38</sup>. The incorporated plasticizers were found to emigrate gradually from the PLA matrix, a disadvantage caused by the cold crystallization of PLA during long-term usage. It arises from, in principle, the excessive phase separation caused by inherent immiscibility between the PLA matrix and the incorporated biopolymers.

The creation of actual polymer-polymer micro/nanocomposites distinguished by perfect distribution of micro/nanodomains in the matrix achieved via the application of the new converting instead of adding concept, i.e., converting the bulk polymer into nano-sized material instead of blending it with nanofillers, thus avoiding the practically nonsoluble problem of proper dispersion. In situ polymer-polymer microfibrillar composites obtained from immiscible polymer blends have been suggested as promising substitutes for traditional fiber-reinforced composites <sup>32, 39, 40</sup>. The selection of two immiscible polymers is carried out based on the final goal, i.e., toughening and/or reinforcement, and the final form of the composite, i.e., highly oriented or isotropic. Appropriate dispersion and distribution of induced fibrils, no need for mineral

additives, advanced mechanical properties, simple processing, controlling matrix crystallization, and complete recycling are some advantages of MFC novel materials with tailored morphologies<sup>41, 42</sup>. In the case of MFCs based on poly (lactic acid) (PLA), such benefits are integrated with renewability, biodegradability, and biocompatibility<sup>1, 43</sup>.

### 2.2.1 Highly oriented in situ fibrillar micro/nanocomposites

Pioneering exploration toward converting polymer blends into in situ fibrillar composites has been launched by Fakirov et al., revealing that intense shearing/stretching flow emerged as an advantageous strategy to control the phase morphology<sup>44, 45</sup>. Applying intense shear/elongational flow on the PLA/flexible biopolymer blends (e.g., PLA/PBS, PLA/PHB, and PLA/PBAT) to fibrillate the second phase has attracted many researchers' interest<sup>46-54</sup>. He et al. reported super-toughed in situ nanofibrillar PLA/thermoplastic poly (ester)urethane (TPU) composites<sup>52</sup>. Aligned TPU nanofibrils and favorable interfacial adhesion eventuated significant heterogeneous nucleating sites and enhanced notch impact strength extraordinarily. Xie et al. claimed improved mechanical properties were achieved for PLA/PBS highly oriented in situ nanofibrillar and nanolaminar composites prepared through melt stretching<sup>33, 47</sup>. Zhou et al. reported that the dispersed phase of PBAT in situ formed into nanofibrils by an intensive elongational flow field. Simultaneously sufficient row-nuclei for PLA were induced<sup>46</sup>. After appropriate thermal treatment with the acceleration effect of PBAT on PLA crystallization, oriented lamellae of PLA tend to be much more aligned in a preferential direction and constitute an interconnected network. The unique structure manifested superior ability in ameliorating the performance of PLA film. **Figure 2-1** schematically represents the structure evolution for the PLA/PBAT composite films.

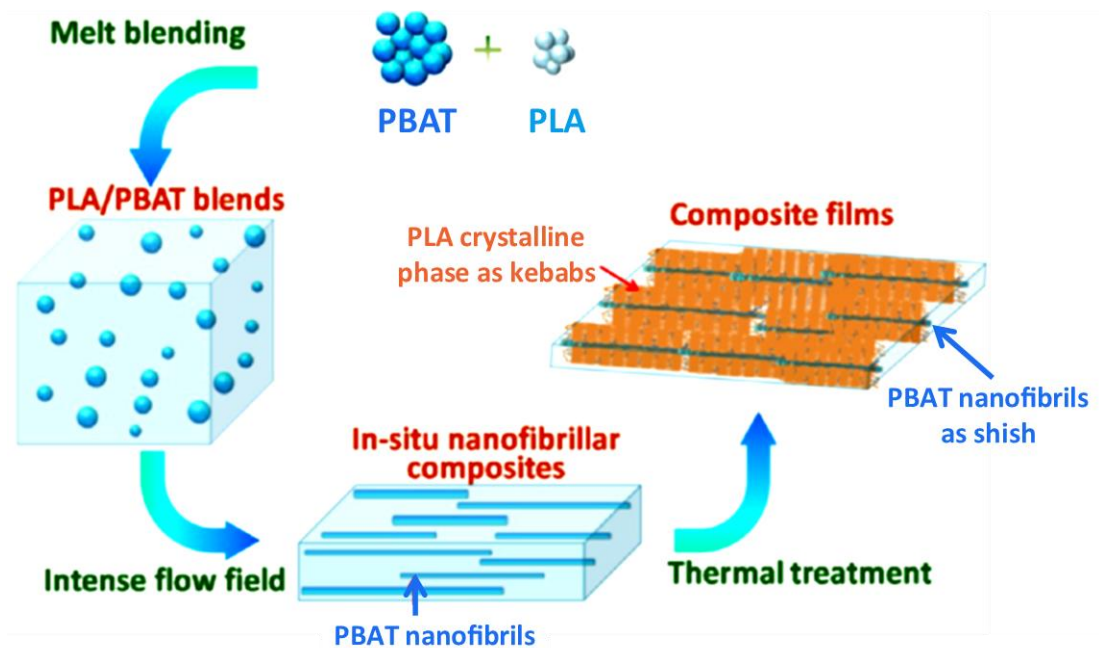


**Figure 2-1.** Schematic representation describing the processing approach and structure evolution for the PLA/PBAT composite films [7].

Liu et al. fabricated eco-friendly PLA/PBAT in situ nanofibrillar composites using the loop oscillating push-pull molding technique<sup>55</sup>. They showed that in situ PBAT nanofibrils acted as shish to nucleate PLA crystals (kebabs), resulting in a highly oriented hybrid shish-kebabs structure. The hybrid shish-kebab structure resulted in high mechanical performance and excellent heat resistance. They presented that the fibrillar structure of PBAT droplets and the hybrid shish-kebab structure did not form via a simple injection molding process.

Despite all the advantages of this approach, the prepared composite is not isotropic, and the second phase is not consistent for the post-processing of the matrix. Since the matrix's melting temperature is higher than that of fibrils, any future melt forming destroys the developed nano/microstructure. Besides, the structure can be achieved only under high shear and/or elongational flow, which limits the number of processing techniques and the shape of the composite. Hence, fibrillation of the second phase with a melting temperature much higher than that of the matrix (30-40 °C), which guarantees reinforcement and the consistency of the fibrils during the post-processing, has been noticed<sup>24, 56, 57</sup>.



## 2.2.2 Isotropic in situ fibrillar micro/nanocomposites

Two different techniques can be employed to create isotropic in situ fibrillar composites through the formation of reinforcing microfibrils. Herein, a significant number of investigations are categorized based on the techniques, parallelly describing each technique's manufacturing steps.

### 2.2.2.1 Hot-stretching of the melt blended constituents

In this technique, a well-distributed polymer blend is compiled from two polymers (the major phase A as a matrix and the minor phase B as a dispersed phase with the melt temperature of  $T_{mA}$  and  $T_{mB}$ ) by using conventional melt blending equipment. The melt passes through a spinneret die and forms fibers by hot-stretching. Meanwhile, the minor phase in the blend is oriented in the die direction and subsequently transforms into highly oriented and high aspect ratio microfibrils<sup>58, 59</sup>. To transfer the fibers into isotropic MFCs (e.g., laminates), the spun fibers which contain the microfibrils are chopped and then processed (e.g., compression molding) in a temperature window ( $T_{process}$ ) between the melt temperature of the two polymers ( $T_{mA} < T_{process} < T_{mB}$ ). Control of the  $T_{process}$  is critical to the successful creation of M/NFCs as it ensures the formation of an isotropic matrix while retaining the reinforcing fibrils. It should be high enough to let the matrix fuse and forms an isotropic structure. While if  $T_{process}$  is too high, the fibrils will melt, and the reinforcing effect will be lost<sup>32</sup>. **Figure 2-2** presents the scheme of a setup for the manufacturing of MFCs<sup>60</sup>.

The draw ratio is defined as  $Dr = U_s/U_0 = \left( D_{die}/D_{fiber} \right)^2$ , where  $U_s$  is the collection velocity or spool velocity,  $U_0$  is the average velocity of the melt passing through the spinneret,  $D_{die}$  is the die diameter and  $D_{fiber}$  is the fiber diameter<sup>61</sup>. Draw ratios over 2000 has been used in industrial scale and reported by researchers<sup>25</sup>. Many melt spinning setups are equipped with a collection system including spools with different velocities to apply a second drawing on the extruded filaments or fibers. The second drawing takes place under controlled temperatures higher than the glass transition temperature ( $T_g$ ) of the extrudates. In this case, the draw ratio can be calculated as the ratio of the spool speeds which is usually reported in the range of 2 to 7<sup>62, 63</sup>. In the current study a second draw ratio was not applied and the fibers were directly winded.

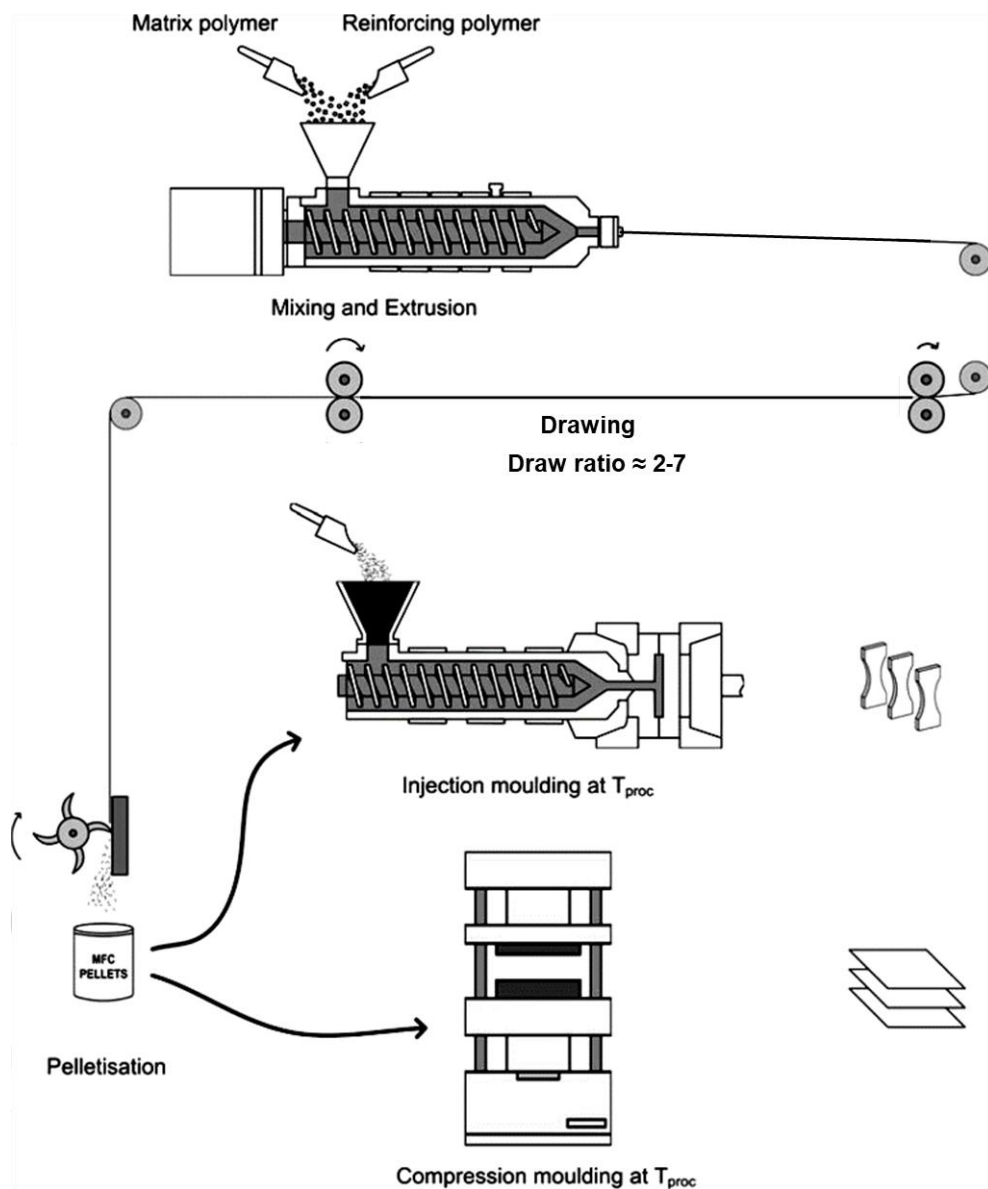


**Figure 2-2.** Schematic setup for the manufacturing of MFCs <sup>60</sup>.

Three key requirements must be fulfilled to manufacture the MFCs which are: i) the polymer components should have a sufficient drawability for the formation of reinforcing microfibrils; ii) processing of the polymers must be possible at a single temperature without significant degradation of one of the constituents; and iii) the melting temperature of the reinforcing polymer should be at least 40 °C higher than the melting temperature of the matrix, to guarantee constancy of the microfibrils during the matrix consolidation <sup>60</sup>. On the other hand, for the preparation of MFCs, the two components should not be miscible but should be highly compatible. The interactions of the two polymers at their interface and their rheological behavior at the processing conditions determine the deformability of the droplets <sup>64</sup>.

Fakirov et al. obtained a morphological confirmation of the contribution of coalescence to the fibril formation mechanism, and in this way, they explained the large differences in sizes of the starting spheres and the resulting long microfibrils <sup>65</sup>. Using PP/PET blends with and without compatibilizer, the peculiar property of compatibilizers has been exploited, namely coating the dispersed particles and thus preventing them from eventual coalescing after coming in contact. With the progress of drawing, the initially spherical particles were transformed into rotational ellipsoids (**Figure 2-3**). As the drawing continues, these ellipsoids become thinner and longer, transforming into cylindrical bristles, and are brought closer to each other initiating end-to-end coalescence to build up uniform microfibrils. In contrast, the MFCs from compatibilized blends show much shorter microfibrils because the compatibilizer inhibits the coalescence process. After that, researchers reported on the minimum amount of reinforcing component, which is necessary for the end-to-end mechanism resulting in the coalescence of the droplets and long fibril formation <sup>62, 66</sup>. For instance, Xing et al. reported that the melt-spinning process of PP/PS blends at low contents of PS (<4 wt%) was incapable of fibrillating the dispersed phase <sup>66</sup>. However, Bigdeli et al. showed that the compatibilization of PP/PBT blends resulted in a fine distribution of PBT droplets and uniform long microfibrils of the dispersed phase <sup>67, 68</sup>.

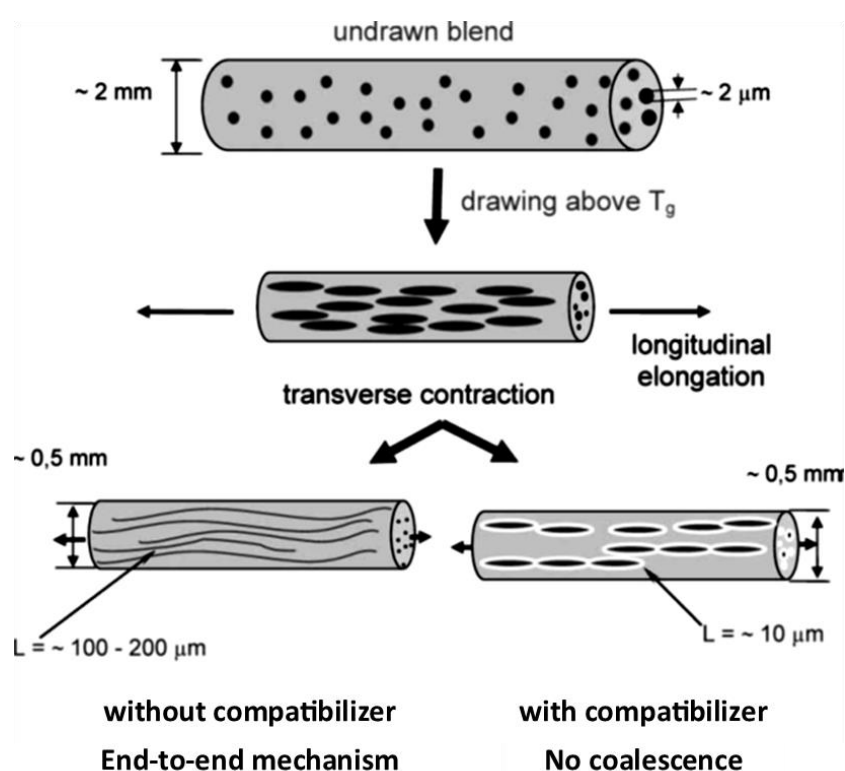


**Figure 2-3.** Schematic of the transformation of the spherical particles into microfibrils via coalescence under transverse contraction <sup>65</sup>.

Recently, Zhao et al. elucidated the matrix viscosity influences and the reinforcement content on the nano-phase morphology development in a PP/PET system <sup>69</sup>. The study found that the coalescence and morphology change in the nanofibrillation process depends on both the matrix viscosity and the reinforcement (PET) concentration. With a low melt flow rate (MFR) matrix, the second phase was easily deformed, and coalescence occurred at a low concentration. However, for a high MFR matrix, the critical concentration was much higher than samples using a low MFR matrix. By applying these findings, a PP/PET composite with PET fibrils with a diameter of less than 200 nm was successfully made.

Zuo et al. unveiled a melt-blowing process equipped with a new die design (**Figure 2-4**) for the fibrillation of polymer blends with poor melt strengths that could not be stretched efficiently in the hot-stretching process <sup>70</sup>. The melt-blowing of the blends of poly (ethylene-co-chlorotrifluoroethylene) (PECTFE) in PBT, PECTFE in PS, and PBT in PS were successfully performed. The melt-blowing of the three sets of immiscible polymer blends containing 25 % by volume of the minor phases led to well-stretched fibers with average diameters of about 13  $\mu\text{m}$  and length of about 100  $\mu\text{m}$ . The nanofibrils of the minor phases with diameters less than 100 nm were formed in the melt-blow fibers.

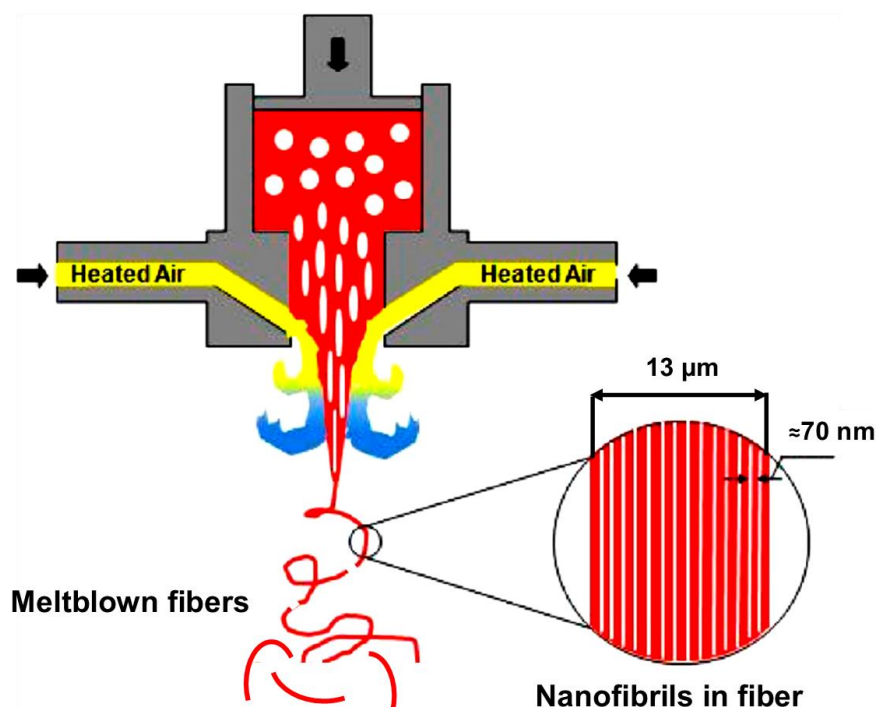


**Figure 2-4.** Schematic of nanofibrils in fiber fabrication by melt blowing <sup>70</sup>.

Soltani et al. produced melt-blown fibers with a diameter of 1-2  $\mu\text{m}$  out of immiscible blends of sulfonated poly (ethylene terephthalate) (SP)/PBT and PS/PBT <sup>71</sup>. By comparing the two blends at different blend ratios, the PBT drop size in PS/PBT blends was significantly smaller (**Figure 2-5A**). Since the viscosity ratios of the two blends were almost similar, this size difference was related to significantly lower interfacial tension between PBT and SP in comparison with PBT and PS. The low interfacial tension was possibly a result of the transesterification reactions. The PBT nanofibrils formed in PS matrix were about 300 nm in diameter, while the PBT nanofibrils formed in SP had roughly half of that diameter (**Figure 2-5B**).

The same study also investigated the effect of dispersed phase viscosity using two kinds of hydrophobic polyvinylidene fluoride (PVDF) as dispersed phases in the SP matrix. The viscosity of PVDF1 was 3 times higher than that of PVDF2. At a high shear viscosity ratio,  $\eta_{\text{minor}}/\eta_{\text{matrix}} > 3$ , that was the specification of SP/PVDF1, the nanofibrils showed a higher level of irregularities. With PVDF2, a record low average nanofibril diameter of 36 nm was achieved. For both matrixes (4 blends), despite a significant increase in blend drop size upon increasing the minor phase fraction, the nanofibril diameter increased only slightly (**Figure 2-5**). Thus, Soltani et al. conjecture that nanofiber diameter was mainly controlled by fiber pinch-off, induced by quick stretching during the melt blowing process, rather than initial drop size. The stretch/pinch-off combination was speculated to be controlled by interfacial tension and also the viscosity of the minor phase. Similar observations about a significant increase in droplet size upon increasing the minor phase fraction while a slight increase in microfibrils diameter was reported on PBS/PLA isotropic MFCs, including 3-20 wt% of PLA microfibrils, in which the two polymers are well-known as highly compatible bio-polymers <sup>72</sup>.

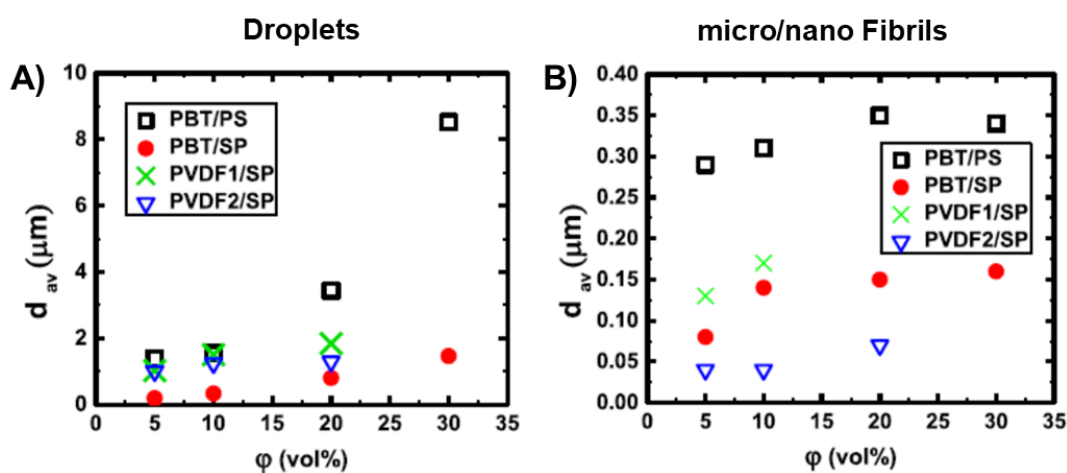


**Figure 2-5.** (A) Blend drop diameter vs. dispersed phase content, and (B) Nanofibril diameter variation vs. dispersed phase content <sup>71</sup>.

Kakroodi et al. introduced extrusion and hot-stretching for the production of PLA/polyamide 6 (PA6) MFCs for improving PLA's properties while minimizing the required PA6 content<sup>24, 25</sup>. The MFCs, including 3 wt% of PA6 microfibrils with an average diameter of 200 nm, were shown to have dramatically improved crystallization kinetics, melt elasticity, foamability, and mechanical strength compared to a droplet-matrix morphology. Mahmud et al. reported on isotropic PA6-based NFCs containing polyphenylene sulfide (PPS) nanofibrils, which were produced combining melt compounding and hot stretching<sup>57</sup>. Before stretching, the PPS droplets with an average diameter of 210 nm were dispersed and distributed uniformly in the PA6 matrix (**Figure 2-6**), regardless of its concentration, which was attributed to the low interfacial tension between these two phases. The compatibility between the two blends was confirmed by measuring the component's surface free energy at room temperature and extrapolating the interfacial tension between the components to the processing temperature. The nanofibrillar networks formed after hot-stretching and consolidation of the matrix with an average diameter of 60 nm. The fine structure of PPS nanofibrils at different concentrations are shown in **Figure 2-7**. Up to 5 wt% of PPS nanofibrils did induce a significant difference in the stress-strain curves with the evolution of multiple necking and strain hardening. This behavior was explained by the formation of transcrystalline structures and small crystal size in the presence of the fibril network.

Kakroodi et al. observed that the transformation of a dispersed PLA phase into stretched nanofibrils drastically improved PCL/PLA interfacial adhesion, which could be due to PCL's heterogeneous crystal nucleation on the nanofibrillated PLA domains<sup>56</sup>. The isotropic NFCs showed improved mechanical properties and dramatically improved oxygen barrier properties due to the improvements in the PCL/PLA compatibility.

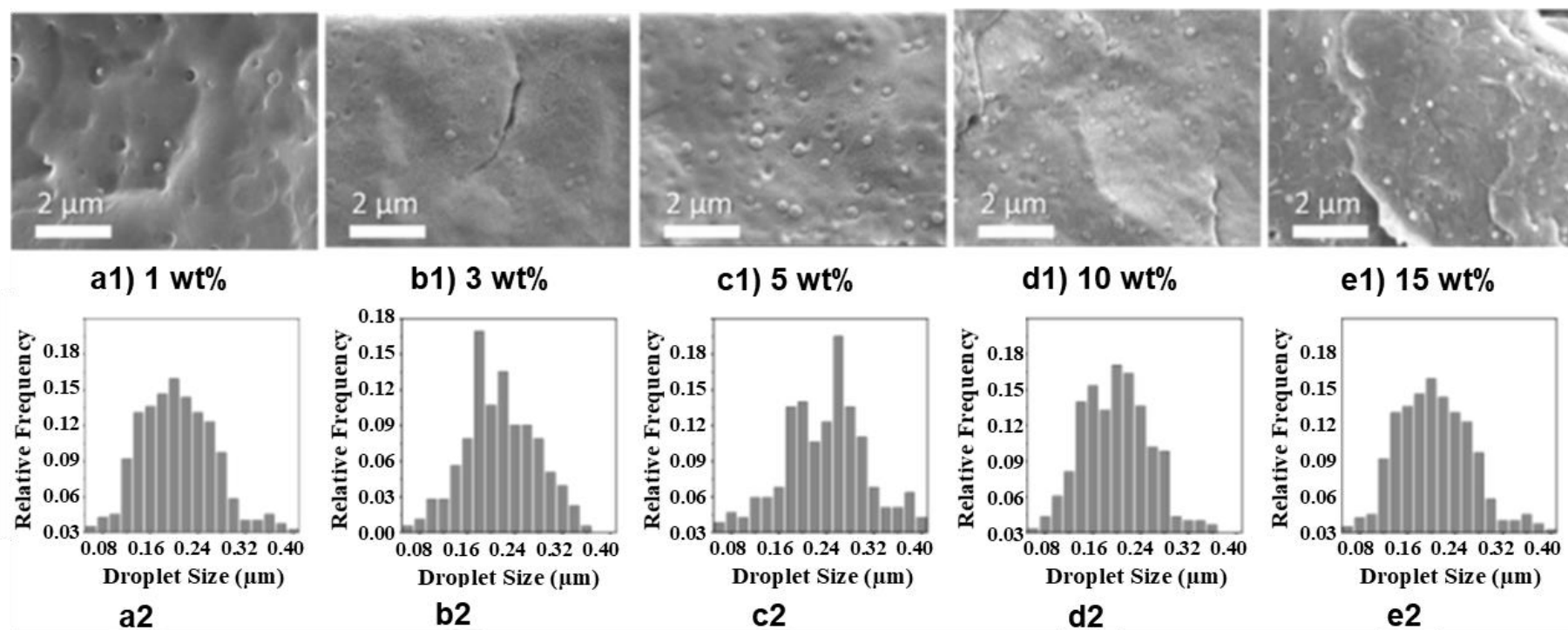


**Figure 2-6.** PA6/ PPS blends with different PPS concentrations; (a1) 1 wt%, (b1) 3 wt%, (c1) 5 wt%, (d1) 10 wt%, and (e1) 15 wt% SEM photographs, and (a2) 1 wt%, (b2) 3 wt%, (c2) 5 wt%, (d2) 10 wt%, and (e2) 15 wt% droplet size distribution <sup>57</sup>.

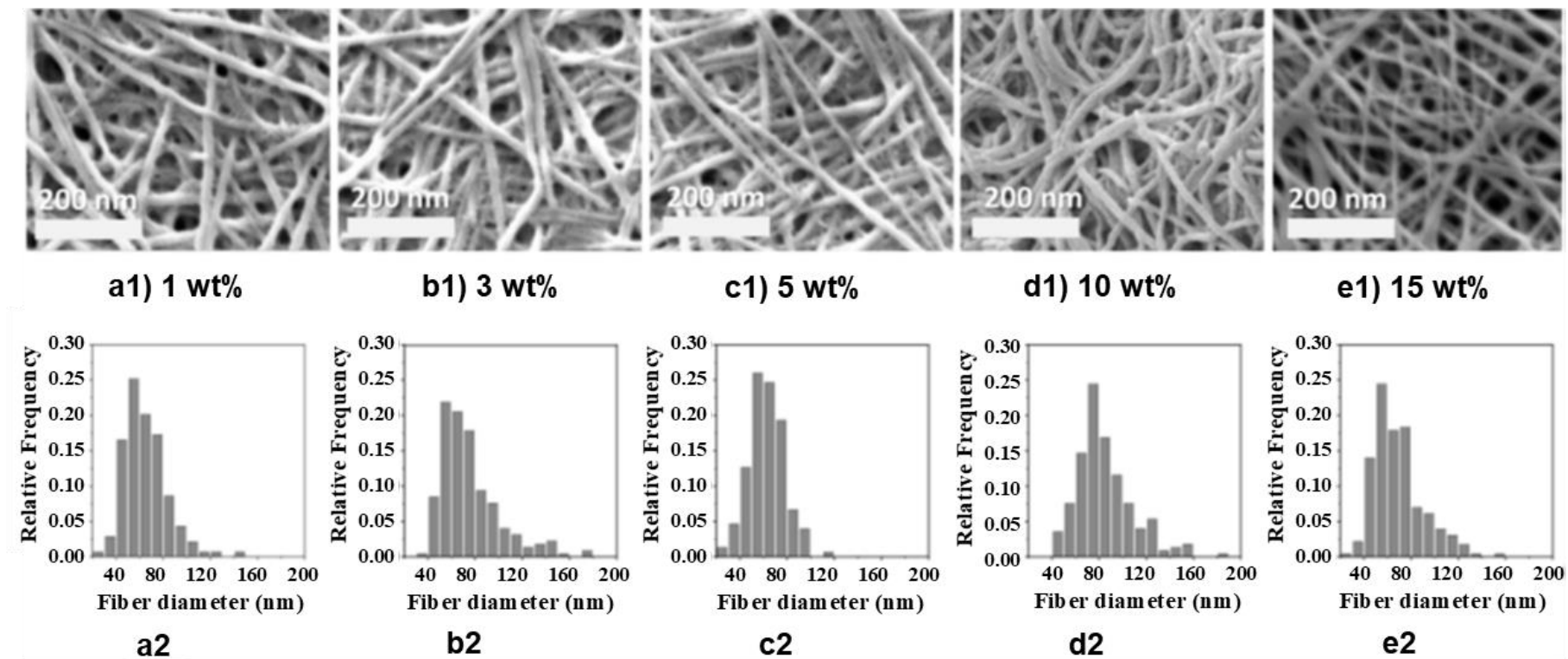


**Figure 2-7.** PPS nanofibrils after etching of the PA6 matrix from PA6/ PPS NFCs with different PPS concentrations; (a1) 1 wt%, (b1) 3 wt%, (c1) 5 wt%, (d1) 10 wt%, and (e1) 15 wt% SEM photographs, and (a2) 1 wt%, (b2) 3 wt%, (c2) 5 wt%, (d2) 10 wt%, and (e2) 15 wt% fibril size distribution <sup>57</sup>.



### 2.2.2.2 Shearing dispersed crystalline polymer in another molten polymer

In this method, polymer fibrils form via a single-step extrusion process. The most critical points for such a fibrillation method are first, selecting fibrillating polymer based on the criteria of low chain entanglements along with their high crystallinity; second, applying intensive uniform shear rate. Under intensive shear flow field, deformation of polymer crystals to large strains is possible when the density of entanglements persisting in the amorphous phase is drastically reduced<sup>73</sup>. Jurczuk et al. introduced applying intensive shear during compounding for the generation of polytetrafluoroethylene (PTFE) nanofibrils and, thus, forming all-polymer nanocomposite<sup>73</sup>. PTFE powder particles should be of high crystallinity with unentangled macromolecules and consist of crystals with melting temperatures (332-336 °C) exceeding that of the melt processing temperature. The larger the deformation ratios and shear rates, and the longer the shearing times, the thinner and stronger PTFE nanofibers were obtained. The nanofibrils could be generated during the uniform shearing of solid PTFE particles dispersed in a molten polymer like isotactic PP, high-density PE, low-density PE, and PS. The fibrillar morphology adopted by the PTFE component is a consequence of its low yield strength to undergo plastic deformation, particularly at elevated temperatures<sup>74</sup>.

Rizvi et al. used this approach to prepare isotropic MFCs out of PP/PTFE, metallocene-catalyzed polyethylene (mPE)/PP, and PP/PET immiscible blends<sup>58, 75, 76</sup>. **Figure 2-8** represents the PTFE fibrillar structures of large aspect ratios (the diameter of fibrils is less than 500 nm, and their lengths seem to exceed 100 µm).

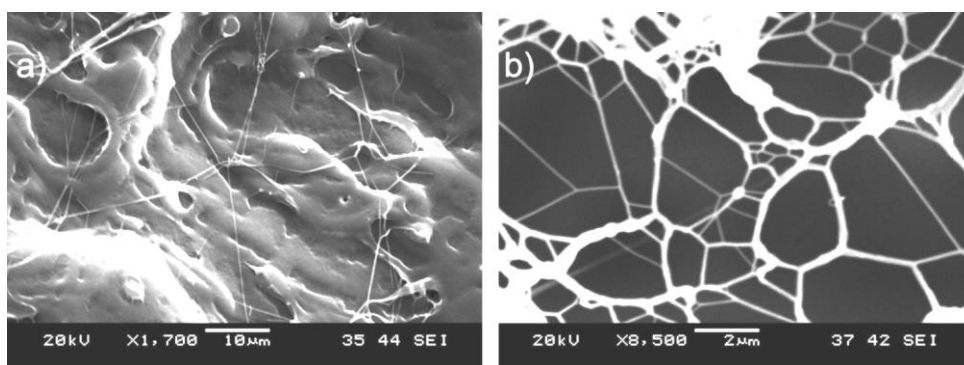


**Figure 2-8.** SEM micrographs of the morphology of PTFE nanofibrils: a) obtained after solvent-vapor etching; b) obtained after removal of PP using xylene<sup>75</sup>.

## 2.3 Rheological studies

### 2.3.1 Melt rheological studies for in situ development of polymer fibrils

Melt blending of polymers with specifically tailored morphology has been studied as a promising method to gain satisfactory improvements in the different demanding properties such as thermal, mechanical, and electrical properties<sup>33, 47, 77</sup>. Melt rheology and interfacial tension between the blend constituents play major roles in sketching the final morphology<sup>78, 79</sup>. The morphology of immiscible polymer blends is formed by droplet deformation, breakup, and coalescence, within the matrix<sup>65</sup>. Taylor found that in a Newtonian droplet-matrix system, at low strains, the droplet deformation can be expressed based on the following two dimensionless parameters. First, the viscosity ratio of the dispersed phase ( $\eta_d$ ) to that of the matrix ( $\eta_m$ ) which is designated as  $\lambda = \eta_d/\eta_m$  and second, the capillary number (Ca) which explains the competition between the applied stresses on the droplet by the extensional field to deform it, and the interfacial tension between the two phases, which recovers the spherical shape of the droplet<sup>80</sup>. The capillary number is defined as follows<sup>81</sup>:

$$Ca = \frac{\sigma_{ij} R}{\nu_{12}} \quad (2-1)$$

Where  $\sigma_{ij}$  denotes the stress, either of shear or extensional type (for which  $ij = 12$  or  $11$ , respectively),  $R$  is the droplet diameter and  $\nu_{12}$  is the interfacial tension coefficient between the two phases. In a shear flow, the minimum necessary shear rate at which viscous forces dominate the interfacial ones and breakup the droplet is called the critical shear rate ( $\dot{\gamma}_c$ ). The corresponding capillary number (i.e., the critical capillary number), designated as  $Ca_{(c)}$ , is calculated using **Equation ( 2-2 )**:

$$Ca_{(c)} = \frac{\eta_m \dot{\gamma}_c R}{\nu_{12}} \quad (2-2)$$

Taylor (1934) and Grace (1971) showed that the critical Capillary number depends both on the type of flow and on the viscosity ratio,  $\lambda$ , between the dispersed and continuous phases<sup>82</sup>. The Grace curve<sup>83</sup> with an empirical equation gives a U-shaped plot of  $Ca_{(c)}$  vs.  $\lambda$  in a pure shear flow and/or 2D elongational flow for the breakup of a droplet in a Newtonian system (**Figure 2-9**). The curve shows a minimum in the range of  $0.1 < \lambda \leq 1$ , which is indicative of the maximum possibility of droplet deformation and tends to infinity for  $\lambda > 4$ , which is recognized as a non-

dispersible blend in shear flow. It should be noticed that the critical Capillary number considers drop breakup under quasi-equilibrium conditions, without including the time.

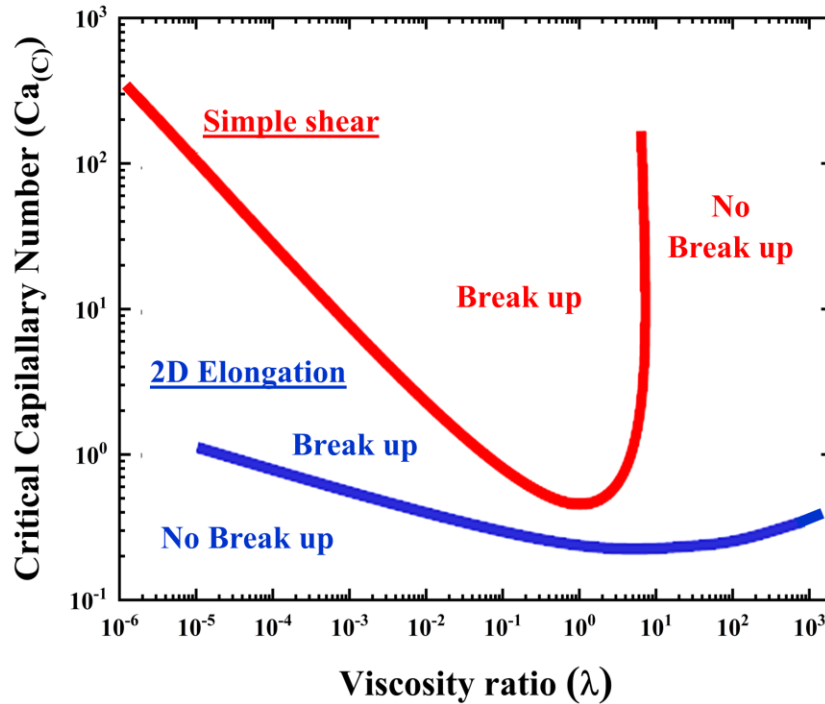


**Figure 2-9.** The Grace curve gives the relation between the critical capillary number  $Ca(c)$  and the viscosity ratio  $\lambda$  for the breakup of an initially spherical droplet in quasi-steady homogeneous flow (in simple shear and 2D elongational flow) <sup>83</sup>.

Wu reported that the critical capillary number  $Ca(c)$  is more important in the case of viscoelastic blends compared to newtonians ones. He suggested an empirical equation that results in a V-shaped curve for the dependency of  $Ca(c)$  to  $\lambda$ , with a minimum at  $\lambda \approx 1$  given by <sup>84</sup>:

$$Ca_{(c)} = 4 \left( \frac{\eta_d}{\eta_m} \right)^{\pm 0.84} \quad (2-3)$$

Here, the exponent is positive if  $\lambda > 1$  and negative if  $\lambda < 1$ . It is noteworthy that in an elongational flow field,  $Ca(c)$  is less dependent on the viscosity ratio. Therefore, a high deformation of droplets can be achieved over a broader range of  $\lambda$  in an elongational flow compared to the shear flow <sup>85</sup>. At a given viscosity ratio, the ratio of a capillary number to the critical capillary number of the flow field,  $\lambda' = Ca/Ca_{(c)}$ , defines the mode of droplet deformation and breakup <sup>81, 86, 87</sup>:

If  $\lambda' < 1$ , the droplet deforms slightly but does not break.

If  $1 \leq \lambda' \leq 2$ , the viscous stress dominates the interfacial stress, and the drop breaks into two equal parts before elongation occurs.

If  $2 \leq \lambda' \leq 4$ , the droplet deforms into unstable elongated fibril and experiences fragmentation to smaller droplets subsequently.

If  $\lambda' > 4$ , the shear stresses overwhelm the interfacial tension and intense deformation of the droplet leads to an elongated stable fibril<sup>88</sup>.

A clarified limitation of this concept is that in conventional mixing processes, the capillary number is generally much larger than the critical capillary number<sup>89</sup>. Therefore, the elasticity ratio ( $\lambda''$ ) between the dispersed phase and the matrix should be taken into account to obtain the optimal conditions for fibril formation<sup>90-93</sup>. Based on the literature, when the matrix is more elastic than the dispersed phase, a fine dispersion and transformation to elongated fibrils are more likely to occur in shear and elongational flows.

In summary, a low interfacial tension between the dispersed phase and the matrix, along with a viscosity ratio of  $\lambda \leq 1$ , a capillary number to the critical capillary number ratio of  $\lambda' > 4$ , and an elasticity ratio of  $\lambda'' \ll 1$ , are necessary to transform a droplet-matrix morphology into a fine fibrillar structure. However, these are not sufficient to define a condition for forming a stable fibrillar morphology. The relaxation time of the elongated droplets and the residence time inside and outside the die can also play essential roles in determining the stability of the fibrils<sup>64, 81</sup>.

The elasticity ratio ( $\lambda''$ ) is characterized by the ratio of the storage modulus of the dispersed phase to that of the matrix ( $G'_d/G'_m$ ) as well as the Weissenberg number (Wi) ratio, which is known to represent the melt elasticity<sup>91, 94</sup>. In a simple shear flow, Wi gives the ratio of the elastic forces to the viscous ones:

$$Wi(\dot{\gamma}) = Wi(w) = \frac{G'}{G''} \quad (2-4)$$

Accordingly,  $\lambda''$  can be calculated based on the Wi ratio as follows:

$$\lambda'' = \frac{Wi_d}{Wi_m} = \frac{(G'/G'')_d}{(G'/G'')_m} \quad (2-5)$$

Some researchers developed in situ micro/nanofibrils of polyolefins in thermoplastic polyurethane (TPU) and polypropylene (PP) matrixes by adjusting the viscosity ratio<sup>95, 96</sup>. Yousofi

et al. compared the in situ fibrillation of PLA/PA11 blends with PLA/PA6 blends processed by a twin-screw extrusion followed by injection molding <sup>91</sup>. Additionally, using a multi-step reactive extrusion route, they modified the melt elasticity of PLA with an epoxy-based chain extender (PLA-j) and conducted in situ fibrillation of PLA-j/PA11 and PLA-j/PA6 blends. They deeply discussed the morphological observation of the extruded blends and NFCs via rheological investigation to highlight the contribution of viscosity, elasticity, and interfacial tension. The existence of a critical shear rate was emphasized for the transition from nodular to fibrillar morphology, which was in good agreement with the condition of fibrillation  $Ca/Ca_{(c)} \geq 4$ . Interestingly, with the exception of PLA/PA6 specimens, all blends obviously displayed uniform thin-thread fibrillar morphologies after injection molding.

García-Masabet et al. improved the elasticity of PLA by reactive extrusion <sup>97</sup>. They induced the in situ nanofibrillation of PLA/bio-based Polyamide 1010 (PA1010) blends, which resulted in enhanced mechanical properties of PLA-based NFCs. They induced the in situ nanofibrillation of PLA/bio-based Polyamide 1010 (PA1010) blends, which resulted in enhanced mechanical properties of PLA-based NFCs. They found that the coalescence and morphology development in the nanofibrillation process depends on both the matrix viscosity and the reinforcement concentration. Meanwhile, other researchers concentrated on the rheological behavior of the components in the elongational flow after a spinneret <sup>62, 63</sup>.

The stability of the induced droplet deformation in the die could be evaluated by comparing breakup time and residence time inside the die. In a simple shear flow with an affine deformation, Huneault et al. suggested **Equations ( 2-6 )** and **( 2-7 )** to estimate the breakup time of the fibrils <sup>81, 98</sup>:

$$t_b = \left[ \frac{\eta_m \ln(\alpha_f/\alpha_i)}{2\nu_{12}\Omega(X_m, \lambda)\dot{\gamma}^{1/2}} D_0 \right]^{2/3} \quad ( 2-6 )$$

$$\alpha_i = \left( \frac{21k_b T}{8\pi\nu_{12}} \right) \quad ( 2-7 )$$

Where  $D_0$  is the initial fibril diameter, and  $\Omega$  is a function of the viscosity ratio ( $\lambda$ ) and of the instability wave number  $X_m$  <sup>99</sup>. The  $\alpha_i$  and  $\alpha_f$  are the initial and breakup amplitudes, respectively, and  $k_b$  is Boltzmann constant ( $1.38 \times 10^{-23} \text{ m}^2\text{kg/s}^2\text{K}^{-1}$ ). By assuming that breakup occurs when the amplitude of the sinusoidal deformation is equal to the average diameter of the fibril,  $\alpha_f$  is  $0.82D_0$  <sup>98</sup>. Therefore, under shear flow, breakup time is a function of the initial particle diameter

and shear rate. Using the same assumptions as in the shear flow, Huneault et al. developed an equation for the breakup time under elongational flow as follows:

$$t_b = \left(\frac{2}{\dot{\epsilon}}\right) \ln \left( \frac{\eta_m \ln(\alpha_f / \alpha_i) \dot{\epsilon}}{2v_{12}\Omega(X_m, \lambda)} D_0 \right) \quad (2-8)$$

Where  $\dot{\epsilon}$  is the strain rate in the shear-free flow.

## 2.3.2 Melt rheological studies of isotropic M/NFCs

### 2.3.2.1 Shear rheology

In pure polymers, the melt rheological properties are controlled by the degree of topological interactions (entanglement) of the polymer chains as well as by the friction between the molecules<sup>100</sup>. The addition of fillers can alter the rheological properties of polymers significantly depending on the filler's concentration, size, shape, deformability, level of dispersion, and the degree of interaction between the polymer and the fillers<sup>100</sup>. Thus, the study of the viscoelastic behavior of polymer composites can provide insight into their microstructure.

Kakroodi et al. studied the viscoelastic behavior of PLA/PA6 blends and MFCs in the matrix melt state to compare the effect of solid spherical PA6 domains on the viscoelastic behavior of PLA with that of the fibrillar structure (**Figure 2-10**)<sup>25</sup>. The pure PLA and the blends, including up to 7 wt% of spherical PA6 domains, had a classic viscoelastic response over the studied angular frequency range (**Figure 2-10A1–A3**). The semilogarithmic plots of the phase angle ( $\delta$ ) versus the complex shear modulus ( $G^*$ ) (van Gurp plots) of these blends were calculated to be about  $90^\circ$  implying the dominance of the viscous flow. Only high concentrations (that is, 15 and 25 wt%) of PA6 spheres caused a significant increase in  $G'$  and decreased the loss tangent of the PLA melt. In the blends with high PA6 contents, the increase in the melt elasticity was confirmed by a dramatic reduction in the values of phase angles. The increase in the PLA melt elasticity at high concentrations of PA6 spheres was explained by the restriction of the PLA chain mobility (slower relaxation) in the vicinity of the solid PA6 spheres.

**Figure 2-10B1** shows that the presence of only 3 wt% of in situ generated PA6 microfibrils was sufficient to increase the PLA melt elasticity by an impressive 3 orders of magnitude at very low shear rates. Further, the frequency-dependence of  $G'$ , especially at low frequencies, was substantially weakened after the addition of PA6 microfibrils. This was indicative of the transition from a liquid-like to a solid-like state. The addition of 3 wt% PA6 microfibrils also reduced the loss tangent (**Figure 2-10B2**) and the phase angles (**Figure 2-10B3**) of the MFCs, indicating the elastic behavior dominance. Such an increase in the melt elasticity suggests the formation of a physically entangled network, which would have been created by the topological interactions of the PA6 microfibrils. This phenomenon is also known as physical gelation or rheological percolation. Such a network is a typical characteristic of composites with deformable and high aspect ratio fibrils.

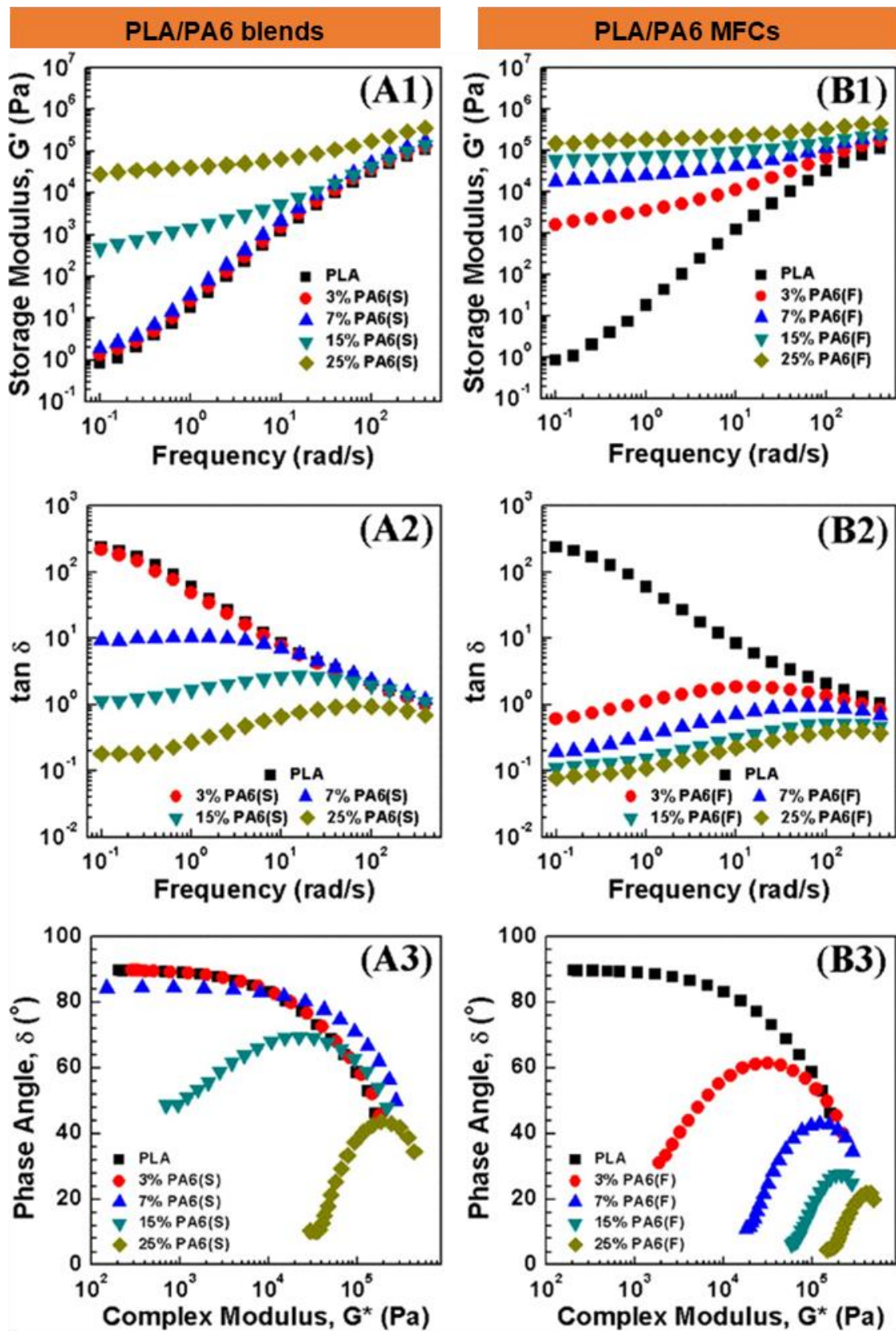
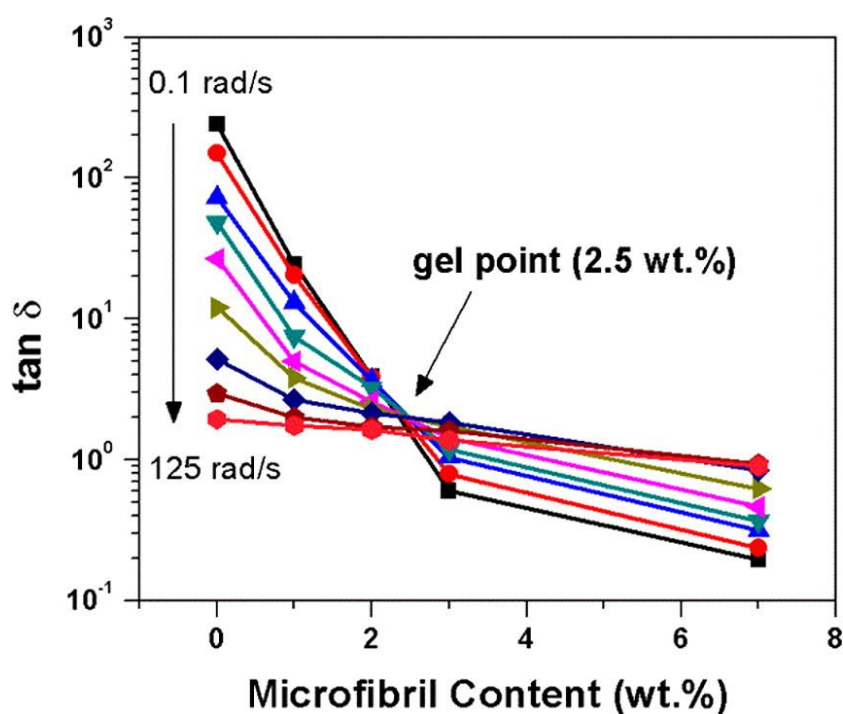


Figure 2-10. Linear viscoelastic behavior (at 180 °C) of pure PLA compared with PLA/PA6 blends with spherical (A1–A3) and microfibrillar (B1–B3) domains of PA6. (S) and (F) stand for blends with spherical and microfibrillar PA6 domains, respectively <sup>25</sup>.



Winter and Chambon suggested that at the gel point, where physical or chemical gelation occurs,  $G'$  and  $G''$  have similar dependencies on the frequency<sup>101</sup>. As a result, the loss tangent is independent of frequency at the gel point. Based on Winter and Chambon's criterion, the gel point in PLA/PA6 MFCs can be depicted at a microfibril content of nearly 2.5 wt% at which the lines of loss tangents ( $\tan \delta$ ) of different frequencies intersect (**Figure 2-11**).



**Figure 2-11.** Loss tangent vs. microfibril content at different frequencies ranging from 0.1 to 125 rad/s. The frequency tests were performed at 180 °C. The different lines represent different frequencies. The gel point appears as the point where the loss tangent is independent of the frequency (that is, where lines intersect)<sup>25</sup>.

Huang et al. showed that the storage modulus and complex viscosity of PP/PA66 MFCs were improved with increasing fibrillar aspect ratio<sup>102</sup>. Meanwhile, the  $\tan \delta$  values decreased, and the radius of the Cole-Cole plot circle increased with an increase in the fibrillar aspect ratio. The gel point concentration decreased with the increasing fibrillar aspect ratio due to the increased interfacial area and enhanced the entangled network structure. Similar results were reported on the linear viscoelastic behavior of other MFCs<sup>103-105</sup>.

### 2.3.2.2 Elongational rheology

The physical entanglement of macromolecules mainly controls a polymeric melt response to an extensional flow <sup>106</sup>. These entanglements, in turn, depend on the molecular structure, such as length, deformability, and the degree of branching. Extensional viscosity  $\eta_E$  measures the resistance against extensional flow. The transient extensional viscosity is a function of both the strain rate and time and is expressed as the tensile stress growth coefficient,  $\eta_E^+$ :

$$\eta_E^+(t, \dot{\epsilon}) = \frac{\sigma_E^+(t, \dot{\epsilon})}{\dot{\epsilon}} \quad (2-9)$$

Where  $\sigma_E^+$  is the tensile stress growth function and  $\dot{\epsilon}$  is the extensional strain rate. According to the Trouton relation, the transient extensional viscosity,  $\eta_E^+$ , is equal to 3 times the transient shear viscosity in the linear viscoelastic regime,  $\eta^+(t)$ , for a sufficiently small strain rate <sup>107, 108</sup>. Deviation from the Trouton relation can be used to evaluate the degree of strain hardening through:

$$\chi = \frac{\eta_E^+(t, \dot{\epsilon})}{3\eta^+(t)} \quad (2-10)$$

While the biaxial extension is the primary mode of deformation during foam processing, uniaxial extensional measurements are more readily available and used to measure the strain hardening behavior of the polymers <sup>75</sup>. Many research groups followed the chemical modification approach and suggested a wide variety of substances to modify the low melt strength of PLA <sup>3</sup>; however, so many studies have exploited the incorporation of additives <sup>23</sup>. Kakroodi et al. showed that the inclusion of 3 wt% of PA6 microfibrils led to significant improvements in the PLA melt elongational viscosity (**Figure 2-12**) and thus foaming ability <sup>25</sup>. They showed strong strain hardening effects (nearly one order of magnitude increase in the elongational viscosity) due to a three-dimensional network of deformable and well-dispersed PA6 in situ generated microfibrils. Wang et al. showed similar results about the presence of 10 wt% of PET nanofibrils on the strain hardening and foaming ability of PLA/PET NFCs <sup>103</sup>.

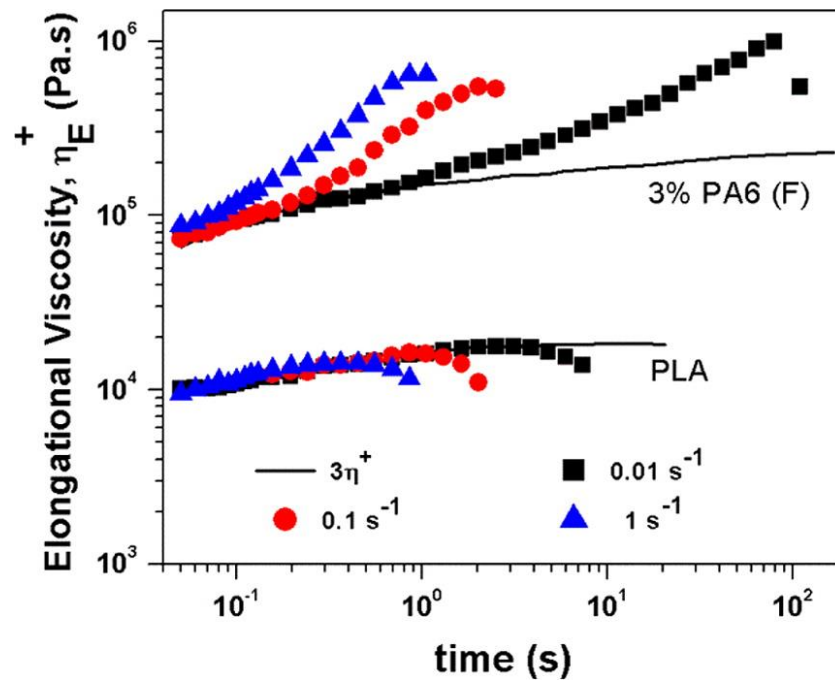


**Figure 2-12.** Uniaxial elongational responses of PLA and PLA/PA6:97/3 wt% MFC melts at strain rates of  $0.01$ ,  $0.1$ , and  $1 \text{ s}^{-1}$  <sup>25</sup>. The elongational viscosity tests were performed at  $170 \text{ }^\circ\text{C}$ .

## 2.4 Crystallization phenomena

PLA drawbacks in the amorphous state, such as poor mechanical performance and thermal stability, changed this goal to a dream. Amorphous PLA turns brittle rapidly upon physical aging, which occurs readily during several hours of storage at room temperature <sup>109</sup>. Concurrently, imperative investigations have been carried out to enhance PLA's slow crystallization rate since the degree of crystallinity and modified crystallization morphology have been known as skeleton keys for improving the mechanical and thermal performances of semicrystalline polymers. In this regard, incorporating different kinds of additives has been studied to benefit from their features <sup>110-112</sup>. Nevertheless, the  $T_g$  of PLA that is higher than the room temperature in association with crystallinity resulted in brittle behavior. Therefore, PLA applications have been restricted to a few specialized areas, such as disposable dishes prepared by injection molding <sup>113</sup>, films, and fibers <sup>109, 114, 115</sup>.

The crystallinity of PLA is intrinsically a function of its two enantiomeric isomers ratio (L-lactide to D-lactide) <sup>116</sup>. The most common PLLA crystal form is  $\alpha$ -form, which occurs in conventional melt and solution crystallization conditions <sup>117</sup>. The disorder  $\alpha$ -form ( $\alpha'$ ) was proposed for a PLLA sample crystallized below 120 °C <sup>118</sup>. However, more studies suggested that only the  $\alpha'$  crystal is formed at crystallization temperatures below 100 °C while crystallization between 100 and 120 °C gives rise to the coexistence of  $\alpha$  and  $\alpha'$  crystal forms. The  $\alpha$  and  $\alpha'$  forms are structurally similar, but  $\alpha'$  form has a looser chain packing. Zhang et al. explained that during heating runs of PLLA in differential scanning calorimetry (DSC) measurements, the small exothermal peak corresponds to the transition of  $\alpha'$  to  $\alpha$  which makes these two forms of crystals distinguishable <sup>118, 119</sup>.

### 2.4.1 Shish-kebab structure and hybrid shish-kebab structure

The direct effects of crystallinity and crystalline phase morphology developed from the melt state on the final mechanical properties of semicrystalline polymers have been frequently reported. A shish-kebab superstructure of the crystalline phase has been known as flow-induced crystallization in polymer processing and still gains great interest from both scientific and technological viewpoints <sup>120-126</sup>. If a chain is longer than a threshold chain length, when stress exceeds a particular amount, the molecular orientation introduces so much local order that small regions of crystallinity are formed and keeping molecules from relaxing <sup>127</sup>. The model for the formation of shish that emerges from the above considerations is pictorially summarized in

**Figure 2-13.** When the orientation of the entangled longer chains along the intense flow field establishes the first nuclei as shish, shorter chains find the chance to form the folded chain lamellae, i.e., the kebabs <sup>128-130</sup>.

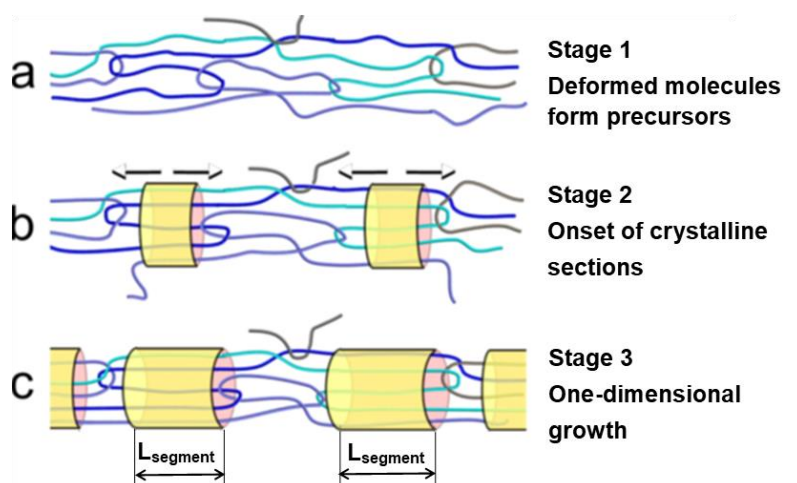


**Figure 2-13.** A pictorial description of the two-phase model for the formation of shish of isotactic polypropylene <sup>127</sup>.

Nevertheless, the shear rate, temperature, and endurance time must be strictly controlled to make the polymer chains oriented along the applied flow field, which eventually forms shish. In this regard, managing the processing conditions is critical even though polyethylene has a flexible chain backbone with high steric regularity and favorable crystallization kinetics <sup>131</sup>. Therefore, the idea of using fibrous fillers for controlling the crystalline phase morphology became very welcome. The formation of hybrid structures depends on reducing the critical enthalpy for nucleation at the polymer melt/filler interface. If the particle surface can initiate a high density of active nuclei on its surface during crystallization of a polymer matrix, this would hinder the lateral extension of spherulites and force their growth normal to particle surfaces resulting in columnar transcrystalline layers <sup>132</sup>.

It is well recognized that the fiber-matrix interface controls the mechanical properties of fiber-reinforced composites. Thus, one of the major concerns in the design of reinforced materials is achieving stable and robust interphase. The following strategies are adopted to enhance interfacial strength: (1) chemical or physical surface modification of fillers, (2) functionalization of the polymer matrix, (3) adding compatibilizer, and (4) preparing polymer composites via in situ polymerization method. Many studies have demonstrated that the formation of interface crystallization between the matrix and fiber provides a new solution to enhance the interfacial

adhesion in composite systems composed of semicrystalline polymer and filler with a high aspect ratio. Transcrystallinity is a well-known phenomenon which usually caused by heterogeneous nucleation at the fibers interface. Morphological features of transcrystallinity, such as spherulites size, lamella thickness, and crystallite density, profoundly affect the ultimate material properties<sup>133</sup>. The nature of filler/polymer linking arising from the interfacial crystalline structure, however, is challenging to elucidate clearly, and there is still a question of whether interfacial crystallization can ultimately bring effective interfacial enhancement or not.

#### **2.4.1.1 The factors controlling the hybrid crystalline structure**

##### **2.4.1.1.1 Surface chemical and physical characteristic of fillers**

The specific surface chemical structure of filler, the crystal lattice structure of the fillers, and their surface roughness play critical roles in the formation of interfacial crystallization structure. Surface treatment of fillers (surface energy modification) also was used to improve the interfacial adhesion of polymer/filler composites<sup>134</sup>. Furthermore, thermal conductivity mismatch and thermal expansion mismatch could also favor heterogeneous nucleation and significantly influence interfacial crystallization of polymer fillers composites<sup>135</sup>. For example, Ning et al. reported the effect of surface groove structure (topography) of CNT bundles on the formation of NHSK structure in poly (L-lactide) via (PLLA) solution crystallization<sup>136</sup>. It is also well established that the geometry and size of fillers also significantly influence the hybrid crystalline structure of polymer composites.

##### **2.4.1.1.2 Effect of polymer matrix**

The molecular weight of a polymer matrix dominates the molecular chain mobility of the matrix and thus can affect the crystal growth at the polymer/filler interface. Molecular chain structure and conformation could dramatically influence the adsorption of polymer molecules onto the surface of fillers and lateral crystal growth and thus can also affect interfacial crystallization. Pan et al. comparatively studied the effect of stereoregularity of PLA on the TC formation around basalt fibers<sup>133</sup>. The functional groups of a polymer matrix have the potential to form some special interactions with the surface of fillers and affect interfacial crystallization<sup>132</sup>.

##### **2.4.1.1.3 Processing conditions**

It is well known that external extensional/shear fields can strongly affect the polymers' crystallization behaviors. Generally, the crystallization rate can be significantly promoted with

extensional deformation or shearing flow, and some highly anisotropic crystal superstructures, such as shish-kebab, can be obtained from the oriented polymer melts. Although in quiescent crystallization, the lowest molecular weight of the matrix showed the highest nucleation density on the fiber and the densest transcrystalline layer<sup>133, 137</sup>, the presence of an ultra-high molecular weight fraction in flowing polymer melts is known to facilitate the formation of oriented crystalline structures significantly<sup>138</sup>.

#### 2.4.1.2 Formation mechanisms of a hybrid crystalline structure

Epitaxy is most generally defined as the oriented overgrowth of one phase (guest crystal) on the surface of a crystal of another phase (host crystal). The epitaxial match could be due to a unit-cell dimensional match or crystal structure similarity between the crystalline filler and the polymer matrix. It has been widely reported that polymer interfacial crystallization on various fillers (such as graphite, talc, mica) obeyed the epitaxial relations. However, for fillers with a very small diameter, such as CNTs, the formation mechanism of interfacial crystallization is “soft epitaxy” (geometric confinement). In this case, the epitaxial mechanism no longer exists, which is due to the curvature of small-diameter CNTs<sup>132</sup>. If the interfacial crystallization of polymers on CNTs still obeys the epitaxial relationship, the curved surface of CNTs would lead to curve polymer crystals with distorted lattice, which presumably is not stable. Therefore, the interfacial crystallization mechanism of polymers on the surface of CNTs is geometric confinement (soft epitaxy), as proposed by Li et al.<sup>139</sup>.

In order to explain the mechanism of epitaxy and soft epitaxy, a schematic representation is shown in **Figure 2-14**. For two-dimensional (2D) lamellar fillers (see **Figure 2-14a**) or fibers with a diameter much larger than the radius of gyration ( $R_g$ ) of the polymer (see **Figure 2-14b**), the interfacial crystallization of polymer matrix on such fillers may strictly obey the epitaxial relationship, as shown in **Figure 2-14a, b**. At first, the polymer molecular chains will adsorb onto the surface of the 2d lamellar fillers or fibers due to physical interactions; then, these molecular chains will be orientated and nucleated on the surface of fillers obeying epitaxial relationship. As a result, the various crystal orientations on the surface of the fillers lead to different orientations of the polymer crystal lamellae. However, for fillers with a diameter similar to the polymer  $R_g$ , such as CNTs, as shown in **Figure 2-14c**, the polymer chains are exclusively parallel to the long axis of these kinds of fillers due to the geometric confinement. As a result, a novel NISK structure with polymer crystal lamella perpendicular to the long axis of such fillers is obtained<sup>140</sup>.

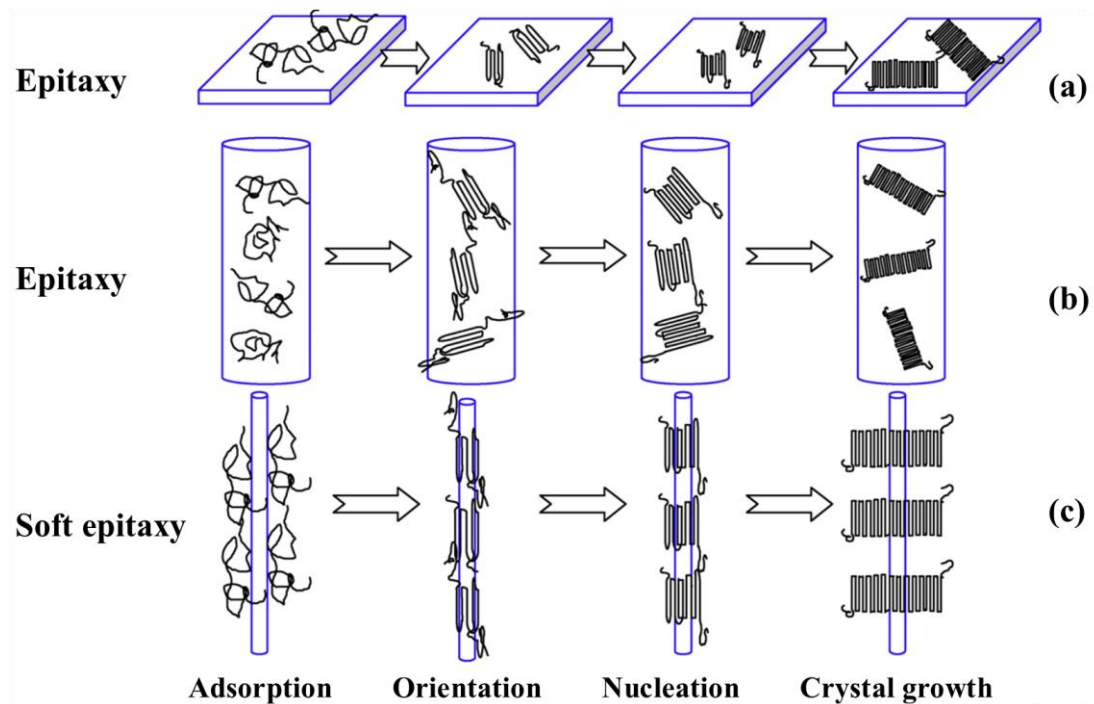


**Figure 2-14.** A schematic representation of epitaxy and soft epitaxy: (a) the interfacial crystallization process of 2D lamellar fillers obeying epitaxy mechanism; (b) fibers with a diameter much larger than the radius of gyration ( $R_g$ ) of the polymer obeying epitaxy mechanism; and (c) fillers with a diameter similar to the radius of gyration ( $R_g$ ) of the polymer obeying soft epitaxy mechanism <sup>132</sup>.

#### 2.4.1.3 Crystalline phase morphology of PLA/fiber nanocomposites

The crystallization rate of PLA/CNT nanocomposites has been reported to be improved effectively through the incorporation of CNT. The heterogeneous nucleation effect of CNTs increased the number of nucleation sites and decreased the average size of spherulites <sup>141, 142</sup>. Samthong et al. investigated the effect of PBT domain size (in a constant PBT content of 5 wt%) on the crystalline phase morphology of PLA in the melt blended PLA/PBT samples and PLA/PBT MFCs <sup>143</sup>. They showed that reducing the diameter of droplets (in the blends) and PBT fibrils (in MFCs) increased the crystallization rate of PLA by increasing the nucleation density.

In contrast to polyolefins <sup>144, 145</sup>, it still remains challenging to establish orthogonal disk-shape ordering of the crystalline phase in biodegradable semicrystalline polyesters such as PLA due to relatively short chains with semi-rigid molecular backbone and poor chain mobility <sup>146, 147</sup>. Applying strong shear/elongational flow on PLLA and PLLA/PBS, PLLA/PBAT, PLLA/PEG blends for a remarkable time resulted in a skin-deep shish-kebabs crystalline morphology <sup>33, 46, 148-150</sup>. Incorporating fillers, especially CNTs, have successfully suppressed the relaxation or



disengagement of oriented chain segments and deepened the superstructure<sup>151, 152</sup>. Long-chain branched PLA molecules provided the required entanglements to transform the shear field on linear PLA chains forming the shish<sup>153</sup>. Subsequently, the increased relaxation time of the system supported the evolution of the kebabs during isothermal crystallization.

Lie et al. explored the evolution of crystalline phase morphology in PLA under a quantitative shear flow close to the actual processing by coupling an in situ polarized optical microscopy with a fiber-pulling apparatus. The apparatus was assembled to pull a glass fiber (GF) at a constant rate while it was sandwiched between two layers of melted PLA. In the quiescent melt, sporadic dispersion of PLA spherulites indicated no nucleating effect of GFs. They evaluated the minimum required shear flow of  $120 \text{ s}^{-1}$  to trigger the PLA semi-spherulites around the glass fibers (hybrid shish-calabash structure showed in **Figure 2-15a**). The high density of row nuclei was induced by the strong shear flow around the pulled GF. As the shear rate rose to 280 and  $420 \text{ s}^{-1}$ , nuclei density on the surface of pulled GF was further increased, and the cylindrites became more compact, generating the fan-shaped and brush-shaped morphology, respectively (**Figure 2-15b and c**)<sup>154</sup>.

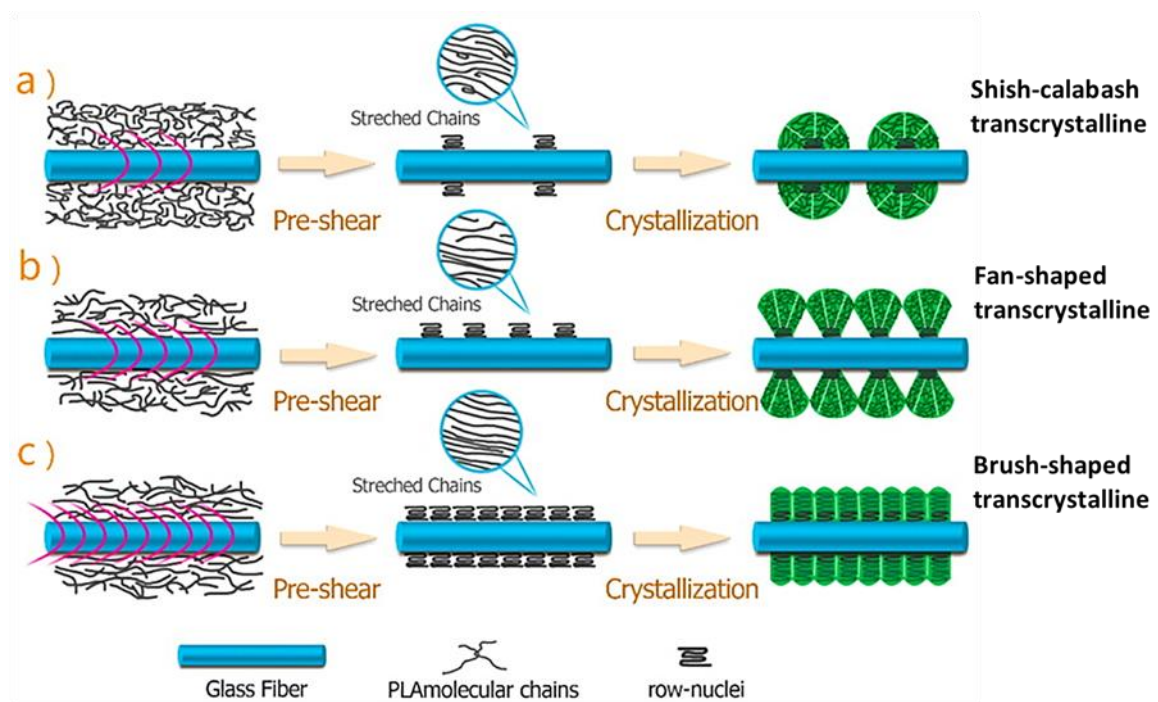


**Figure 2-15.** Schematic representation for the formation of cylindrites induced by pulling the GF at different rates, which correspond to different shear rates<sup>154</sup>.

A strong shear flow field was applied to PLA/natural fibers (ramie fiber) composites using a modified injection molding, namely oscillation shear injection molding<sup>155</sup>. By providing abundant nucleation sites on the surfaces of natural fibers, stretched PLA chains are located at these sites

to form a sequence of crystalline domains, constituting the interfacial structure of row nuclei. Subsequently, the lamellae develop onto the row nuclei and form columnar transcrystallinity superstructures due to the spatial restriction of compact nuclei. Compact transcrystallinity was achieved on the surface of the ramie fiber with a diameter of 2–5  $\mu\text{m}$  (**Figure 2-16b, c**); however, a hybrid shish-kebab superstructure was observed, where nano-sized fiber as a shish is wrapped by regularly aligned kebabs perpendicular to the axis (**Figure 2-16d**). Geometric confinement might render polymer chains to align along the tube axis regardless of the lattice matching as long as the fiber diameter decreases into the size of the radius of gyration ( $R_g$ ) of polymers, which is typically approximately 10 nm.

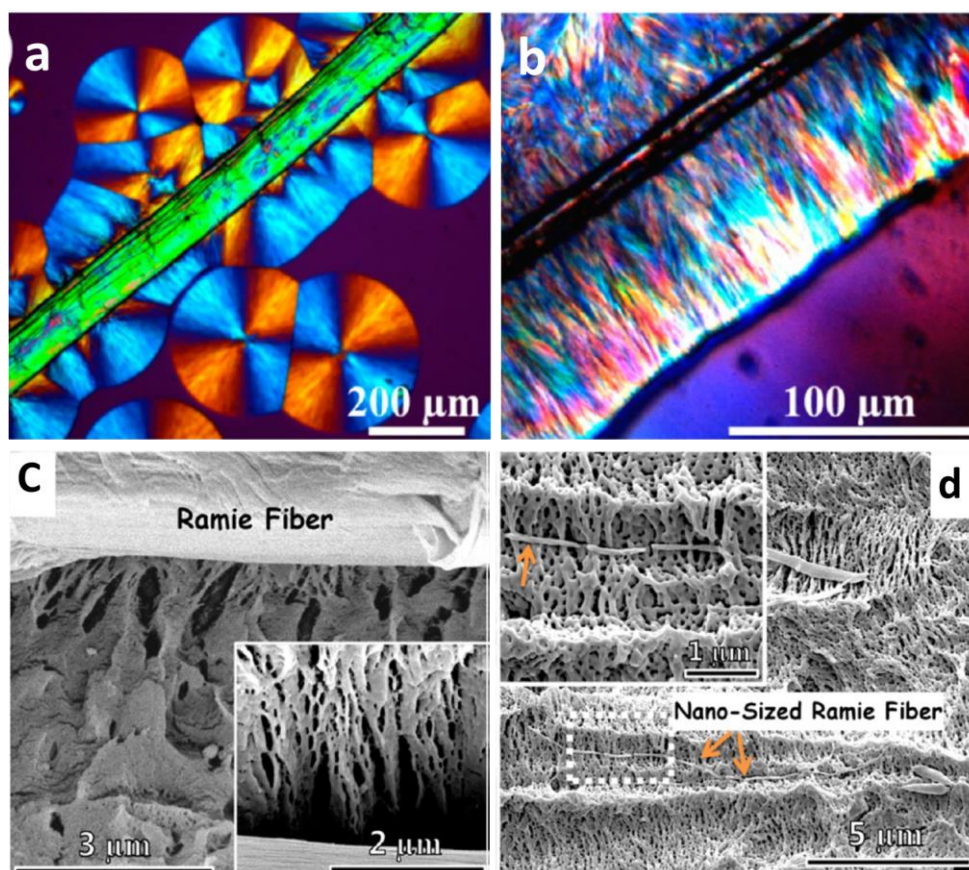


**Figure 2-16.** POM observation of transcrystallinity around a ramie fiber under quiescent melt isothermal condition (a). POM (b) and SEM (c) observations of fan-shaped shear flow-induced transcrystallinity superstructure around ramie fibers with a diameter of a few micrometers. SEM observations of shear-induced hybrid shish-kebab superstructure around nanosize ramie fibers (d). Inset of (d) presents the high-resolution micrograph of local morphology in the white dashed rectangle. The flow direction is horizontal <sup>155</sup>.

However, prolonged exposure to such intensive shear fields at elevated temperatures promotes mechanical and thermal degradation. Degradation in the case of polyesters illustrates as chain scission and consequently leads to a dramatic depression in mechanical performance<sup>156-158</sup>. Additionally, apart from energy consumption, most industrial processes suffer from limitations in applying such intensive shear homogeneously. As a result, the produced crystal morphology is non-uniform, and possible improvements in the mechanical properties are non-isotropic. Nevertheless, the formation of nanohybrid shish-kebab (NHSK) superstructures in the absence of flow field for PLA and polyolefins have been attained in dilute solution systems containing nanotubes as shish<sup>136, 159-161</sup>. Interestingly NHSK structure of PLLA were formed around melt-soluble self-assemblies molecules that act as strong nucleating agents<sup>162</sup>.

The few numbers of publications on the development of the shish-kebab crystalline structure of PLA, either from melt processing under shear/elongational flow field or from solution coagulation, presented improved mechanical properties. This observation indicates the importance of the crystalline phase inducing in shish-kebab structure. In the case of isotropic MFCs, enhanced melt crystallization kinetics and dispersed tiny spherulites were claimed<sup>25, 143, 163</sup>. However, to the best of the author's knowledge, the development of a randomly oriented crystalline phase with a disk-shape in the quiescent melt state around the polymeric fibrils has not been reported.

#### **2.4.2 Melt crystallization kinetics**

Different types of nanoparticles have been reported to be efficient in increasing the crystallization rate and degree of crystallinity of PLA as nucleating agents<sup>164-166</sup>. These particles provide a surface with a reduced energy barrier for nucleation<sup>139, 167</sup>. One-dimensional CNTs and two-dimensional graphene nanosheets (GNSs), were used to prepare carbon-based PLLA nanocomposites through solution coagulation. Both CNTs and GNSs could serve as nucleating agents by accelerating the crystallization kinetics of PLLA; however, the ability of CNTs to induce crystallization was stronger than that of GNSs<sup>161, 168</sup>.

Isothermal melt crystallization kinetics of PLA has been studied using a number of macro kinetics models (e.g. Avrami model, Tobin model, Mo model and Ozawa model) to quantitatively describe the macroscopic evolution of the crystalline phase<sup>169-172</sup>. The Avrami theoretical model is widely used to acquire the relevant parameters from the isothermal crystallization curve of polymers as follows<sup>173, 174</sup>:

$$1 - V_c(t) = \exp(-Kt^n) \quad (2-11)$$

Where  $V_c(t)$  is the relative volumetric crystalline fraction, and  $n$  is the Avrami exponent, which provides information on nucleation and growth geometry of the crystalline phase in the primary part of crystallization. Parameter  $K$  is the temperature-dependent overall crystallization rate constant (it contains contributions from both nucleation and growth) with the physical dimension of  $s^{-n}$  <sup>175, 176</sup>. The double-logarithm expression of **Equation ( 2-11 )** can be written as:

$$\text{Log}[-\text{Ln}(1 - V_c(t))] = n \text{Log}(t) + \text{Ln}(K) \quad (2-12)$$

The kinetic parameters  $n$  and  $K$  can be obtained from the slope and intercept of linear fitting for the plots of  $\text{Log}[-\text{Ln}(1 - V_c(t))]$  vs.  $\text{Log}(t)$ , respectively. The modified physical dimension of the crystallization rate constant ( $\text{min}^{-1}$ ) is provided by **Equation ( 2-13 )**. The calculated crystallization half-time ( $t_{1/2}$ ) based on the Avrami model (**Equation ( 2-14 )**) can be double-checked with experimental values ( $t_{1/2,exp}$ ) obtained from the relative crystallinity curves ( $t_{1/2}$  is the time at which  $V_c(t)$  reaches to 50 %) to verify the accuracy of the fitted model <sup>142</sup>.

$$k = K^{1/n} \quad (2-13)$$

$$t_{1/2} = (\ln 2/K)^{1/n} \quad (2-14)$$

Di Lorenzo et al. studied the crystallization behavior of PLA in PLA/PBT blends <sup>177</sup>. They presented a higher amount of crystallinity and an improved crystallization rate using PBT concentrations higher than 10 wt% for droplet-matrix and co-continuous morphologies. Samthong et al. reported the enhanced PLA crystallinity and crystallization rate for both PBT domain morphologies (droplets or in situ microfibrils), which was more pronounced for fibrillar morphology <sup>163</sup>. Kakroodi et al. studied the melt crystallization of PLA in the presence of PA6 droplets and in situ microfibrils under atmospheric pressure and 45 bar  $\text{CO}_2$  gas pressure. They also reported a more significant nucleating effect of PA microfibrils than droplets at atmospheric pressure and under  $\text{CO}_2$  gas pressure. By applying the Avrami model, they described the increased  $n$ -exponent due to the heterogeneous crystal nucleation effect at the interface <sup>25</sup>. The increased crystallization rate under  $\text{CO}_2$  gas pressure was attributed to the plasticization effects of dissolved  $\text{CO}_2$  gas. However, they did not observe any variation in nucleation and growth mechanism through increasing the PA6 microfibrils content <sup>81</sup>.

## 2.5 Immiscible polymer blends containing nanoparticles

Phase separation of polymer A (matrix) and B (dispersed) is an essential phenomena to occur in a polymer blend for the approach of in situ fibrillation. However the morphology development is dependant on the two polymer interactions at the interface, rheological properties and processing conditions. Since in this project in situ nanofibrillation of the polymer blend and localization of nanoclay in the matrix are the main objectives of the processing step, the affective parameters are briefly explained.

It is generally accepted that in low-viscosity emulsions, nanoparticle localization is predominantly controlled by the thermodynamic preferential attraction between nanoparticles and blend constituents. In high viscosity immiscible blends, however, due to a highly reduced Brownian diffusion coefficient and hence minimized thermodynamic induced localization contribution, the kinetic parameters such as the blend component viscosity differences and sequence of feeding can also play competitive roles. Consequently, in most nanofilled polymer blends, the nanoparticles are distributed unevenly between the blend components. Very recently, some increasing research activities have been directed toward studying the role of these two competitive groups of parameters <sup>178</sup>.

### 2.5.1 Thermodynamic parameters (wetting parameters)

Thermodynamic preferences of nanoparticles for selective localization in polymer blends can be predicted by estimating the interaction between polymer pairs as well as nanoparticles with each blend component. The thermodynamic equilibrium localization of solid particles in a polymer blend can be predicted by Young's model or the wetting parameter  $W_{AB}$  <sup>179</sup>. The wettability  $W_{AB}$  determines the ability of the particle to be wetted by liquid A and B and directly related to the contact angle:

$$W_{AB} = \frac{\upsilon_{Particle-A} - \upsilon_{Particle-B}}{\upsilon_{AB}} \quad (2-15)$$

Where  $\upsilon_{x-y}$  represents the interfacial energy between x and y. If  $W_{AB} > 1$ , the nanoparticles are localized only within polymer B, if  $W_{AB} < -1$ , the nanoparticles are selectively distributed within polymer A, and if  $-1 < W_{AB} < 1$ ; the particles are concentrated at the interface. The third case is more likely to occur in polymer blends, exhibiting a high degree of incompatibility when the differences

in the particle–polymer interaction are small. The interfacial tension ( $\nu_{AB}$ ) between constituents A and B can be calculated as follows <sup>81, 180</sup>:

$$\nu_{AB} = \nu_A + \nu_B - \frac{4\nu_A^d \nu_B^d}{\nu_A^d + \nu_B^d} - \frac{4\nu_A^p \nu_B^p}{\nu_A^p + \nu_B^p} \quad (2-16)$$

where  $\nu_A$  and  $\nu_B$  refer to the total surface free energy of the two polymers.  $\nu^p$  and  $\nu^d$  account for the polar and dispersive components of surface free energy, respectively.

The Sumita group performed such a prediction by utilizing the Owens–Wendt equation for PB/PMMA, PP/PMMA, and PB/PP blends, all filled with carbon black <sup>181, 182</sup>. They checked their predictions with experimental results obtained by electrical conductivity measurements and electron microscopy. It was shown that, as long as the viscosities of the two polymers are comparable, the interfacial energy is the main parameter determining the uneven distribution of the CB filler in polymer blend matrices. Zaikin et al. also focused their study on the prediction of the redistribution conditions for carbon black particles from bulk to the interface in blends of a number of different polymers <sup>178</sup>.

### 2.5.2 Kinetic parameters

It is now well recognized that the final nanofiller localization in high-viscosity polymer blends may be controlled through selecting an appropriate order of the feeding of different components (polymers and nanofillers). It has also been found that the effectiveness of this approach is highly dependent on other parameters such as the viscosity of the blend components, mixing time, and the type and concentration of the nanofiller. On the other hand, the nanoparticle distribution has proved to have a significant effect on determining morphology and, hence, the final properties of these ternary systems. This has motivated increasing activities toward producing polymer blend containing nanoparticles <sup>178</sup>.

### 2.5.3 Effect of feeding sequence

The addition of nanofillers into polymer blends to produce nanofilled polymer blends may be carried out through three different feeding routes. In the first feeding route, also known as direct feeding, all the components (polymers and nanofillers) are fed into the mixer simultaneously. In this mixing route, due to the interaction of different parameters, it would be challenging to decouple the effect of individual parameters on determining the nanofiller localization. If the polymer pair has a significantly different melting temperature, the nanofiller will be first localized

in the lower melting polymer phase, even if it has a greater affinity toward the second polymer. In the later mixing stage, the nanofillers may tend to transfer to the more thermodynamically preferred molten polymer phase. Thus, by knowing this and the fact that the morphology evolution is taking place all along the mixing process, one can realize that it is tough to distinguish the real role of the individual parameter in determining the final nanofiller localization in this mixing route. In the second feeding route, the polymer components are first melt-blended for an appropriate time period, and nanofillers are added afterward while the blending is still running. In the third route, the nanofiller is first mixed with one polymer, and the resulting premixed compound is mixed with the second polymer.

Thus, depending on the feeding sequence, the filler may need to follow a different path or transfer from one phase to another in order to reach their thermodynamic equilibrium or preferred localization. By knowing this and the fact that the melt mixing period is usually well below the Brownian diffusion time, one will be able to control the final nanoparticle localization and morphology in the final ternary system product.

#### **2.5.4 Effect of viscosity**

The effect of the viscosity difference of the blend polymer pairs on the nanofiller localization in immiscible blends has been studied by a few researchers<sup>183,184</sup>. Persson et al., for example, studied this effect on PE/PIB blends filled with the aluminum borate whisker using a different feeding sequence in which the polymer pairs had different viscosities but a comparable interaction with the aluminum whisker<sup>184</sup>. Their observation evidenced that the whisker accumulates in the higher viscosity polymer phase. They supported their hypothesis by estimating the viscosities calculated based on appropriate models with the assumption that the filler can be localized in one polymer or the other. In their similar study on the PA/SAN/whisker system, they observed that in contrary to the PE/PIB/whisker, the filler particles were concentrated in the PA phase, although they had lower viscosity compared to SAN. By comparing these findings, they reached a conclusion that the effectiveness of the viscosity ratio is weak and can dominate only when the filler has a comparable affinity toward the polymers. By contrast, when one of the polymers has much greater thermodynamic interaction with the filler (PA in the PA/SAN blend), the thermodynamic effect will dominate the viscosity ratio effect<sup>178</sup>.

## 2.6 Foaming basics

### 2.6.1 Nucleation

Nucleation is simply defined as the first random formation of a distinct thermodynamic new phase that has the ability to irreversibly grow into a larger sized nucleus within the body of a metastable parent phase. The resulting new phase has free energy lower than the parent phase. The basic driving force for such transformation is the difference in free energies between the two systems<sup>16</sup>. The classical nucleation theory classifies cell nucleation into homogenous and heterogeneous nucleation. Homogenous nucleation involves the spontaneous and random formation of bubbles (cells) with no foreign bodies or additives. It usually occurs in response to random fluctuations or changes in temperature or pressure. Heterogeneous nucleation does not occur spontaneously and is triggered by the presence of additives that act as nucleation centers. The introduction of additives lowers Gibb's free energy maximum depending on the particle type, shape, and topography of the surface. Polymer–filler interaction is of utmost importance to assess nucleation efficiency. An ideal nucleating agent must fulfill the following criteria: (i) They must not have firm adhesion to the matrix (equivalent to a large wetting angle). (ii) They should be easily dispersed and properly dispersed within the polymer matrix. (iii) They must be present in a sufficient amount to foster the creation of more nucleation centers. (iv) The nucleants should be characterized by uniform size, shape, and surface properties<sup>185</sup>.

### 2.6.2 CO<sub>2</sub> sorption and diffusivity in polymers

One of the advantages of foam processing is that it can be done at relatively low temperatures due to the plasticizing effect of the blowing agents on the polymer chains into which they are incorporated. The sorption capacity (i.e., how much blowing agent the polymer matrix can absorb), especially of an amorphous polymer under certain pressure and temperature, determines the extent to which the  $T_g$  of the polymer can be depressed<sup>186</sup>. There are two widely used methods to estimate or calculate the total amount of CO<sub>2</sub> absorbed by a polymer, which are extensively discussed by Okolieocha et al.<sup>16</sup>.

The solubility of a high-pressure physical blowing agent in a polymer impregnates the polymer, and thereby the polymer starts to swell. The amount of swelling depends on how much gas dissolves in the polymer and also depends on the polymer's molecular configuration and architecture. The polymer's swelling behavior can be analyzed through a pressure-volume-temperature (PVT) apparatus (i.e., a dilatometer) to evaluate the polymer/gas mixture's PVT



behavior<sup>23</sup>. The foaming behavior of a polymer (i.e., cell nucleation and growth) is generally governed by the following thermodynamic properties: solubility<sup>187</sup>, diffusivity<sup>188</sup>, and surface tension<sup>189</sup>. All of these heavily depend on the PVT properties of the polymer/gas mixtures. With increased pressure and decreased temperature, the swelling volume ratio and the gas solubility increased in the PLA/CO<sub>2</sub> mixtures. As the CO<sub>2</sub> pressure increased, more CO<sub>2</sub> molecules dissolved in the PLA matrix and increased the volume of the PLA/CO<sub>2</sub> mixtures. In other words, when a polymer was solubilized by being exposed to a pressurized gas, the dissolved gas increased the intermolecular distance and thereby caused a swelling, despite the hydraulic pressure effect. Consequently, the free volume and the volume of the polymer/gas mixture both increased. In addition, when the temperature increased, the PLA's molecular movement further increased. Thus, the free volume and specific volume increased. But this increase was insufficient to enhance the CO<sub>2</sub> solubility, and thereby the CO<sub>2</sub> solubility in the PLA was reduced<sup>23</sup>. Mahmood et al. found that when PLA is in the melt state (temperature range of 180-200 °C was studied), the swelling and solubility of CO<sub>2</sub> did not change significantly at different D-Lactide content<sup>190</sup>.

### 2.6.3 Terminologies

In this section, commonly used properties to characterize polymer foams are described.

*Foam density*: is a foaming property evaluated by the water-displacement method based on the Archimedes principle and according to ASTM D792. What is measured is the weight of the sample in the air (A) divided by the weight of the sample in water (B), and by using the expression in **Equation ( 2-17 )**, the foam density ( $\rho_{foam}$ ) is obtained.

$$\rho_{foam} = \frac{A}{A - B} \quad (2-17)$$

*Relative foam density ( $\rho_{rel}$ )*: is the  $\rho_{foam}$  divided by the density of the solid polymer (unfoamed polymer) (**Equation ( 2-18 )**), and it is the inverse of the volumetric foam expansion ratio (VER) designated as  $\phi$ .

$$\rho_{rel} = \frac{\rho_{foam}}{\rho_{polymer}} = \frac{1}{\phi} \quad (2-18)$$

*Cell density:* The cell density,  $N_0$  (cells/cm<sup>3</sup>), is expressed as the number of cells per unit volume with respect to the unfoamed solid polymer (**Equation ( 2-19 )**).

$$N_0 = (n/A)^{1.5} \phi \quad ( 2-19 )$$

Where  $n$  is the number of cells within the statistical area,  $M$  is the magnification factor, and  $A$  is the statistical area in SEM micrographs (cm<sup>2</sup>).

*Cell-size:* The cell-size is usually the average value of all the foam's cell-sizes calculated from various scanning electron micrographs. Cell distribution is also another essential characteristic to consider as it gives an indication of how homogeneous the foam morphology is.

Polymer foams are generally classified according to the cellular structure (open-cell or closed-cell), volume expansion ratio (inverse of relative density), and cell-size (fine cell-size, microcellular or nanocellular) <sup>16</sup>.

## 2.7 PLA foaming

Microcellular foaming is an advanced foaming technology with green gas, such as carbon dioxide and nitrogen, as the blowing agent. It effectively reduces polymer consumption and product weight and endows its new functional properties, such as heat insulation, energy adsorption, and shocking adsorption<sup>22</sup>. The foamability of biodegradable polymers, such as PLA, PBS, polyhydroxyalkanoates, polyvinyl alcohol, has been extensively studied<sup>191-193</sup>. Among these, PLA has a comparable mechanical strength compared to many petroleum-based plastics at room temperature<sup>194</sup>; besides, the continuous process improvement has been reducing its production cost significantly, making it relatively inexpensive<sup>195</sup>. Therefore, many efforts have been devoted to producing PLA foams, specifically microcellular foams, through various manufacturing methods. Batch foaming in an autoclave (pressure-induced or temperature-induced), foam extrusion, foam injection molding, and bead foaming have been applied to PLA<sup>3</sup>. In order to enhance the foamability of PLA, several strategies are summarized<sup>23,196</sup>.

### 2.7.1 Degree of crystallinity and crystal morphology

Enhancing PLA's crystallization kinetics during foaming has been recognized as an effective way to overcome its weak viscoelastic properties and improve its foaming behavior (i.e., cell nucleation and expansion). This will consequently increase PLA's ability to expand by minimizing gas loss and cell coalescence. It should also be noted that too high crystallinity content and large crystal domains would also suppress foam expansion due to excessive stiffness increase of the matrix and less gas dissolution. On the other hand, according to heterogeneous cell nucleation theory, cell nucleation can be promoted around the nucleated crystal through local pressure variations, thereby significantly improving the foamed samples' final cell density<sup>23</sup>.

The crystallization behavior of PLA is strongly dependent on the molecular weight and molecular structure, as the elevated molecular weight would restrict the chain mobility. During the pressure-induced batch foaming process, the crystallization behavior of PLA can be assumed as being quite complex and the following processing parameters strongly impact the final foam properties<sup>196</sup>:

- (1) Temperature most directly affects the crystallization behavior by changing chain mobility.
- (2) The pressure dominates the solubility of the blowing agent and, thereby, the amount of it that is solved in the polymer matrix. Hence, the plasticization effect, as well as the gas-induced crystallization, is directly influenced by the applied pressure.

(3) During an isothermal saturation phase (time), the crystallization kinetics of PLA is promoted by elevated temperature and the plasticization effect of a dissolved blowing agent.

(4) As a consequence of a sudden pressure drop, which actually induces a thermo-dynamic instability and the prompt oversaturation of the sample, the foaming takes place. Hence, the pressure drop rate guides the nucleation rate and the extent of the strain-induced crystallization.

Li et al. showed that a pre-isothermal treatment step significantly enhanced the PLA's foaming ability, resulted in a microcellular structure<sup>22</sup>. Besides, the PLA's maximum expansion ratio (VER) increased from about 6-fold to 18-fold, and the uniformity of the cellular structure was also improved obviously. **Figure 2-17**a, b series schematically compares the cold crystallization step, effect of saturation, and the final foam morphology of PLA foams in a regular batch foaming process and the one with isothermal pre-treatment.

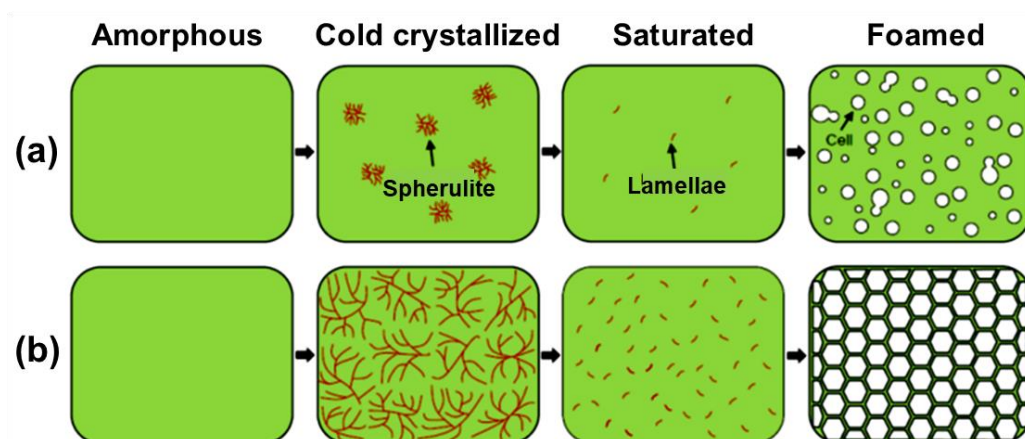


**Figure 2-17.** Schematic diagrams of foaming mechanism for (a) regular process and (b) pre-isothermal process<sup>22</sup>.

### 2.7.2 Molecular architecture

The foamability of PLA depends greatly on these molecular structures because they affect its molecular mobility, crystallization kinetics, and rheological properties. The introduction of chemical modifications such as chain extenders to increase molecular weight and/or introduce branched or even cross-linked structures strongly affect PLA foaming behavior<sup>197, 198</sup>. The conventional chemical modifications include (i) ring-opening copolymerization, (ii) reactions of low-MW prepolymers of PLA with chain extenders, such as epoxy, diisocyanate, and oxazoline, and (iii) post-polymerization reactions, including melt modification and radiation treatment<sup>3</sup>.

The modification of commercial grades of PLA by reactive extrusion with chemical modifiers is a complex process in which both polymer chain scission and chain recombination take place. Additionally, secondary reactions, such as transesterification or homopolymerization could happen. Chain extension, branching, and/or cross-linking of PLA depend on various factors such as the type and concentration of modifier, processing temperature, and reaction time<sup>3</sup>. There are different branched structures reported for modified PLA, such as star-shaped, comb-shaped, dendritic/hyperbranched, H-shaped, long-chain branched, or dumbbell-shaped, exhibiting different properties<sup>199</sup>. Chen et al. introduced Phenylphosphonic acid zinc salt (PPZn) as a crystallization nucleating agent and multi-functional epoxy-based chain extender to enhance the crystallization property and the melt elasticity of PLA, respectively<sup>200</sup>. Using a batch foaming method in an autoclave under 10 MPa supercritical CO<sub>2</sub> gas pressure as the physical blowing agent, the corresponding foams cell density was over  $9.5 \times 10^{10}$  cells/cm<sup>3</sup>, their cell-sizes were about 4.5 μm, and a maximum VER of 12-fold was obtained.

### 2.7.3 D-lactide content

The ratio between L-Lactide and D-lactide (L/D ratio) governs the chain regularity of PLA, hence its crystallization behavior. It is already known that PLA grades with a D-content below 10 % usually crystallize during foaming<sup>201</sup>. Reducing the D-lactide content increases PLA's crystallization kinetics while increasing its melting temperature. Mihai et al. reported that, during foam processing, the crystallinity of the PLAs with low D-lactide content was further enhanced by dissolved CO<sub>2</sub>. This resulted in foams with finer cells and a more uniform morphology. Higher expansion ratios were also achieved, and a larger number of cell nucleation sites were created around the nucleated crystals<sup>197,202</sup>. It should be mentioned that PLA grades with D-content above 10 to 12 % are hindered from crystallization even after depressurization (expansion step) in which the chains have the chance of orientation due to strain-induced crystallization<sup>196, 203</sup>. However, these grades are foamable<sup>196</sup>.

### 2.7.4 Blending and compounding

Several studies have investigated the foaming behavior of PLA samples blended with other biodegradable polymers such as starch, poly (butylene adipate-co-terephthalate) (PBAT)<sup>204</sup>, poly[(butylene succinate)-co-adipate] (PBSA)<sup>205</sup>, poly (caprolactone) (PCL)<sup>206</sup>, polyvinyl alcohol (PVOH), and polyhydroxybutyrate-valerate (PHBV)<sup>207</sup>. However, many researchers preferred to

apply a compatibilizer or a micro/nano-sized additive simultaneously to achieve better foaming behaviors (i.e., cell nucleation and cell morphology) and, consequently, improvements in physical-mechanical properties<sup>23</sup>. Microcellular PLA/TPU foams were fabricated using a supercritical CO<sub>2</sub> (scCO<sub>2</sub>) assisted batch foaming process due to the enhanced cell nucleation by the presence of the interfaces between PLA and TPU<sup>208</sup>. Biocompatible shape memory polymer blending foams composed of TPU and PLA were prepared by Song et al.<sup>209</sup>.

Melt blending of PLLA and PDLA was suggested to wider the foaming processing window, which is favorable for actual industrial fabrication such as the continuous extrusion foaming process<sup>210, 211</sup>. The gap between the melting temperature of homocrystallites ( $T_m(\text{HC})$ ) and stereo-complex crystallites ( $T_m(\text{SC})$ ) has been utilized to improve PLA's melt foaming behaviors owing to the existence of exclusive SC crystallites when the foaming temperature fell in between  $T_m(\text{HC})$  and  $T_m(\text{SC})$ . Besides, PLA foams possessing more SC crystallites exhibit higher heat resistance, which further broadens their applications in high-temperature conditions.

Many researchers have demonstrated that physical modification with micro or nanofillers effectively promotes crystallization and increases melt strength, hence improving the foaming ability of PLA<sup>212</sup>. The fillers that can significantly improve foaming include talc<sup>213</sup>, graphite<sup>214</sup>, graphene oxide<sup>215</sup>, carbon nanotube<sup>216, 217</sup>, cellulosic fibers<sup>194</sup>, cotton fiber<sup>218</sup>, glass fibers<sup>212</sup>, etc. PLA/organically modified layered silicate nanocomposites were foamed by scCO<sub>2</sub>, showing high cell density and small cell-size from microcellular to nanocellular, which were prepared at low foaming temperature and high CO<sub>2</sub> pressure<sup>219</sup>. The positive effect of heterogeneous fillers in promoting foaming can be attributed to the following reasons. Firstly, fillers provide a heterogeneous interface for cell nucleation, which reduces the energy barrier of cell nucleation. Secondly, fillers can increase melt viscoelasticity, which helps to stabilize cellular structure. Moreover, fillers can promote crystallization, and it is beneficial not only to promote cell nucleation but also to stabilize cellular structure. In recent years, in situ fibrillation technology was developed to reinforce PLA and improve its foaming ability<sup>24, 25</sup>.

## 2.8 Foamability of isotropic in situ microfibrillar composites

Rizvi et al. compared the foamability of metallocene-catalyzed polyethylene (mPE) with that of mPE containing fibrillated polypropylene domains (mPE/fibrillated-PP) and mPE containing spherical PP domains (mPE/spherical-PP) using a batch foaming process at a temperature of 95 °C and scCO<sub>2</sub> pressures ranging from 4.1 MPa to 17.3 MPa <sup>76</sup>. In the presence of spherical PP, the average cell-size decreases from 700 μm to 90 μm, and the cell density increases from 5.9 × 10<sup>4</sup> cells/cm<sup>3</sup> to 1.2 × 10<sup>5</sup> cells/cm<sup>3</sup>. In mPE/fibrillated-PP, the average cell-size decreased to 27.6 μm, and the bubble density increased to 9.7 × 10<sup>8</sup> cells/cm<sup>3</sup>. The higher cell density was observed for mPE/fibrillated-PP relative to mPE/spherical-PP, and mPE was attributed to its solid-like viscoelastic character, which was not observed for the other two samples. The enhanced solid-like behavior increased the internal local pressure variations, which make the bubble nucleation rate faster.

Kakroodi et al. compared the foamability of PLA/PA6 MFCs with that of PLA and PLA/PA6 blends using a batch foaming process at a temperature of 140 °C and scCO<sub>2</sub> pressure of 14 MPa <sup>25</sup>. **Figure 2-18** shows that the addition of only 3 wt% of PA6 microfibrils reduced the PLA foam's average cell-size from 70 to 23 μm, while its cell density increased by a remarkable 2 orders of magnitude (from 2.4 × 10<sup>6</sup> cells/cm<sup>3</sup> to 1.8 × 10<sup>8</sup> cells/cm<sup>3</sup>). However, the foam density or VER was not reported. The MFC melt's strain hardening behavior prevented the cells from collapsing during the extensional flow, which had been induced in the cell growth stage of the foaming process. When a polymer is foamed, bubbles' growth exerts a biaxial extension on the polymer matrix. If the polymer matrix shows weak strain hardening, it is not able to withstand this extensional force, and the bubbles rupture lead to the diffusion of gas out of the polymer, and ultimately, the foam collapses. Consequently, strain hardening plays a critical role in facilitating gas retention by preventing bubble opening and gas escape. **Figure 2-18B2**, on the other hand, shows a very poor microstructure for the foamed samples of PLA/PA6:97/3 wt% with spherical PA6 domains. The spherical PA6 domains' incapability to enhance the PLA's rheological properties was responsible for the undesirable foam microstructure. **Figure 2-18C1** shows that foaming of the compound with 7 wt% PA6 microfibrils was impossible. No cells were generated in the sample, while the escaping gas formed huge pockets just beneath the skin layers. This behavior was the result of an excessive increase in the melt viscosity of the blend. Samples with higher concentrations of PA6 microfibrils showed similar behaviors.

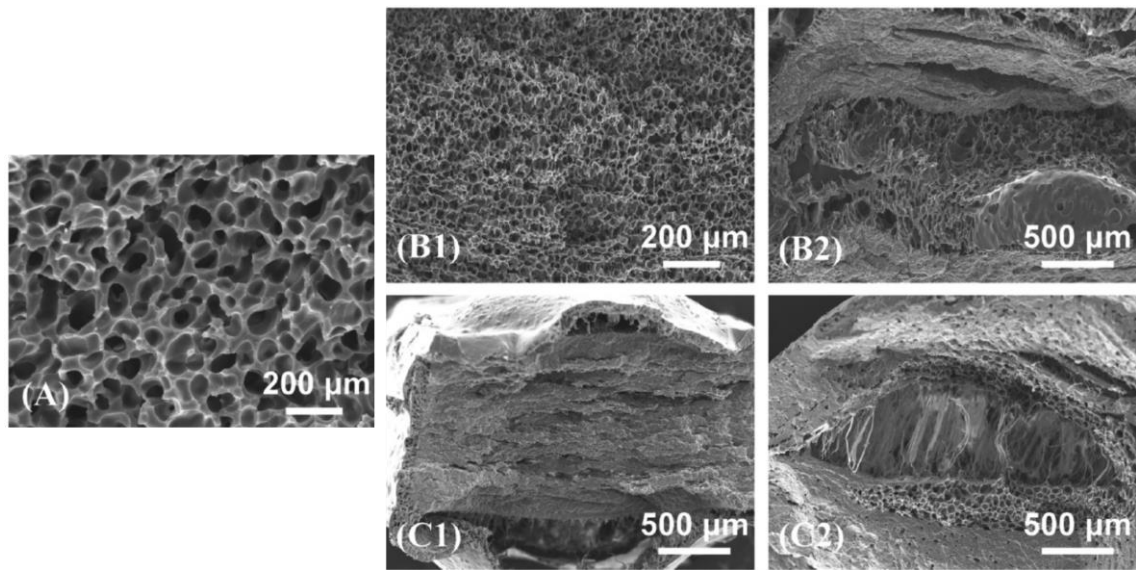


**Figure 2-18.** SEM micrographs of cryogenically fractured surfaces of foamed samples of pure PLA (A), PLA/PA6:97/3 wt% with microfibrillar (B1) and spherical (B2) PA6 domains, and PLA/PA6:93/7 wt% with microfibrillar (C1) and spherical (C2) PA6 domains <sup>25</sup>.

Wang et al. prepared a nanofibrillar PLA/PET composite by coupling twin-screw compounding and melt-spinning. Subsequently, regular microcellular injection molding (RMIM) and high-pressure microcellular injection molding (HPMIM) were used to foam the isotropic microfibrillar composites <sup>103</sup>. The relative foam density of the samples produced by RMIM and HPMIM was 80 %. The foam density in RMIM is tailored by manipulating the shot size, while that in HPMIM is tailored by manipulating mold-opening distance. **Figure 2-19** presents the cellular morphologies of the pure PLA foam and the nanofibrillar PLA/PET composite foam, fabricated by RMIM and HPMIM, respectively. **Figure 2-19a** shows that the RMIM-fabricated pure PLA foam has a rather uneven and irregular cellular morphology. The RMIM fabricated PLA/PET NFC foam shows a much more uniform cellular morphology, although cells are still strongly oriented along the direction of melt flow, as **Figure 2-19d** shows. The improved cellular morphology can be attributed to the significantly enhanced viscoelasticity and melt strength of the PLA/PET NFCs, which reduces cell collapse and coalescence. However, because foaming and melt filling occur simultaneously, the cells will inevitably be oriented along the melt flow direction. It can be found that the pure PLA foam's cellular morphology is greatly improved by using HPMIM technology (**Figure 2-19b** and c). The HPMIM-fabricated pure PLA foam has an average cell-size of 17.3  $\mu\text{m}$  and a cell density of  $7.2 \times 10^7$  cells/cm<sup>3</sup>. Aside from the decoupled foaming and filling of the polymer melt, another important reason for the improved cellular morphology is the enhanced melt strength by manipulating the high-pressure holding duration in the HPMIM process.



Compared with the HPMIM-fabricated pure PLA foam, the HPMIM fabricated PLA/PET NFC foams showed further remarkably improved cellular morphology, as **Figure 2-19e** and **f** show. Notably, a sub-microcellular morphology with an average cell-size of 322.8 nm and a cell density of  $1.1 \times 10^{13}$  cells/cm<sup>3</sup> was obtained. Remarkably, the Izod and Gardner impact strengths of the HPMIM-fabricated PLA/PET foam are respectively more than 7-fold and 6-fold higher than those of the PLA foam fabricated by MMI.

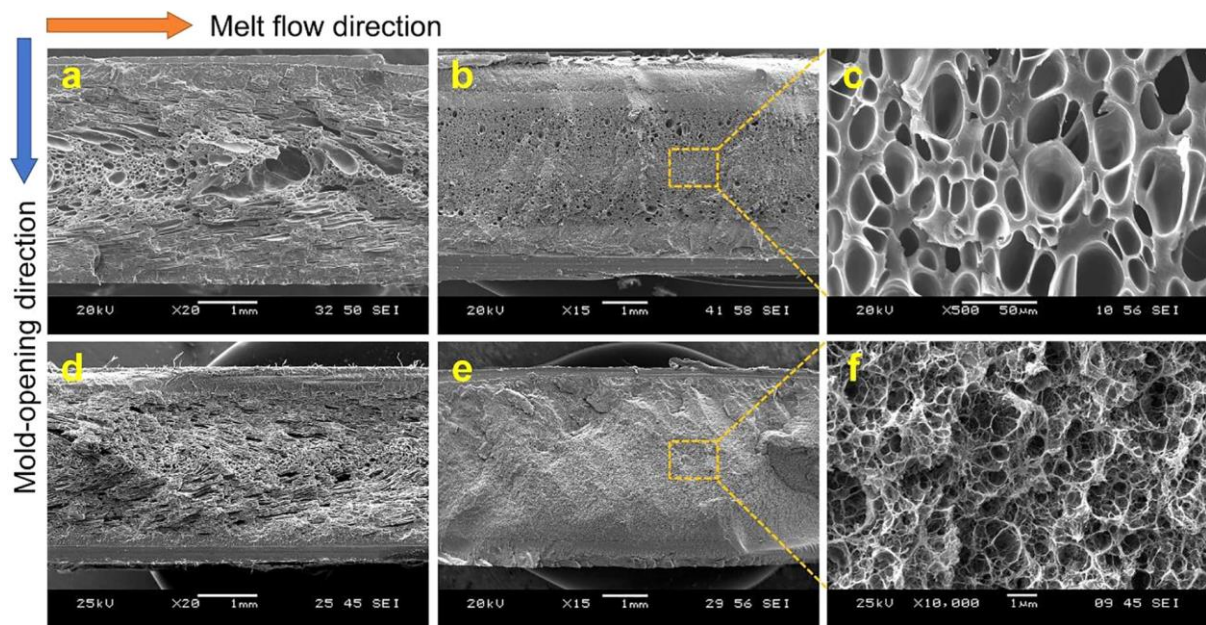


**Figure 2-19.** Cellular morphology of (a) RMIM-fabricated pure PLA foam, (b) HPMIM-fabricated pure PLA foam (low-magnification), (c) HPMIM-fabricated pure PLA foam (high-magnification), (d) RMIM-fabricated PLA/PET foam, (e) HPMIM-fabricated PLA/PET foam (low-magnification), and (f) HPMIM-fabricated PLA/PET foam (high-magnification) <sup>103</sup>.

Many researchers studied the effect of in situ fibrillated PTFE on the foamability of different polymers, especially PP <sup>75, 104, 105, 220-223</sup>. Rizvi et al. declared that continuous foam extrusion of the PP/PTFE MFCs revealed three orders of magnitude increase in cell density, a ten-fold increase in volume expansion ratio, and a marked broadening of the foaming window compared to neat PP <sup>75</sup>. These improvements were attributed to the simultaneous enhancement in CO<sub>2</sub> solvency and strain-hardening behavior of the melt in the presence of in situ fibrillar structure.

Later on, Zhao et al. fabricated PP/PTFE MFC foams with a low thermal conductivity of 36.5 mW m<sup>-1</sup> K<sup>-1</sup> using a high-pressure mold-opening foam injection molding process (MOFIM) with CO<sub>2</sub> as a blowing agent <sup>105</sup>. The DSC results, dynamic shear, and extensional rheology measurements demonstrated that the well-dispersed in situ fibrillated PTFE fibrils could significantly improve

crystallization rate, viscoelastic performance, and strain-hardening behavior, respectively. All these factors confirmed that PTFE fibrils were very effective in enhancing melt strength and thus foamability of PP. The foam injection molding results showed that in the presence of PTFE fibrils, the foam's cell-size was reduced by nearly one order of magnitude, while its expansion ratio increased by approximately three times.

Wang et al. fabricated lightweight and tough PP/PTFE NFC foams with defect-free surfaces by combining in situ fibrillation and mold-opening foam injection molding (MOFIM)<sup>224</sup>. Scanning electron microscopy, rheological measurements, and differential scanning calorimetry analysis, combined with online optical microscopy observation, demonstrated the network structure of PTFE nanofibrils and its positive effects on melt strength and promoting crystallization. At a constant weight reduction of the foamed samples (about 25 %) compared with the unfoamed sample, nanocellular foams were achieved thanks to the transcrystalline structure around the nanofibrils and MOFIM process (**Figure 2-20**). The nanocellular PP/PTFE NFC foams thus obtained significantly enhanced mechanical properties compared to the regular PP foams and even superior strength and ductility compared to unfoamed PP.

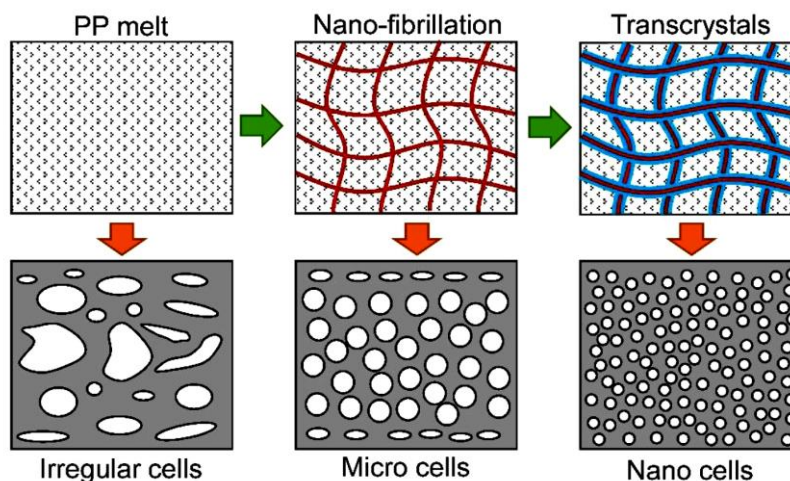


**Figure 2-20.** The effect of nanofibrillar network and transcrystallinity on the cellular structure of PP/PTFE nanofibrillar composite foams fabricated using the high-pressure mold-opening foam injection molding process<sup>224</sup>. Different foam morphology at a constant weight reduction of 25 %.

Microcellular injection molding of PLA/TPU blends in the presence and absence of in situ generated PTFE fibrils confirmed that the presence of PTFE nanofibrils dramatically improved the foamability of PLA<sup>225</sup>. Compounding of PS/PTFE with poly (propylene carbonate) (PPC) via a triple-screw extruder resulted in multiphase composites<sup>222</sup>. It was found that PS was immiscible

---

with PPC and formed a dispersion phase, and PTFE was in situ fibrillated into the nanofibrillar network within the PPC/PS matrix. The introduction of rigid PS domains and PTFE nanofibrils showed remarkable effects on PPC properties and improved the extrusion foamability of PPC. Later on, Kuang et al. studied PPC/PBS/PTFE ternary in situ nano-fibrillar bio-composites to significantly improve the strength and foaming ability of PPC without sacrificing their excellent biodegradability <sup>221</sup>. The in situ nano-fibrillar networks in the PPC/PBS matrix demonstrated significant reinforcement effects on the matrix strength, dynamic mechanical, and rheological properties at low PTFE contents. In the continues extrusion foaming process, the PBS domains and the PTFE nano-fibrils network generated remarkable synergistic effects on the foaming behavior, resulted in higher cell densities ( two orders of magnitude), compressive modulus (30 times), and compressive strength (20 times) of PPC/PBS/PTFE (70/30/3) bio-composites.

### 3 Goals and Approaches

Reviewing the literature revealed that among the fillers with different geometries, the micro/nanofibrillar additives could effectively modify various properties of thermoplastic polymers such as crystallization behavior, viscoelastic properties, mechanical behavior, and foamability. However, the effectiveness of nanofibrillar additives was much less than expected due to the lack of uniform distribution or poor dispersion. Therefore, special chemical modification alongside solution casting methods has been applied for achieving a fine dispersion of nanoparticles within the matrix. Since such methods were not applicable in industrial scales, the approach of in situ nanofibrillar composites was offered. In situ fibrillar composites were achieved by converting a droplet-matrix morphology in a melt-blended pair of polymers to a fibrillar morphology. Although converting the morphology (instead of the addition of fillers) could efficiently solve the dispersion problem, based on literature, this method was restricted to the production of microcomposites which include high amounts of the second phase ( $> 6$  wt%). On the other hand, many researchers reported that fibrillation was inhibited at low contents of minor phases since the droplet coalescence could not occur. Accordingly, the first challenge in this field is developing high aspect ratio nanofibrils at low concentrations of the minor phase, which is highly demanded to improve properties such as foamability while surviving the matrix's biodegradability.

The main goal of this thesis was to enhance the foamability of PLA using the approach of isotropic in situ nanofibrillar composites. In other words, the drawbacks of PLA, such as its slow crystallization kinetics, low melt strength, and brittle behavior, should be eliminated via uniform dispersion and distribution of in situ generated PBT nanofibrils (PBT NFs). Additionally, the massive interface of the matrix with the high aspect ratio of the nanofibrils was supposed to act as a cell nucleating agent in the foaming process.

In order to achieve this goal, the following sub-goals were investigated:

- 1. To implement a melt-spinning process on the PLA/PBT blends for developing in situ nanofibrils in the PLA matrix with diameter and aspect ratio comparable to those of well-dispersed MWCNTs (diameter  $\cong 20$  nm and aspect ratio  $\gg 500$ ).** MWCNTs are known as the thinnest available nanofibers that encounter serious dispersion problems, especially when using the melt mixing processes. By concerning them as a benchmark,

based on the literature, appropriate dispersion of them up to now could be achieved through solution coagulation of PLA/MWCNTs. In this thesis, the development of well-dispersed PBT nanofibrils through PLA matrix using a simple environmentally friendly process will be pursued. Enhancement of the matrix's melt elasticity, which was required for a strong elongation of the PBT domains, will be achieved by optimizing the temperature profile of the extrusion process or the addition of nanoclay (localized in the matrix).

**2. To rheologically rationalize the in situ development of the PBT NFs in the PLA matrix under conditions matching the melt-spinning processing conditions.** Such studies evaluate the offered criteria for morphology development, which is highly valuable in predicting fibrillation in every similar system. Realizing the nanofibrils formation's governing mechanisms reveals essential knowledge about material selection and process implementation. The contribution of coalescence in fibril formation is a well-known mechanism describing microfibrils' generation at minor phase compositions of approximately more than 6 wt%. In this study, melt rheological behavior of the components under the die condition, and morphological observations of the blends at the die and out of the die should be followed to determine the formation mechanisms of the PBT nanofibrils at compositions of 1-10 wt%. The dominant mechanism can be found out better by comparing the final morphology of PLA/PBT NFCs and PLA/PBT/nanoclay nanocomposites.

**3. To understand the effect of PBT domain geometry (spherical or fibrillar) on the PLA crystallization behavior (crystallization kinetics and morphology).** The crystallization behavior of the NFCs should be compared with that of PLA/PBT blends. In addition, the effect of fibril diameter on the nucleation mechanism can be pursued by investigating the crystallization behavior of the NFCs containing various amounts of PBT nanofibrils. In this regard, the morphology of melt crystallized PLA and NFCs in quiescent bulk should be investigated using microscopic observations.

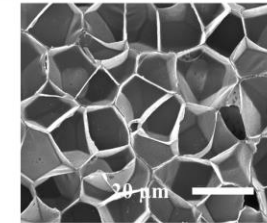
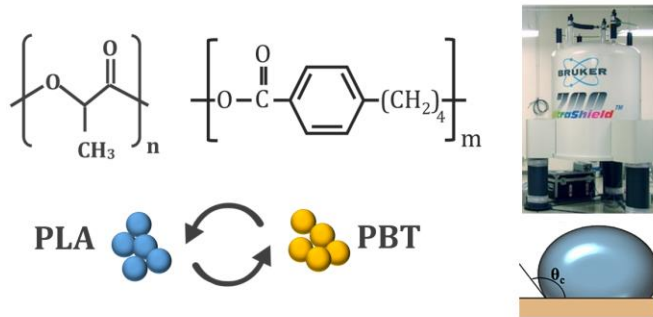
**4. To determine the effect of temperature on the crystalline phase morphology in the absence of any flow fields.** Changes in nucleation mechanism govern the crystalline phase morphology and, thereby, final mechanical properties. Therefore, the effect of annealing temperature on crystalline phase morphology should be investigated to find a micro/nanostructure, which improves mechanical properties.

**5. To evaluate mechanical properties of the NFCs in amorphous and crystalline states.** The effect of the nanofibrillar network on the mechanical properties of the PLA matrix

should be pursued separately from the impact of the crystalline phase. In addition, the effect of crystalline phase morphology will be studied by testing samples that are prepared at various annealing temperatures.

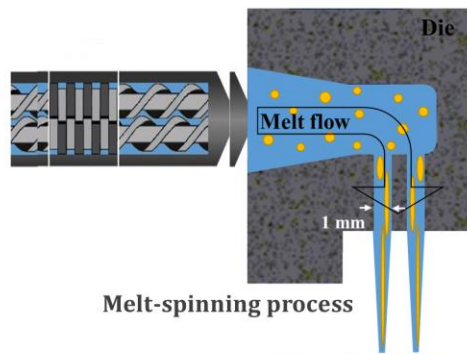
**6. To evaluate the foamability of the NFCs and PLA/PBT/clay nanocomposite samples compared to PLA.** With the hypothesis of the beneficiary effect of modified viscoelasticity and crystallinity behaviors (either in the presence of the PBT nanofibrillar network or in the samples containing nanoclay), foam properties should be characterized.

Chapter 5.1: Chemical and physical interactions

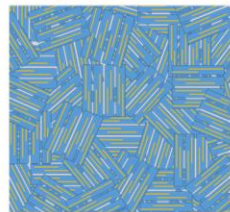


Chapter 5.9: Foamability

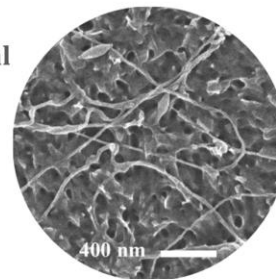
Chapter 5.2 & 5.3: Rheology for process optimization and morphology development



PBT nanofibrils in chopped PLA fibers

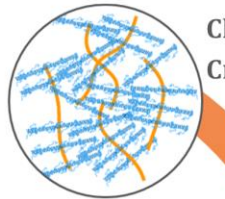


Chapter 5.4: Morphological observations



compression molding

Chapter 5.5: Crystallization behavior



Chapter 5.8: Shear and elongational rheological studies



Chapter 5.6 & 5.7: Mechanical and thermomechanical characterization



Figure 3-1. Graphical abstract of the thesis summarizing the chapters in the result section.

**Figure 3-1** gives a schematic overview of the strategy development in this thesis. Chapter 1.5 will discuss the compatibility between the components by investigating their chemical and physical interactions because compatibility plays a significant role in morphology development. The chemical interactions between the two polyesters should be understood on the molecular scale using solid state nuclear magnetic resonance ( $^{13}\text{C}$ -NMR) spectroscopy. The physical interactions between PLA and PBT must be explored at the die temperature, therefore the components' surface free energies will be measured at room temperature and will be extrapolated to the die temperature.

Chapter 5.2 and chapter 5.3 rheologically explains the optimized processing conditions for the in situ generation of PBT nanofibrils in the PLA matrix. In chapter 5.2, the melt rheological criteria suggested for fibrillation of minor phase within the matrix under shear flow will be calculated and compared with the related borders. A mathematical model of the extensional flow out of the die in chapter 5.3 helps understanding the stability of the droplet deformation in the flow. In chapter 5.4 morphological observation of the blends, fibers, nanofibrillar composites and PLA/PBT/clay nanocomposites will be presented, discussed and correlated to the compatibility of the components (chapter 5.1) and the rheological studies in chapters 5.2 and 5.3.

Chapter 5.5 concentrates on the crystallization behavior of PLA, PLA/PBT fibers and PLA/PBT NFCs. The investigations cover isothermal crystallization, non-isothermal crystallization (at atmospheric pressure and high-pressure  $\text{scCO}_2$ ) and crystallization morphology (developed from cold crystallization or melt crystallization).

In chapter 5.6, thermomechanical behavior of the NFCs will be compared to PLA. Mechanical properties of amorphous and crystalline PLA and NFCs will be discussed in chapter 5.7. Melt rheological behavior of PLA, PLA/PBT blends and NFCs will be surveyed under dynamic shear flow in chapter 5.8 to investigate the melt elasticity of the samples. Additionally, uniaxial elongational viscosity of the nanofibrillar composites and PLA/PBT/clay nanocomposites will be discussed in chapter 5.8. Last but not least, the foamability of the PLA, NFCs and PLA/PBT/clay nanocomposites will be investigated at different foaming conditions in chapter 5.9. The foams will be characterized regarding their density and cellular structure.

The contents of this thesis are partially published by the author in the form of 2 peer reviewed articles. Permissions to reprint the text and figures from them for this dissertation are obtained from each journal. 2 more papers from the results in this work are ready for submission.



## 4 Experimental

### 4.1 Materials

Extrusion grade, semicrystalline PLA under the trade name of 2003D comprising ~4.5 % of D-Lactide content and with a melt flow rate of 6 g/10 min (210 °C/2.16 kg) was purchased from NatureWorks LLC (U.S.A). The values of its weight-average molecular weight ( $M_w$ ), number-average molecular weight ( $M_n$ ), and polydispersity index (PDI) were measured as  $2.08 \times 10^5$ ,  $1.35 \times 10^5$  g/mol, and 1.54, respectively, using a gel permeation chromatography (GPC) (PSS SECcurity 1260 HPLC-Pumpe). Semicrystalline PBT (Pocan B1300) with a melting temperature of 225 °C and a melt volume rate of 45 cm<sup>3</sup>/10 min (250 °C/2.16 kg) was purchased from Lanxess AG (Germany). PBT (Pocan B1300) is non-reinforced, suitable for food contact, injection molding grade, and extrusion grade. The  $M_w$ ,  $M_n$ , and PDI of PBT were measured as  $7.36 \times 10^4$ ,  $4.18 \times 10^4$  g/mol, and 1.76, respectively. The neat materials were cryomilled using a centrifugal mill (ZM 200, Retsch) equipped with a sieve of 1 mm. Organically modified MMT, Cloisite 20A (C20A), was obtained from Southern Clay Co. (U.S.A.). The organic modifier of the C20A is reportedly to be dimethyl dehydrogenated tallow quaternary ammonium. Before processing, PLA and C20A were dried for 12 hours at 80 °C under 1 mbar vacuum. PBT was dried at 120 °C for 4 hours and under 1 mbar vacuum<sup>226</sup>.

The differential scanning calorimetry results of neat PLA (second heating run) and neat PBT (cooling and second heating runs) are presented in **Figure 4-1**, which helps understand the settings in the process temperature profile. The  $T_m$  of 224 °C,  $T_g$  of 66 °C, and melt crystallization temperature onset of 191.5 °C were obtained for PBT.

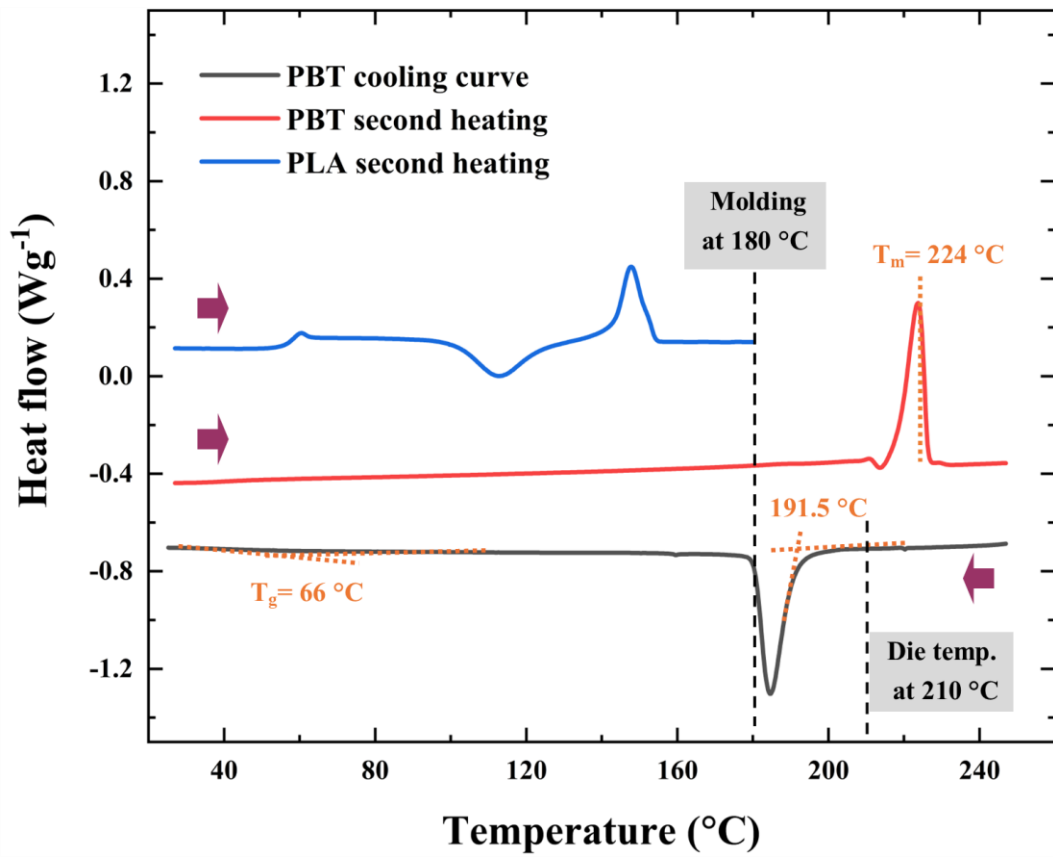


**Figure 4-1.** DSC results of neat PLA (second heating run); and neat PBT (first cooling run and second heating run).

## 4.2 Processing

### 4.2.1 PLA/PBT fibers and composites

First, PLA and PBT were dry blended in different weight percentages of PBT (1, 2, 3, 5, and 10 wt%). The mixtures were then fed into a co-rotating twin-screw extruder (Process11, Thermo scientific, Germany) via a gravimetric dosing system (Brabender, Germany). Extruder and die in total have 8 thermal zones. The screws are fully segmented with an L/D ratio of 40 and 11 mm diameter. **Figure 4-2** shows the equipment and the screw design used for the melt-spinning process.

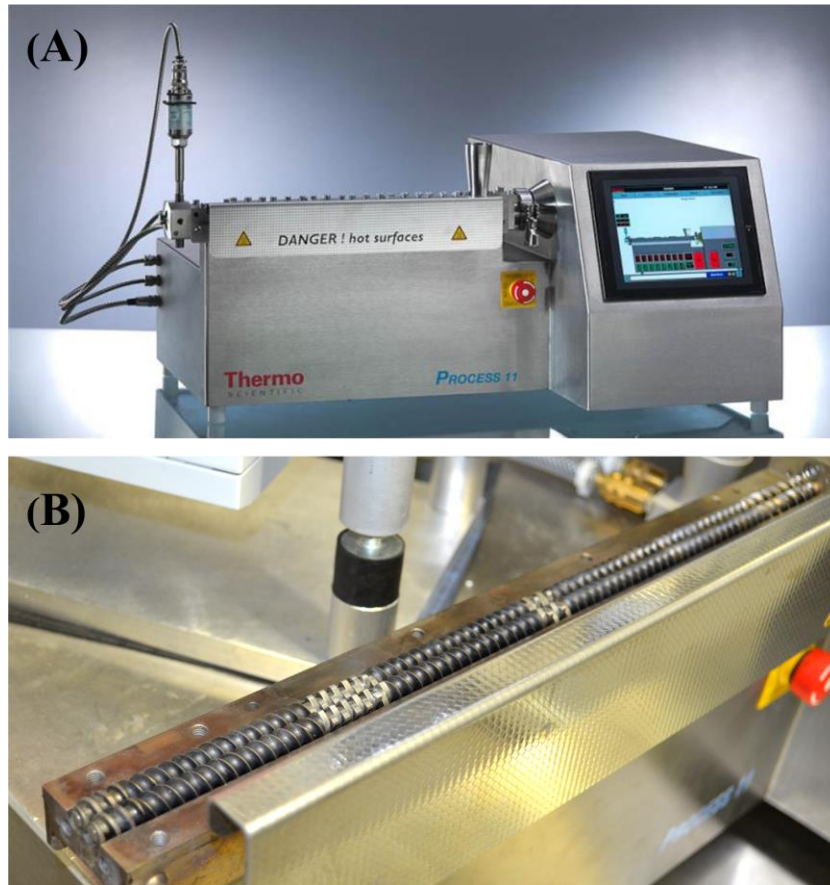


**Figure 4-2.** (A) Twin screw micro compounder; namely Process11, and (B) the co-rotating screw design used for the melt-spinning process.

A custom-made spinneret (die) with seven holes of 1 mm diameter and 8 mm length was well-designed to be adopted by the extruder (**Figure 4-3**). The extruder and die had totally 8 thermal zones, with temperature profile of 160, 180, 200, 220, 240, 240, 230 and 210 °C. The screw speed of 80 rpm and a feeding rate of 220 g/h resulted in 80 seconds of residence time, and 13 bar die

pressure. The above processing conditions were chosen to provide a high level of mixing while minimizing PLA degradation. The die temperature was adjusted in a temperature window with a higher limit as melt temperature of PBT and a lower limit as its onset of melt crystallization which is 191.5 °C (**Figure 4-1**). Therefore, after melt blending of PLA and PBT up to zone 7, the die temperature was decreased to 210 °C. This temperature setting was planned for two reasons:

- 1) to increase the PLA elasticity and thus enhance its capability for an intense stretching of the PBT dispersed phase.
- 2) to minimize the possibility of phase coarsening at the die chamber as there were no mixing elements.

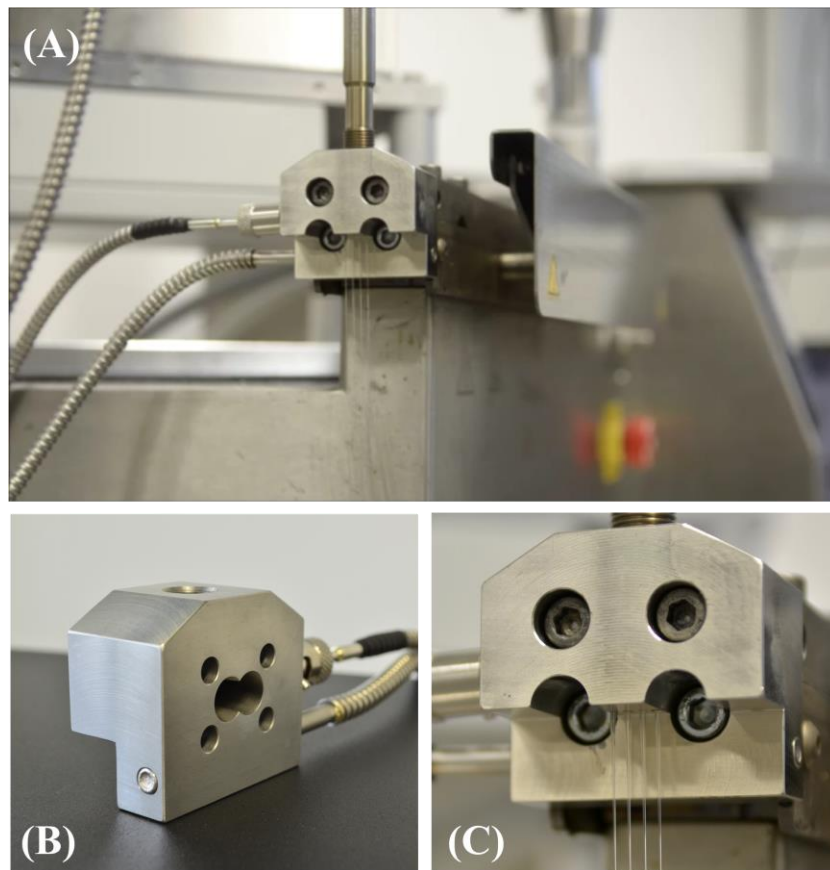


**Figure 4-3.** Spinneret design for the melt-spinning process: (A) Inlet of the melt; (B) Installed die on the extruder; (C) Outlet of the melt and the conic shape of the melt under stretch.

The melt-blended samples were stretched at the die and collected using a take-up roller rotating with a 190 m/min speed that resulted in 80  $\mu\text{m}$  diameter fibers. The Draw ratio was about 156, which is the ratio of die cross-section area to that of a fiber  $\left(\left(\frac{D_{die}}{D_{fiber}}\right)^2\right)^{25}$ . It should be noted that a

second drawing (cold draw above  $T_g$ ) was not used in this study. Before the spool, the fibers were cooled down to room temperature, as touching an aluminum fixed roller located 1.5 m lower than the die position. In order to fabricate the isotropic NFCs, PLA fibers, including PBT nanofibrils, were chopped into 1 to 2 mm long pieces. The chopped fibers were then compression-molded using a laboratory hydraulic hot press from PW10 (Paul-otto Weber, GmbH), operating at 180 °C and 60 kN for 3 minutes. Finally, the molds were quenched to 25 °C under a cold hydraulic press with a water cooling system for 3 minutes. The neat PLA was melt-spun, chopped, and molded in the same procedure and named as processed PLA. A schematic of the spinning line, individual PLA/PBT fiber, and the manufactured NFCs are presented in **Figure 4-4**. For clarification purposes, henceforth, the term “fiber” reflects the PLA/PBT melt-spun fibers, while “nanofibrils” or “NFs” refer to the fibrillated PBT domains in the PLA matrix. For instance, PLA/PBT 2 wt% fiber implies a PLA fiber with a diameter of 80  $\mu\text{m}$ , including 2 wt% of PBT nanofibrils. The isotropic NFCs with 1, 2, 3, 5 and 10 wt% of PBT NFs are named NFC1, NFC2, NFC3, NFC5 and NFC10, respectively. **Table 4-1** presents the compositions of each NFC and, accordingly, their name <sup>226</sup>.

**Figure 4-5A** shows the melt-spun PLA fibers, and **Figure 4-5B** shows the melt-spun PLA/PBT 2 wt% fibers. As can be seen, the phase separation of PLA and PBT in PLA/PBT 2 wt% fibers reduced their transparency compared to PLA fibers. The average diameter of the fibers was 80  $\mu\text{m}$  based on optical microscopy observations. **Figure 4-6** presents the compression-molded NFC2 sheets.

**Table 4-1.** Dry-blended mixtures of PLA and PBT encompass various amounts of PBT composition and, accordingly, the fabricated NFCs.

Dry-blended pre-mixture	Throughput (g/h)	PLA (wt%)	PBT (wt%)	Name
PLA/PBT 1 wt%	220	99	1	NFC1
PLA/PBT 2 wt%	220	98	2	NFC2
PLA/PBT 3 wt%	220	97	3	NFC3
PLA/PBT 5 wt%	220	95	5	NFC5
PLA/PBT 10 wt%	220	90	10	NFC10

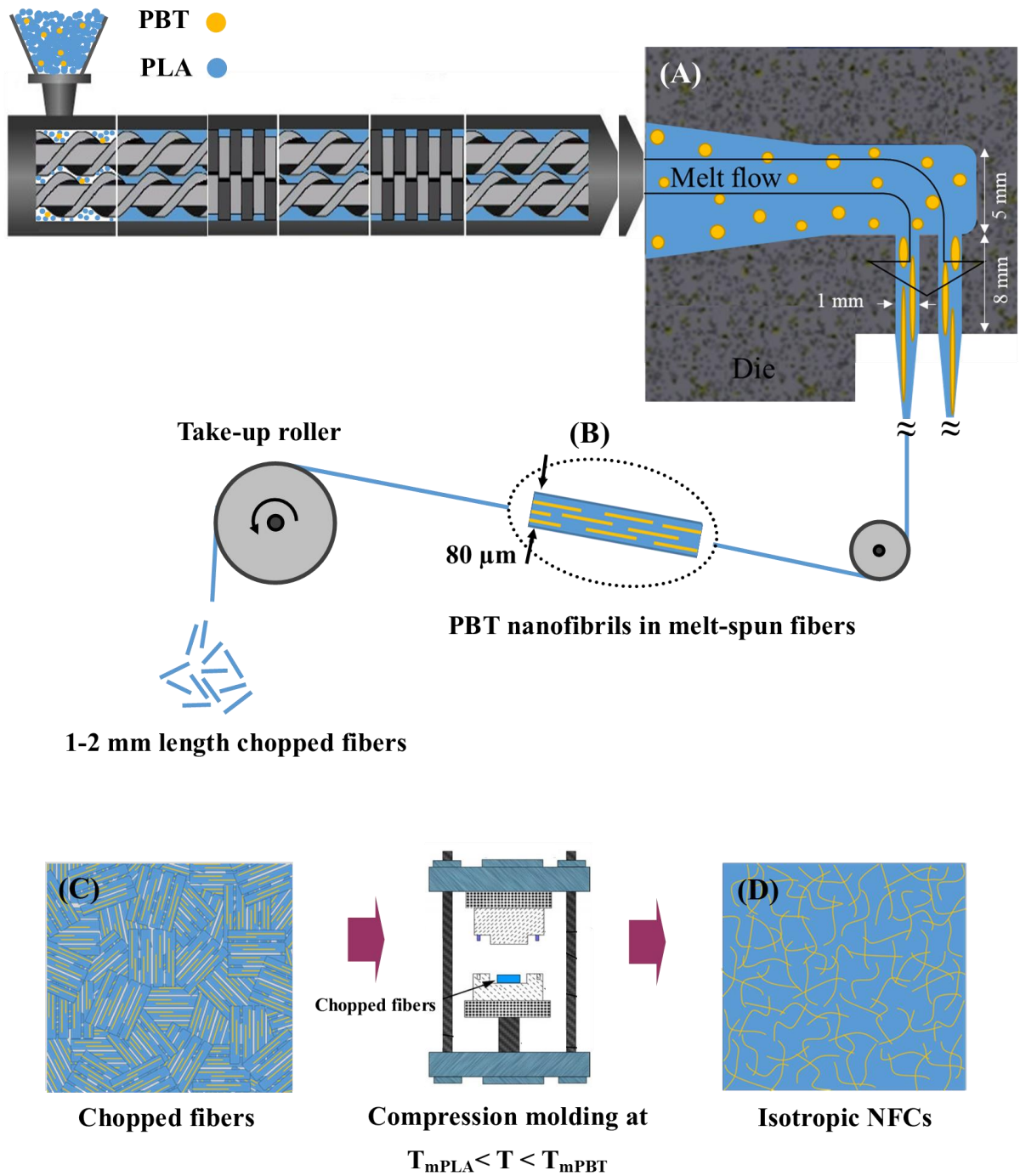


**Figure 4-4.** Schematic of melt blending, spinning, collection, and composite manufacturing; (A) PBT domains orientation in a spinneret die and their fibrillation through the hot stretching of the blend (B) A PLA/PBT fiber (C) Chopped fibers (D) Isotropic compression-molded NFCs at 180 °C <sup>226</sup>.

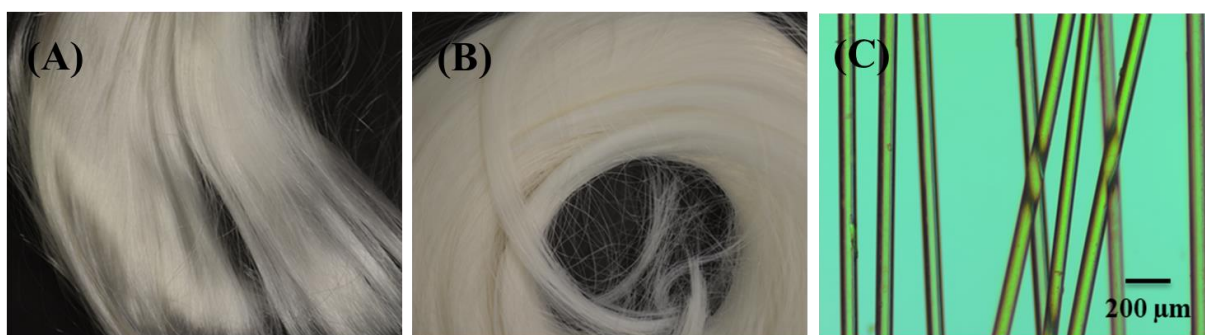


**Figure 4-5.** (A) melt-spun PLA fibers; (B) melt-spun PLA/PBT 1 wt% fibers; and (C) Average fiber diameter of 80 μm.

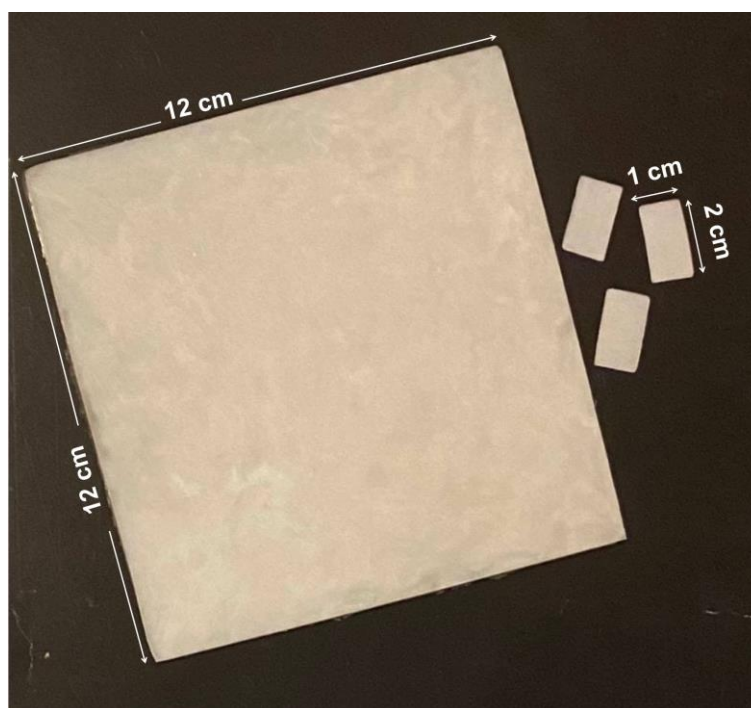


**Figure 4-6.** Fabricated in situ nanofibrillar composite including 2 wt% of PBT (NFC2).

#### 4.2.2 PLA/PBT/nanoclay fibers and nanocomposites

To enhance the PLA matrix's elasticity and achieve effective stretching of PBT domains, nanoclay Closite20A was introduced to the PLA matrix before blending with the PBT component. For this purpose, Closite20A was chosen because it has the highest compatibility with PLA relative to the other clays<sup>227, 228</sup>. The migration of nanoclay to the PBT droplets should be minimized because it would reduce their deformability due to the elasticity increase. The processing's consequences were planned by considering the desirable nanoclay partitioning and feeding limitations.

The powdered PLA and C20A were dry-blended at two compositions by weight percent 98/2 and 97/3 and were compounded using the Process11 equipped with a round die of 2 mm diameter. The co-rotating screws with 3 kneading zones and a screw speed of 150 rpm were selected to maximize the nanoclay dispersion. The temperature at the feeding zone was 160 °C, and at the seven other zones was fixed at 180 °C. The PLA/C20A compounds were granulated and then melt-blended with PLA/PBT dry-blended mixtures in the spinning line. Two gravimetric feeders were used to accurately control the feeding rates of PLA/C20A granulates and PLA/PBT mixtures. The spinning process was performed in the same setup and conditions as in section 4.2.1. However, increased elasticity of the melt flow restricted the throughput to 200 g/h. The PLA/PBT mixtures, including 4 and 8 wt% of the PBT component, made the feeding of a small amount of PBT possible. The nanocomposites were prepared through compression molding of the chopped fibers and were designated as PLA/PBT<sub>x</sub>/C<sub>z</sub>, where x and z present the weight percent of PBT and C20A, respectively. **Table 4-2** listed the four different final samples, their compositions, the methods of premixing, and the feeding rates of premixed components. The desired morphology of the hybrid nanocomposites is presented in **Figure 4-7**, where the exfoliated clay is supposed to enhance the elasticity of PLA to develop PBT nanofibrils.



**Table 4-2.** The different feeding rates of PLA/C20A compounds and PLA/PBT dry-blended mixtures resulted in four different compositions in the final PLA/PBT/C20A nanocomposites.

Pre-mixtures	Methods of pre-mixing	Throughput (g/h)	PLA (wt%)	PBT (wt%)	Clay (wt%)	Brief name
PLA/PBT 4 wt%	Dry-blending	50	97.5	1	1.5	PLA/PBT1/C1.5
PLA/C20A 2 wt%	Melt compounded and granulated	150				
PLA/PBT 4 wt%	Dry-blending	50	96.5	1	2.5	PLA/PBT1/C2.25
PLA/C20A 3 wt%	Melt-compounded and granulated	150				
PLA/PBT 8 wt%	Dry-blending	50	97	2	1	PLA/PBT2/C1
PLA/C20A 2 wt%	Melt compounded and granulated	150				
PLA/PBT 8 wt%	Dry-blending	50	64.5	2	2.5	PLA/PBT2/C2.25
PLA/C20A 3 wt%	Melt compounded and granulated	150				

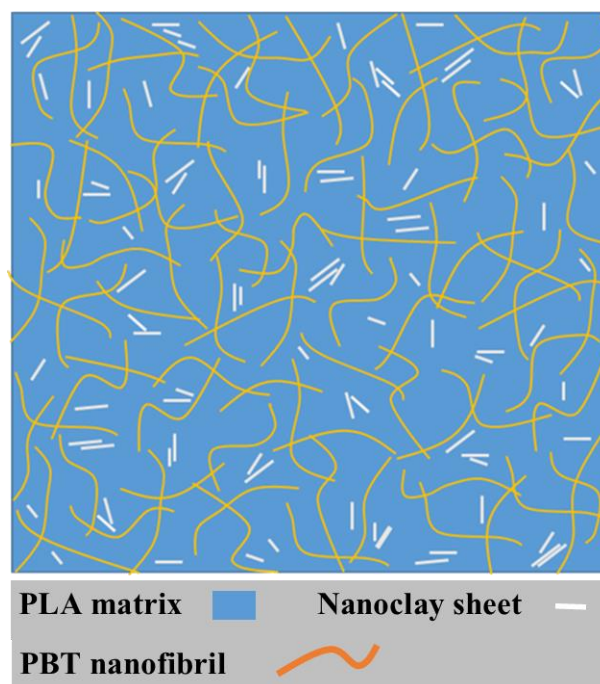


**Figure 4-7.** The ideal schematic of the hybrid system of rheologically modified PLA matrix using the dispersion of nanoclay resulted in the development of PBT nanofibrils.

## 4.3 Characterization

### 4.3.1 Solid-state nuclear magnetic resonance

The ester exchange reaction of two polyesters is a common reaction that can occur during the melt blending of the components and affect their compatibility and intrinsic behavior. Neat PLA, neat PBT, and PLA/PBT fibers, including 10 wt% of PBT NFs, were cryomilled using a centrifugal mill (ZM 200, Retsch) equipped with a sieve of 80  $\mu\text{m}$ . Solid-state nuclear magnetic resonance ( $^{13}\text{C}$ -NMR) spectra of PLA, PBT, and PLA/PBT 10 wt% fibers were recorded at room temperature on a Bruker Avance II spectrometer operating at a  $B_0$  field of 7.1 T using a triple-resonance 4 mm Bruker magic angle spinning (MAS) probe at a rotational frequency of 12.5 kHz.  $^{13}\text{CH}$ (100.6 MHz) MAS spectra were obtained using a ramped cross-polarization experiment, where the nutation frequency  $\nu_{\text{nut}}$  on the proton channel was varied linearly by 50 %. The corresponding  $\nu_{\text{nut}}$  on the  $^{13}\text{C}$ -NMR channel and the contact time were adjusted to 70 kHz and 3 ms, respectively. During the acquisition period, proton broadband decoupling was applied using a spinal-64 sequence with  $\nu_{\text{nut}} = 70$  kHz.  $^{13}\text{C}$ -NMR spectra were referenced indirectly with respect to tetramethylsilane using adamantane as a secondary reference <sup>226</sup>.

Northern Bavarian NMR Center kindly provided the solid-state NMR equipment and test results in the Faculty of Biology, Chemistry & Earth Science at the University of Bayreuth.

### 4.3.2 Contact angle measurements

The properties of immiscible polymer alloys are crucially dependent on their morphology, which is thermodynamically governed by the interfacial tension between the two components. Contact angle measurements of PLA and PBT were performed at 25  $^{\circ}\text{C}$ , using water and diiodomethane as standard probe liquids and a drop shape analyzer (DSA4, Kruss GmbH, Germany). The reproducibility of the reported data was guaranteed through the deposition of twenty drops of each liquid on the compression-molded sheets of the polymers under investigation. The total surface energy, the disperse, and the polar parts were determined using the Wu method <sup>229</sup>, which is appropriate for low-energy systems such as polymer blends. The measured surface free energy of the components at 25  $^{\circ}\text{C}$  should be extrapolated to the die temperature. Assuming that the polarity ratio remains constant, the thermal coefficients of the surface tension ( $-\frac{d\gamma}{dT}$ ) for PLA and PBT were set to 0.06 and 0.065 mN/m, respectively, according to the reports <sup>81, 91, 230</sup>. The measurements were performed in the Keylab Glass Technology, Faculty of Engineering, the Department of Ceramics at the University of Bayreuth.

### 4.3.3 Rheological measurements

Studying the melt viscoelastic behavior of neat polymer components, blends, and composites under shear or elongational flow provides valuable knowledge for process implementation, morphology development, and structure identification. Rheology as a strong tool supplies information about the bulk, which is complementary to conventional electron/atomic microscopy methods can be very useful for recognizing morphology, the effective mechanisms in controlling morphology, and the properties concluded from that, e.g., mechanical, electrical.

#### 4.3.3.1 Shear rheology

Shear rheological studies were performed in two separate stages: (I) a combination of steady shear and oscillatory rheological measurements on the neat components were applied to investigate the droplet deformation under shear flow inside the spinneret. (II) After the NFCs fabrication, oscillatory rheological measurements were carried out to identify the nanostructure and its effect on the viscoelastic behavior of the fibrillar composites. The equipment, experimental conditions, selected parameters, and geometries in each stage are described below .

##### 4.3.3.1.1 Rheological studies of the melt-spinning process

A capillary rheometer (Göettfert, Trico Ram model, Germany) equipped with three capillaries die having a diameter of 1 mm and lengths of 10, 20, and 30 mm (L/D ratio of 10, 20, and 30) has been used to obtain the flow curve of neat PLA at 210 °C in the shear rate range of 20 to  $2 \times 10^3 \text{ s}^{-1}$ . The rheometer with three independently speed-controlled pistons was capable of providing a speed range within 0.00005 to 40 mm/sec. A power law index ( $n_p$ ) of 0.7 was obtained through the linear fitting of the shear-thinning region (**Figure 4-8**).

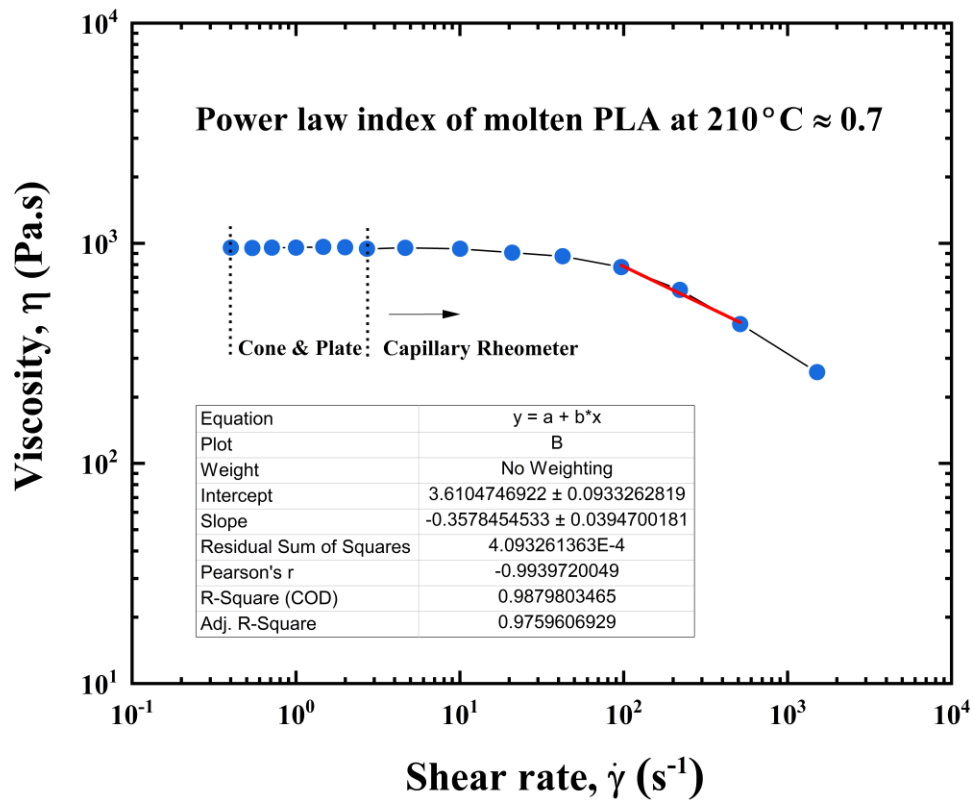


**Figure 4-8.** Steady shear viscosity as a function of the applied shear rate, linear fitting of the shear-thinning region <sup>81</sup>.

Considering a melt density of  $1100 \text{ kg.m}^{-3}$  for PLA at  $210 \text{ }^\circ\text{C}$  (NatureWorks datasheet), the shear rate at the wall of each hole of the spinneret (die) could be calculated employing the Rabinowitsch correction <sup>231</sup>:

$$\dot{\gamma}_{die} = \frac{3n + 1}{4n} \left( \frac{4Q_v}{\pi (r_{die})^3} \right) \approx 90 \text{ s}^{-1} \quad (4-1)$$

Where  $r_{die}$  is the die radius (0.5 mm), and  $Q_v$  is the volumetric flow rate ( $8 \times 10^{-3} \text{ cm}^3/\text{s}$ ) passing through each hole.

The dynamic rheological measurements of both polymer components were performed using a strain-controlled rheometer (Rheometric Scientific SR 5000, U.S.A) equipped with a plate-plate geometry with 25 mm diameter and a 1 mm gap distance. The measurements were performed under a dry nitrogen atmosphere and at a common amplitude ( $\gamma$ ) of 1 % to remain within the linear viscoelastic region. The neat PLA and PBT were molded according to the plate geometry at 180 and  $240 \text{ }^\circ\text{C}$ , respectively, by applying an 80 kN load for 90 seconds. By considering the fact that the Cox-Merz rule is applicable for the rheological behavior of individual polymer

components,  $|\eta^*(\omega)| = \eta(\dot{\gamma})$  the time sweep and temperature sweep tests were performed on the neat materials<sup>81</sup>. In which  $\omega$  is the angular frequency in rad/s and  $\dot{\gamma}$  shear rate in s<sup>-1</sup>.

Since 210 °C (the die temperature) had been known as the highest isothermal melt crystallization temperature of PBT<sup>232</sup>, the time sweep test was run for PBT at 210 °C and an angular frequency ( $\omega$ ) of 90 rad/s to find out the possibility of its melt crystallization at the die conditions through time. In this case, PBT samples were melted and trimmed at 240 °C, and then the temperature was reduced to 210 °C before beginning the test. Dynamic storage modulus ( $G'$ ), dynamic loss modulus ( $G''$ ), and complex viscosity ( $|\eta^*|$ ) were recorded as functions of time.

The temperature sweep tests for PLA and PBT at different frequencies were run from 240 °C (as the highest processing temperature) down to 175 °C with a temperature ramp of -4 °C/min to study the rheological behavior of materials in the die under roughly simulated processing conditions. The viscosity ratio ( $\lambda$ ) and the ratio of a capillary number to the critical capillary number ( $\lambda'$ ) were calculated based on the viscosities of PLA and PBT at the die temperature and shear rate<sup>81</sup>.

#### **4.3.3.1.2 Rheological studies of NFCs**

Dynamic rheological measurements were conducted on a MCR 702 rheometer (Anton Paar, RheoCompass) using a parallel-plate fixture with a 25 mm diameter and a 1 mm gap to study linear viscoelastic behaviors of processed PLA, PLA/PBT blends, and NFC samples. Under nitrogen gas (N<sub>2</sub>) purging, chamber temperature was controlled at 190 °C, which was above the melting temperature of PLA and yet low enough to preserve the consistency of PBT NFs. Strain sweep tests were performed at a frequency ( $\omega$ ) of 10 rad/s to all the samples to select a strain amplitude ( $\gamma$ ), 1 %, within the nanocomposites' linear viscoelastic response. The time sweep test for processed PLA was performed at a frequency ( $\omega$ ) of 10 rad/s to explore the PLA degradation by the time during rheological measurements. The frequency sweep tests were carried out in the frequency range of 0.1–200 rad/s and  $\gamma$  of 1 %.

#### **4.3.3.2 Uniaxial extensional viscosity measurements**

Uniaxial extensional viscosity growth was recorded versus time to evaluate the influence of the nanofibrillar network on the strain hardening behavior of NFCs. The measurements were carried out using an Extensional Viscosity Fixture (EVF, TA Orchestrator) attached to an Advanced Rheometric Expansion System (ARES). Rectangular specimens with the dimensions of 20 × 10 × 0.6 mm<sup>3</sup> were compression-molded at 180 °C and 60 kN for 3 minutes. The specimens were tested

under a nitrogen atmosphere at strain rates ( $\dot{\epsilon}$ ) of 0.01, 0.1, and 1 s<sup>-1</sup>, which are the dominant strain rates during bubble growth<sup>75, 233-235</sup>. The sample environment temperature of 170 °C was chosen that provided the most consistent results. At higher temperatures, sagging of processed PLA disrupts the tests; and at lower temperatures, NFC samples could not stick to the drums of the EVF fixture.

Since rheological measurements of PLA (either shear or elongation) are so sensitive to humidity, all the samples after compression molding based on intended geometry were dried overnight in a vacuum oven at 80 °C, 1 mbar.

#### 4.3.1 Polarized optical microscopy

Polarized optical microscopy was used to observe the effect of oriented PBT NFs on PLA crystalline phase morphology in PLA/PBT 2 wt% fibers. An optical microscope (Nikon, DIAPHOT 300) equipped with the cross-polarized filters and hot stage (Mettler Toledo, U.S.A., FP82HT) was used. PLA fibers and PLA/PBT 2 wt% fibers were separately sandwiched between two heat-resistant microscope slides and placed in the hot stage. The hot stage temperature increased from room temperature to 170 °C with a rate of 5 °C/min, and a digital camera (Nikon, DS-Ri2) recorded the micrographs<sup>226</sup>.

#### 4.3.2 Scanning electron microscopy

Scanning electron microscopy (SEM) was employed to observe the morphology of PBT domains across and along the longitudinal direction of the die. In addition, the visualization of PBT nanofibrils in the PLA/PBT fibers and NFCs; and the crystalline phase of PLA was achieved using SEM observations. The non-stretched filaments containing different PBT amounts coming out of the die were immediately cooled down in a cold-water bath. These filaments were quenched in liquid nitrogen for 10 minutes and cryogenically fractured perpendicular to the die direction. Thereafter, their cross-sections were sputter-coated with platinum and carbon and observed using a field-emission SEM instrument (LEO 1530, Zeiss, Germany) operating at a 3 kV accelerating voltage<sup>226</sup>.

Small pieces of the filaments, fibers, and NFCs were immersed in a water/methanol (1:2 by volume) solution containing 0.025 mol/L sodium hydroxide for 24 hours at room temperature to etch a thin layer of PLA on the surface and observe the PBT domains and nanofibrils<sup>25</sup>. The

samples were placed in an ultrasonic bath for 15 minutes at room temperature before washing with distilled water. All samples were dried overnight at 55 °C under 1 mbar vacuum.

In order to observe the crystalline phase morphology of PLA, SEM images were obtained after annealing processed PLA and NFC samples. Annealing times of the samples were determined based on the time duration required to complete the isothermal curves. Accordingly, the annealing of processed PLA at 100 and 114 °C was finalized after 1 and 2.5 hours, respectively. However, annealing of NFC1 at  $T_{iso}$  of 100, 114, 117, 120, and 124 °C in DSC pans was accomplished within 9, 12, 15, 20, and 36 minutes, respectively. The samples were etched for 12 hours using the solvent mentioned above to gently hydrolyze the amorphous phase of PLA and allow visualization of the crystalline structure<sup>81</sup>.

### 4.3.3 Transmission electron microscopy

To gain deep morphological information of the PLA/PBT blends at higher concentrations of PBT, the non-stretched filaments were cut into thin sections (80 nm) at a temperature of -140 °C using a Leica EM FC7 cryo-ultramicrotomy equipped with a diamond knife. After cutting, the ultrathin sections were placed on a copper grid, and heavy-element staining was performed by 15 minutes of exposure to vapor of Ruthenium tetroxide ( $RuO_4$ ). This reagent preferentially stains the aromatic rings; therefore, the dark area in the micrographs is attributed to the PBT dispersed phase<sup>236</sup>. The Transmission electron microscopy (TEM) images were recorded with a LEO EM922 Omega energy filtering transmission electron microscope operated at 200 kV<sup>226</sup>.

The state of nanoclay dispersion and the PBT domain morphology in PLA/PBT/C20A nanocomposite were also observed using the transmission electron microscope.

### 4.3.4 Atomic force microscopy

Atomic force microscopy (AFM) images were taken using a Dimension Icon AFM instrument (Bruker, U.S.A) to observe the crystallite morphology of PLA in processed PLA and NFC1. Images were acquired in the PeakForce tapping mode in the air and using an OTESPA-R3 cantilever purchased from Bruker Nano Inc. with a typical spring constant of 26 N/m and a resonant frequency of 200 kHz. Images were recorded using 512 up to 2048 scan-lines depending on the image size and required resolution. Moreover, scan sizes of  $4 \times 4 \mu m^2$  up to  $60 \times 60 \mu m^2$  and scan rates between 0.12 Hz and 0.3 Hz were employed for imaging. The Peak Force set point was set to



a value between 0.01 and 0.03 V, while the Peak Force amplitude and frequency were 100 nm and 2 kHz, respectively. AFM images were processed using NanoScope Analysis 1.80. Data were leveled with a first-order plane fit and flattened via subtracting a first-order polynomial background<sup>81</sup>.

In order to observe the crystalline phase of PLA, after annealing, etching, and drying of the samples (see section 4.3.2), the films were adhered to a metal plate holder with double side tape and were tested using one specific cantilever.

### 4.3.5 Differential scanning calorimetry

#### 4.3.5.1 Non-isothermal investigations

The non-isothermal crystallization of the processed PLA and NFC samples was conducted at atmospheric pressure using a differential scanning calorimeter (DSC 1, Mettler Toledo, U.S.A). Measurements were carried out on 10 to 12 mg of each sample under dry nitrogen purging at a rate of 50 ml/min and a temperature ramp of 5 °C/min. The crystallization behavior of PLA in the presence of PBT NFs was studied in the temperature range of 20 to 180 °C. All of the heating or cooling steps were followed by an isotherm step at the final temperature for two minutes to ensure the melting, stability, or history removal. The degree of crystallinity was calculated using the following equation<sup>237</sup>:

$$X_c = \left( \frac{H_m - H_{cc}}{H_{m0} \times w} \right) \times 100 \quad (4-2)$$

Where  $X_c$  (%) is the normalized crystallinity of PLA,  $H_m$  (J/g) represents the heat of fusion,  $H_{cc}$  (J/g) is the heat of cold crystallization,  $H_{m0}$  accounts for the heat of fusion for the 100 % crystalline PLA and is set to 93.7 J/g<sup>238</sup> based on the literature, and  $w$  is the weight fraction of PLA in the NFCs.

In order to compare the effect of PBT domains' morphology, namely nanofibrillar and droplets on the crystallinity of PLA, one sample of NFC2 was heated up quickly from 20 to 240 °C with a temperature ramp of 50 °C/min. Melting and heat-reverse of the PBT NFs could be accomplished during 2 minutes isothermal treatment at 240 °C. The heat flow of the treated sample, which is named as NFC2-240, was subsequently recorded at -5 °C/min rate of cooling<sup>226</sup>.

#### 4.3.5.2 Isothermal melt crystallization

The isothermal melt crystallization of processed PLA and NFCs was studied at atmospheric pressure using a differential scanning calorimeter (DSC 1, Mettler Toledo, U.S.A). Samples of 10 to 12 mg were sealed in aluminum pans and subjected to the following thermal procedure under nitrogen flow: (i) heating to 180 °C at a heating rate of 50 °C/min; (ii) isothermal treatment at 180 °C for 3 minutes to remove any thermal history of the samples; (iii) cooling to the isothermal crystallization temperature ( $T_{iso}$ ) of 100 °C, 103 °C, 107 °C, 110 °C, 114 °C and 117 °C at a cooling rate of 50 °C/min; (iv) isothermal treatment at  $T_{iso}$  for 160 minutes; (v) quenching to 20 °C with a cooling rate of 50 °C/min. Consequently, the heating run of the quenched samples was conducted from 20 to 180 °C at a heating rate of 5 °C/min to investigate the degree of crystallinity (using **Equation ( 4-2 )**) and crystal forms of PLA nucleated at different  $T_{iso}$  levels. A schematic representation of the thermal program is depicted in **Figure 4-9**<sup>81</sup>.

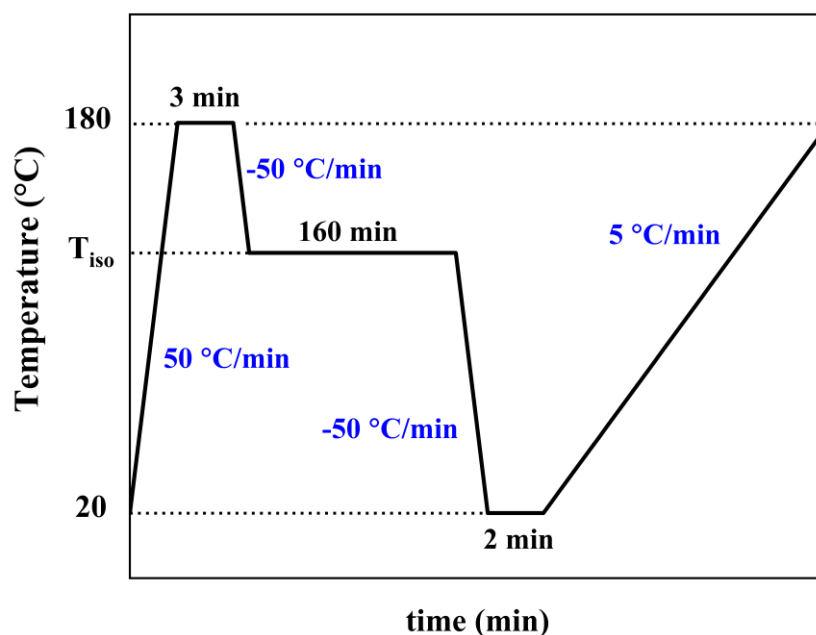


**Figure 4-9.** The thermal program was employed for the DSC measurement of processed PLA and NFCs<sup>81</sup>.

#### 4.3.5.3 High-pressure differential scanning calorimetry

In order to study the effect of  $scCO_2$  on the crystallinity of PLA and NFCs during the foaming process, DSC measurements were performed at atmospheric pressure and under  $scCO_2$  pressure. The DSC experiments were implemented on amorphous samples of 16-20 mg using a high-

pressure DSC (HP-DSC) from NETZSCH (DSC 204 HP Phoenix, Germany). In a nitrogen atmosphere at atmospheric pressure, the temperature rapidly increased from room temperature to the foaming temperatures (saturation temperatures,  $T_{\text{sat}}$ ) of 128, 116, and 108 °C with a ramp of 20 °C/min. The isothermal cold crystallization of the samples was developed at different  $T_{\text{sat}}$  for 30 min. Then the temperature increased from  $T_{\text{sat}}$  to 180 °C with a ramp of 5 °C/min to melt all the formed crystals and gain information about crystallinity and melting peaks.

In order to analyze the crystallinity of processed PLA and NFC samples under the foaming conditions, a similar procedure was followed under  $\text{scCO}_2$  pressure. Since the highest applicable pressure to the HP-DSC was 140 bar, the isothermal cold crystallization of the samples was developed at the saturation temperatures under 140 bar  $\text{CO}_2$  pressure, which were the closest possible conditions to the foaming experiments. For this purpose, the samples were heated from room temperature to  $T_{\text{sat}}$  at a heating rate of 20 °C/min and then equilibrated for 3 min. The 3 min time was considered because it was required for the sampling in the autoclave. Subsequently, the DSC chamber was pressurized with  $\text{scCO}_2$  up to 140 bar. For supplying such pressure, the pump needed to be refilled 7 to 10 times depending on the  $T_{\text{sat}}$ , obviously less refilling times for higher  $T_{\text{sat}}$ . The samples were maintained at these conditions for 30 min, which was equal to the autoclave saturation time. Then the temperature was increased from  $T_{\text{sat}}$  to 180 °C to melt all the formed crystals. The thermal program employed for DSC and HPDSC measurement of processed PLA and NFC samples are presented in **Figure 4-10**.

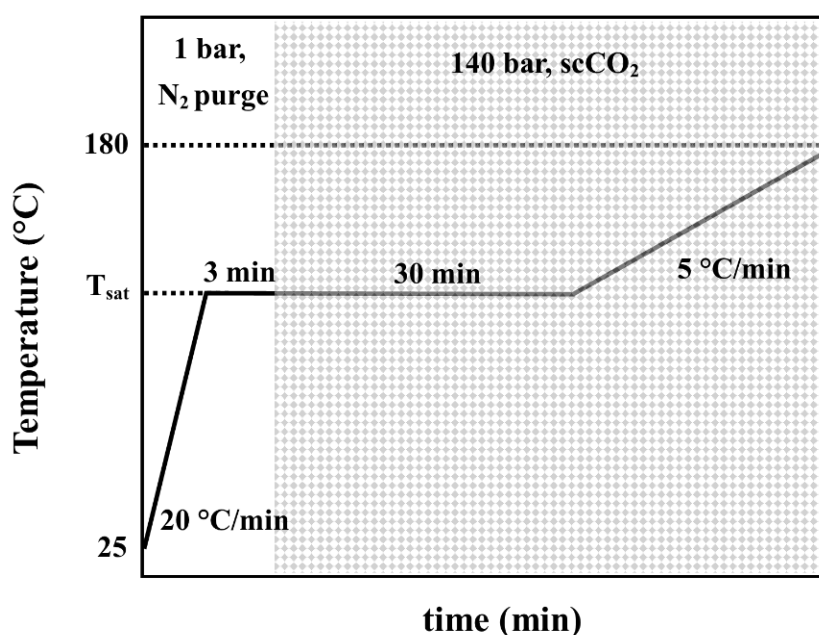


**Figure 4-10.** The schematic of the thermal program in HP-DSC is based on the batch foaming process.

### 4.3.6 Mechanical properties

#### 4.3.6.1 Dynamic mechanical thermal analysis

Dynamic mechanical thermal analysis (DMA) was performed on rectangular specimens with the dimensions of  $50 \times 10 \times 2 \text{ mm}^3$ ) using Gabo Eplexor instrument (500 N HT, NETZCH, Germany). Crystalline samples were prepared using compression molding at  $180 \text{ }^\circ\text{C}$  and then immediately transferred under a second hot press with a set temperature of  $100 \text{ }^\circ\text{C}$ . All the samples were annealed at  $100 \text{ }^\circ\text{C}$  for 10 minutes, which is slightly more than the required time for temperature stabilization and the complete evolution of the crystalline phase in all the NFCs. The difference in the crystallinity of NFCs is less than 2 %. The test setup applied tensile forces to the specimens at a constant frequency of 1 Hz. The applied strain was kept small enough to ensure recording the linear viscoelastic behaviour of the samples. The temperature range of 0 to  $160 \text{ }^\circ\text{C}$  was swept with a heating rate of  $2 \text{ }^\circ\text{C}/\text{min}$ .

#### 4.3.6.2 Tensile test

In order to investigate the mechanical properties of NFCs at the amorphous state and after the development of the NBSK superstructure, standard dumbbell specimens were prepared according to DIN EN ISO 527-2 with a thickness of 2 mm and a width of 4 mm by compression molding at  $180 \text{ }^\circ\text{C}$ . The amorphous samples were attained by quenching under a hydraulic press, while samples containing 20 % crystallinity were attained through annealing under a second hot press at a temperature of  $100 \text{ }^\circ\text{C}$ . The required annealing times for processed PLA, NFC2, and NFC3 were approximately obtained from relative crystallinity curves of isothermal crystallization studies. Then the crystallinity of the samples was measured using DSC to correct the required time experimentally. The considered time for stabilizing the mold temperature under the second hot press was calculated by mathematical modeling of the system and compared with the indicated temperatures by a thermocouple. After annealing, the molds are quenched to room temperature using the hydraulic press equipped with a water cooling system. Then tensile tests under uniaxial loading were performed at  $23 \text{ }^\circ\text{C}$  and 50 % relative humidity using a Zwick universal testing machine (Model 1485, U.S.A.) with a cross-head speed of 50 mm/min, a gauge length of 50 mm, and a 10 kN load cell. At least five specimens were tested for each sample, and the mean values and standard deviations are calculated and presented. Young's modulus was measured with a cross-head speed of 1 mm/min and analyzed in the linear viscoelastic area interval.

In order to scrutinize the effect of longer kebabs and their interlocking on the mechanical properties of NFCs, new tensile test specimens, after compression molding at  $180 \text{ }^\circ\text{C}$ , were

annealed at 114 °C. The required times for each sample's annealing to attain 20 % crystallinity were approximately calculated using relative crystallinity curves, which were adjusted experimentally.

#### 4.3.7 Foaming experiments

The physical foaming process was conducted using scCO<sub>2</sub> as a blowing agent to study the effect of the PBT NFs network on the foamability of PLA. A temperature-pressure regulated autoclave was used in which the chamber was connected to two parallel syringe pumps from Teledyne Isco (260D model, U.S.A.). Compression-molded amorphous samples of processed PLA and NFCs with dimensions of 20 × 10 × 0.6 mm<sup>3</sup> were placed in the chamber stabled at the selected temperature. The average required time for safely closing the autoclave was 3 minutes, which was supposed to trigger the cold crystallization of PLA. After the placement of each sample inside the chamber, it was pressurized by purging scCO<sub>2</sub> to 140 or 180 bar. In order to determine the proper temperatures for the two selected pressures, separated foaming tests were carried out in the temperature range of 100-135 °C. After 30 min saturation time, the chamber was depressurized quickly, and the samples were removed and cooled in a water bath. The lowest foam densities of PLA were acquired at two foaming conditions; 128 °C and 140 bar, and 116 °C and 180 bar. Therefore, the foam properties of PLA and NFCs were compared under these conditions. Besides, foaming of NFCs at 180 bar scCO<sub>2</sub> and 108 °C was probed to find out the effect of PBT NFs at a higher degree of crystallinity (lower saturation temperature,  $T_{\text{sat}}$ ) on the cellular structure. The three studied foaming conditions are schematically presented in **Figure 4-11**.

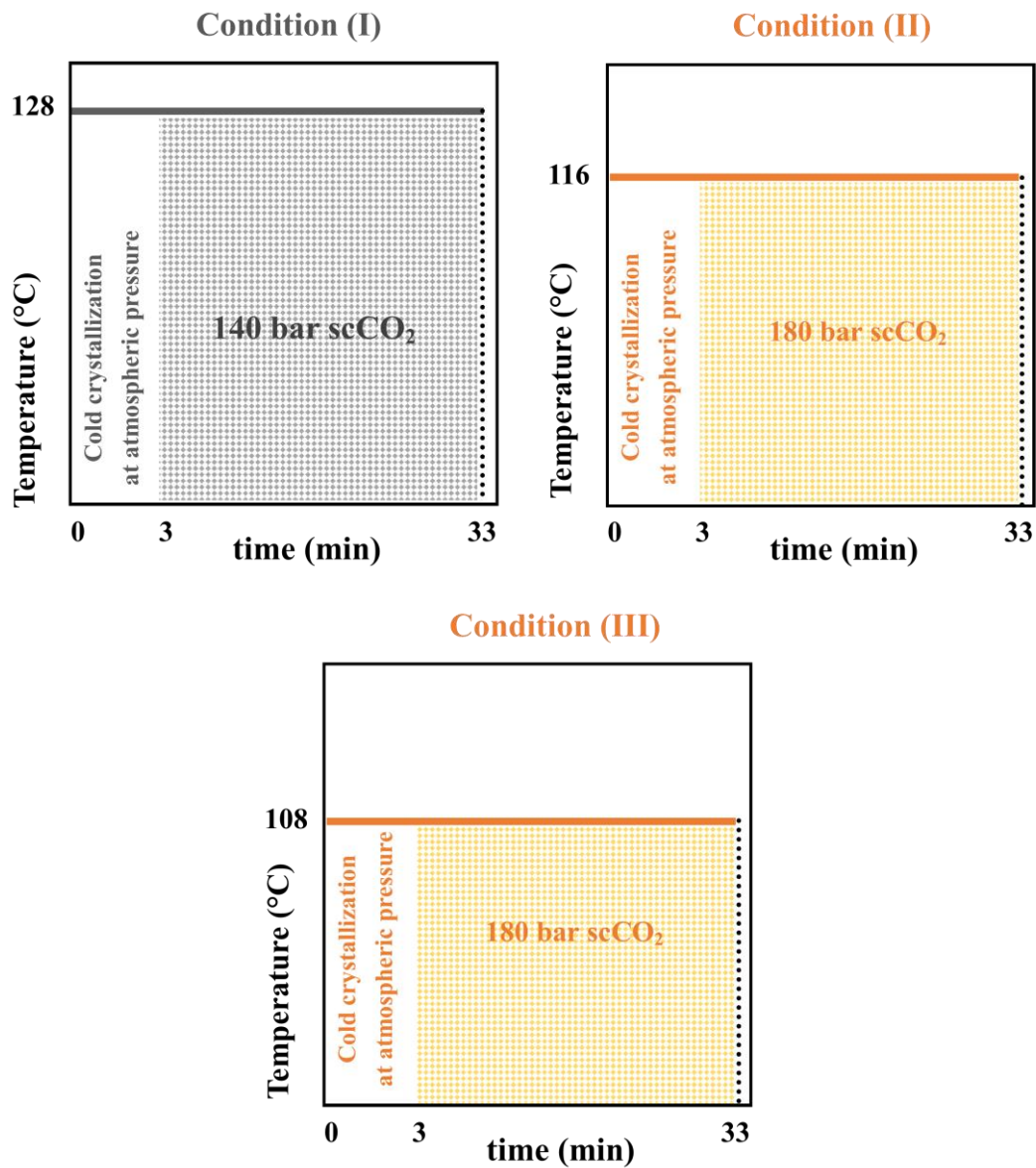


**Figure 4-11.** Schematic of foaming conditions: (I) 140 bar and 128 °C, (II) 180 bar and 115 °C, and (III) 180 bar and 108 °C.

The foam samples were placed for more than 30 min in a liquid nitrogen bath to gain brittle fractured surfaces. After sputter coating of the surfaces with platinum and carbon, the SEM micrographs were recorded for their characterizations. The average cell-size for each foam sample was measured using ImageJ software analysis on 4 different specimens. The cell density ( $N_0$ ) was calculated using **Equations ( 2-18 )** and **( 2-19 )**. The foam density of each sample was evaluated (see section 2.6.3) based on the water displacement method according to ASTM D792 and was reported by an average value of 3 measured specimens.

## 5 Results and Discussions

### 5.1 Chemical and physical interactions between the two polyesters

Investigating the interactions between the two polymer components is essential for adjusting the process implementation and explaining their role in morphology development. Accordingly, the possible chemical reactions between the two polyesters, such as ester exchange reactions during melt processing, have been analyzed using  $^{13}\text{C}$ -NMR spectra. The physical interaction between PLA and PBT was probed through the interfacial tension value obtained from the contact angle measurements method.

#### 5.1.1 Solid-state NMR spectra

CP-MAS  $^{13}\text{C}$ -NMR spectra of neat PLA, neat PBT, and NFC10 were derived in order to detect possible new chemical peaks and/or shifts that present special new groups or interactions generated by ester exchange reaction during the extrusion (**Figure 5-1B**)<sup>239</sup>. Among the NFCs, NFC10 was chosen because it includes the highest amount of PBT, increasing the possibility of detecting new chemical bonds. Three peaks for PLA were observed, which are corresponding to the carbonyl, methine, and methyl groups at 170.07, 69.8, and 17.4 ppm, respectively<sup>240, 241</sup>. Carbon groups of PBT, which are assigned as (a) to (e) on the structural schematic in **Figure 5-1A**, are detected at five different chemical shifts: the carbonyl bands at 164.9 ppm, the non-protonated aromatic carbons at 134.33 ppm, the protonated aromatic carbons at 130.04 ppm, the  $\text{OCH}_2$  groups at 65.5 ppm and the internal  $\text{CH}_2$  groups at 26.12 ppm<sup>242, 243</sup>. In the PLA/PBT 10 wt% spectra, the chemical peaks of PBT and PLA are separately settled, and no appreciable shifts or new peaks are detectable. This observation rejected the occurrence of possible chemical reactions between the functional groups of the components, such as copolymerization during the melt processing. It is noteworthy that since the molar weight ratio of PBT to PLA is 3.1, the indicative peaks of PBT in NFC10 are tiny<sup>226</sup>.

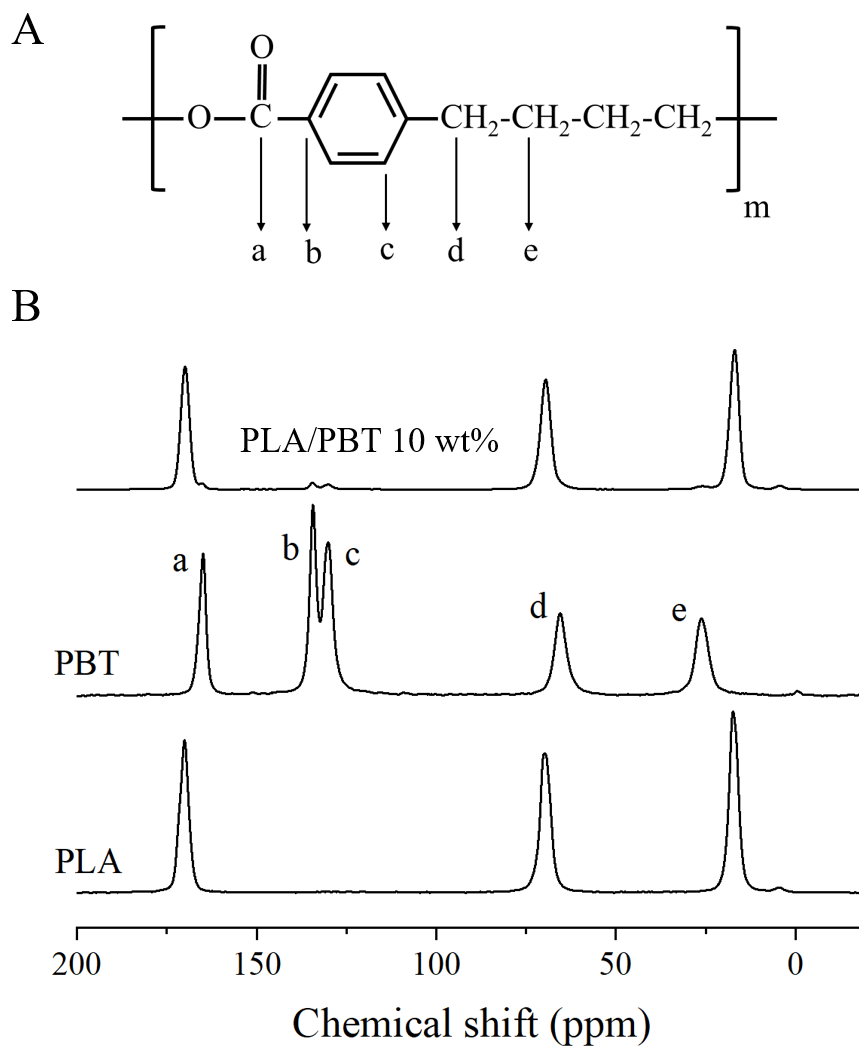


**Figure 5-1.** (A) Schematic of PBT molecular structure and five carbon groups signed as a, b, c, d, and e (B) Solid-state <sup>13</sup>C-NMR spectra of neat PLA, neat PBT, and NFC10 measured at 23 °C <sup>226</sup>.



### 5.1.2 Surface free energy and interfacial tension

Total surface free energy, at 25 °C along with its polar and dispersive components for the neat PLA and PBT are listed in **Table 5-1**. These data are extrapolated to 210 °C using the corresponding thermal coefficients<sup>91, 230</sup> and are summarized in **Table 5-2**. The calculated interfacial tension, which is equal to 0.1 mN/m at the die temperature, indicates an adequate affinity between the two immiscible polymers. The low interfacial tension and miscibility were reported for the blends of PLLA with lower homologs of PBT<sup>244</sup>. Lorenzo et al. claimed interactions between the ester functional groups of PLLA and PBT that established upon melt mixing, resulting in the compatibility between the constituents<sup>38, 81</sup>.

**Table 5-1.** Total surface free energy, its polar and dispersive components, and their ratio for the neat PLA and PBT measured at 25 °C<sup>81</sup>.

	$\upsilon^p$ (mN/m)	$\upsilon^d$ (mN/m)	Polarity ratio ( $\frac{\upsilon^p}{\upsilon^d}$ )	$\upsilon$ (mN/m)
<b>PLA</b>	12.3	38.9	0.316	51.2
<b>PBT</b>	11.2	38.4	0.292	49.6

**Table 5-2.** The extrapolated total surface free energy, its polar and dispersive components at 210 °C for the neat PLA, and PBT using the corresponding thermal coefficients<sup>81</sup>.

	$\upsilon^p$ (mN m <sup>-1</sup> )	$\upsilon^d$ (mN/m)	$\upsilon$ (mN/m)	$-\frac{d\upsilon}{dT}$ (mN/m °C)
<b>PLA</b>	9.6	30.4	40.0	0.06 <sup>91</sup>
<b>PBT</b>	8.5	29.1	37.6	0.065 <sup>230</sup>

## 5.2 Rheological rationalization of the nanofibrils PBT nanofibrils development

The time dependency of the storage modulus of PBT under the simulated die conditions (refer to chapter 4.3.3.1.1; a temperature of 210 °C and a frequency of 90 rad/s) are presented in **Figure 5-2**. It should be mentioned that the frequency of 90 rad/s is calculated based on the calculated shear rate on the wall and Rabinowitsch correction, which are presented in section 4.3.3.1.1. Since the die temperature is lower than the static melt temperature of PBT (225 °C), the isothermal melt crystallization of PBT at 210 °C leads to an increase in storage modulus over time. The significant increase observed in the elastic behavior of PBT within the required time for a frequency sweep test was convincing to study the viscoelastic behavior of components at different frequencies via the temperature sweep experiments <sup>81</sup>.

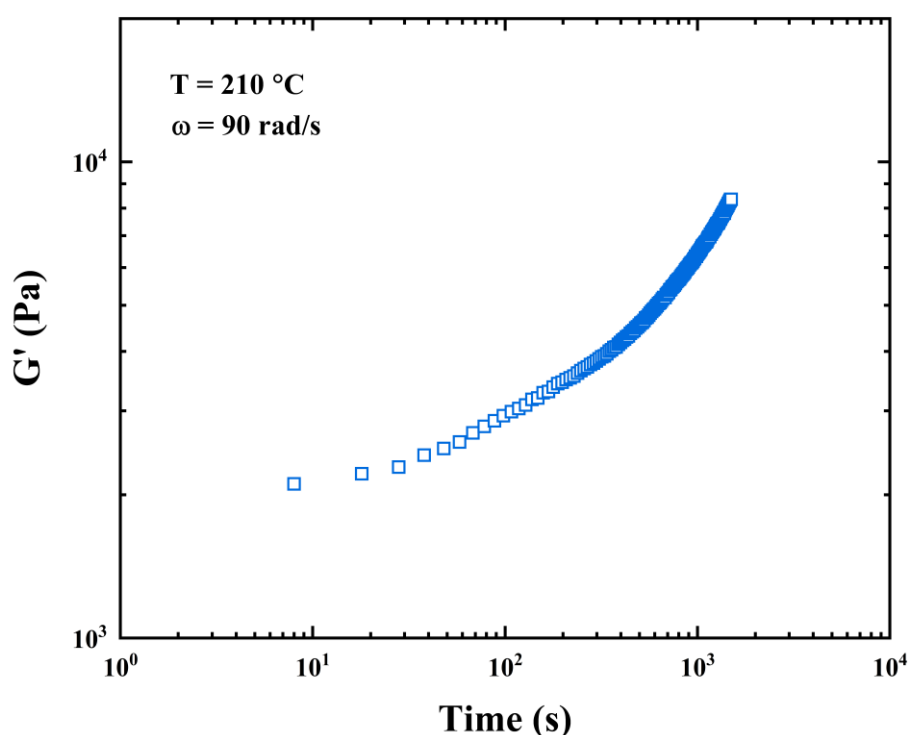


**Figure 5-2.** Time dependency of storage modulus for neat PBT at the die condition (refer to chapter 4.3.3.1.1) <sup>81</sup>.

The complex viscosity and storage modulus vs. temperature at three different frequencies are plotted in **Figure 5-3A, B** for the neat PLA and PBT. The viscoelastic behavior of PLA is manifested by a slight shear thinning (**Figure 5-3A**) and an increase in storage modulus (**Figure 5-3B**). On the other hand, the Newtonian-like behavior of PBT can be seen with a constant complex viscosity

at different frequencies. As seen, the complex viscosity of PBT increased with decreasing the temperature, while it remained independent of frequency. A significant viscosity upturn occurred at 186 °C, which is attributed to the onset of melt crystallization of PBT that had been measured to be 191.5 °C using DSC experiments. The storage modulus of the neat PBT increased through frequency increase at each temperature. Although the storage modulus of PBT is one order of magnitude less than that of PLA, it shows a stronger dependency on frequency and temperature. Accordingly, the constant viscosity of PBT and the shear-dependent viscosity of PLA led to a possibility of tuning the viscosity and elasticity ratio ( $\lambda$  and  $\lambda''$ , respectively) at the die. Other researchers have observed the Newtonian behavior of medium viscosity PBT, too <sup>81, 87, 245</sup>.

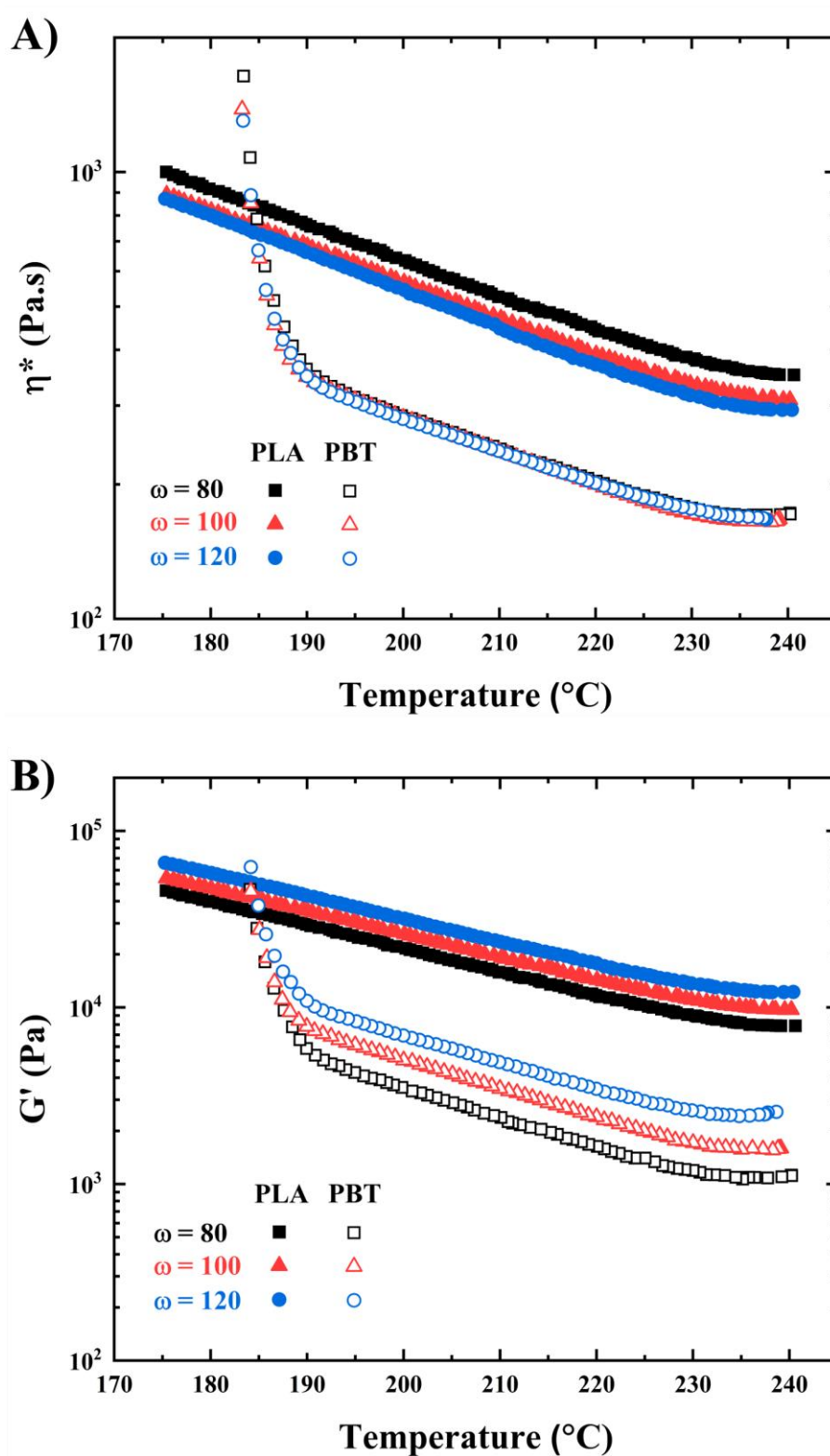


**Figure 5-3.** The viscoelastic behavior of PLA and PBT at different angular frequencies as a function of temperature (rate of  $-4^{\circ}\text{C}/\text{min}$ ); (A) complex viscosity, and (B) storage modulus <sup>81</sup>.

The rheological behavior of the neat PBT and PLA at the shear rate in the die, considering the validity of the Cox-Merz rule, is presented in **Figure 5-4A, B**. Based on these curves, the calculated values of the three mentioned rheological criteria are listed in **Table 5-3**. Regarding **Figure 5-4A**, an almost constant viscosity ratio of 0.5 over the temperature range of 230 to 195 °C could be calculated, which falls in the minimum range of the Grace curve. Thereupon, the critical capillary number was determined to be 1.8 using the Wu empirical equation. The ratio of the capillary number to the critical capillary number was calculated based on the matrix viscosity at the die and the extrapolated interfacial tension between the phases (see section 5.1.2). The high amount of  $\lambda'$ , which is beyond the Rayleigh capillary instabilities<sup>246</sup>, suggests a large deformation of droplets into the long fibrils. The storage and loss moduli of PLA and PBT are demonstrated in **Figure 5-4B**. The results for the elasticity ratio of the components show that  $\lambda'' \ll 1$ , which is calculated using the storage modulus ratio and Weissenberg number ratio of the components (**Table 5-3**). Therefore, the elasticity of the matrix was high enough to promote the deformation of the PBT droplets. The constant viscosity and the noticeable increase in the storage modulus of PBT through frequency increase resulted in longer relaxation time and higher stability of the developed deformation in the dispersed phase. Fang et al. have noticed a morphological evolution from droplets to uniform elongated fibrils as a result of the increased relaxation time (increased elasticity)<sup>81, 247</sup>.

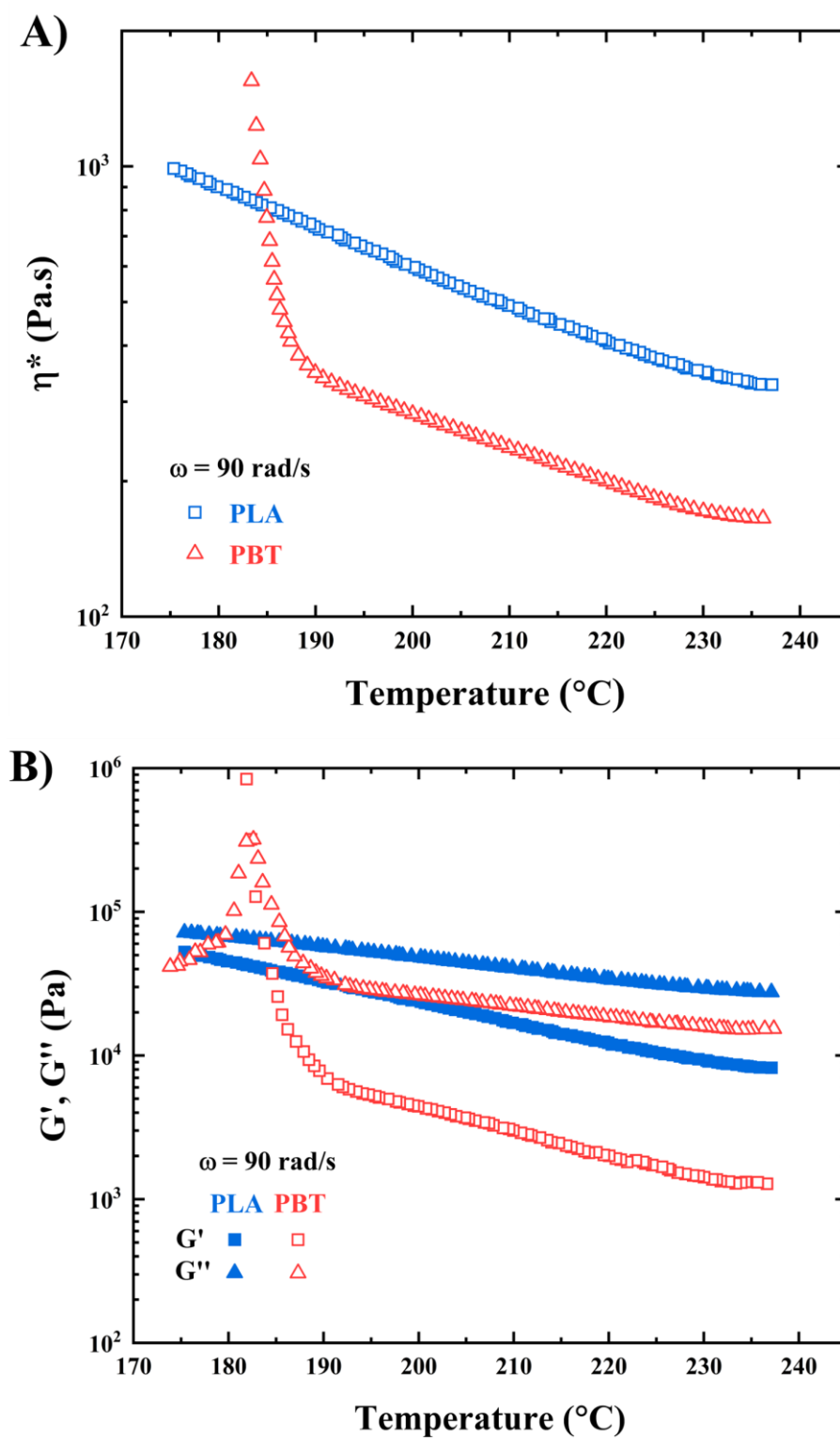


**Figure 5-4.** (A) Complex viscosities of PLA and PBT; (B) storage and loss moduli of PLA and PBT (temperature rate of  $-4$  °C/min)<sup>81</sup>.

**Table 5-3.** Viscosity ratio ( $\lambda$ ), the capillary number to the critical capillary number ratio ( $\lambda'$ ), and elasticity ratio ( $\lambda''$ ) of PLA/PBT blend at 210 °C <sup>81</sup>.

$\lambda$	$\lambda'$	$\lambda'' (G'_d/G'_m)$	$\lambda'' (Wi_d/Wi_m)$
0.5	12	0.17	0.3

### 5.3 Mathematical model of the spinning line

The mass balance, momentum and heat transfer equations (Equations ( 5-1 ) -( 5-12 )) were solved together in order to model the spinning process, derive the velocity profile ( $U_x$ ), calculate the strain rate ( $\dot{\epsilon}$ ) and thus, the droplet breakup time in the melt-spinning line out of the die. After the die swell zone that is a complex flow field of shear and elongation, the kinematics of continuous drawing induced by fiber collection is close to those of uniform uniaxial drawing (schematically shown in **Figure 5-5**)<sup>81, 248, 249</sup>.

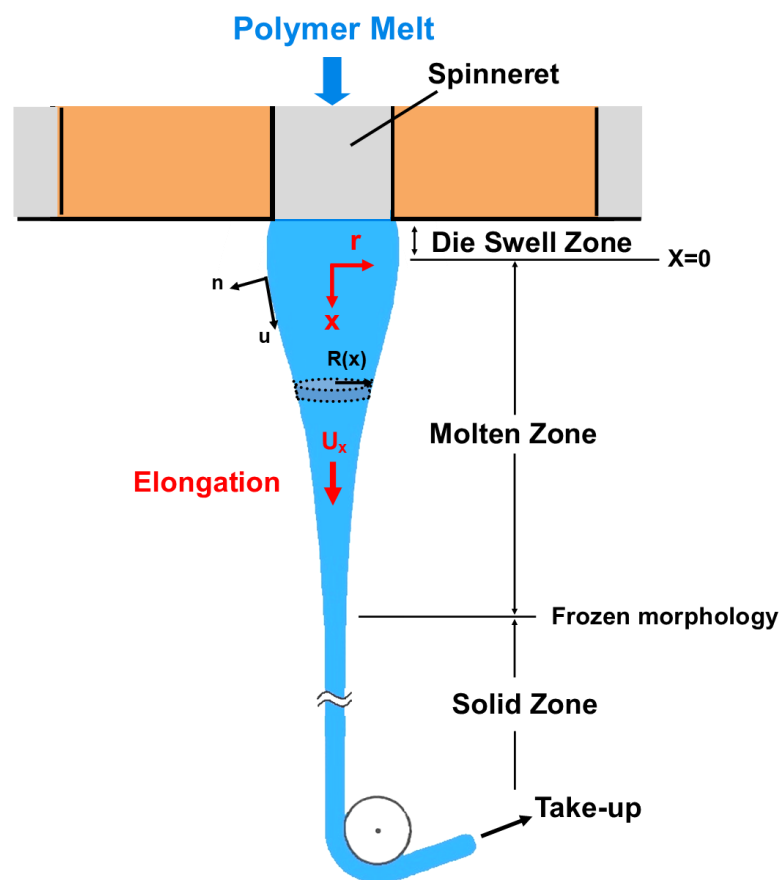


**Figure 5-5.** Schematic diagram of a melt-spinning process under tension<sup>81</sup>.

Since the die swell is quite small compared to the total spinning length between the die outlet and take-up point, it is not considered in the model. The origin was defined to be the point after the die swell when the diameter of the melt flow is  $R_0 = r_{die} = 0.5 \times 10^{-3}$  m. The energy balance over a cross-section of the filament can be written in differentiation form as **Equation ( 5-1 )** where  $T$  is the average temperature of an infinitely small element<sup>250</sup>. **Equation ( 5-2 )** is the integration form of **Equation ( 5-1 )** between the origin and freeze line. The boundary conditions are:



$$x = 0 \qquad T_i = \text{initial temperature} = 210 \text{ }^\circ\text{C}$$

$$x = l_f \qquad T_f = \text{freeze line temperature} = 180 \text{ }^\circ\text{C}$$

The freeze line is typically defined as the length where the filament temperature is reduced to  $T_g$  of polymer (in the case of PLA  $\cong 60 \text{ }^\circ\text{C}$ ). However, in this study, the melt flow includes two constituents with very different melting temperatures. The PBT domains with the onset of melt crystallization temperature of  $191.5 \text{ }^\circ\text{C}$  (using a cooling ramp of  $-5 \text{ }^\circ\text{C}/\text{min}$ ) under intensive elongational flow experience flow-induced crystallization out of the die. The solidification of the PBT fibrils affects the matrix's velocity profile and reduces the freeze line. The determination of the freeze line at the temperature of  $180 \text{ }^\circ\text{C}$  (instead of  $60 \text{ }^\circ\text{C}$ ) is a pessimistic assumption for obtaining breakup time or stability of the ellipsis in elongational flow. Indeed, this assumption reduces the length of the freeze line  $l_f$  where the velocity of the melt along that increases from  $U_0$  to  $U_s$  (spool speed). Thus, this assumption increases the calculated strain rate ( $\dot{\epsilon}$ ) at the exit of the die and, accordingly, reduces the calculated breakup time. This assumption was applied to show the stability of the PBT fibrils under the elongational flow. However, by using this assumption, the isothermal momentum equation of a power-law fluid (**Equation ( 5-9 )**) could be applicable with a good approximation <sup>251</sup>.

All the parameters for modeling the system, their definitions, and dimensions are summarized in **Table 5-4**. **Equation ( 5-3 )** is a linear estimation of fiber diameter as a function of  $x$ . **Equation ( 5-4 )** is a linear trend for the melt density of PLA, provided by NatureWorks for fiber manufacturing. This equation is applicable for modeling the current study with a temperature gradient between  $210 \text{ }^\circ\text{C}$  and  $180 \text{ }^\circ\text{C}$ . Based on the literature, the heat capacity ( $C_p$ ) of PLA at temperatures higher than its melt temperature is almost constant and has been chosen to be  $2060 \text{ J/kg K}$  in this study <sup>14, 252</sup>. The temperature dependence of matrix viscosity ( $\eta_m$ ) in the **Equation ( 5-5 )** has been substituted from experimental values presented in **Figure 5-4A**.

By substitution of **Equation ( 5-9 )** in the **Equation ( 5-2 )** and integration based on the boundary conditions mentioned above,  $l_f$  was obtained as  $40.2 \text{ cm}$ . **Table 5-5** presents the temperature gradient, strain rates ( $\dot{\epsilon}$ ), breakup times ( $t_b$ ) and residence times ( $t_{re}$ ) of the melt as a function of  $x$  along the first  $5 \text{ cm}$  of the filament. The stability of the ellipses under the elongational flow is evident by comparing the breakup time and residence time at different  $x$  values. As presented in **Table 5-5**, the melt flow temperature in the  $x$  range of  $0\text{-}5 \text{ cm}$  is almost constant ( $210 \text{ }^\circ\text{C}$ ). Thus, the matrix's viscosity for the calculation of breakup time (**Equation ( 2-8 )**) has been assumed to

be constant at 490 Pa.s. It should be mentioned that the initial fibril diameter ( $D_0$ ) at the different PBT compositions has been measured using the morphological observations in **Figure 2-8**<sup>81</sup>.

$$\rho C_p U_x \frac{dT}{dx} = -\frac{2h}{r_x} (T - T_a) \quad 250 \quad (5-1)$$

$$\int_{T_i}^{T_f} \rho C_p \frac{dT}{(T - T_a)} = -\int_0^{l_f} \frac{2h dx}{r_x U_x} \quad (5-2)$$

$$r_x = \frac{r_f - r_{\text{die}}}{l_f} x + r_{\text{die}} \quad (5-3)$$

$$\rho = -0.75T + 1459.25 \quad (5-4)$$

$$Re = \frac{\rho U_0 l_f}{\eta_m \ln Dr} \exp\left(\frac{x}{l_f} \ln Dr\right) \quad 250 \quad (5-5)$$

$$Dr = U_s / U_0 \quad (5-6)$$

$$U_0 = \frac{Q_V}{\pi r_{\text{die}}^2} \quad (5-7)$$

$$h_c = 0.21 \frac{k_{\text{air}}}{r_x} Re^{1/3} \quad 250 \quad (5-8)$$

$$U_x = U_0 \left(1 + (Dr^q - 1) \frac{x}{L}\right)^{1/q} \quad 250 \quad (5-9)$$

$$q = 1 - 1/n \quad (5-10)$$

$$\dot{\epsilon}_x = \frac{1}{l} \frac{dl}{dt} = \frac{dU_x}{dx} \quad 250 \quad (5-11)$$

$$t_{re} = \int_x^{x+dx} \frac{dx}{U_x} \quad (5-12)$$

**Table 5-4.** Parameter description of the **Equations ( 5-1 ) ( 5-12 )** <sup>81</sup>.

Parameter	Definition	Unit
$Q_V$	Volumetric flow rate passing through each hole ( $8 \times 10^{-9} \text{ m}^3/\text{s}$ )	$\text{m}^3/\text{s}$
$U_0$	Melt velocity at the die (0.0102 m/s)	m/s
$U_s$	Stretching velocity (spool velocity) (31.67 m/s)	m/s
$R_{die}$	Die diameter	
$r_{die}$	Die radius	m
$r_x$	Radius of the fiber as a function of x	m
$U_x$	Velocity of the fiber as a function of x and Dr	m/s
$n_p$	Power-law exponent ( $\eta = k\dot{\gamma}_{app}^{n-1}$ )	
$T_a$	Ambient temperature (298 K)	K
$T_i$	The initial temperature of the melt (483 K)	K
$T_f$	Freeze temperature	K
$T$	Fiber temperature as a function of x	K
$l$	Spinning length	m
$l_f$	Freeze line	m
$\rho$	Melt density of PLA	$\text{kg}/\text{m}^3$
$C_p$	Heat capacity of PLA	J/kg.K
$h$	Heat convection coefficient	$\text{W}/\text{m}^2.\text{K}$
$k_{air}$	Thermal conductivity of air at 298 K (0.02 W/m.K)	$\text{W}/\text{m.K}$
$\eta_m$	Matrix viscosity	Pa.s
$Dr$	draw ratio, defined as the ratio of the stretching velocity ( $U_s$ ) to the die velocity ( $U_0$ )	
$Re$	Dimensionless Reynolds number	
$\dot{\epsilon}$	Strain rate	1/s
$t_{re}$	Residence time	s

**Table 5-5.** The temperature profile, the distribution of strain rate, residence time, and breakup time at the different PBT compositions along the first 5 cm of the spinning line <sup>81</sup>.

<b>t<sub>b</sub> (s) vs. PBT component inclusion</b>							
<b>x (mm)</b>	<b>T (°C)</b>	<b><math>\dot{\epsilon}</math></b>	<b>t<sub>re</sub> (s)</b>	<b>1 wt%</b>	<b>3 wt%</b>	<b>5 wt%</b>	<b>10 wt%</b>
0	210	5.3083	...	1.577	1.916	2.052	2.157
2	209.92	5.3896	0.1953	1.559	1.893	2.027	2.130
4	209.85	5.4725	0.1932	1.541	1.870	2.002	2.103
6	209.77	5.5571	0.1912	1.523	1.847	1.977	2.077
8	209.7	5.6435	0.1891	1.505	1.824	1.952	2.051
10	209.62	5.7315	0.1871	1.488	1.801	1.928	2.024
12	209.54	5.8214	0.1851	1.470	1.779	1.903	1.998
14	209.46	5.9131	0.1831	1.453	1.757	1.879	1.973
16	209.38	6.0067	0.1811	1.435	1.734	1.855	1.947
18	209.30	6.1022	0.1791	1.418	1.712	1.831	1.922
20	209.22	6.1997	0.1771	1.400	1.690	1.807	1.897
22	209.14	6.2992	0.1752	1.384	1.669	1.784	1.872
24	209.06	6.4008	0.1732	1.367	1.648	1.760	1.847
26	208.98	6.5046	0.1713	1.350	1.626	1.737	1.822
28	208.9	6.6106	0.1694	1.333	1.605	1.715	1.798
30	208.81	6.7188	0.1674	1.316	1.584	1.692	1.774
32	208.73	6.8293	0.1655	1.300	1.563	1.669	1.750
34	208.64	6.9422	0.1637	1.284	1.542	1.647	1.727
36	208.56	7.0576	0.1618	1.267	1.522	1.624	1.703
38	208.47	7.1754	0.1599	1.251	1.502	1.602	1.680
40	208.39	7.2958	0.1581	1.235	1.481	1.580	1.657
42	208.3	7.4189	0.1562	1.219	1.461	1.559	1.633
44	208.21	7.5447	0.1544	1.203	1.441	1.537	1.611
46	208.12	7.6732	0.1526	1.187	1.421	1.516	1.588
48	208.03	7.8047	0.1508	1.172	1.402	1.495	1.566
50	207.94	7.9390	0.1490	1.156	1.383	1.474	1.544

## 5.4 Morphology development in the blends, fibers, and NFCs

The phase morphology of the extruded blends directly affects the formation and diameter of nanofibrils. Therefore, the SEM analyses were performed on the non-stretched extrudates either across the die or along the die. Then the morphology development in PLA/PBT fibers was followed to evaluate the material selection and processing conditions. Finally, the morphology of NFCs was pursued to find out the heat stability of the PBT fibrils and the formation of the fibrillar network in the composites.

### 5.4.1 Morphological observations of non-stretched PLA/PBT strands

#### 5.4.1.1 Morphological observations of strands across the die

**Figure 5-6(A-D)** illustrates the cryo-fractured cross-section of non-stretched filaments of PLA/PBT blends with different PBT compositions. As is revealed in **Figure 5-6A**, the phase separation of PLA and PBT has been accomplished at the lowest PBT composition (1 wt%). PBT droplets in all the compositions are distributed within the PLA matrix homogeneously. The droplets' diameter was measured in several zones, and log-normal curves fitted the droplet size distribution. Accordingly, standard deviation ( $\sigma_{SD}$ ) and average diameter of the PBT droplets in different compositions are presented next to each micrograph. PBT domains average diameter is submicron in all the compositions, and submicron phase separation has been frequently reported as proof for high compatibility and efficient mixing<sup>25, 253, 254</sup>. In the case of high interfacial tension between the phases, incompatibility, or non-efficient mixing, the dispersed phase diameter is expected to be several microns, which would be challenging to develop fine micro/nanofibrils during the hot-stretching step<sup>33, 41, 42</sup>. On the contrary, the non-uniform size distribution of PBT domains at 5 and 10 wt% of PBT loading (the increased value of  $\sigma_{SD}$ ), and evident voids between the dispersed domains and matrix raises doubts about the compatibility of the mixing components and efficiency. However, looking at the literature, similar non-uniform size distribution can be revealed for well-mixed compatibilized blends<sup>25, 226, 253, 255</sup>.

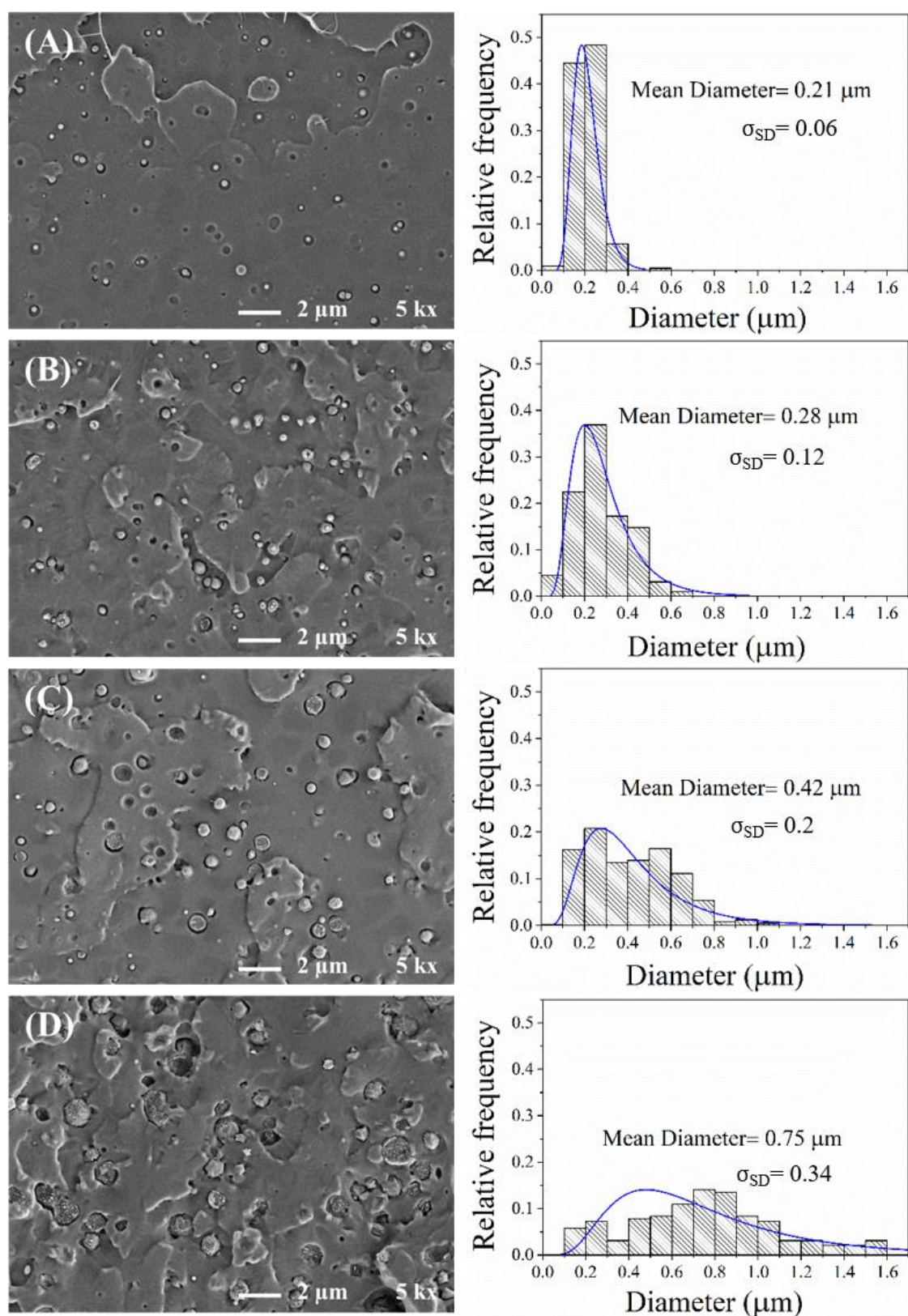


**Figure 5-6.** SEM micrographs of the cross-section of cryo-fractured non-stretched PLA/PBT blends with different amounts of PBT (A) 1 wt%, (B) 3 wt%, (C) 5 wt%, and (D) 10 wt%. Histograms of diameter distribution of PBT domains with a log-normal fitted curve placed next to each micrograph <sup>226</sup>.

A high-resolution insight into the morphology of PLA/PBT blends is presented in **Figure 5-7** using SEM and TEM micrographs to provide information about the interface of the two phases and the rough morphology on the PBT domains in **Figure 5-6C** and **D**. **Figure 5-7A** and **C** demonstrate the SEM micrographs of the blends containing 5 and 10 wt% of PBT, respectively; showing two regions of interfaces: i) interfacial bonding between the two phases, and ii) the voids between the PBT droplets and PLA with some bridging fibrils that connect the phases. The bridging fibrils debate interfacial interactions between the phases and have been stated as a pancake interfacial structure in compatibilized PBT/PET blends in literature <sup>255</sup>. Accordingly, morphological observations of the blends in **Figure 5-6** and **Figure 5-7** suggest partial compatibility between PLA and PBT. This compatibility level between the phases provided prerequisite morphology in the blends to be transformed into nanofibrils, later in the hot-stretching step. Di Lorenzo et al. expressed some degree of compatibility explained by functional group interactions <sup>38</sup>. Samthong et al. stated that PBT particles bonded to the PLA matrix after cryo-fracturing implied a good adhesion between the two phases at the interface <sup>143,226</sup>.

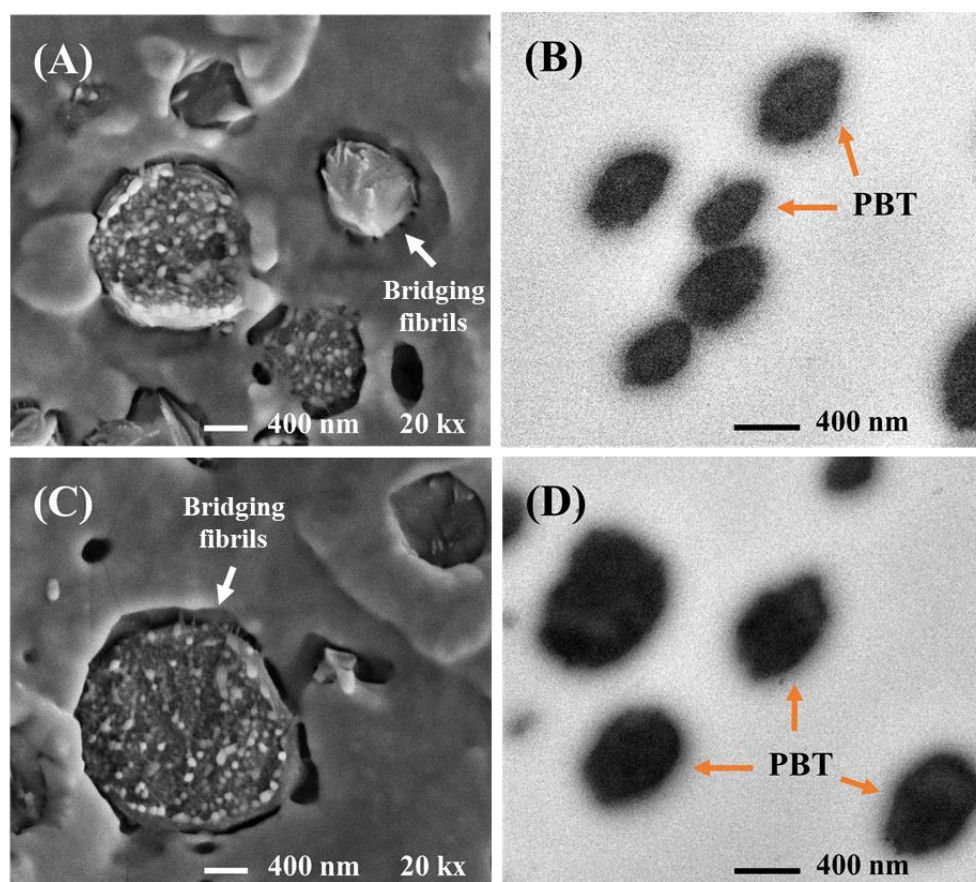


**Figure 5-7.** (A) and (B) SEM and TEM micrographs of PLA/PBT blend containing 5 wt% PBT; (C) and (D) SEM and TEM micrographs of PLA/PBT blend containing 10 wt% PBT <sup>226</sup>.

To describe the evident rough surface of PBT domains in **Figure 5-7A** and **C** and to identify possible multi-level structures, i.e., PBT domains containing dispersed PLA drops<sup>38</sup>, transmission electron microscopy images were obtained after staining aromatic rings of PBT. The dark areas in **Figure 5-7B** and **C** are related to the PBT domains at 5, and 10 wt% content, respectively, with no trace of PLA droplets. Therefore, the rough surface of the dispersed phases is attributed to the cohesive fracture of PBT domains, which have been formed due to crazing during rupture. Cohesive fracture of the PBT domains is more probable at its higher concentrations due to the merging of the droplets at the die, resulting in longer domains. The droplets' coalescence due to high shear rates at the die has been extensively discussed<sup>65,226</sup>.

#### 5.4.1.2 Morphological observations on the skin of strands along the die

**Figure 5-8A-E** demonstrate representative SEM micrographs of the surface of non-stretched PLA/PBT filaments at different PBT contents after selective etching of PLA. The ellipsoidal nanometric phase-separated PBT domains at the lowest concentration of PBT component (1 wt%), shown in **Figure 5-8B**, indicate the accurate processing conditions and rheological parameters for inducing the fibrillar morphology. The pronounced deformation of submicron droplets at higher PBT contents shown in **Figure 5-8C** and **D** is in accordance with the principles of Taylor's equation<sup>80</sup>. However, the elongated PBT domains observed in the case of 10 wt% PBT content can be recognized as the deformation of droplets under shear, which is followed by coalescence. Although the short length of the spinneret cannot cause the fibrillation of droplets, the fulfilled rheological criteria required for fibrillation under a simple shear flow has conveyed the stable elongated dispersed phase to the subsequent flow field.

The breakup time of the elongated PBT under shear flow inside the die ( $T = 210\text{ }^{\circ}\text{C}$ ,  $\eta = 490\text{ Pa}\cdot\text{s}$ ) can be calculated using **Equation ( 2-6 )**. Based on information obtained from literature, a value of  $\Omega$  for our blends with  $\lambda = 0.5$  was estimated to be 0.1<sup>99</sup>. Accordingly, the breakup time of the ellipses in the blends containing 10 wt% PBT ( $D_0 \cong 500\text{ nm}$ ), 5 wt% PBT ( $D_0 \cong 400\text{ nm}$ ), 3 wt% PBT ( $D_0 \cong 300\text{ nm}$ ) and 1 wt% PBT ( $D_0 \cong 150\text{ nm}$ ) were calculated as 3.3, 2.8, 2.2, and 1.2, respectively. It is worth mentioning that, in reality, the droplet breakup could hardly occur in slightly deformed ellipses for the blends containing 1 wt% PBT (**Figure 5-8B**). By comparing the volumetric flow rate ( $8 \times 10^{-3}\text{ cm}^3/\text{s}$ ) passing through each hole and the volume of each hole ( $6.3 \times 10^{-3}\text{ cm}^3$ ), it is demonstrated that the residence time of a control volume is less than 1 second. Therefore, the ellipsoidal domains would pass through the die without breakup. Since the deformation of the droplets in the spinneret increases the interface of the two phases,



regarding the adequate interfacial interactions, the matrix can efficiently stretch the ellipses in the next flow field. Be noted that the calculations above were made for the shear rate on the wall (frequency of 90 rad/s calculated in section 4.3.3.1.1) and shear rate distribution across the 1 mm die diameter was not considered<sup>81</sup>.

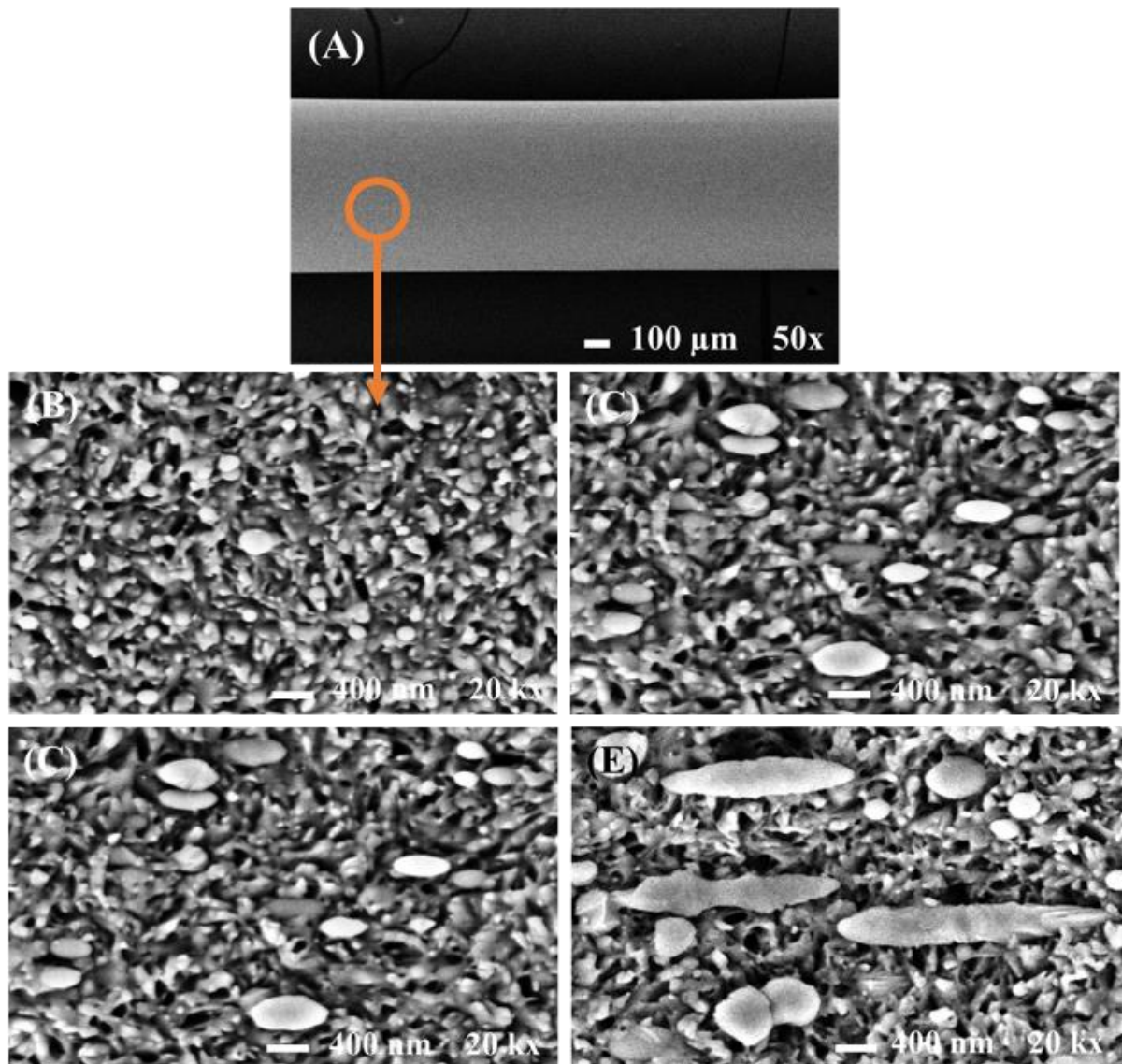


**Figure 5-8.** SEM micrographs of the surface of PLA/PBT non-stretched filaments after selective etching of PLA; (A) and (B) 1 wt% ; (C) 3 wt% ; (D) 5 wt% ; and (E) 10 wt% PBT content<sup>81</sup>.

The stability of the ellipses in elongational flow could also be studied by comparing the breakup time of the ellipses and their residence time under this flow field. Since the polymer melt temperature and velocity change along the spinning line, the strain rate under the elongational

flow will be a function of the flow direction,  $x$  (see **Figure 5-5**). Accordingly, the distribution of strain rate ( $\dot{\epsilon}_x$ ), breakup time ( $t_b$ ) (calculated based on **Equation (2-8)**), and residence time ( $t_{re}$ ) were obtained for the elongational flow. The strain rates, breakup times, and residence times calculated for small control volumes in the first 5 cm of the spinning line are presented in **Table 5-5**. As can be seen, the stability of the fibrils is confirmed by comparing the relevant  $t_{re}$  and  $t_b$ . For instance, at  $x=2$  mm, with strain rate of  $5.4 \text{ s}^{-1}$  and residence time of 0.2 seconds, the breakup time of fibrils with  $D_0 \cong 500, 400, 300$  and  $150 \text{ nm}$  were found to be 2.13, 2.02, 1.89 and 1.56 s, respectively<sup>81</sup>.

#### 5.4.2 Morphological observation on the surface of PLA/PBT fibers and in the NFCs

**Figure 5-9A** demonstrates the surface of PLA/PBT fibers containing different contents of PBT after etching a thin layer of PLA. The arrows in **Figure 5-9A** and **B** define the directions along ( $x$ ) and across ( $r$ ) the fibers. The well-etched parts of the fibers (signed by the orange circle) were observed at high magnification. The orientation of the PBT NFs in the fibers **Figure 5-9(B-E)** is illustrated. The diameter distribution of PBT NFs at different PBT compositions is presented after measuring the diameter of more than 60 of them in several etched fibers. A log-normal curve fitted the distribution of PBT NFs diameter. Accordingly, the mean fibril diameter and  $\sigma_{SD}$  are presented next to each micrograph. The nanofibrils' mean diameters for 1, 3, 5, and 10 wt% of PBT content are 23, 30.4, 41.3, and 51.4 nm, respectively. Be noted that one constant draw ratio (156) was used in this work for all the spinning processes, as explained in experimental section 4.2<sup>226</sup>.

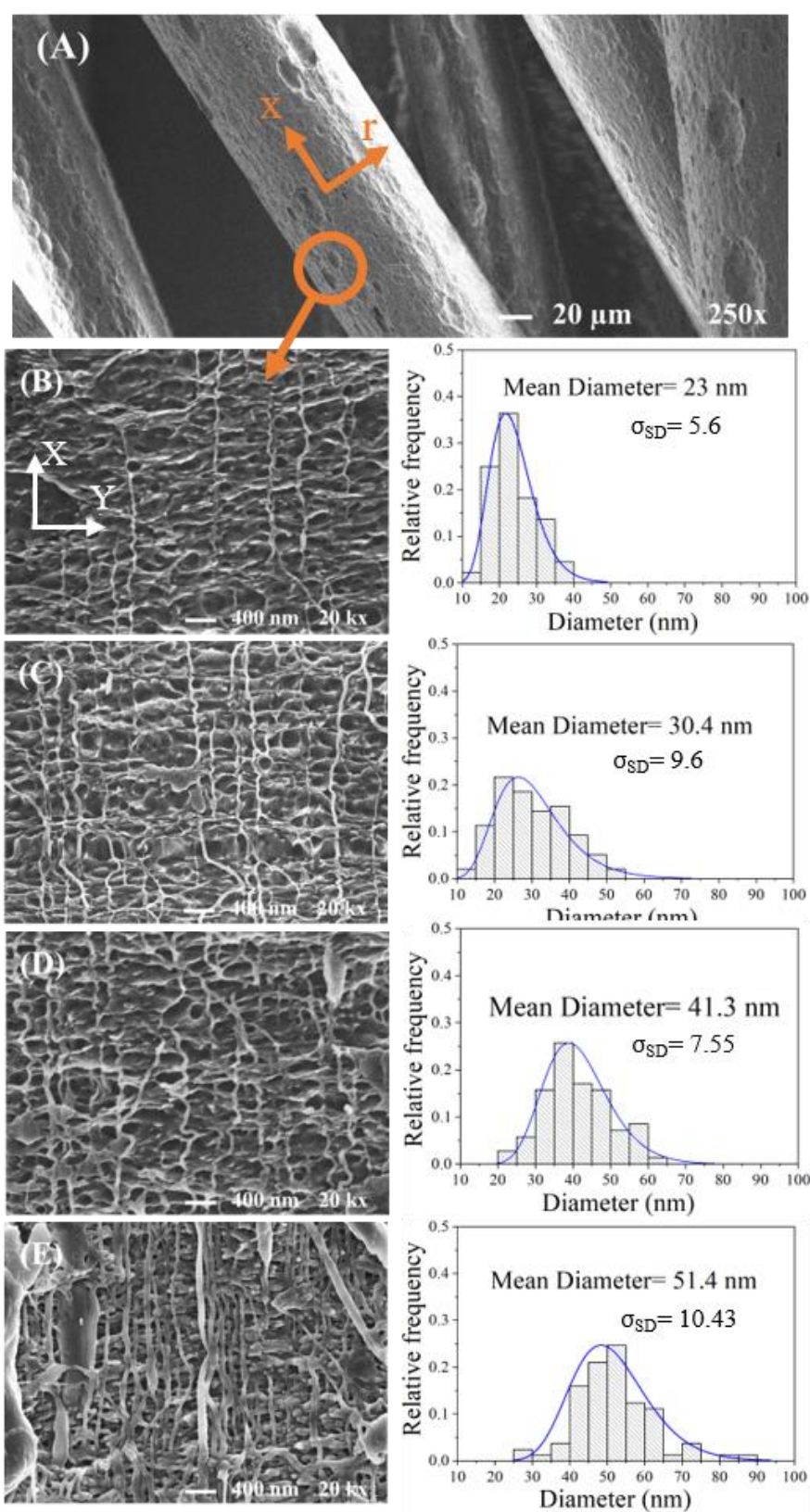


**Figure 5-9.** SEM micrographs of etched PLA/PBT fibers with different PBT contents; (A) and (B) 1 wt% at different magnifications; (C) 3 wt%; (D) 5 wt% and (E) 10 wt% of PBT nanofibrils. Histograms of diameter distribution of PBT nanofibrils with a log-normal fitted curve placed next to each micrograph <sup>226</sup>.

To estimate the aspect ratio ( $L/D$ ) of PBT NFs, tens of PLA/PBT 2 wt% fibers with a length of 10 cm were oriented parallel and compression-molded to form a thin film. The SEM images in **Figure 5-10** were taken from the thin film after the PLA was etched away by the solvent. Low magnification is selected to make possible scaling of the nanofibrils' length. It is noteworthy that the thicker fibrils in **Figure 5-10A** are bundles of nanofibrils, which are not well dispersed in this specific sample. Concerning **Figure 5-10A** and B, the minimum  $L/D$  of PBT NFs is 500, which is very similar to that of MWCNTs<sup>168</sup>. A similar observation of  $L/D$  was observed for the other PLA/PBT blends of this research containing different PBT concentrations.

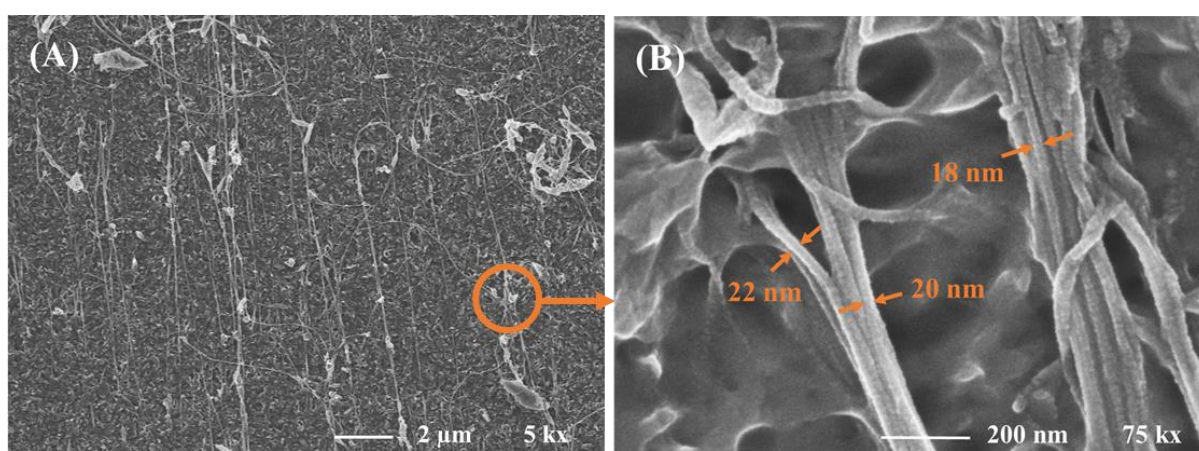


**Figure 5-10.** SEM micrographs of parallel PBT nanofibrils at different magnifications (A) after compression molding of long parallel PLA/PBT 2 wt% fibers and selective etching of PLA, (B) PBT NFs diameter and their bundle at a higher magnification<sup>226</sup>.

**Figure 5-11A-D** illustrate the PBT nanofibrillar network in the NFCs after etching a thin layer of matrix. The first impression of morphological observations in the NFCs is the strong consistency of PBT NFS during matrix consolidation. The formed nanofibrils in NFC1 drew attention to the literature on suggested mechanisms. Hajiraissi has reported that the melt-spinning process of PP/poly (trimethylene terephthalate) (PTT) blends at low contents of PTT (<6 wt%) was incapable of fibrillating the dispersed phase<sup>66</sup>. A similar observation has been presented for the non-stretched dispersed polystyrene (PS) phase in PP melt-spun fibers, in which at least 8 wt% PS content was necessary to promote the fibrillation mechanism<sup>62</sup>. In the aforementioned studies, the authors have described their observations at low contents of the dispersed phase, based on the low capillary number in the elongational flow (due to small droplets size); and the non-realized end-to-end mechanism. The end-to-end mechanism was first proposed by Fakirov et al. to describe the contribution of droplet coalescence in fibril formation<sup>65</sup>. However, recently,

Soltani et al. have conjectured that the nanofibril diameter is more controlled by pinch-off (quick stretching) than being affected by the droplet size <sup>71</sup>. In the present study, considering the die temperature, which was lower than the melt temperature of PBT and hindered coalescence, it is also believed that the way the dispersed phase undergoes the elongational field is prior to coalescence. The rheological explanation of such a fine nanofibrillar morphology is suggested as a combination of (i) the notable deformation of PBT domains within the short die via adjusting  $\lambda$ ,  $\lambda'$  and  $\lambda''$ ; (ii) the increase in the elastic components of ellipsoidal PBT domains in the die, which inhibits fast relaxation of the induced deformation; and (iii) quick stretching of the deformed droplets with an enhanced proper interface through the elongational flow. These factors, along with less coalescence of PBT droplets in the die, and cold drawing during collection, resulted in a unique structure using a simple melt-spinning process. It is noteworthy that the production of NFCs with average diameters below 100 nm has been known as a challenging task <sup>70</sup>. However, a huge number of nanofibrils in the presence of 3 wt% of PBT led to bundling during compression molding in the absence of mixing elements. In some regions, local bundling of more than three nanofibrils caused local microfibrils with a larger diameter than 100 nm <sup>81</sup>.

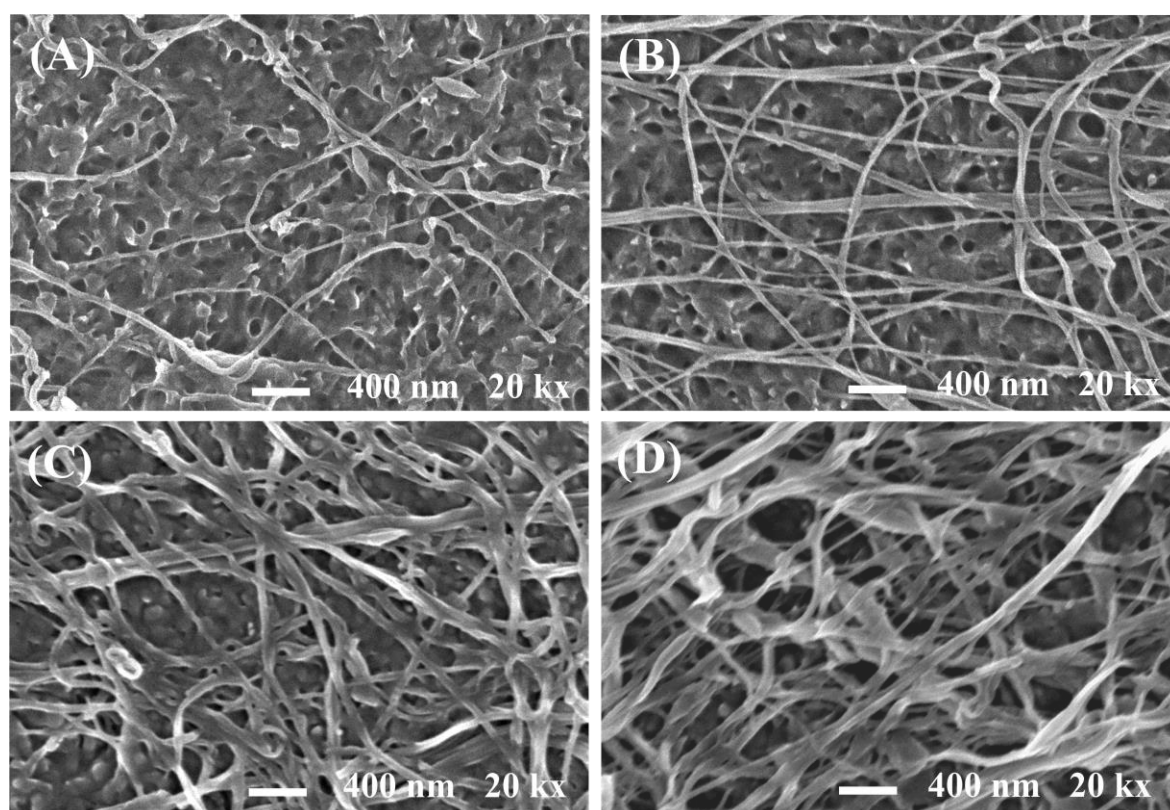


**Figure 5-11.** SEM micrographs of PBT NF networks in (A) NFC1, (B) NFC3, (C) NFC5, and (D) NFC10 after selective etching of a thin layer of PLA <sup>81</sup>.

It can be assumed that the oriented domains of PBT at the die are cold drawn during the hot stretching, which is due to the lower temperature of the die in comparison to the melt temperature of PBT (226 °C). Indeed, the low die temperature leads to the strengthening of the PBT domains to withstand the stretching without breaking up. On the other hand, the increased viscosity of PBT prohibits the merging of several droplets in the flow during the hot stretching. The merging of the droplets at the die and during the hot stretching has been reported concerning the higher volume of nanofibrils compared to the droplets <sup>65</sup>. **Figure 5-12** schematically shows the formation of PBT nanofibrils, which is influenced by controlling the die temperature to get: first, less PBT droplets merging, second preventing fibril breakup, and third, to achieve cold draw in the glassy state of the PBT fibrils. Setting the die temperature to lower than the PBT melt temperature and higher than its melt crystallization onset synchronized these three parameters. To the best of the author's knowledge, there is not any report on gaining PBT nanofibrillar morphology even by using a separated cold draw step or introducing compatibilizers and nanoparticles <sup>67, 68, 143, 163</sup>.

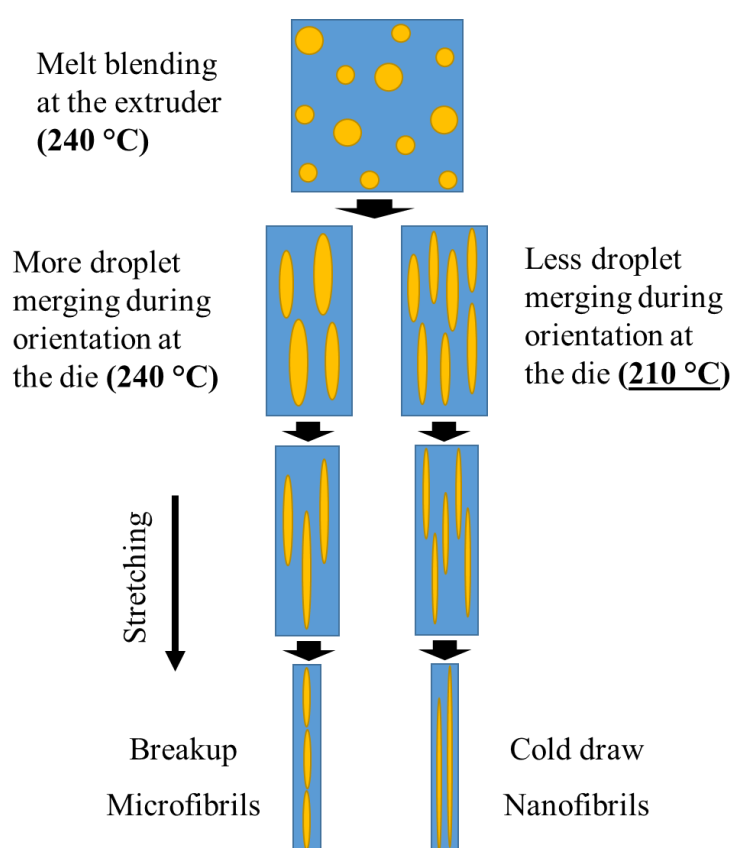


**Figure 5-12.** Effect of die temperature on the rheological behavior of the flow and final fibrillar structure <sup>226</sup>.

### 5.4.3 Morphological observation of PLA/PBT/nanoclay nanocomposites

**Figure 5-13A1** and **A2** represent the TEM images of NFC2 samples showing the PBT fibrils, either along their length or cross-section. **Figure 5-13B1** and **B2** demonstrate the morphology of PLA/PBT2/C20A1.5 nanocomposite. By comparing the morphology of these two series, it can be revealed that the black domains in **Figure 5-13B1** and **B2** are the spherical or slightly deformed PBT component, which was not fibrillated via hot-stretching in the spinning line. The smaller gray particles are the intercalated or exfoliated Closite20A nano platelets; those are more evident in **Figure 5-13B3, B4**.

As can be seen, although the clay nanoparticles are well-dispersed within the matrix according to the objective of their inclusion, the drawability of the PBT component is dramatically reduced. In other words, the localization of Closite20A in the PLA matrix has been achieved using predefined feeding sequences, but the improved elasticity of the matrix did not lead to fibrillation of the PBT droplets. This can be described considering the important contribution of surface tension between the components in the pinch-off mechanism. The dispersion of Closite20A reduced the polarity of the matrix because the polarity of Closite20A is less than that of PLA<sup>256</sup>. The reduced hydrophilicity of PLA resulted in more considerable interfacial tension with PBT droplets and suppressed the deformability of PBT domains. The effect of increased interfacial tension on the morphology development can be discussed regarding the dependency of breakup time on  $v_{12}$  in both shear and elongational flow. However, what raises doubt about this mechanism's acceptance is the many articles that do not consider the interaction between PLA and Closite20A appropriate and have not reported a suitable dispersion for this nanoparticle in PLA. From the point of view of such articles, a significant reduction in the polarity of the PLA/C20A compound is not a correct assumption. Such a view holds that the non-fibrillated PBT domains are due to the partial placement of nanoparticles in the interface of PLA and PBT, which inhibits the deformation of droplets. Although this approach seems logical, it cannot explain the strain hardening behavior of PLA/PBT/nanoclay nanocomposites (reported below). However, providing a more precise mechanism requires further and more profound studies in this area.

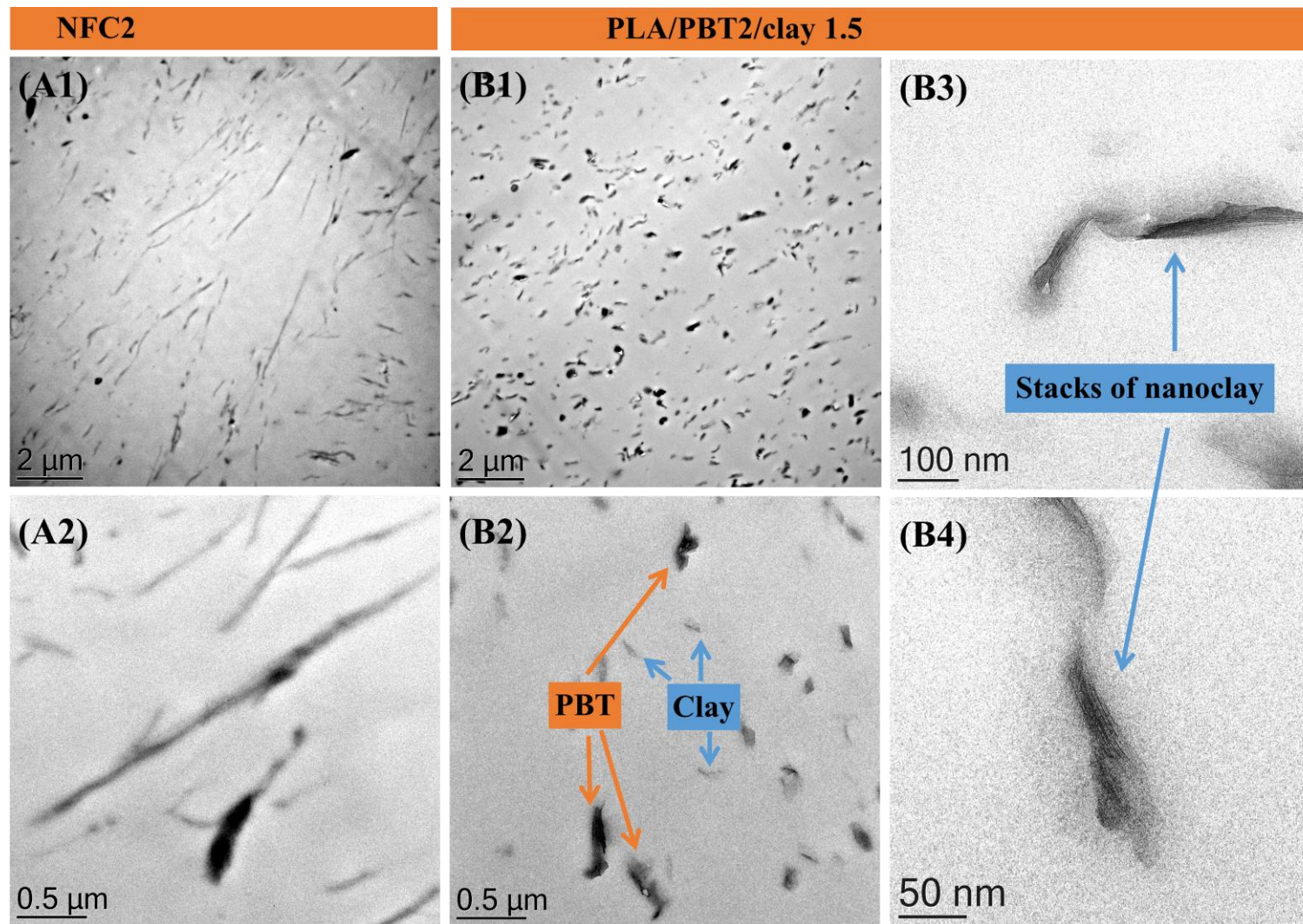


**Figure 5-13.** (A1) and (A2) TEM images of NFC2; and (B1)-(B4) PLA/PBT2/C20A1.5 nanocomposite.



## 5.5 PLA crystallization in the presence of PBT nanofibrils

### 5.5.1 Non-isothermal crystallization

PLA crystal morphology in the prepared fibers in the presence and absence of PBT NFs was presented using polarized optical microscopy in the range of 50 to 180 °C at a heating rate of 5 °C/min (**Figure 5-14** and **Figure 5-15**). The non-isothermal crystallization was developed to clarify the effect of molecular alignment of PLA and PBT in the process flow direction on PLA crystallization. **Figure 5-14** shows the crystal morphology in two PLA fibers with 80 μm diameter during the cold crystallization and melting afterward. It was observed that no crystalline phase is visible at 60 °C, and the cold crystallization has started at 100 °C and intensified by increasing the temperature up to 140 °C. The crystalline phase that appeared as scattered spherulites did not show any impression of molecular alignment. Then, the spherulites' population was diluted by increasing the temperature up to 150 °C that was visualized by the illumination of smaller spherulites and by contrast reduction, which is shown in **Figure 5-14G**. Finally, all the crystals were disappeared at 158 °C.

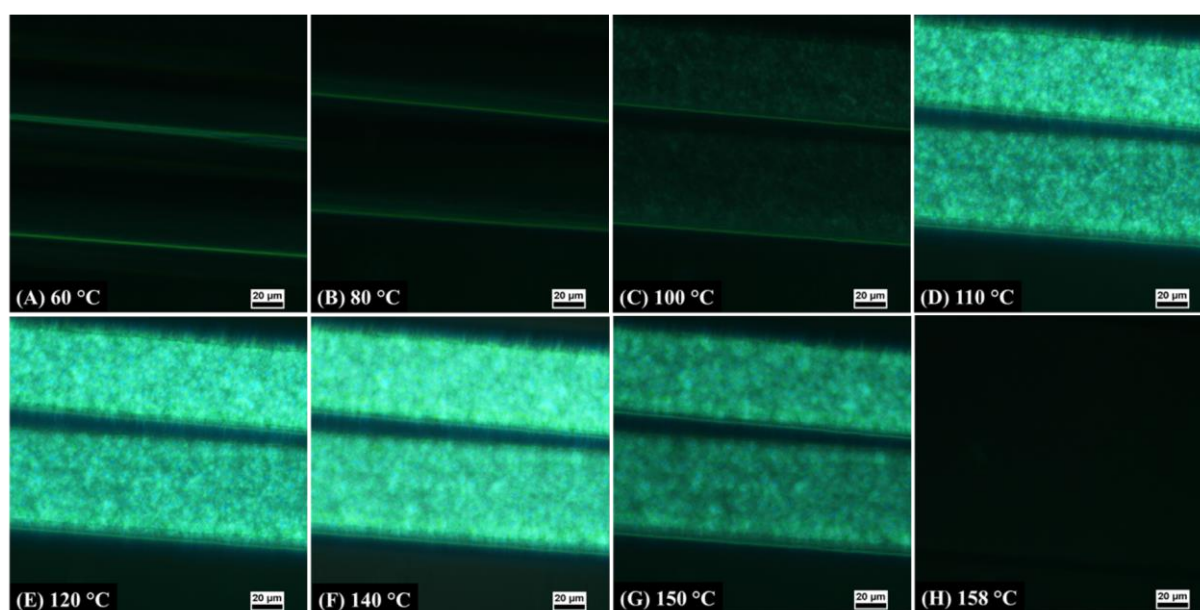


**Figure 5-14.** Hot stage polarized optical microscope pictures of neat PLA fibers during cold crystallization and melting recorded at (A) 60 °C, (B) 80 °C, (C) 100 °C, (D) 110 °C, (E) 120 °C, (F) 140 °C, (G) 150 °C and (H) 158 °C <sup>226</sup>.

**Figure 5-15** (a-e) displays the cold crystallization of PLA/PBT 2 wt% fibers, which were visualized at 60 °C. Obviously, PBT NFs acted as nucleating sites and decreased the cold

crystallization temperature of PLA. Therefore, fine crystallites are oriented along the fibers, and no spherulites are distinguishable with the light microscope when used at its highest magnification. During the hot stretching, the proper affinity of the two phases and solidification of the PBT NFs applied shear forces on the PLA chains adjacent to the NFs. The evidence of the PLA local conformational order in PLA/PBT 2 wt% fiber is 4.5 % of crystallinity. The oriented PLA chains acted as nuclei as soon as the temperature increased and molecules gained mobility. The nucleation mechanism is affected by ordered PLA chains; therefore, no spherulites were observed. Other researchers have reported the local orientation of PLA chains for the PLA/PBT droplet-matrix and MFCs, where the reduction of crystallization energy barrier and finer spherulites were observed<sup>143, 177</sup>. The contrast of the images was intensified up to 120 °C (**Figure 5-15e**), and the dilution of the crystalline phase started at 140 °C due to the smaller crystal size, which was melted at lower temperatures.

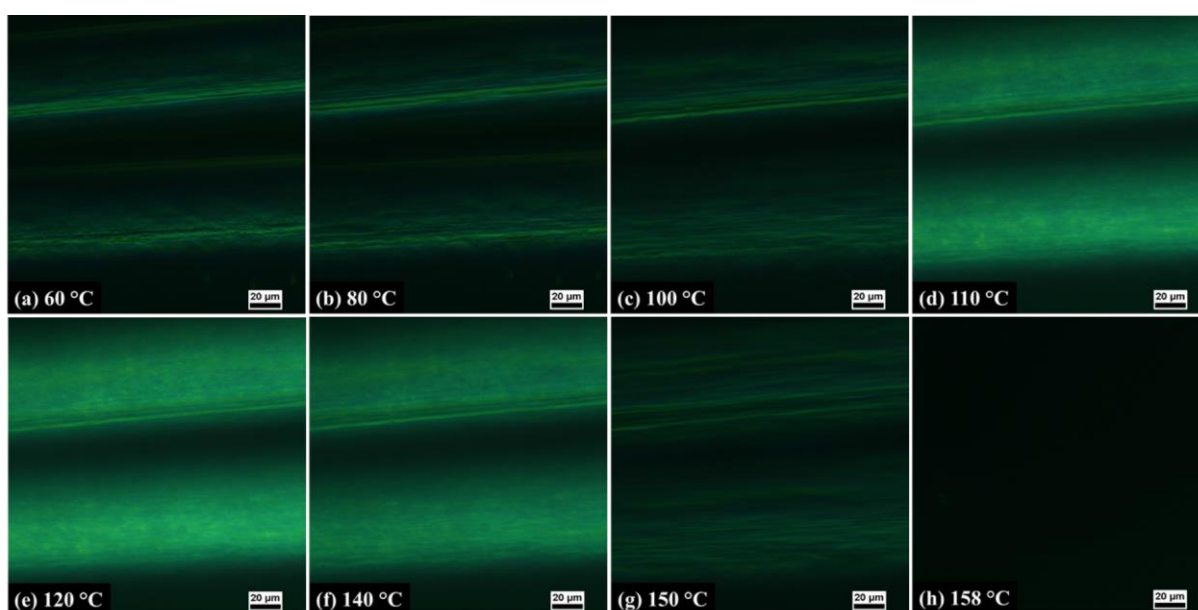


**Figure 5-15.** Hot stage polarized optical microscope pictures of neat PLA fibers during cold crystallization and melting recorded at (A) 60 °C, (B) 80 °C, (C) 100 °C, (D) 110 °C, (E) 120 °C, (F) 140 °C, (G) 150 °C and (H) 158 °C<sup>226</sup>.

Heating and cooling thermographs of processed PLA and NFCs are presented in **Figure 5-16(A-C)**. In the first heating (**Figure 5-16A**), residual stresses of the chains because of fast cold-press released by heating up to  $T_g$ ; therefore,  $T_g$  is followed by a jump. Before the jump, a two-step  $T_g$ , which is observed for NFC samples, discriminates mobility of the PLA chains adjacent to the stiff PBT NFs from the mobility of those in bulk. A huge amount of well-dispersed PBT NFs in NFC10

uniformed the chain mobility and the first step of  $T_g$  is disappeared. Two-step  $T_g$  has been reported as an indication for different chain mobility of the mobile amorphous fraction and the rigid amorphous fraction of PLLA<sup>257</sup>. The total crystallinity calculated from the first heating run of processed PLA and NFCs has not exceeded more than 1.5 %, indicating that almost all the crystals were nucleated in the cold crystallization region and the samples prepared by compression molding are almost amorphous because of the fast quenching afterward. For processed PLA, the typical cold crystallization and melting peaks are observed at 113 and 148 °C, respectively. Increasing the PBT NFs content from 1 to 10 wt%, the cold crystallization peak for NFCs shifted to the lower temperatures between 97.8 to 92.5 °C due to the nucleating effect of PBT NFs. It can be assumed that the number of the  $\alpha'$  crystal form is enhanced as the cold crystallization temperatures shifted to the lower temperatures<sup>119</sup>. The thermographs of NFCs display broader and double melting peak curves with a low melt temperature ( $T_{LM}$ ) of 145 °C and a high melt temperature ( $T_{HM}$ ) of 152 °C. Double melting peak behavior for semi-crystalline polymers have been explained according to the melt-recrystallization model<sup>258, 259</sup>. On the other hand, the massive surface of PBT NFs possibly donated stability to the  $\alpha'$  loose structure and facilitates the recrystallization. Therefore, the broader melting peak is a result of recrystallization to a stronger structure in the same time scale.

**Figure 5-16B** represents the corresponding cooling run from 180 °C. As can be seen, the melt crystallization peak of the processed PLA was not achievable at a cooling rate of 5 °C/min. In contrast, the presence of only 1 wt% of the PBT NFs boosted the crystallization kinetics significantly, and a pronounced melt crystallization peak was observed. The PBT NFs that remained solid in the swept temperature range of DSC thermographs made a huge interface with PLA molecules. This huge stiff surface with appropriate interactions reduced the PLA chains' dynamics at the interface and the energy barrier for the crystallization. The remarkable step for the  $T_g$  of processed PLA is smoothed by the addition of PBT NFs. This descent demonstrates slower dynamics of the PLA chains because of the interactions with the consistent surface of PBT NFs and being trapped in the crystals. The onsets of melt crystallization and the calculated crystallinity from the cooling runs are reported in **Table 5-6**. Melt crystallization for the NFC3 sample starts at higher temperatures in comparison to other NFCs. It seems that at 3 wt% of the PBT NFs, there is an optimum between the thickness and population of the NFs, which can improve the PLA crystallization kinetics efficiently. The crystallinity of PLA in different NFC samples is in the same range, reflecting that the maximum crystallization capability of the PLA has already been applied even using the lowest PBT NFs composition (1 wt%)<sup>226</sup>.

The second heating curves of NFCs in **Figure 5-16C** are not presenting a two-step  $T_g$ . The affinity of PLA chains with the PBT NFs on one hand and involving the chains in the crystalline phase (established during the cooling step), on the other hand, resulted in one  $T_g$ , which is assigned to the rigid amorphous phase. The evaluated  $T_g$  of PLA from second heating for NFC samples showed a slight increase with PBT NFs content. In the second heating, the processed PLA sample followed the same trend and the total crystallinity in the first heating run (1 %). In contrast, the cold crystallization peaks for the samples containing PBT NFs are dramatically reduced. The calculated area for the cold crystallization peak is less than 4 % of the melting peak for the NFCs. This considerable depression in the PLA cold crystallization can be explained by the intensive crystal formation during the cooling induced by the presence of the NFs; therefore, the crystallization capability of the PLA was exhausted. Accordingly, the melting peak of the second heating is approximately representative of the crystals, which were formed during the cooling step. The calculated crystallinity for the NFC samples based on the second heating is presented in the last row of **Table 5-6** to demonstrate the negligible difference between the crystallinities obtained during the cooling and second heating (e.g., the degree of crystallinity evolved during cold crystallization and melt crystallization for NFC1 are 26.6 % and 28.4 %, respectively). Therefore, it is logical to discuss the crystal forms nucleated during the cold crystallization and melt crystallization by comparing the two heating runs. In the second heating, the double melting peak is observed with the same  $T_{HM}$  and  $T_{LM}$  (145 and 152 °C) as the first heating. However, an increment in the population of the  $\alpha'$  form and a reduction in  $\alpha$  form is conspicuous in comparison to the first heating. This is evaluated by deconvolution of the double melting peak of the first and second heating curves. Accordingly, the melt crystallization of the PLA was dominated by  $\alpha'$  form. A high PLA chain dynamics in the molten state combined with the high crystallization rate could explain the observation of a more intensive population of  $\alpha'$  form nucleated during the melt crystallization rather than nucleated during cold crystallization at a reduced cold crystallization temperature<sup>226</sup>.

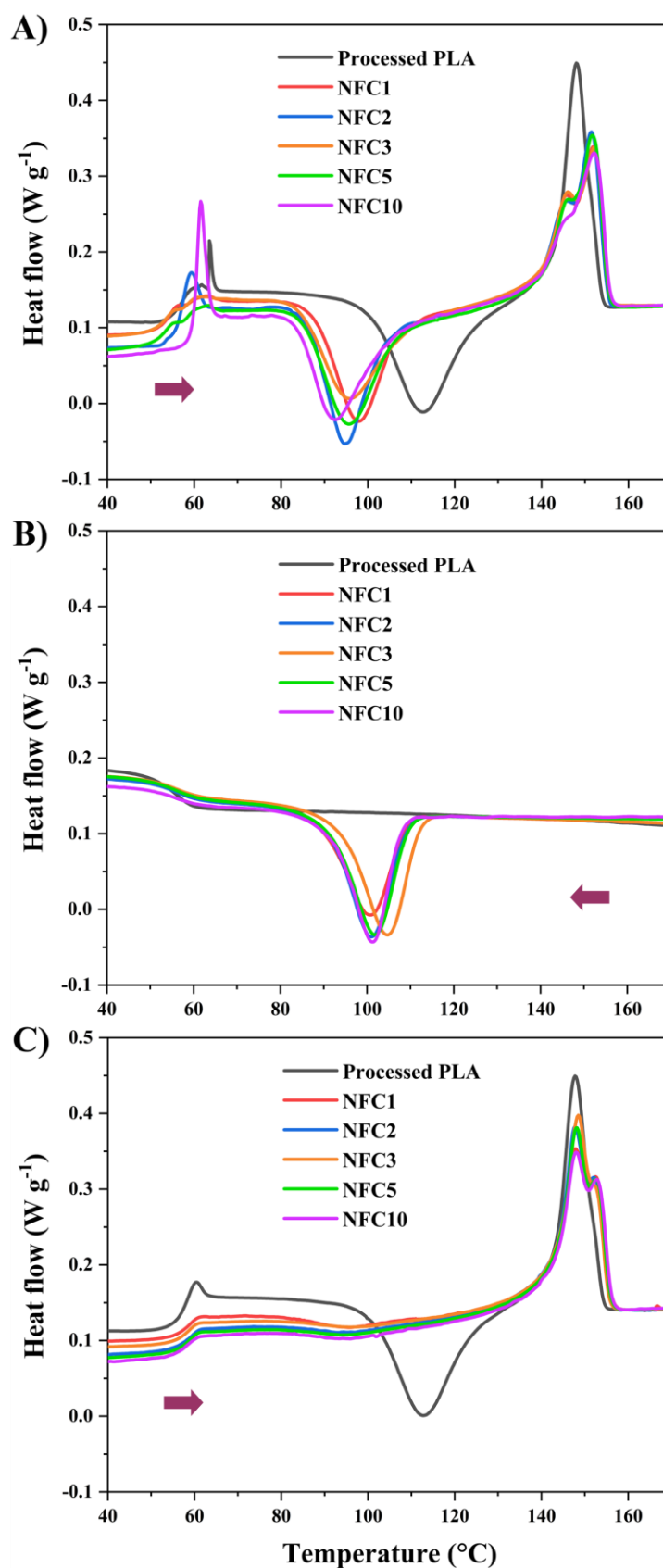


**Figure 5-16.** DSC thermographs of processed PLA and NFCs containing different amounts of PBT NFs (1, 3, 5, and 10 wt%); (A) First heating, (B) Cooling, and (C) Second heating <sup>226</sup>.

**Table 5-6.**  $T_g$  and non-isothermal crystallization data for processed PLA and NFC samples obtained by DSC <sup>226</sup>.

PBT NFs content (wt%)	0	1	2	3	5	10
$T_g$ (°C)	56.8	57.1	57.4	57.8	58	58.7
Cold Crystallization peak (°C)	113	97.8	96.8	95.8	95.6	92.5
Melt crystallization onset (°C)	-	109.3	110.7	112.75	109.7	108
Crystallinity-cooling (%)	-	26.6	30.1	30.2	29.3	27.7
Crystallinity-second heating (%)	1	28.4	31.7	32	31.3	30.3

In order to understand the strong effect of the enormous interface of PBT NFs on the thermal behavior of PLA, the NFC2 sample was studied. **Figure 5-17A** displays the cooling curves of this sample from 180 to 20 °C and 240 to 20 °C. The corresponding samples are designated as NFC2-180 and NFC2-240, respectively. The melt crystallization peak for NFC2-180 in **Figure 5-17** is the same as NFC2 in **Figure 5-17B**. The melt crystallization peaks of PLA and PBT in the NFC2-240 curve are indicated by arrows at 115 and 205 °C, respectively. Since the PBT NFs were molten at 240 °C, the small melt crystallization peak for PLA is barely visible. Such a huge difference in the PLA crystallization behavior notifies the effect of the PBT nanofibrillar structure on the crystallization compared to droplet-matrix morphology. It is noteworthy that the crystallinity of PBT is significant, 35 % (**Figure 4-1**), and its melt crystallization rate is fast <sup>260</sup>. The small melt crystallization peak for PBT is due to its small amount (2 wt%). Lorenzo et al. observed no effect of PLA on PBT crystallization <sup>38, 177</sup>. However, the observed small peak (**Figure 5-17A**) with the onset of 205.5 °C belongs to PBT melt crystallization. The increase from 191 °C to 205.5 °C could be attributed to the plasticization effect of PLA chains on the stiff structure of PBTs' phthalate group, which facilitates nucleation and growth. The second heating curve of the NFC2-240 sample in **Figure 5-17B** is quite similar to that of processed PLA as the huge interface of PBT with PLA is missing. The larger step for the  $T_g$  in cooling and second heating of NFC2-240 is remarking the not entrapped chains in crystal lamella. The arrow in **Figure 5-17B** points to the melting point of PBT at 225 °C <sup>226</sup>.

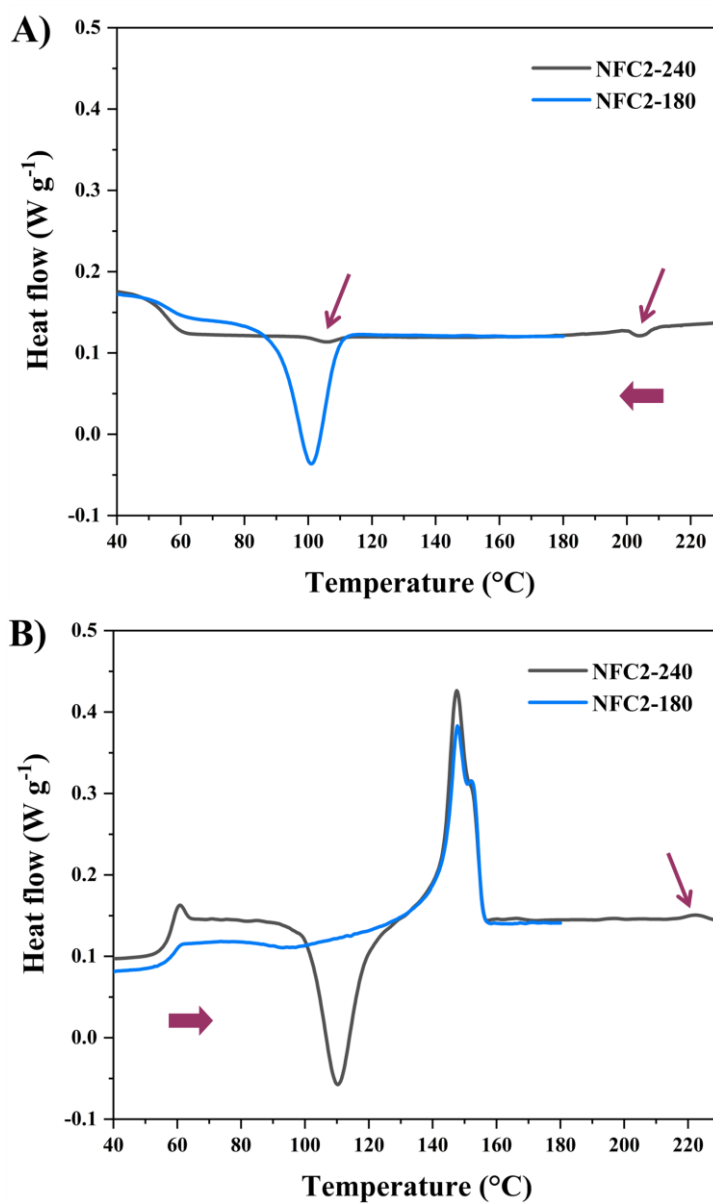


**Figure 5-17.** DCS thermographs of NFC2 after experiencing the first heating run up to 180 °C (NFC2-180) and 240 °C (NFC2-240); (A) Cooling curves; (B) Second heating <sup>226</sup>.

### 5.5.2 Crystallite morphology of NFCs evolved from the quiescent melt

Direct SEM observations in **Figure 5-18** indicate the crystalline phase morphology of processed PLA and NFC1 at 100 °C, respectively. Through the melt crystallization (annealing) of processed PLA, 3D spherulites with an average diameter of 12  $\mu\text{m}$  have been formed (**Figure 5-18A**). The molecular structures in the spaces between the spherulites are parts of underneath spherulites, incomplete spherulites, or some stacked lamellae. The overall view of NFC1 in **Figure 5-18B**, at the same resolution as **Figure 5-18A** shows no traces of spherulites. A more in-depth view of the morphology in **Figure 5-18C** reveals stacks of few parallel disks around randomly distributed PBT NFs. The spots with an accidentally parallel orientation of PBT NFs in **Figure 5-18D** represent a clear observation of a nanohybrid shish-kebab (NHSK) superstructures of the PLA crystallites (with a mean diameter of 0.7  $\mu\text{m}$  and thickness of 80 nm) around PBT NFs<sup>81</sup>.

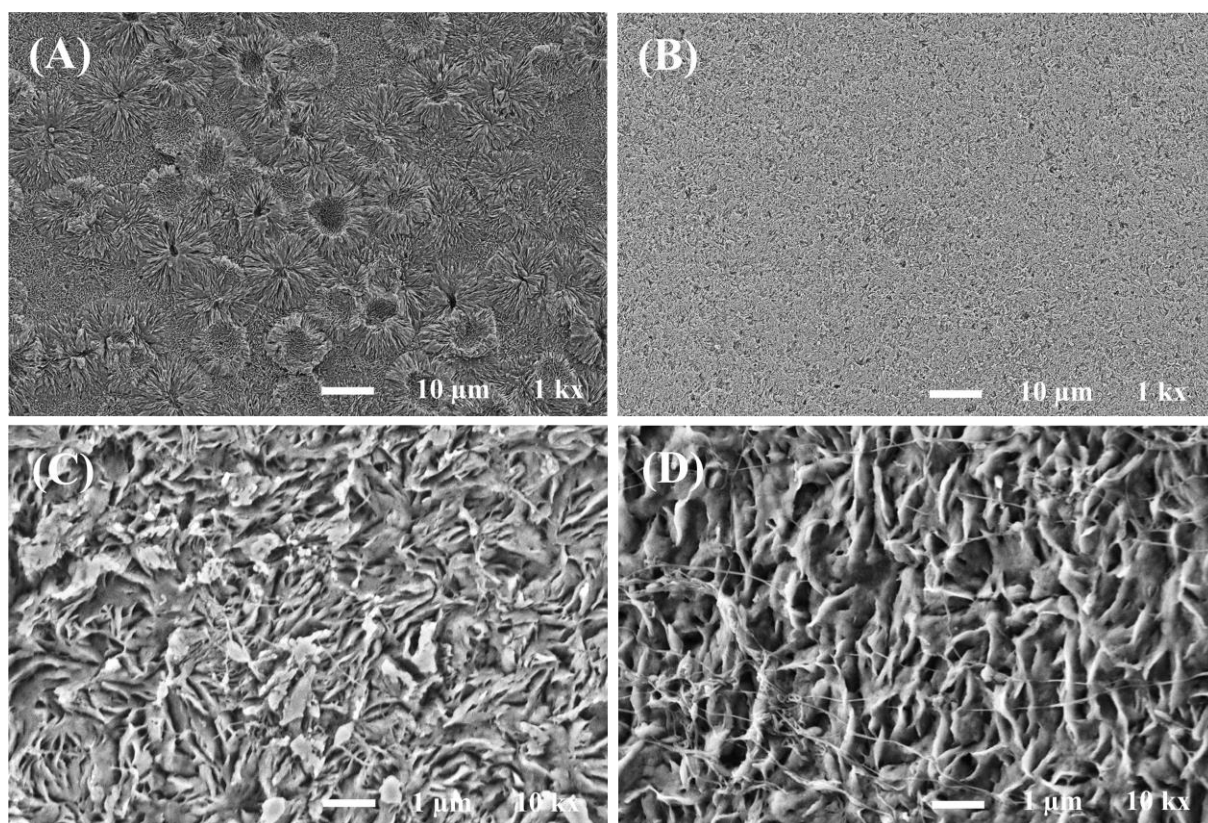


**Figure 5-18.** SEM micrographs of PLA crystalline phase after etching the amorphous phase; (A) spherulitic morphology of processed PLA crystalline phase; (B)-(D) Crystalline structure in NFC1 at different resolutions: (B) no trace of spherulites, (C) NHSK superstructures of crystalline phase around PBT NFs in NFC1, (D) clear observation of NHSKs superstructure due to accidentally parallel orientation of PBT NFs<sup>81</sup>.



Atomic force microscope (AFM) images of processed PLA and NFC1 were acquired in PeakForce tapping mode presented in **Figure 5-19**. The 3D topography of NHSKs superstructure with a scan size of  $1 \times 1 \mu\text{m}^2$  is presented in **Figure 5-19C**.

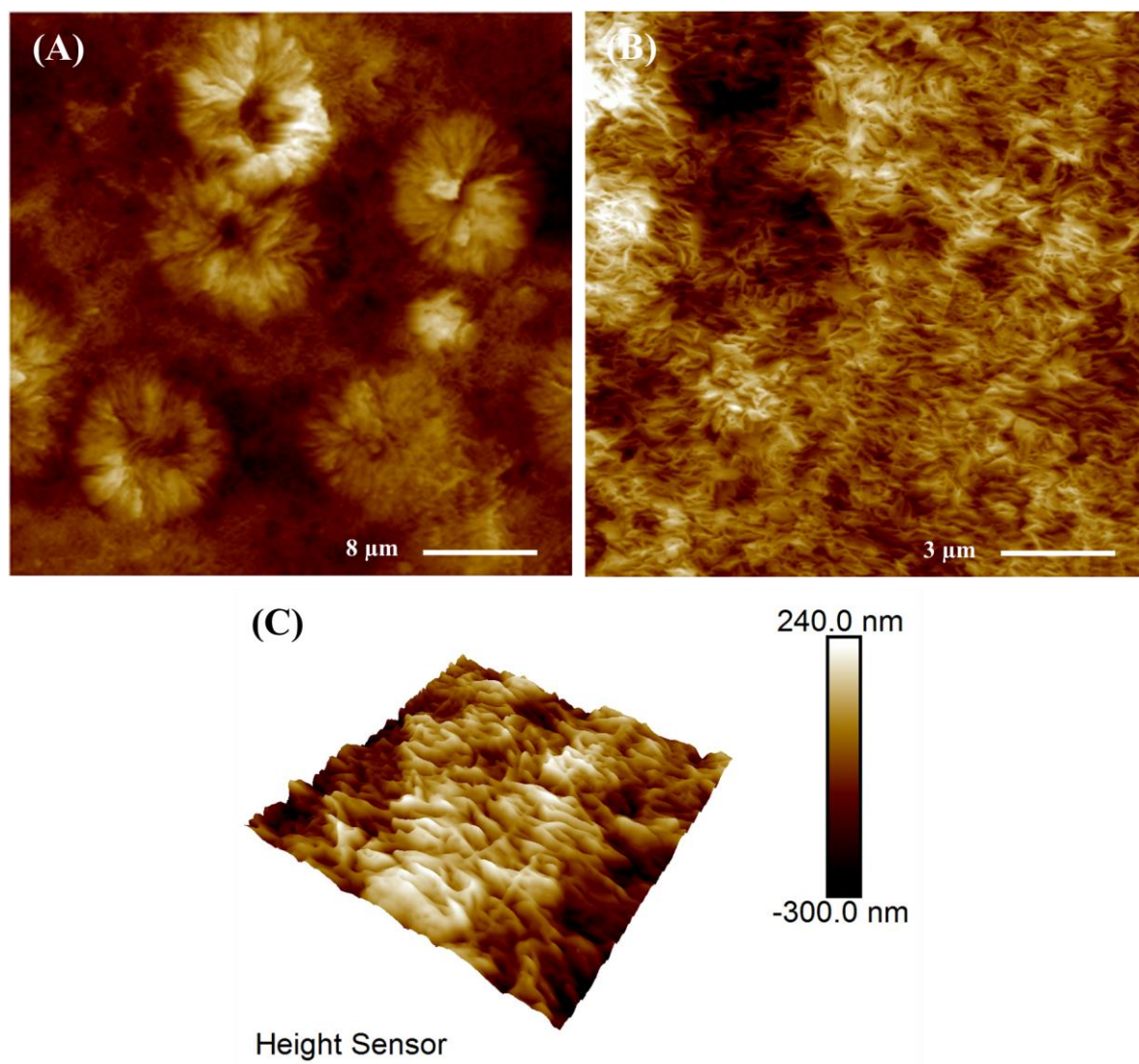


**Figure 5-19.** AFM images of the crystalline phase after melt crystallization at  $T_{\text{iso}}$  of 100 °C in the DSC pan: (A) Processed PLA, (B), and (C) NFC1. (C) 3D image of the NHSK superstructure with a scan size of  $1 \times 1 \mu\text{m}^2$  <sup>81</sup>.

Since bulk pieces were taken as specimens and prepared after history removal at 180 °C, the uniformity of NHSK superstructures inside the bulk is guaranteed. The randomly distributed PBT NFs with proper physical interactions with PLA acted as potent nucleating agents and governed the variable orientation of kebabs sprouting from the quiescent melt state. Similar to polyolefins, the radius of gyration ( $R_g$ ) of the molecules compared to the diameter of the fibrils determines the

nucleation mechanism, which is defined as “soft epitaxy growth”<sup>135, 139, 261</sup>. During the annealing, the molecules near the PBT NFs face a highly curved surface because of the tiny diameter of nanofibrils. The chain segment adjacent to the PBT NF gets oriented along with that, and the rest of the chain is either folded normal to the first-aligned segment or jointed to the amorphous phase. Once the raw nuclei are established, lateral growth of the crystalline phase progresses through folding and forms columns of lamellae surrounding the central shish.

Morphological observations of NFC3 are presented in **Figure 5-20A-C**, demonstrating different features compared to NFC1. Apart from the NHSK superstructures around the single or double PBT NFs in **Figure 5-20A**, different crystallite morphologies of PLA are distinguishable at the interface of the bundle of PBT NFs. In the absence of individual nanofibrils, the crystalline phase manifested fan-shaped 3D transcrystallinity perpendicular to the bundles of NFs and was constrained by the adjacent nuclei. The transition in the nucleation mechanism from soft epitaxy on the individual PBT NF to epitaxy on the bundle of PBT NFs (or seeding) resulted in a transformation of the crystalline phase morphology from 2D NHSK to 3D fan-shaped transcrystallinity (**Figure 5-21**). This transformation emphasizes the crucial effect of fillers’ diameter. In other words, the knotting of the PBT NFs reduces the curvature of the surface, changing the nucleation mechanism of the PLA chains to folding on the surface of the NFs bundle (seeding) followed by transcrystallinity. Ning et al. investigated the solution crystallization of polyethylene on MWCNTs and double-wall carbon nanotubes (DWCNTs) bundles with diameters in the same range<sup>160</sup>. They showed that the “groove structure” of DWCNTs bundles facilitated the orientation of PE chains into a shish-kebabs structure more efficient than MWCNTs with a smooth surface. Even though the groove structure is evident for PBT NFs bundles, the curvature reduction effect is dominant for the change in the crystallization behavior of PLA.

**Figure 5-20C** shows the bald bundle of PBT NFs laying on the NHSK superstructures of the PLA crystalline phase around the single or double PBT NFs. Considering the limited crystallization potential of the PLA, the bald surface of the bundles implies a tendency in the crystallization mechanism. Indeed, the PLA chains prefer the orthogonal ordering around the nanofibrils rather than constrained spherulites on the wall of the PBT NFs bundles. This tendency of the system is kinetically governed due to different crystallization mechanisms. Studying the effect of nanoparticles with different geometries on the crystallization kinetics showed that the partial molecular conformational order significantly affects the induction time of the PLLA crystallization<sup>161, 168</sup>. Additionally, the limited potential of PLA to crystallize due to high D-lactide content might preferentially promote the lateral growth of nanodomain kebabs with adequate inter-kebabs spaces for phase separation of the amorphous region. **Figure 5-21A, B** have schematically shown

the nucleation mechanism and lateral growth around single and bundle of PBT NFs through their evolution over time.

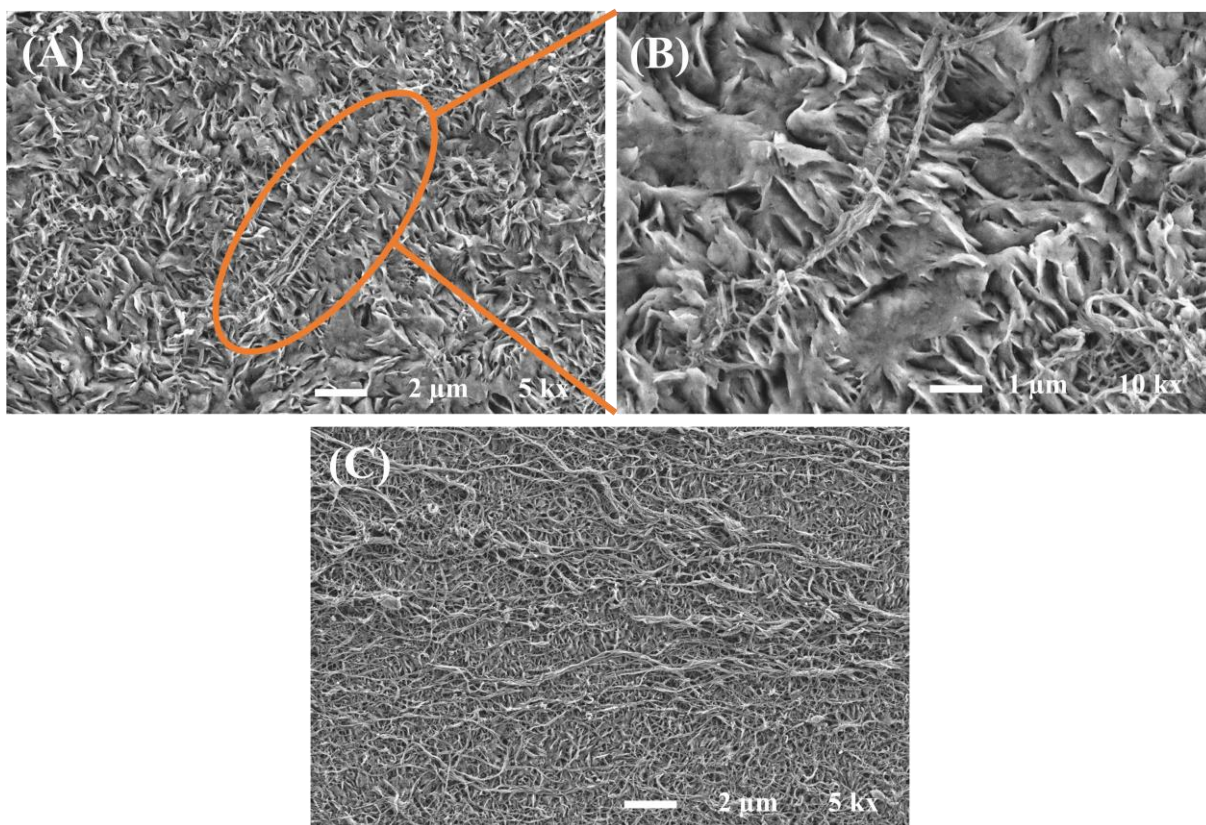


**Figure 5-20.** SEM micrographs of NFC3 after annealing and etching the amorphous phase; (A) random oriented NHSK superstructures and fan-shaped transcrystalline structure of PLA, (B) fan-shaped transcrystalline structure of PLA around a bundle of PBT NFs, and (C) unpatterned bundles of PBT NFs laying out on the NHSK superstructures.

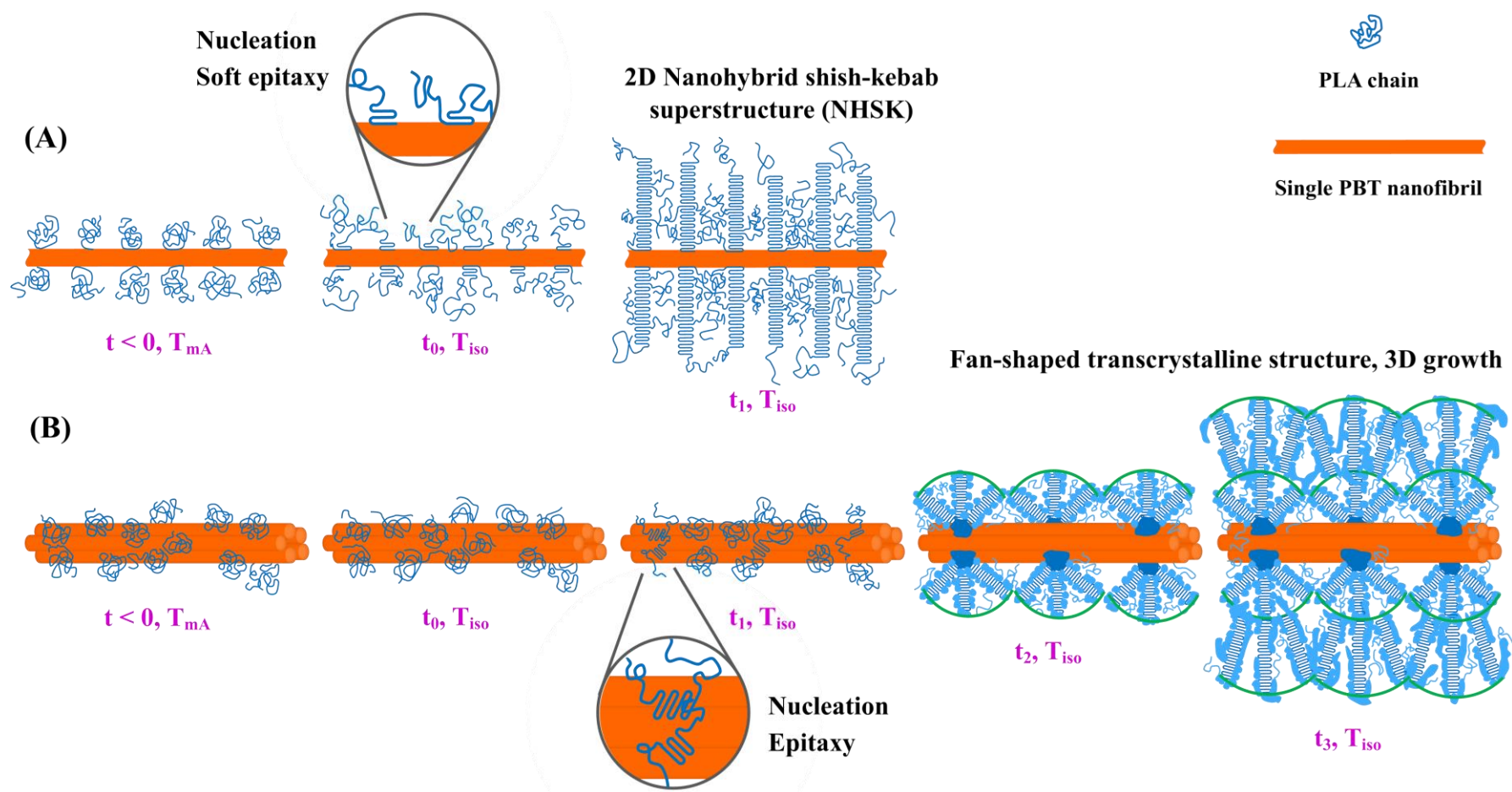


**Figure 5-21.** Schematic of crystallization mechanism and kinetics. (A) Random coils of PLA chains (blue) around single PBT NF (orange) at melting temperature of PLA ( $T_{mA}$ ) before annealing starts ( $t < 0$ ); conformational ordered of PLA chain segments act as nuclei at annealing temperature ( $T_{iso}$ ) ( $t = 0$ ); progress of lateral growth through the folding of chain segments normal to the first-aligned segments and finalized NHSK superstructure ( $t_1$ ). (B) Random coils of PLA chains around the bundle of PBT NFs at  $T_{mA}$  ( $t < 0$ ); induction time for nucleation at  $T_{iso}$  ( $t_0$ ); nucleation by folding on the bundle of PBT NFs ( $t_1$ ); Fan-shape 3D transcrystallinity constrained by the adjacent nuclei ( $t_2$ ); and continued growth ( $t_3$ ).

How the temperature during the process affects the crystallinity defines the borders of the processing window for semicrystalline polymers and their final mechanical properties. The independence of developed superstructures in NFC1 from the flow field provided the chance of probing the crystalline phase morphology changes by temperature and assessing the effectivity of PBT NFs as shish. **Figure 5-22A** depicts the crystalline morphology in processed PLA matured during 160 minutes of annealing at 114 °C. The few and yet, bigger spherulites (with 30 μm average diameter) constrained by the adjacent ones have formed as a consequence of a temperature increase. **Figure 5-22B** and **C** demonstrate the final crystalline structure after crystallinity in NFC1 was completed during 12 minutes of annealing at 114 °C (with a magnification similar to **Figure 5-22A**). As it is evident, no trace of spherulites can be seen. Images attained in higher resolutions from NFC1 in **Figure 5-22C** and **D** reveal the NBSK superstructures with longer kebabs compared to **Figure 5-18B**, as a result of the easier diffusion (due to lower melt viscosity) of PLA chains into the lamellae. The long kebabs cover the PBT NFs, and the interlocking of the kebabs is conspicuous.

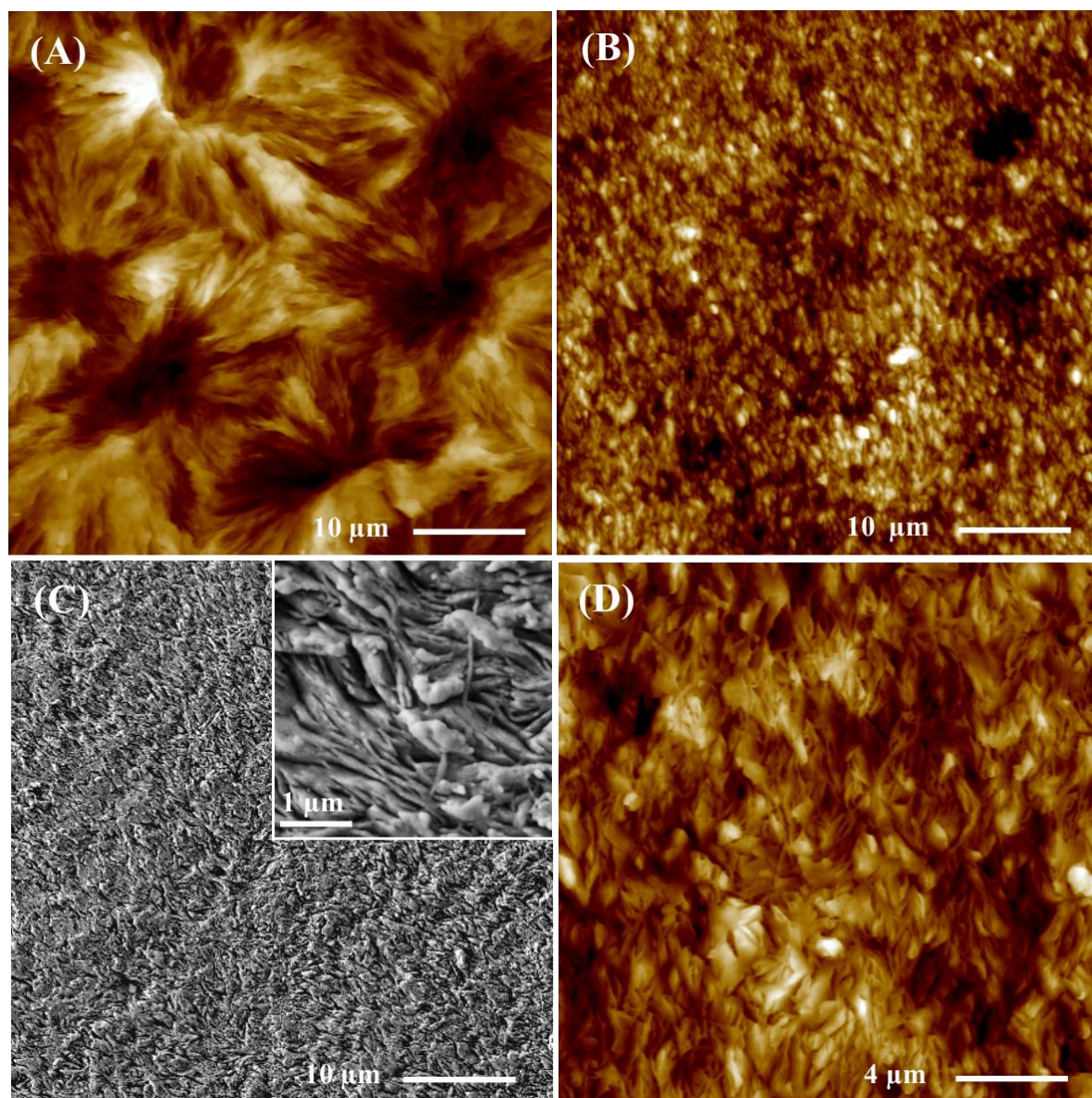


**Figure 5-22.** Crystalline phase morphology at  $T_{\text{iso}}=114$  °C: (A) AFM image showing a spherulitic morphology in processed PLA; (B), (C), and (D) SEM and AFM images are showing the NHSK superstructure in NFC1<sup>81</sup>.

**Figure 5-23A-C** exhibit the crystalline phase morphology of NFC1 at  $T_{\text{iso}}$  of 117, 120, and 124 °C, respectively. At  $T_{\text{iso}}$  of 117 °C, the crystal morphology has changed to a semi or quadruple spherulitic structure. Although in some areas, parallel lamellae can misleadingly look like kebabs, with more attention, it can be distinguished that they belong to fragmental spheres. At  $T_{\text{iso}}$  of 120 °C, the lower melt viscosity supported completing the morphological transition, and small spherulites with obvious displacement have formed. By increasing  $T_{\text{iso}}$  to 124 °C, a significant increase in spherulites diameter is visible in **Figure 5-23C**. Since processed PLA remains amorphous after a long time of annealing at  $T_{\text{iso}} \geq 117$  °C, the nucleation effect of PBT NFs is not

deniable. Therefore, at least in the early stages, the nucleation mechanism is conformational order of PLA chain segments on PNT NFs. After that, regarding the final spherulitic morphology and slow sporadic nucleation at higher  $T_{iso}$  levels, it sounds that nucleation on the first formed lamellae (self-nucleation) was more probable than on the PBT NFs.

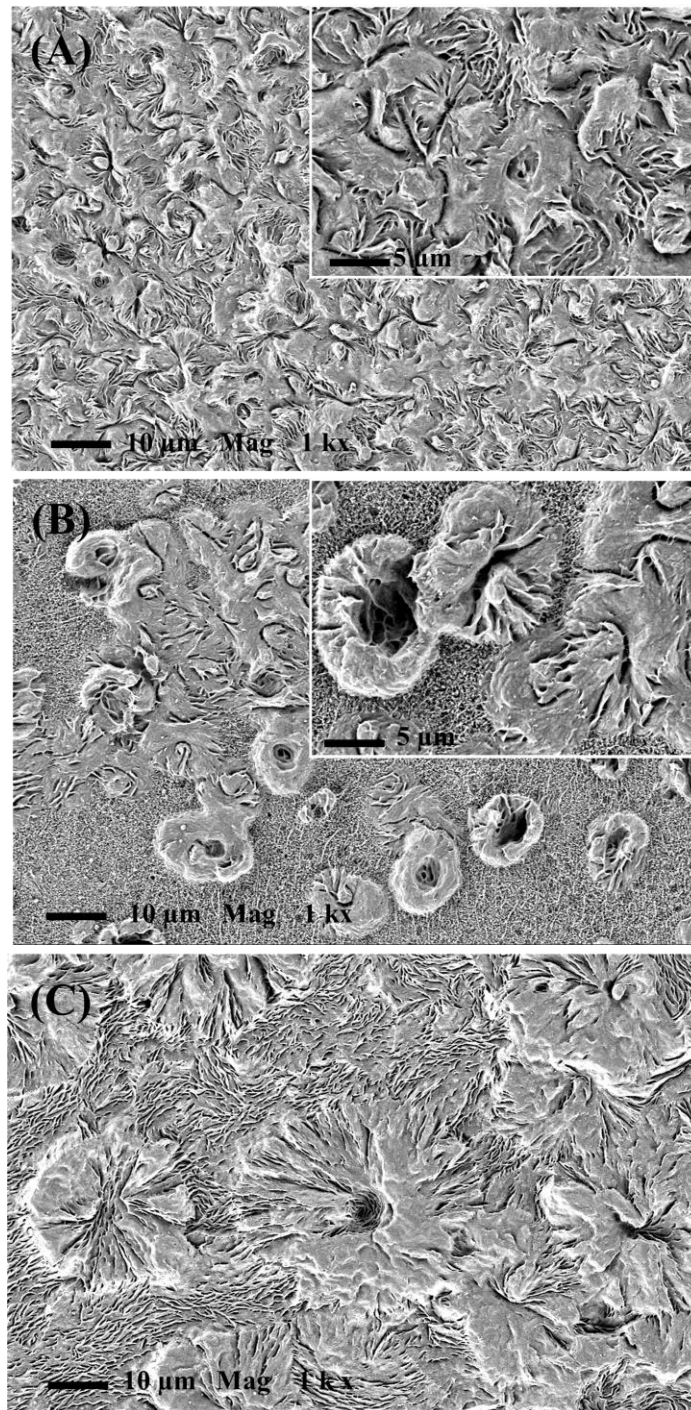


**Figure 5-23.** SEM images of PLA crystalline phase evolution in NFC1 through temperature: (A) 117 °C, (B) 120 °C, and (C) 124 °C<sup>81</sup>.

### 5.5.3 Isothermal melt crystallization kinetics

The normalized exothermic heat flow curves in the isothermal temperature range of 100 to 117 °C for processed PLA, NFC1, and NFC3 are presented in **Figure 5-24**(A1-C1). It is notable that the lower range of  $T_{\text{iso}}$  levels was not considered since the crystallization of PLA started before attaining the desired  $T_{\text{iso}}$  via fast cooling. The bell-shaped peak of the normalized heat flow was attributed to the initial fast rate of crystallization and then slowed down due to the completion of the crystallization process. The required time to complete the crystallization peak ( $t_{\text{iso}}$ ) extended with increasing  $T_{\text{iso}}$  that was well consistent with the nucleation theory, in which a high chain dynamic hinders the formation of raw nuclei. It could be mentioned here that the relatively fast crystallization of PBT<sup>262-264</sup>, triggered by a high conformational order in elongated nanofibrils<sup>149</sup>, could complete the cold crystallization of PBT NFs either during compression molding or during an isothermal step (iv) of the thermal procedure (see **Figure 4-9**). As a result, a single isothermal peak is obtained for NFCs, which measures PLA crystallization. Corresponding curves for NFC2, NFC5, and NFC10 are presented in **Figure 5-25**.

The broad isotherm peaks of processed PLA (**Figure 5-24A1**) with a considerable induction time ( $t_0$ ) in which no crystallization was detectable<sup>265, 266</sup>, changed into sharp peaks in the presence of only 1 wt% of PBT NFs (It should be noticed that the scale of time axis for PLA is different from those of NFCs). The crystallization of NFC1 immediately started at lower  $T_{\text{iso}}$  levels (100-110 °C), while the induction time appeared at higher crystallization temperatures since the size of the critical nuclei and the rate of their formation are both temperature-dependent. A significant improvement in the crystallization rate at 3 wt% PBT NFs interrupted the bell-shaped isotherm peaks for NFC3 at  $T_{\text{iso}}$  levels up to 110 °C, which is due to the formation of a considerable amount of crystals nucleated upon fast cooling.



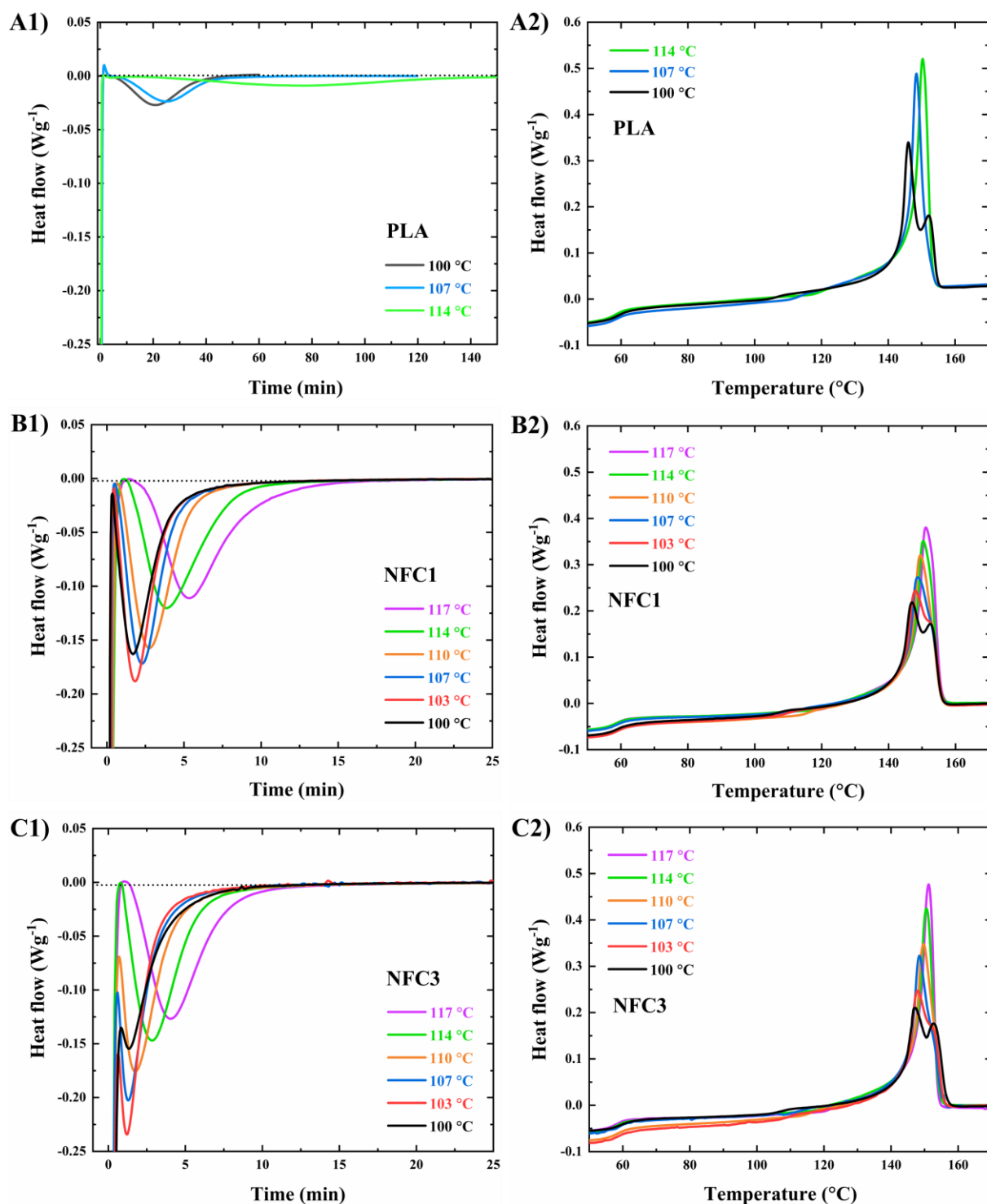


**Figure 5-24.** (A1), (B1), and (C1) Isothermal crystallization at different temperatures for processed PLA, NFC1, and NFC3, respectively; (A2), (B2), and (C2) heating run after isothermal crystallization for processed PLA, NFC1, and NFC3, respectively <sup>81</sup>.

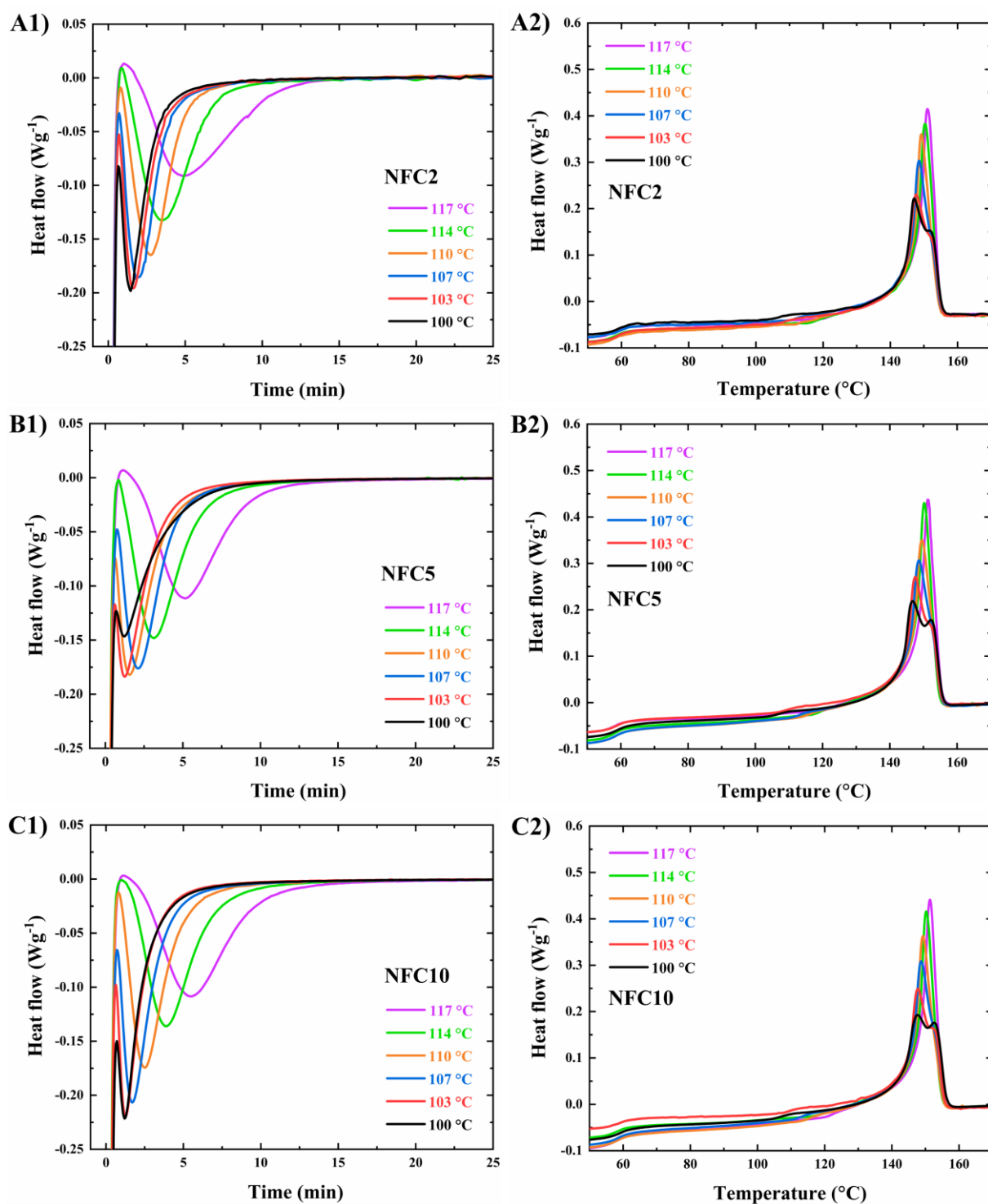


**Figure 5-25.** (A1), (B1), and (C1) Isothermal crystallization at different temperatures for NFC2, NFC5, and NFC10, respectively; (A2), (B2), and (C2) heating run after isothermal crystallization for NFC2, NFC5, and NFC10, respectively<sup>81</sup>.

**Figure 5-26A** represents the relative volumetric fraction of crystals ( $V_c(t)$ ) in NFC1 (after discarding the induction period). A typical time-dependent sigmoidal shape has been developed

that extended to longer  $t_{\text{iso}}$  with increasing  $T_{\text{iso}}$ . The plots for a given time show us the polymer's volume fraction transformed into the crystalline phase as a function of undercooling. The double logarithmic plots of  $\text{Log}[-\text{Ln}(1 - V_c(t))]$  vs.  $\text{Log}(t - t_0)$  for NFC1 at different temperatures are shown in **Figure 5-26B**. **Table 5-7** lists the Avrami exponent ( $n$ ), the crystallization rate constant ( $k$ ) along with the experimental crystallization half-time ( $t_{1/2,\text{exp}}$ ) and that of the model ( $t_{1/2}$ ) at different  $T_{\text{iso}}$ . Although the Avrami model is applicable to the initial stage of crystallization, determining the quantity of the exponent  $n$  can provide valuable information about the nucleation mechanism (whether it is homogeneous or heterogeneous, simultaneous or sporadic) and the dimensionality of crystal growth (whether it is 2D or 3D) <sup>267, 268</sup>. The Avrami model was able to appropriately fit the experimental data for a relative volumetric conversion range encompassing 3 and 20 %. The correlation coefficient of  $R^2 > 99.9\%$  and a negligible difference between  $t_{1/2,\text{exp}}$  and  $t_{1/2}$  confirms the appropriate fitting of the experimental data. In the presence of only 1 wt% PBT NFs (NFC1), the crystallization half-time for processed PLA at  $T_{\text{iso}}$  of 100 °C and 114 °C decreased from 18.9 and 65.7 minutes to 1.75 and 3.7 minutes, respectively. The crystallization rates of PLA and NFC1 decreased by increasing the  $T_{\text{iso}}$  level, and the crystallization half-time increased.

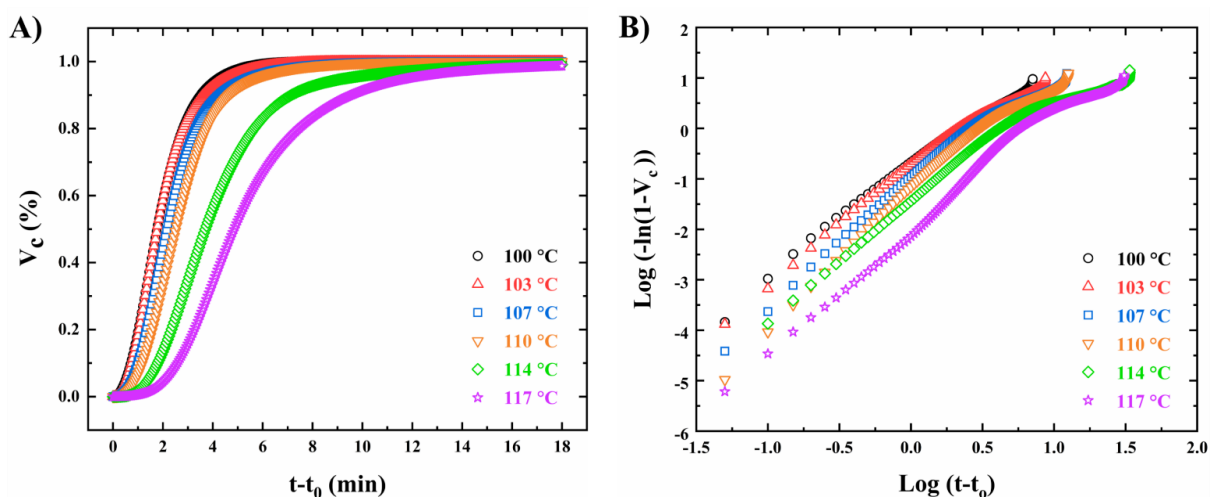


**Figure 5-26.** (A) Relative crystallinity and (B) Avrami double-log plots of NFC1 at different  $T_{\text{iso}}$  <sup>81</sup>.

The exponent  $n$ , for processed PLA, is between 2 and 3, suggesting a 3D truncated spherical structure resulting from instantaneous nucleation controlled by a diffusion process <sup>175</sup>. The obtained exponent  $n$  for NFC1 was found to be in the range of 2.1 to 3.25 when the crystallization temperature increased from 100 °C to 117 °C (**Table 5-7**). The non-integer values of exponent  $n$

indicated a combination of thermal and athermal nucleation mechanisms<sup>269-271</sup>. The  $n$  value of about 2 at lower isotherms determines instantaneous nucleation on the predetermined nuclei<sup>267</sup>. Increasing the  $T_{iso}$ , an increase in  $n$  values (in the range of 2.5–2.9) indicated a change from instantaneous nucleation to sporadic nucleation in the NFs<sup>267, 272</sup>. The change in crystal growth habit from 2D morphology into 3D spherical growth at 117 °C was reflected in the  $n$  exponent value of 3.25<sup>273, 274</sup>.

**Table 5-7.** The Avrami parameters ( $n$ -exponent and  $k$ -rate constant),  $t_{1/2}$  (the Avrami model crystallization half-time) and  $t_{1/2,exp}$  (experimental crystallization half-time) for processed PLA and NFC1 at different isothermal crystallization temperatures<sup>81</sup>.

n, k (R <sup>2</sup> )*, $t_{1/2}$ and $t_{1/2,exp}$		$T_{iso}$ (°C)					
		100	103	107	110	114	117
<b>PLA</b>	$n$	2.69		2.9		2.65	
	$k$ (10 <sup>-1</sup> min <sup>-1</sup> )	0.46		0.4		0.13	
	(R <sup>2</sup> )	(1)		(1)		(1)	
	$t_{1/2}$ (min)	24.7		22.1		66.5	
	$t_{1/2,exp}$ (min)	24.9		22.1		65.7	
<b>NFC1</b>	$n$	2.1	2.3	2.5	2.6	2.9	3.25
	$k$ (10 <sup>-1</sup> min <sup>-1</sup> )	4.9	4.9	4.1	3.6	2.5	1.9
	(R <sup>2</sup> )	(1)	(1)	(1)	(0.9999)	(0.9998)	(1)
	$t_{1/2}$ (min)	1.7	1.74	2.1	2.4	3.5	4.7
	$t_{1/2,exp}$ (min)	1.75	1.8	2.2	2.5	3.7	4.9

\*Correlation coefficients.

The relative volumetric crystalline fraction vs. time and double logarithmic plots of the Avrami model for PLA and NFCs at 114 °C have been illustrated in **Figure 5-27A** and B, respectively. **Table 5-8** lists the representative parameters of the Avrami model and experimental crystallization half-time for PLA and NFCs at  $T_{\text{iso}}$  of 114 °C. It should be noted that the fitting of the Avrami model at lower temperatures is not discussed here since the baseline's determination was not possible due to the flying start of crystallinity (e.g., **Figure 5-24C1**). By increasing the PBT NF content, exponent  $n$  first decreased and then increased, showing a minimum at NFC3. The formation of NHSK superstructures of PLA crystallite domains around single or double PBT NFs and its transition to fan-shaped transcrystallinity perpendicular to the bundle of NFs were discussed earlier. Since at higher PBT contents ( $\geq 3$  wt%), the size of each individual nanofibril increases and simultaneously the bundling of nanofibrils becomes more probable; the 3D growth of transcrystalline structure becomes dominant. Therefore, the initial decreasing trend of exponent  $n$  with PBT NF content and approach to the value of 2 could be due to (i) the formation of 2D NHSK superstructures and that (ii) the dominant sporadic nucleation mechanism in NFC1 at 114 °C is replaced with instantaneous nucleation on the tremendous amount of PBT NFs in NFC2 and NFC3. However, the increasing trend of exponent  $n$  corresponds to the 3D transcrystalline phase<sup>81</sup>.

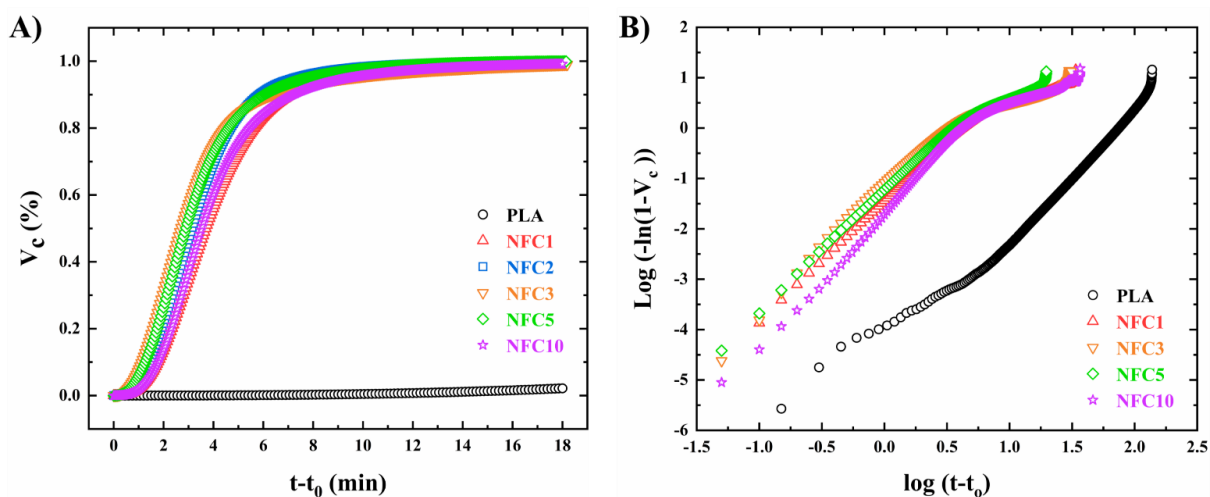


**Figure 5-27.** (A) Relative crystallinity and (B) Avrami double-log plots of processed PLA and NFCs at  $T_{\text{iso}}=114$  °C<sup>81</sup>.

By increasing the PBT NFs content, the crystallization rate ( $k$ ) exhibits an increase and then a decrease with a maximum value for NFC3. Some researchers found that in the nanocomposites prepared through solution coagulation, the locally ordered PLA chains along the carbon

nanotubes (CNTs) enhance the crystallization rate, compared to the epitaxial growth on graphene nanosheets<sup>161, 168</sup>. Accordingly, the initial increase of  $k$  values through PBT NF content is attributed to (i) the increase in the number of nucleation sites; and (ii) fast nucleation due to the conformational order of PLA chains adjacent to the single PBT NFs. Thereafter, the decrease in  $k$  values could be attributed to (i) the longer induction time for nucleation on the bundle of PBT NFs and (ii) the higher viscosity of the system at higher contents of consistent PBT NFs, which restricts PLA chains mobility, thereby preventing them from joining the lamellar structure. As can be seen,  $t_{1/2,exp}$  and  $t_{1/2}$  in **Table 5-8** are close together and their variations by PBT NFs content is in accordance with  $k$  values. Although the crystallization kinetics of semicrystalline polymer-based MFCs have been investigated repeatedly<sup>24, 25, 58, 143</sup>, a similar observation was not reported since the fibrils curvature was not high enough to change the nucleation mechanism.

**Table 5-8.** Avrami parameters ( $n$ -exponent and  $k$ -rate constant),  $t_{1/2}$  (Avrami model crystallization half-time) and  $t_{1/2,exp}$  (experimental crystallization half-time) for processed PLA and NFCs at  $T_{iso}=114$  °C<sup>81</sup>.

	$n$	$k$ ( $10^{-1} \text{ min}^{-1}$ ) ( $R^2$ )*	$t_{1/2}$ (min)	$t_{1/2,exp}$ (min)
<b>NFC1</b>	2.9	2.5 (0.9998)	3.5	3.75
<b>NFC2</b>	2.5	2.8 (0.9999)	3.05	3.15
<b>NFC3</b>	2.25	3.3 (0.9999)	2.6	2.7
<b>NFC5</b>	2.35	3 (1)	2.85	2.9
<b>NFC10</b>	2.95	2.6 (1)	3.36	3.55

\*Correlation coefficients.

The final heating runs were conducted to detect the developed crystallinity and the crystal forms during the isotherms (**Figure 5-24(A2-C2)**). Double peak melting behavior is evident for all the samples experienced  $T_{iso}$  of 100 and 103 °C, confirming the intense population of  $\alpha'$  crystal forms at lower levels of  $T_{iso}$ . The two melting peaks merged for samples annealed at higher  $T_{iso}$  levels and slightly shifted to the  $\alpha$  crystal form's melting temperature. The normalized degree of

crystallinity based on the endotherm curves for processed PLA and the NFCs are presented in **Table 5-9**. Crystallinity increased by increasing  $T_{iso}$  for all the samples. At a constant temperature, the crystallinity of PLA shows a slight increase and then decrease by increasing PBT NFs content, which can be attributed to the different effects of PBT NFs as nucleating sites and reducing the PLA chains mobility. However, the dependency is not noticeable.

**Table 5-9.** Crystallinity of PLA and NFCs at different isotherms <sup>81</sup>.

	$T_{iso}$ (°C)					
	100	103	107	110	114	117
<b>PLA</b>	37.4		40.6		41.5	
<b>NFC1</b>	36	36.8	37.9	39	39.3	41.2
<b>NFC2</b>	37	37.4	39.5	39.9	40.9	42.6
<b>NFC3</b>	36.7	37.8	38.6	40.2	40.9	41.5
<b>NFC5</b>	37.4	38.6	40.2	40.6	42.2	41.05
<b>NFC10</b>	37	38.3	39.6	40.5	40.3	41.8

## 5.5.4 Cold crystallization investigations

### 5.5.4.1 Atmospheric DSC results

The degrees of crystallinity of processed PLA, NFC1, and NFC3 after 30 min cold crystallization at 128, 116, and 108 °C under atmospheric pressure are summarized in **Table 5-10** (left part). It should be mentioned again that the isothermal temperatures in the DSC test are the  $T_{sat}$  of HPDSC or foaming tests. At the isothermal temperature of 108 °C, PLA and NFC1 are with the same degree of crystallinity. The crystallinity decreased by increasing the PBT NFs content to 3 wt% (NFC3), which attributed to the opposite effects of PBT NFs on crystallinity. While PBT NFs act as nucleating sites, reducing the PLA chains' mobility by the 3D network of PBT NFs inhibits the chains to join the lamellae. However, the latter effect declined by increasing the isothermal temperature. Indeed, increasing the isothermal temperature to 116 °C compensated the low chain

dynamics; thus, similar values were obtained for the crystallinity in processed PLA, NFC1, and NFC3. The isothermal temperature of 128 °C is within the cold crystallization temperature range of PLA, while it is in the melting temperature range of the NFCs because the cold crystallization peak of PLA in the presence of PBT NFs shifted to the lower temperatures of more than 20 °C (as explained in detail in previous work <sup>226</sup>). Therefore, the degree of crystallinity after 30 min cold crystallization at 128 °C is obtained only for PLA, which is slightly higher than those obtained at lower temperatures, whereas the NFC samples remained amorphous.

**Table 5-10.** Degree of crystallinity of processed PLA, NFC1, and NFC3 after 30 min isothermal cold crystallization at different  $T_{\text{sat}}$  under atmospheric pressure and 140 bar  $\text{CO}_2$  pressure.

$T_{\text{sat}}$	Atmospheric pressure, $\text{N}_2$ purging			140 bar $\text{scCO}_2$ pressure		
	128 °C	116 °C	108 °C	128 °C	116 °C	108 °C
PLA	33.5	32.4	30.2	-	24.5	33.3
NFC1	-	31.3	30.2	-	24.2	34.1
NFC3	-	29.7	27.6	-	22.6	30

**Figure 5-28** represents the crystalline phase morphology of processed PLA and NFC1 after 30 min cold crystallization at 108 and 116 °C. The fine fragmentary spherulitic morphology of the crystalline phase in processed PLA at 108 °C (**Figure 5-28A**) has been more completed at 116 °C (Figure 6B). The nanohybrid shish-kebab superstructures of crystalline PLA around PBT nanofibrils are clearly visible in NFC1 samples cold crystallized at both  $T_{\text{sat}}$  (Figure 6C1-C3 and D1-D3). In contrast to the morphology of melt-crystallized NFCs, which was studied in our previous study <sup>81</sup>, the crystallite morphology of NFCs evolved through cold crystallization is not notably affected by the isothermal temperature. In other words, increasing the kebabs' length and the interlocking is poorly developed by increasing the  $T_{\text{sat}}$ . This is attributed to the strong nucleation of NFCs through cold crystallization. Once the nucleation heavily engages the crystallization capability of PLA, the nuclei faced with limited growth either at higher chain dynamics (higher  $T_{\text{sat}}$ ). The saturation temperature of 128 °C would lead to the observation of larger separated spherulites in processed PLA. However, 128 °C is in the melting temperature range of NFCs, and thus no crystallinity in NFCs is expected.



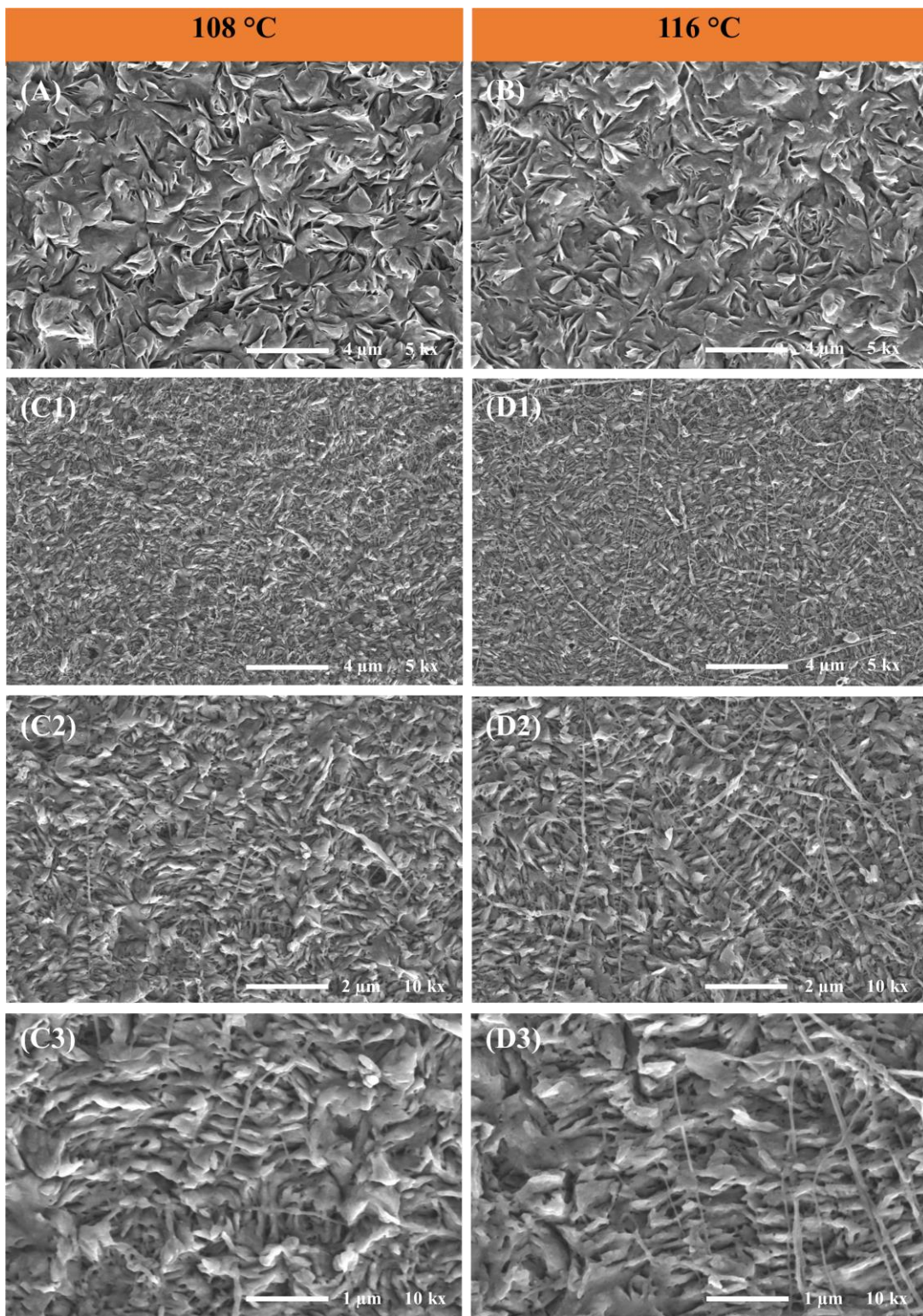


**Figure 5-28.** (A) and (B) crystal morphology of processed PLA at  $T_{\text{sat}}$  of 108 and 116 °C, respectively. (C1)-(C3). Crystal morphology of NFC1 at  $T_{\text{sat}}$  of 108 °C at different magnifications. (D1)-(D3) Crystal morphology of NFC1 at  $T_{\text{sat}}$  of 116 °C at different magnifications.

#### 5.5.4.2 High-pressure DSC results

High-pressure DSC tests were performed to estimate the crystallinity of processed PLA, NFC1, and NFC3 under the three different foaming conditions based on the protocol presented in **Figure 4-10**. All the samples were firstly cold crystallized for 3 minutes at the relevant  $T_{\text{sat}}$  and atmospheric pressure, then the  $\text{scCO}_2$  was applied. The heat flow curves recorded for heating runs after 30 min saturation at 128 °C and 140 bar  $\text{scCO}_2$  pressure showed no melting peaks for PLA or NFCs. **Figure 5-29** shows the HP-DSC results presenting the melting peak of the samples after 30 min saturation at 108 and 116 °C under 140 bar  $\text{scCO}_2$  pressure. All HP-DSC curves show a double peak melting behavior, and the thermal stability of the crystals increased through increasing the PBT NF content and  $T_{\text{sat}}$ . The areas under the melting peaks are much more prominent for the samples crystallized at 108 °C compared to the crystallized samples at 116 °C.

The crystallinity in PLA, NFC1, and NFC3 at different  $T_{\text{sat}}$  under 140 bar  $\text{scCO}_2$  pressure are listed in **Table 5-10** (right side). By comparing these values with the degree of crystallinity at similar  $T_{\text{sat}}$  but atmospheric pressure, the effect of  $\text{scCO}_2$  pressure can be clearly seen. At 116 °C, the plasticization effect of  $\text{scCO}_2$  hindered the crystallization of the samples. Considering the high crystallization rate in NFC1 and NFC3, the plasticization effect also dissolved some of the crystals that were developed during the 3 min sampling time. However, crystallinity survived significantly (22.6-24.5 %). On the contrary, at 108 °C, the diffusion of  $\text{scCO}_2$  increased the chain dynamic of PLA molecules and led to a slight increase in the degree of crystallinity compared to the crystallinity developed at atmospheric pressure. Accordingly, the crystallinity was strongly dependent on the temperature and slightly affected by the pressure. At foaming conditions (II) and (III), in which the pressure of  $\text{scCO}_2$  is 40 bar higher than the applied pressure in the HP-DSC measurements, it is predictable that at least 50 % of the crystallinity measured in HP-DSC will be preserved.

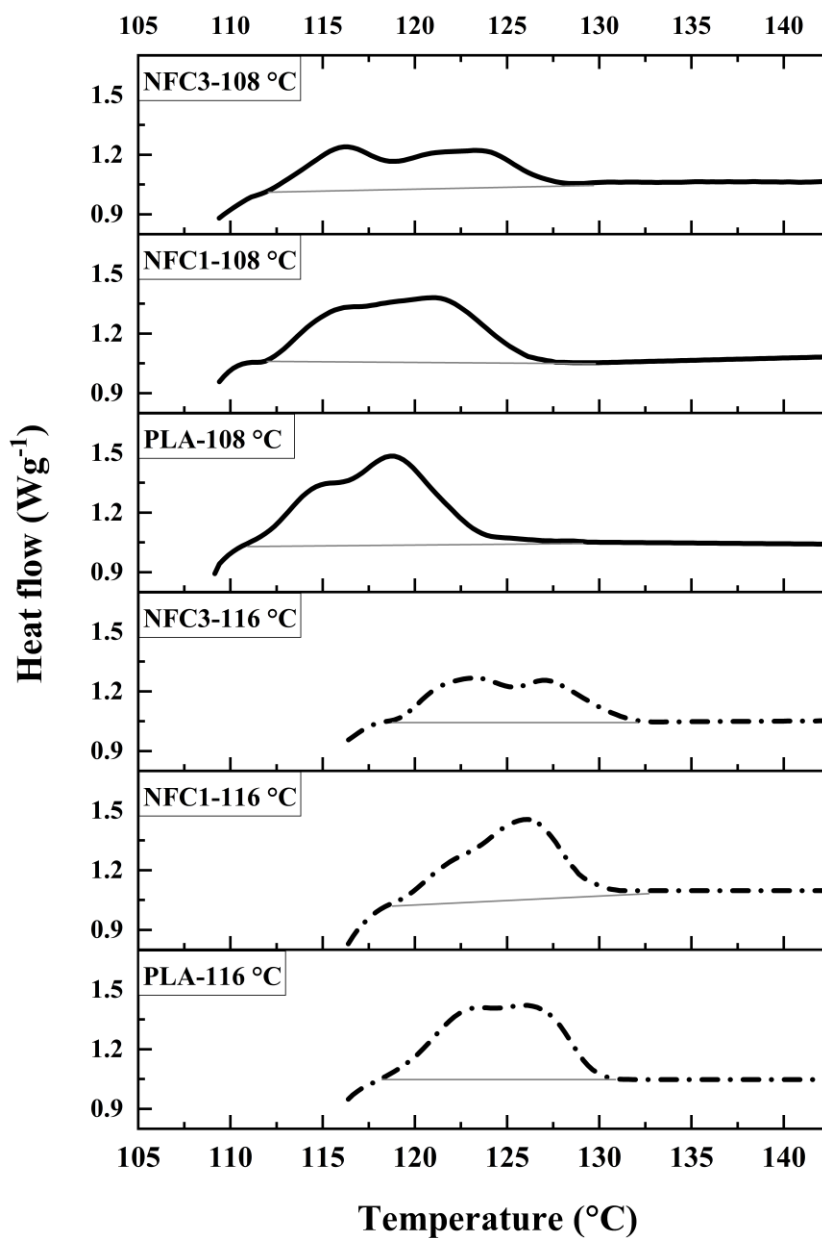


**Figure 5-29.** HP-DSC thermographs of processed PLA, NFC1, and NFC3 under 140 bar  $\text{scCO}_2$  pressure. The solid line graphs were obtained at the saturation temperature of  $108^{\circ}\text{C}$ , and the dash-dot graphs were obtained at the saturation temperature of  $116^{\circ}\text{C}$ .

## 5.6 Thermo-mechanical properties of crystalline NFCs

The thermal instability of PLA has been known as one of the most important limitations for PLA's application. Dynamic mechanical thermal analysis (DMTA) was performed to evaluate the NHSKs network's effect on the poor thermal stability of PLA. **Figure 5-30** shows the temperature dependence of dynamic storage modulus ( $E'$ ) of processed PLA and NFCs after isothermal melt crystallization of the samples at 100 °C for 10 minutes. Since the crystallization rate of PLA has been enhanced considerably by the PBT NFs, the annealed NFC samples are highly crystalline. The storage modulus of the NFCs increased in the whole temperature range compared to processed PLA. The first decrease in  $E'$  corresponded to the dynamic  $T_g$ , which changed from 56 °C for processed PLA to the temperature range of 59 to 61 °C for NFC1 and NFC2, NFC3, and NFC5. Although the  $T_g$  of PBT is close to that of PLA the increase in  $T_g$  of NFCs is more than the amount calculated based on mixture law. This can be attributed to the restricted PLA chains mobility either in the amorphous fraction nearby the high aspect ratio PBT NFs or in the rigid amorphous fraction adjacent to the crystalline phase <sup>257</sup>.

The storage modulus of NFCs at low temperatures increased by increasing the PBT NF content, which is inserted in **Figure 5-30** on a linear scale. By increasing the PBT NF content, the crystallinity slightly varies between 36-37.4 %; therefore, the increase in the storage modulus can not be due to the degree of crystallinity. Indeed, the load transfer to the nanofibrillar network through kebabs or transcrystalline structure is responsible for the increase in the storage modulus at temperatures lower than the  $T_g$  of PLA. After the  $T_g$  of PLA, there is a sharp fall in  $E'$  on passing through the  $T_g$  in the case of processed PLA. However, the level of  $E'$  drop for NFCs is considerably smaller, and even at temperatures much higher than the  $T_g$  of PBT (temperatures up to 120 °C), the modulus of the NFCs is still comparable to that of PP, which is widely used in various industrial applications <sup>275</sup>. The NHSK superstructure established on the 3D nanofibrillar network acted as a physical crosslinking agent, resulting in improved heat resistance.

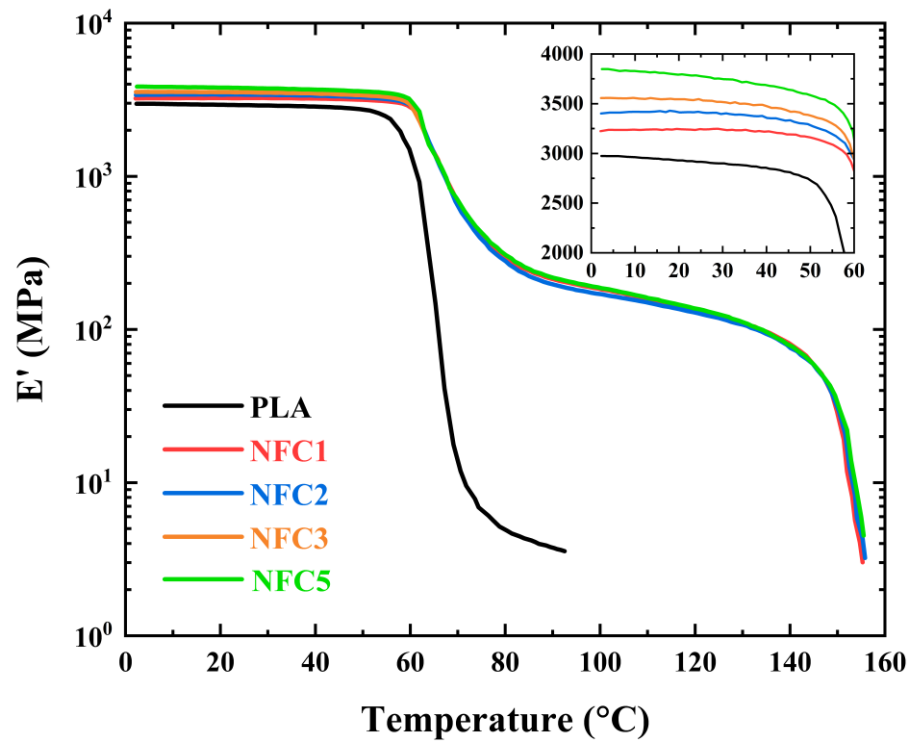


**Figure 5-30.** Variation of dynamic storage modulus with temperature for processed PLA and NFCs after 10 minutes annealing at 100  $^{\circ}\text{C}$ ; in stretching mode and frequency of 1 Hz.

## 5.7 Mechanical reinforcement by nanofibrils and NHSK superstructures

In order to find out the effect of random distributed PBT nanofibrils on the mechanical properties of PLA, the tensile test measurements were implemented for the processed PLA and NFCs containing 1, 2, and 3 wt% PBT NFs. **Figure 5-31A** shows the typical stress–strain curves of the amorphous dogbone specimens prepared by compression molding and fast cooling. The mean and standard deviations of the mechanical properties are summarized in **Table 5-11**. Although the mechanical behaviors of the NFCs are close to each other, a maximum in toughness and elongation at break was observable at 2 wt% of PBT NFs. The brittle mechanical behavior of PLA with average elongation at break of 3 % has been improved to 6.8 % in NFC2 with a slight increase (about 12 %) in the yield stress simultaneously. The tensile modulus and tensile strength of the NFCs are shown to be similar to those of PLA. In other words, the PBT nanofibrils network in the amorphous state of PLA branched between the short PLA chains, which results in strain-softening. The strain-softening leads to an increase in toughness of about 280 %, which could be explained by energy dissipation due to slippage at the interface of the two components.

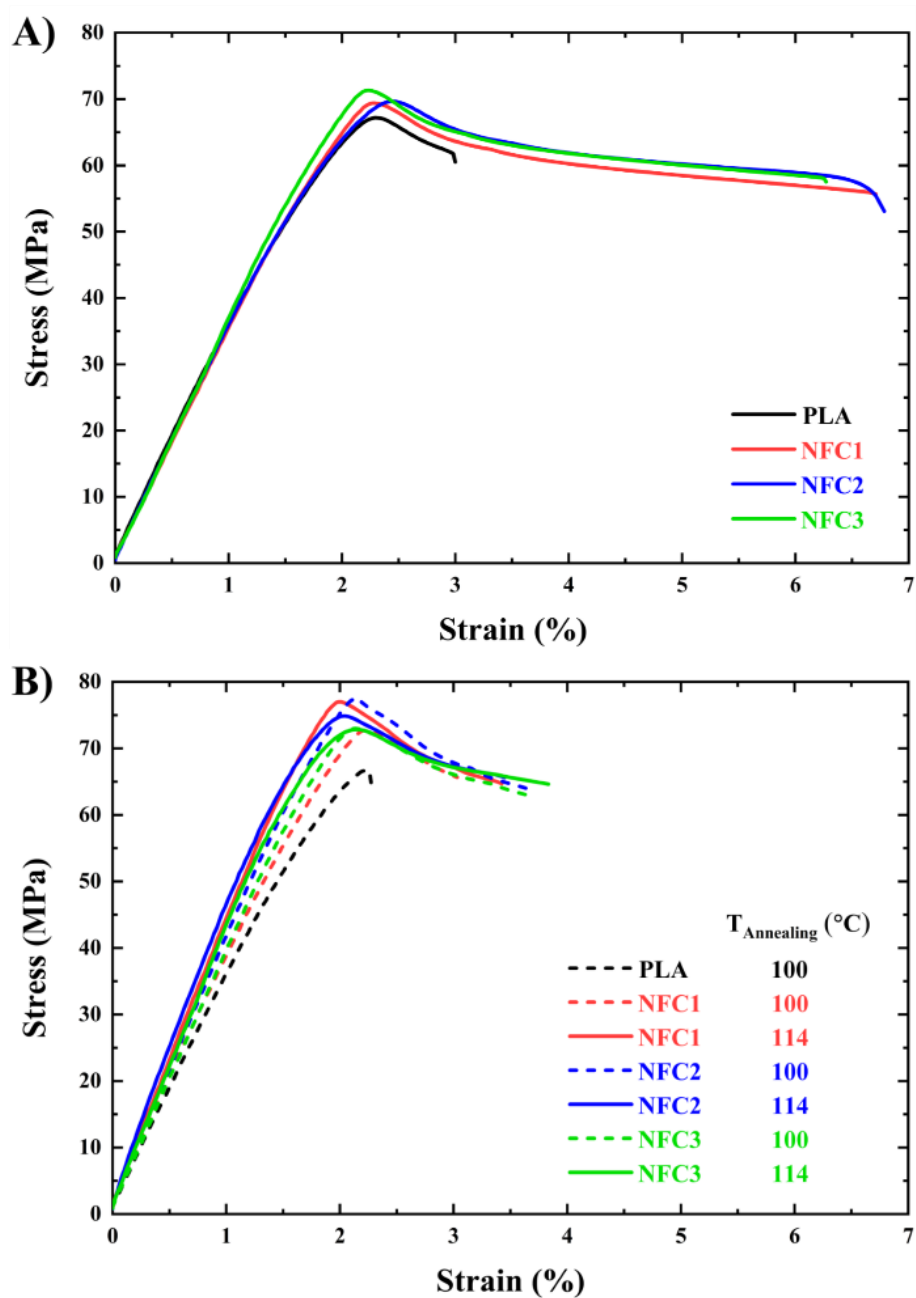


**Figure 5-31.** The representative stress-strain curves of processed PLA and NFCs; (A) all amorphous samples, (B) all samples contain 20 % crystallinity due to annealing at 100 and 114 °C.

**Table 5-11.** Tensile modulus (E), elongation at break ( $\epsilon_b$ ), yield stress ( $\sigma_y$ ), stress at break ( $\sigma_b$ ) and toughness values for amorphous processed PLA and NFCs at room temperature and cross-head speed of 50 mm/min.

	E (MPa)	$\epsilon_b$ (%)	$\sigma_y$ (MPa)	$\sigma_b$ (MPa)	Toughness (kJ.m <sup>-3</sup> )
<b>PLA</b>	3500 ± 100	3 ± 0.5	65.3 ± 3	58.6 ± 3	1300.1 ± 150
<b>NFC1</b>	3530 ± 125	6.4 ± 0.7	70.6 ± 4	57.3 ± 4	3380.8 ± 220
<b>NFC2</b>	3600 ± 110	6.8 ± 0.4	72.2 ± 3	56 ± 6	3520.8 ± 120
<b>NFC3</b>	3560 ± 130	5.8 ± 0.5	74.1 ± 4	57.8 ± 5	3240 ± 180

The mechanical properties of semicrystalline polymers strongly depend on crystallinity, crystal forms, and crystal morphology. Since the contribution of crystallinity to the mechanical properties of PLA has been reported to be much more efficient than that of additives<sup>25</sup>, the next concern is to reveal the bulky performance of PLA and NFCs after isothermal melt crystallization. Crystallization evolution with the morphology of NHSKs from quiescent bulk provided the chance of comparing mechanical properties with different kebab lengths. **Figure 5-31B** represents the stress-strain behavior of processed PLA and NFCs annealed at different isothermal temperatures (100 or 114 °C) while containing a constant degree of crystallinity (20 %). The method of controlling the particular amount of crystallinity is described in chapter 4.3.6.2 and measured mechanical properties are presented in **Table 5-12**. Annealing of PLA at 100 °C for 30 minutes resulted in a higher modulus and a lack of yielding point, implying dramatically brittle behavior. Interestingly, the plastic deformation of crystallized NFCs (crystallized at 100 or 114 °C) has been survived with a significant increase in the elastic modulus and yield stress in the crystallized samples at 114 °C. Strain softening and, subsequently, elongation at break of crystalline samples are reduced compared to amorphous samples since the more robust interfaces via kebabs inhibit the slippage. However, the elongation at break of crystalline NFCs is yet more than that of amorphous processed PLA.

The effect of the shish-kebab structure on the reinforcement of the composite has been recognized with two mechanisms<sup>135</sup>: (i) improvement of interfacial bonding between the fibrils and matrix, which transfers the load on the fibrils; and (ii) interlocking of the kebabs, which distribute the load on the strong crystalline phase. The developed NHSK superstructures at 100 °C are not



significantly interlocked, and the borders between shish-kebabs are almost distinguishable (see **Figure 5-18** and **Figure 5-19**). Therefore, at low isothermal levels, the first mechanism is dominant.

The mechanical properties of PLA after annealing at 114 °C are not measured since it needs more than 1 hour of annealing time. Such a long annealing time destroys the mechanical properties. By increasing the isothermal temperature to 114 °C at a constant degree of crystallinity (20 %), the elastic modulus notably increased in all the NFCs. This increase through temperature was more significant for NFC1, indicating the contribution of kebabs' interlocking. Indeed the kebabs' growth would be maximum at the lowest amount of PBT NFs as nucleating sites. The observed improvement for NFC2 could be a combination of both mechanisms. However, in NFC3, the massive number of PBT NFs facilitated nucleation and limited lateral growth. Consequently, in a constant degree of crystallinity, small kebabs can not effectively bind the overlapped fibrils.

Ning et al. reported that mechanical properties of highly crystalline PLLA/CNT nanocomposites with NHSK superstructure, prepared via solution coagulation, improved significantly by the increase in kebabs length<sup>136</sup>. Accordingly, despite numerous attempts that recommended lower annealing temperatures to induce smaller crystals in PLA (which requires fast cooling), higher annealing temperatures are suggested in the present study. As a result, up to 30 % improvement in the storage modulus; 70 % increase in elongation at break could be achieved. This is noteworthy that in the present system, the development of the NHSK superstructure from the bulk is achievable until the temperature of 114 °C, and it transforms to spherulitic at the higher temperature levels as presented before. It is worth mentioning that among the two well-known crystal forms of PLA,  $\alpha$  and disordered  $\alpha$  ( $\alpha'$ ),  $\alpha$  form have shown superior mechanical properties due to higher chain packing<sup>276, 277</sup>. Therefore, increasing the temperature from 100 to 114 °C, besides increasing the kebab length and interlocking, manifested the contribution of packed chains in crystallites.

**Table 5-12.** Tensile modulus (E), elongation at break ( $\epsilon_b$ ), yield stress ( $\sigma_y$ ), stress at break ( $\sigma_b$ ) and toughness values for processed PLA and NFCs at 100 and 114 °C with a degree of crystallinity of 20 %; required annealing time (Ann.) for each sample at the two temperatures. The tests were run at room temperature and cross-head speed of 50 mm/min.

**Samples were annealed at 100 °C. All samples include 20 % crystallinity.**

	E (MPa)	$\epsilon_b$ (%)	$\sigma_y$ (MPa)	$\sigma_b$ (MPa)	Toughness (kJ.m <sup>-3</sup> )	Ann.(min)
<b>PLA</b>	3620 ± 100	2.2 ± 0.5	66 ± 3	60.8 ± 2	810.8 ± 150	20
<b>NFC1</b>	3940 ± 120	3.3 ± 0.5	74 ± 5	64.3 ± 3	1340.2 ± 200	3
<b>NFC2</b>	4200 ± 80	3.6 ± 0.5	79 ± 8	64.3 ± 4	1840.1 ± 120	2.5
<b>NFC3</b>	4100 ± 100	3.2 ± 0.5	73 ± 4	68 ± 5	174.20 ± 230	1.3

**Samples were annealed at 114 °C. All samples include 20 % crystallinity.**

<b>NFC1</b>	4500 ± 130	3.5 ± 0.5	78 ± 5	63.1 ± 4	1820.6 ± 150	5
<b>NFC2</b>	4600 ± 110	3.6 ± 0.5	75 ± 8	65.5 ± 5	1860.2 ± 180	4
<b>NFC3</b>	4280 ± 120	3.8 ± 0.5	73 ± 7	65.1 ± 3	2040 ± 250	3

## 5.8 Rheological behavior of nanocomposites

### 5.8.1 Shear rheology of NFCs

In order to characterize the microstructure adopted by PBT NFs within the PLA matrix, the melt rheology response of processed PLA, PLA/PBAT blends, and NFCs are studied in frequency mode. Time sweep tests under an N<sub>2</sub> atmosphere at 190 °C and frequency ( $\omega$ ) of 10 rad/s revealed that the degradation of PLA is not negligible after 15 minutes. Therefore, the frequency range was limited to 200 rad/s to reduce the measuring time and PLA's degradation. **Figure 5-32** represents the linear viscoelastic properties of the samples at 190 °C, in which the PLA matrix is melted while PBT NFs are preserved. At low frequencies (long time scales), the typical relaxation behavior of polymers was observed for processed PLA, PLA/PBT1, and PLA/PBT3 blends ( $G' \sim \omega^2$ ,  $G'' \sim \omega$ ), which was changed to a terminal response ( $G' \sim \omega$ ,  $G'' \sim \omega$ ) for PLA/PBT5 blend in **Figure 5-32A**. The change of pattern is attributed to the mobility restriction of the PLA chains (slower relaxation) in the vicinity of the solid PBT droplets. Impressively, the storage modulus ( $G'$ ) of NFC1 increases significantly (3 orders of magnitude) at low frequencies at only 1 wt% PBT NFs, and presented a non-terminal response. **Figure 5-32B** compares the frequency dependence of  $G'$  and  $G''$  for the PLA/PBT3 blend and NFC3, exhibiting two crossover frequencies for NFC3 at  $\omega$  of  $4 \times 10^{-3}$  and 200 rad/s. At low frequencies,  $G'$  becomes more significant than  $G''$  and independent of frequency, which is characteristic of a solid-like behavior. The entanglements between the high aspect ratio nanofibrils; and the physical interactions of polymer chains with the huge interface of PBT NFs contributed to such an increase in the melt elasticity, characterized by  $G'$ , of the nanocomposites compared to the blends. After the plateau, at intermediate frequencies, the interplay of the PBT nanofibrillar network with polymer chains results in a more dissipative but non-terminal response.

The predominantly viscous response of all the blends was confirmed according to  $\tan \delta \gg 1$  at low frequencies (**Figure 5-33A**). At higher frequencies, the entanglements of the molecular chains can be the reason for the increase in the melt elasticity of processed PLA and the blends, where  $G'$  was less dependent on the frequency and  $\tan \delta$  was about 1. The effect of morphological change in the PBT component (from spherical to nanofibrillar) on the elasticity of the compounds is well pronounced in the declining trend of loss tangent. The semi-logarithmic plots of the phase angle ( $\delta$ ) versus complex shear modulus ( $G^*$ ) (Van Gorp-Palmen plot) of the blends and NFCs are presented in **Figure 5-33B**. Phase angles of about 90° were found for all PLA/PBT blends, implying the dominance of the viscous flow. A dramatic increase in the melt elasticity of the NFCs

was confirmed by a dramatic reduction in the values of phase angles when lowering  $G^*$  above some critical values.

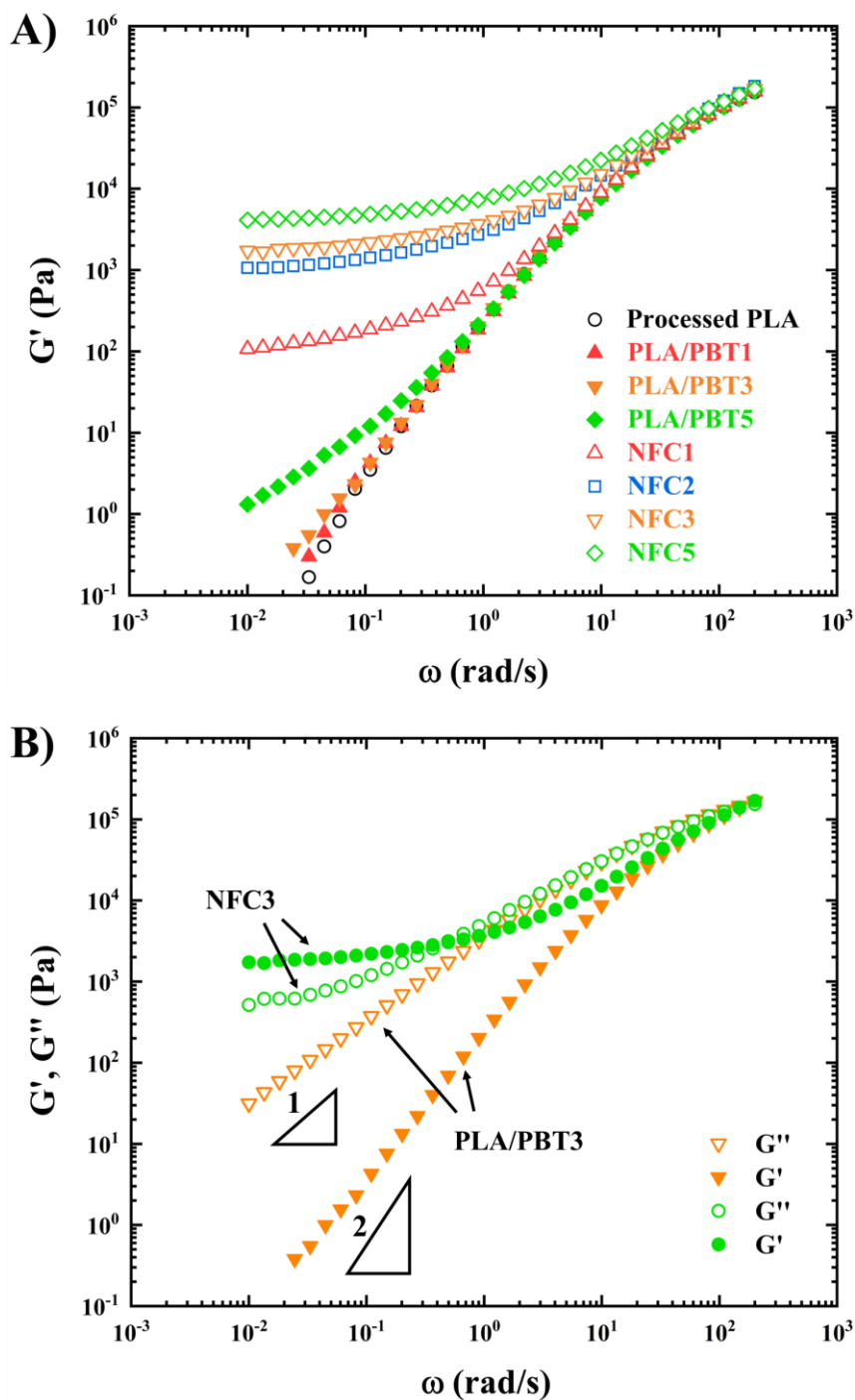


**Figure 5-32.** Linear viscoelastic behavior of processed PLA, PLA/PBT blends, and NFCs at 190 °C and amplitude of 1 %.

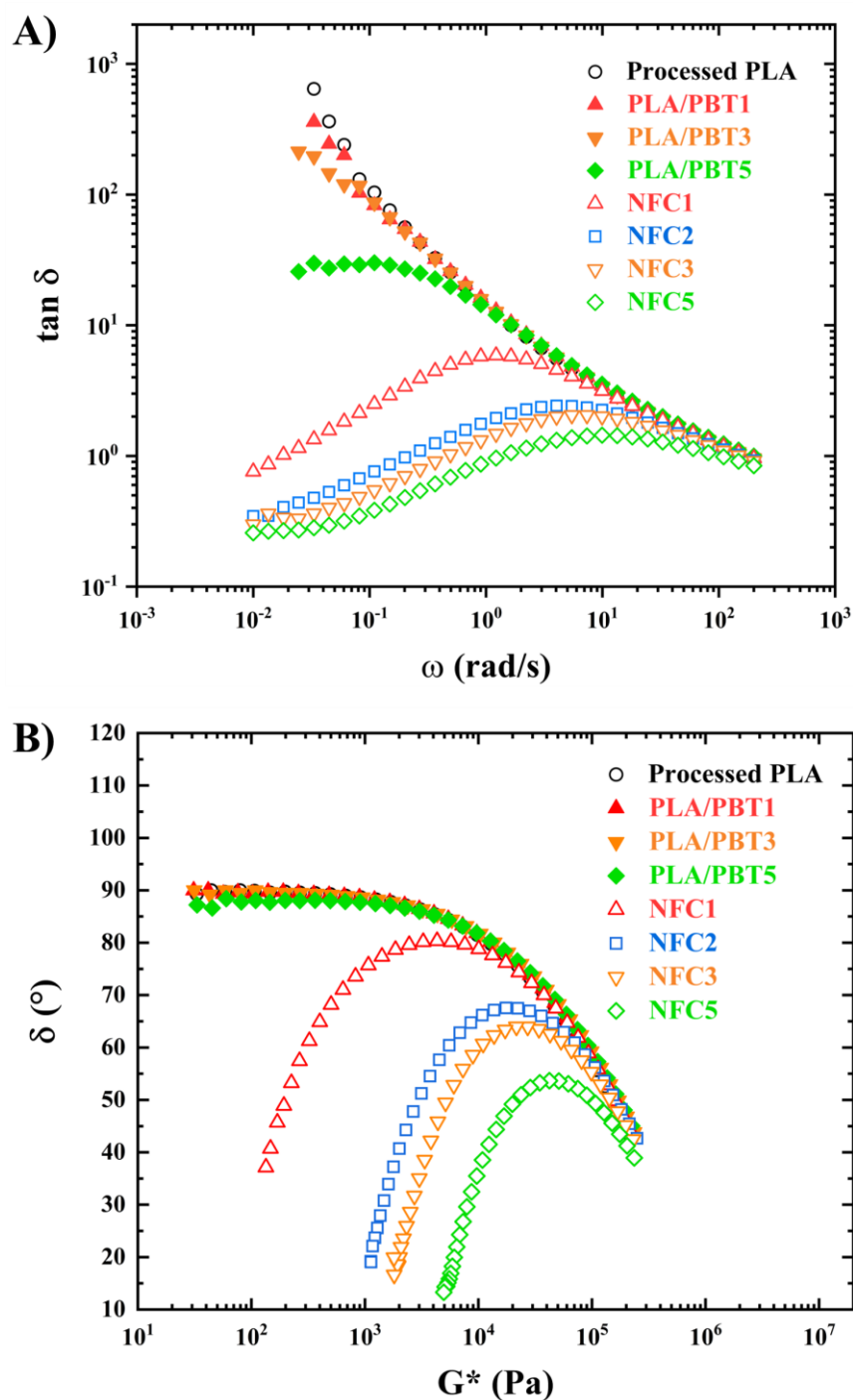


**Figure 5-33.** Damping factor vs. frequency and (B) Van Gorp-Palmen plots of processed PLA, PLA/PBT blends, and NFCs at 190 °C and amplitude of 1 %.

The physical gelation or rheological percolation that is a typical characteristic of composites containing high aspect ratio fillers was calculated based on the Winter-Chambon criterion. The gel point can be depicted at a PBT NFs content of about 0.7 wt%, at which the loss tangent lines vs. PBT NF content at different frequencies intersect (**Figure 5-34**).

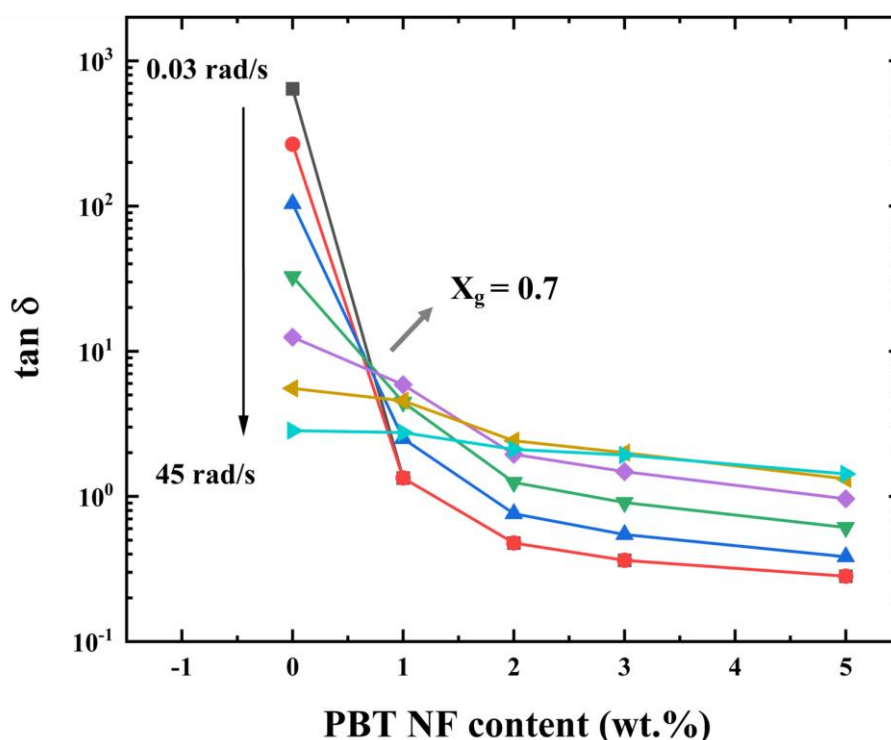


**Figure 5-34.** Loss tangent versus the nanofibril content at frequencies ranging from 0.03 to 45 rad/s. Each line represents one frequency for different PBT NF content. Loss tangent is independent of the frequency (where the lines intersect) at the gel point.

It is worth mentioning that the dynamic shear rheology studies of PLA/C20A nanocomposites and PLA alloys nanocomposites have been extensively studied <sup>278</sup>; therefore, reproducing the data is avoided.

### 5.8.2 Elongational rheology of the nanocomposites

Linear PLA possesses low melt elasticity and low melt strength, which are disadvantageous for its foamability, lead to cell rupture and coalescence during cell growth, resulting in inhomogeneous cell morphology and a low foam expansion <sup>279</sup>. **Figure 5-35A-C** illustrates the uniaxial extensional viscosity,  $\eta_E^+$ , versus time for processed PLA, NFC1 and NFC3 at different extensional strain rates,  $\dot{\epsilon}$ . Linear shear viscosity of the samples was also provided to predict the linear extensional viscosity given by  $\eta_E^+ = 3\eta^+$ . Thereby  $\eta^+$  is the growth curve of shear viscosity in the linear viscoelastic region obtained from the start-up test in a steady shear flow at a strain rate of 0.001 s<sup>-1</sup>. The deviation of the measured elongational viscosities from this envelope is a measure of strain-hardening behavior. As expected, PLA had a very low elongational viscosity and negligible strain hardening behavior at all strain rates.

It is shown in **Figure 5-35** that the inclusion of 1 and 3 wt% of PBT NFs led to significant improvements in the elongational characteristics of the PLA melt. Strong strain hardening effects (more than 2 orders of magnitude increase in the elongational viscosity) were observed in NFC1 and NFC3, which suggested an increase in the relaxation times of the PLA molecules. The deformability of the PLA melt was also significantly improved, especially at a strain rate of  $0.01 \text{ s}^{-1}$ . The formation of a 3D network of deformable and well-dispersed PBT NFs, which was confirmed by the shear viscosity measurements, was responsible for the improved elongational behavior of PLA in the melt state. Similar improvements in elongational viscosity were observed for NFC5 and NFC10 (not presented here). The improvements in the rheological properties of the PLA melt containing PBT NFs (enhanced melt elasticity and strain hardening), promise improvements in the foamability of these NFCs.

**Figure 5-36** shows the elongational viscosity results of PLA/PBT2/C20A1.5 at different strain rates. Well-dispersed nanoclay, in association with the consistent PBT droplets, has improved the elongation viscosity of the sample by less than one order of magnitude. Although the formation of a 3D network of nanoclay platelets is not probable at such a low Cloisite20A concentration (see **Figure 5-13B1, B2**), proper interactions of PLA chains in the melt state with solid nanoclay platelets and PBT solid drops can explain the slight strain hardening behavior of the samples.

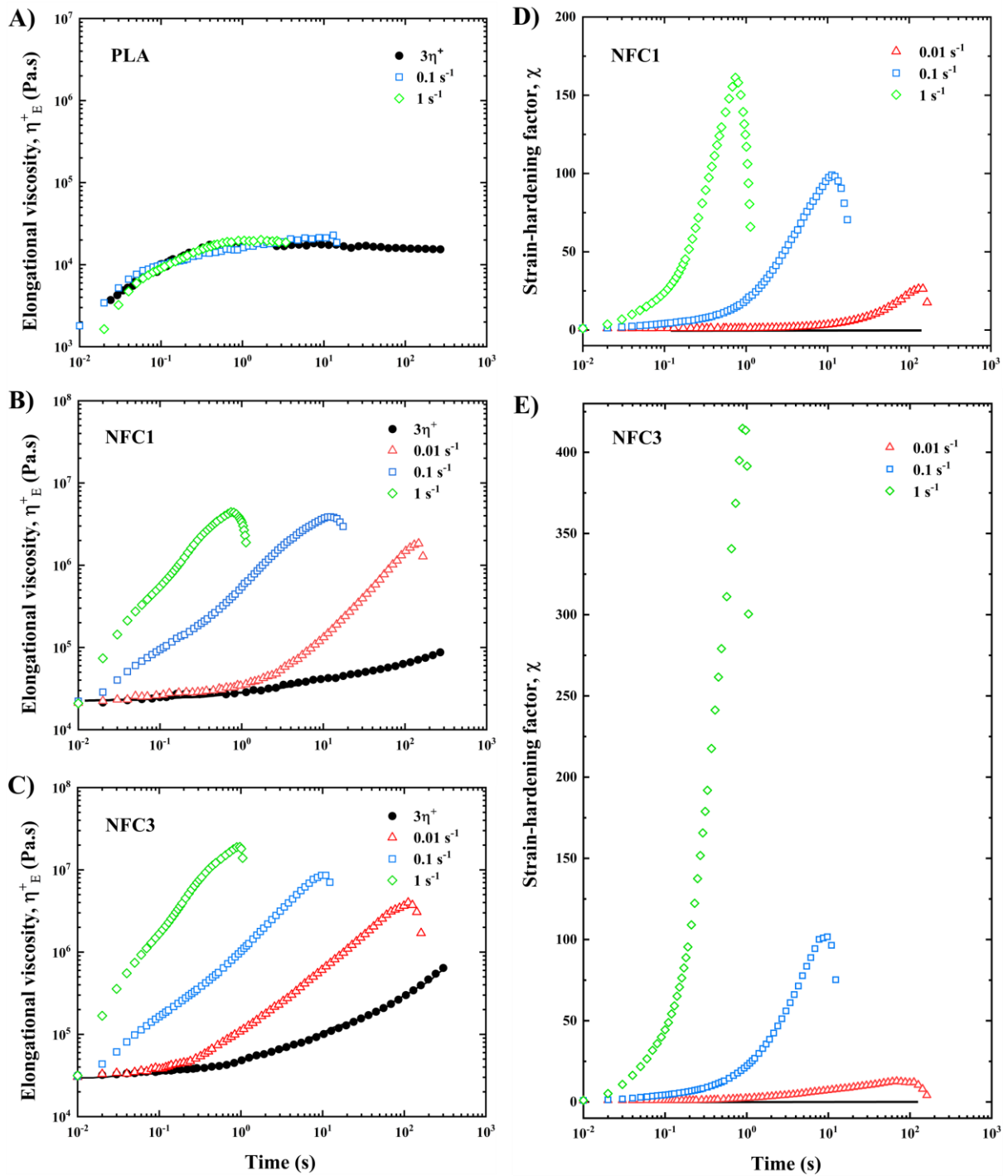


**Figure 5-35.** Uniaxial elongational responses of (A) processed PLA, (B) NFC1, and (C) NFC3 at strain rates of 0.01, 0.1, and  $1 \text{ s}^{-1}$  and temperature of  $170 \text{ }^\circ\text{C}$ . The solid circles for each sample represent the  $3\eta^+(t)$  where  $\eta^+(t)$  is the growth curve of shear viscosity in the linear region obtained from startup shear experiments at a strain rate of  $0.001 \text{ s}^{-1}$  and a temperature of  $170 \text{ }^\circ\text{C}$ . Strain hardening factor,  $\chi$ , as a function of time at different extensional strain rates for (D) NFC1 and (E) NFC3 determined using **Equation ( 2-10 )**.



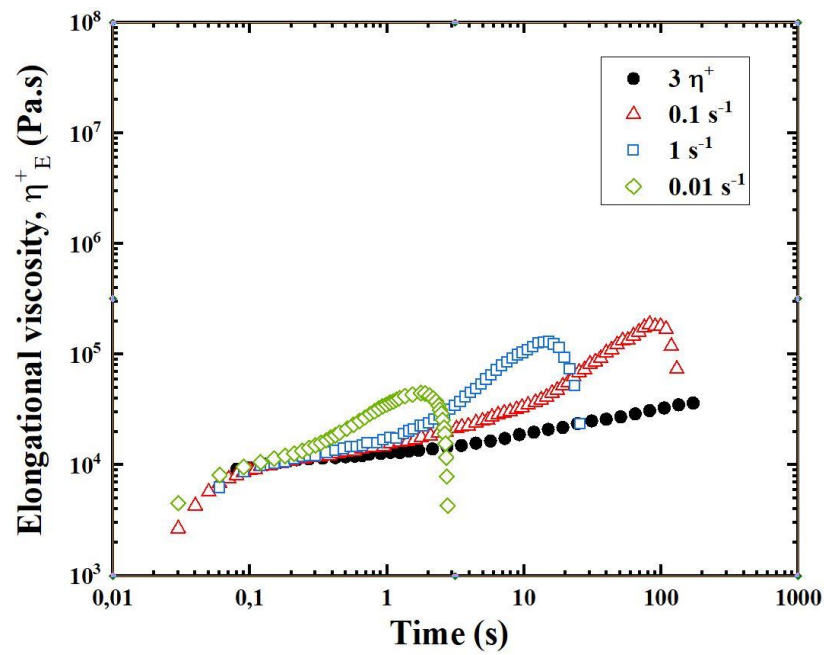


**Figure 5-36.** Uniaxial elongational responses of PLA/PBT2/C20A1.5 at strain rates of 0.01, 0.1, and  $1 \text{ s}^{-1}$  and temperature of  $170 \text{ }^\circ\text{C}$ . The solid circles represent the  $3\eta^+(t)$  where  $\eta^+(t)$  is the growth curve of shear viscosity in the linear region obtained from startup shear experiments at a strain rate of  $0.001 \text{ s}^{-1}$  and a temperature of  $170 \text{ }^\circ\text{C}$ .

## 5.9 Foam results

In this chapter, the foam results of PLA, NFCs, and PLA/PBT/clay nanocomposites are discussed at three different foaming conditions with a constant saturating time of 30 minutes. Two scCO<sub>2</sub> pressures (140 bar and 180 bar) were chosen to follow the effect of saturating pressure. For every scCO<sub>2</sub> pressure, the temperature was swept to obtain the optimum temperature, which resulted in the lowest foam density. Accordingly, condition (I) was determined at 140 bar scCO<sub>2</sub> and 128 °C; condition (II) was determined at 180 bar scCO<sub>2</sub> pressure and 116 °C. Condition (III) was again at 180 bar scCO<sub>2</sub> pressure, but the temperature of 108 °C was selected to follow the effect of higher crystallinity content in fibrillar samples.

Representative SEM micrographs of cryogenically fractured surfaces of foam samples saturated under condition (I) are shown in **Figure 5-37**. **Figure 5-37A1** and **A2** demonstrate the processed PLA foam morphology with big cells and thick walls. The average cell-size of 75 μm, cell density of  $5 \times 10^6$  cells/cm<sup>3</sup>, and a foam density of 338 kg/m<sup>3</sup> were measured for processed PLA at the mentioned foaming conditions. **Figure 5-37B1-B4** show the foam morphology of NFC1 at different locations and magnifications. It is evident that only 1 wt% of PBT NFs significantly improved the cellular structure with a dramatic reduction in cell-size and a remarkable increase in cell density compared to PLA foams. The observation of improved foam microstructure at low magnifications is impressive; however, at higher magnifications the non-uniform structure and collapsed cells become apparent. Although a bimodal cell-size distribution could be a choice for describing the wide cell-size distribution, reporting the average cell-size and cell density was avoided since the cell borders are not clearly defined. A fine net-like tissue can be seen frequently on the cell walls or instead of them; thus, the samples could be described as partially open-cell foams. The net-like tissue is a sign of material rupture at temperatures higher than T<sub>g</sub> under a 3D stress field. However, the foam density decreased from 338 kg/m<sup>3</sup> for processed PLA to 83 kg/m<sup>3</sup> for NFC1. **Figure 5-38** shows that in contrast to similar studies<sup>25</sup>, increasing the amount of PBT NFs to 3 wt% did not improve the cellular structure. Apart from noticeable non-uniformity in the cell-size, the ruptured walls resulted in an almost open-cell foam, and the net-like tissue mostly replaced the cell walls. Although the 3D physical network of entangled PBT NFs improved the elasticity and melt strength of PLA, it seems that at this foaming condition, the nucleating role of PBT NFs is more important than their role in strengthening the melt. These observations could be attributed to the amorphous state of processed PLA, NFC1, and NFC3 samples at 128 °C and 140 bar scCO<sub>2</sub> pressure (**Table 5-10**). In other words, under the foaming condition (I), the flexible PBT

NFs and also amorphous PLA are both at a temperature much higher than their  $T_g$ ; therefore, they are too soft to prevent cell rupture during foam expansion.

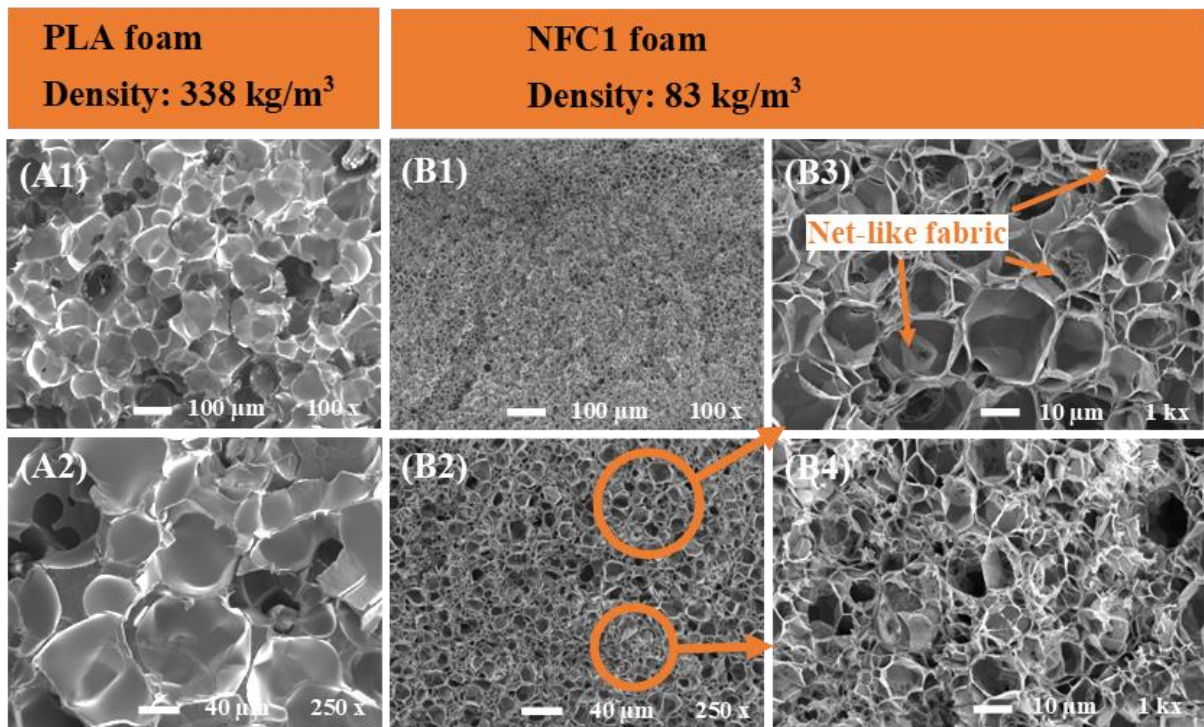


**Figure 5-37.** SEM micrographs of cryogenically fractured surfaces of foam samples saturated at 128 °C and 140 bar (condition (I)). (A1) and (A2) processed PLA foams at different magnifications; (B1-B4) NFC1 foams at different locations and magnifications.

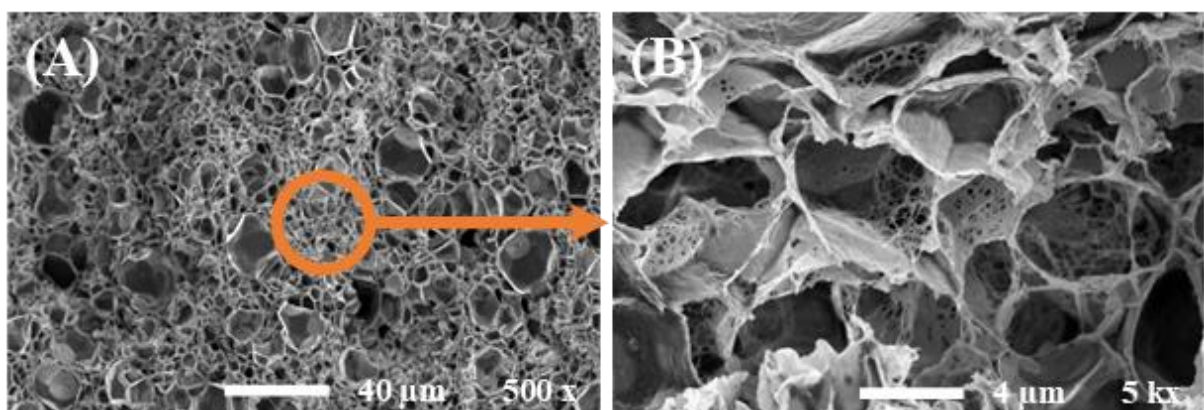


**Figure 5-38.** SEM micrographs of cryogenically fractured surfaces of NFC3 foam samples saturated at 128 °C and scCO<sub>2</sub> pressure of 140 bar (condition (I)).

**Figure 5-39** represents the SEM micrographs of cryogenically fractured surfaces of foam samples using condition (II), meaning prepared at saturation conditions of 116 °C and 180 bar. **Figure 5-39A1** and **A2** obviously show a noticeable increase in cell number and a dramatic decrease in cell size for processed PLA foams compared to the foams prepared under condition (I) in **Figure 5-37A1** and **A2**. The improved foam morphology and decreased foam density to 210 kg/m<sup>3</sup> can be explained as a result of the pressure increase and small crystals formed at the lower  $T_{\text{sat}}$  which were preserved at 180 bar scCO<sub>2</sub> pressure and act as nucleating agents. The effect of increasing the number of nucleated crystallites and reducing their size via cold crystallization on the enhancement of foam morphology has been studied by Ni et al. <sup>280</sup>. However, at higher magnifications (**Figure 5-39A3** and **A4**), the non-uniform cell-size and ruptured structure can be clearly seen. **Figure 5-39B1-B4** show the uniform microcellular structure of superlight NFC1 foams with an average cell-size of 13 μm, cell density of  $1.5 \times 10^9$ , and a foam density of 47 kg/m<sup>3</sup>. Interestingly, the cell walls are consistent, and the net-like fabrics are healed. **Figure 5-39C1-C4** show the cellular morphology of NFC3 foam samples with slightly larger cell-size and less cell density compared to NFC1. Although the cell walls are defined, few bubbles with diameters of about 2 mm were found in the NFC3 foam samples, which makes the foam density not reproducible.

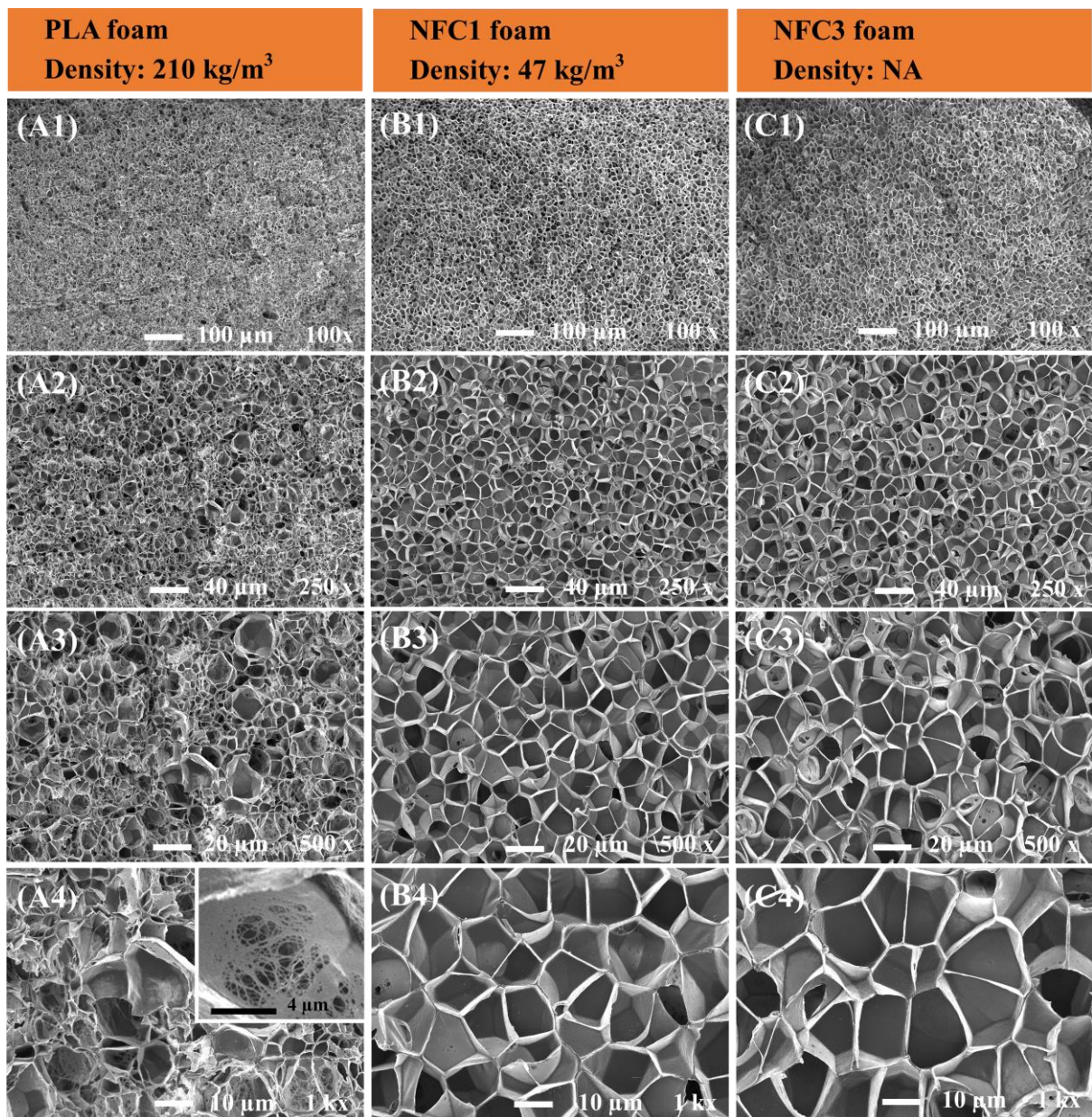


**Figure 5-39.** SEM micrographs of cryogenically fractured surfaces of foam samples saturated at 116 °C and 180 bar (condition (II)). (A1-A4) processed PLA foams at different magnifications; (B1-B4) NFC1 foams at different magnifications; (C1-C4) NFC3 foams at different magnifications. All the white bars have the same length.

To assess the role of the PBT NFs on the foam structure, a thin layer of the amorphous phase of the NFC1 foam samples was etched by hydrolysis. **Figure 5-40A-F** demonstrate the remaining structure after the etching process. Through zooming into the structure, the embedded nanofibrils in the cell walls were revealed. The flexible nanofibrils with rough surfaces in **Figure 5-40C, D** draw attention to the orthogonal patterns on them in **Figure 5-40E, F**. The small discs of crystalline PLA nucleated densely on the PBT NFs and made NHSK superstructures, which were fine and flexible enough (at 116 °C and 180 bar scCO<sub>2</sub>) to incorporate in the cell walls during the expansion step. As discussed in section 3.2, at 116 °C and 140 bar scCO<sub>2</sub> pressure, processed PLA and NFCs are highly crystalline. On the other hand, the SEM observations in **Figure 5-40** confirmed that PLA partially remained crystalline through increasing the scCO<sub>2</sub> pressure up to 180 bar. PLA chain segments partially participated in the cylinders of folded chains growing transverse to the nanofibril axis. The rest of the chain joined the amorphous phase and entangled with the amorphous part of other chains. Eventually, nanodomain PLA kebabs improved the interface of the matrix and PBT NFs; thus, the integrity of the amorphous phase and PBT NFs network was supplied through the crystalline disks. By assuming cell growth as an isostrain condition, the stress would be applied to load-bearing components, i.e., the NHSK superstructures network. Therefore, the net-like tissue, which was due to the ruptured amorphous phase of PLA, did not form. Although the nucleating effect of PBT NFs has been proven in the absence of NHSK superstructure (foaming condition 128 °C and 140 bar scCO<sub>2</sub>), their roughened surface and CO<sub>2</sub> removal from the crystalline phase could have a synergistic effect. Accordingly, the uniform microcellular structure is a result of the enhanced nucleating effect and strain-hardening effect due to the firm interface.

Earlier, nanofibrils bundling and fan-shaped transcrystallinity were discussed when increasing PBT NFs to 3 wt% (see **Figure 5-21**), which can explain the formation of the bubbles in the NFC3 foam samples. The crystallinity of PLA, especially under high scCO<sub>2</sub> pressure, is limited, and the huge number of PBT nanofibrils in NFC3 foam samples remains unpatterned. The fan-shaped transcrystalline phases around PBT NF bundles are much bigger and thus inflexible than NHSK superstructures, resulting in sudden big bubbles during foam expansion.

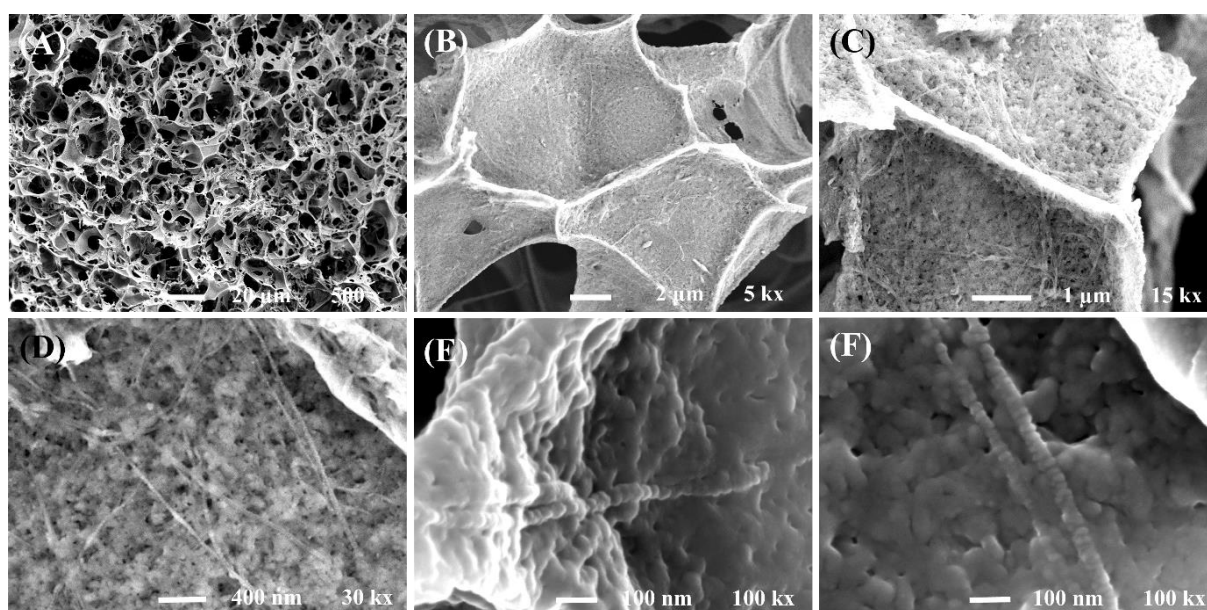


**Figure 5-40.** SEM micrographs of cryogenically fractured and etched surfaces of NFC1 foam samples saturated at 116 °C and 180 bar, (A)-(F) at different magnifications.

**Figure 5-41** presents the cryogenically fractured surface of NFC1 and NFC3 foam samples prepared at foaming condition III (108 °C and 180 bar scCO<sub>2</sub> pressure). **Figure 5-41A1** and B1 were recorded at low magnifications to show the structural uniformity of NFC1 and NFC3 foam samples, respectively. Through zooming into the NFC1 foam morphology in **Figure 5-41A2** and A3 interestingly, a beehive-like frame can be observed and each vessel is filled with an open-cell nanocellular structure. The beehive-like frame is not porous; therefore, it is the crystalline phase of PLA, and its string shape confirms the NHSK morphology of the crystallites. Obviously, the preserved crystallinity of PLA at foaming condition III led to a fine network of randomly oriented NHSK superstructures. This network was yet flexible and changed to a beehive-like frame through the applied thermodynamic-kinematic situation during the depressurization. It is worth mentioning that the thickness of the kebabs is much higher than what was embedded in the cell walls at foaming condition II (**Figure 5-40**). Accordingly, the interconnected nanocellular structure inside each vessel results from the severe expansion of the amorphous phase of PLA. Distinctively, the SEM micrographs of NFC3 foam samples at similar resolutions do not show a beehive-like frame, but clearly, thick crystallite phases placed randomly on the fractured surfaces under investigation (**Figure 5-41B2**). **Figure 5-41B3** presents the simultaneous appearance of (i) NHSK superstructure, (ii) transcrystalline PLA around the bundles of PBT NFs (the thick crystallites), and (iii) closed cell nanocellular morphology of the amorphous phase in the NFC3 foam samples. While the flexible NHSK superstructures strongly acted as foaming nucleating

agents in both samples (NFC1 and NFC3), the rigid fan-shaped transcrystalline phases in NFC3 samples inhibited severe expansion due to depressurization. The lower expansion of the amorphous phase in NFC3 foams led to a foam density of  $612 \text{ kg/m}^3$ , which is higher than the value of  $446 \text{ kg/m}^3$  obtained for NFC1 foams.

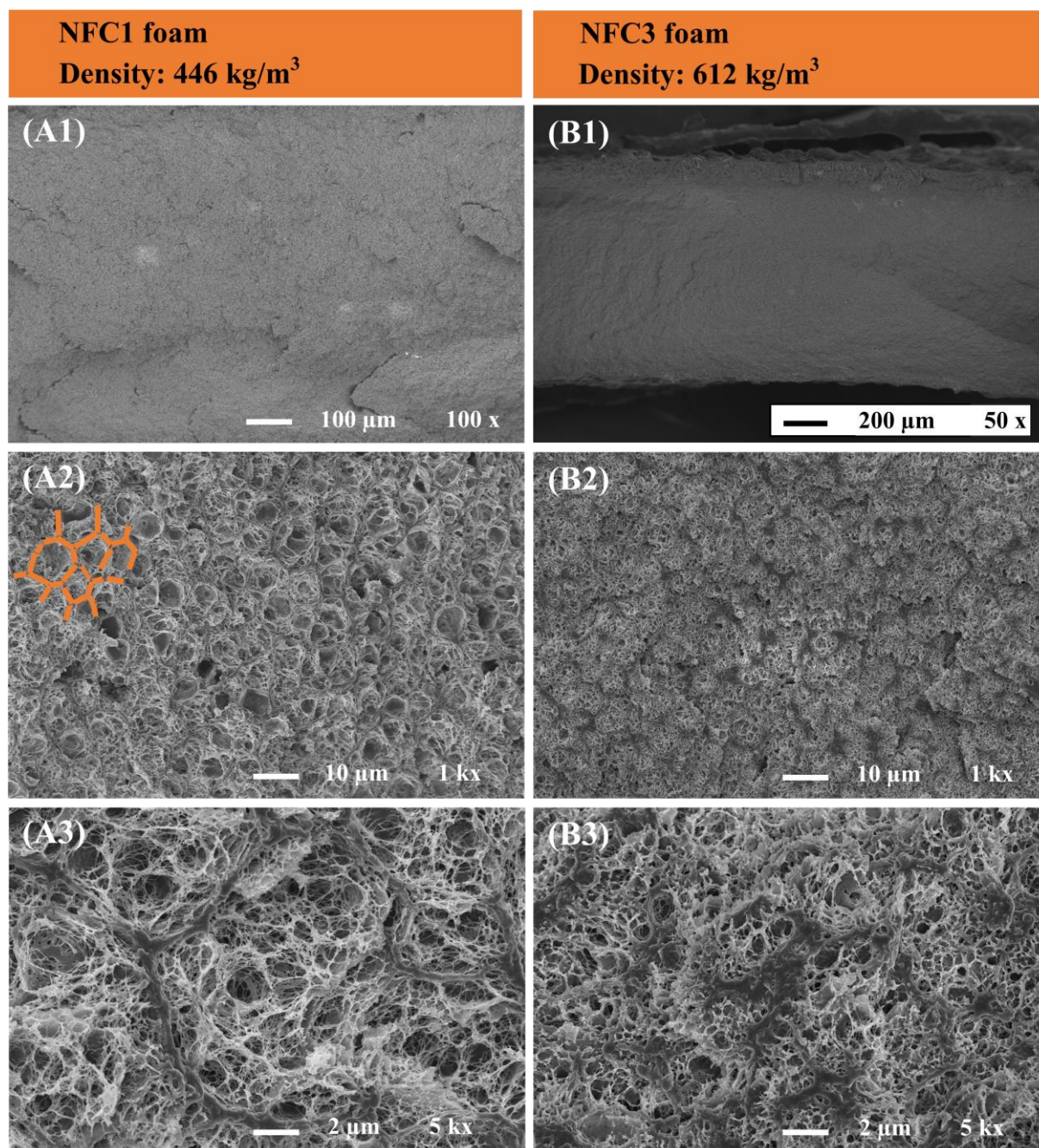


**Figure 5-41.** SEM micrographs of the cryogenically fractured surface of NFCs foam samples saturated at  $108 \text{ }^\circ\text{C}$  and 180 bar  $\text{scCO}_2$  pressure. (A1) – (A3) Open-cell nanocellular structure trapped in beehive-like frame made of NHSK superstructures in uniform NFC1 foam sample. (B1) – (B3) Closed-cell nanocellular structure in NFC3 foam samples.



**Figure 5-42** demonstrates the cryogenically fractured surface of PLA/PBT2/C20A1.5 and PLA/PBT1/C20A1.5 foam samples prepared at foaming condition II (116 °C and 180 bar scCO<sub>2</sub> pressure). Although the elongational viscosity of both samples was slightly improved compared to processed PLA, representing a strain hardening behavior (see **Figure 5-36**), the foam densities increased to 300 and 350 kg/m<sup>3</sup>, respectively. The nucleating effect of nanoclay on PLA has been studied using different foaming processes by other researchers<sup>23</sup>. It can be seen from the SEM images that the nucleated cells of PLA/PBT2/C20A1.5 are more than that of PLA/PBT1/C20A1.5 due to the nucleating effect of submicron solid PBT domains. However, the cell morphology is not uniform, and so many collapsed cells can be observed. Inflexible PBT solid droplets and nanoclay platelets inhibited the nucleated cells in the PLA matrix to expand without rupture in the walls. A similar influence could be considered for the inflexible spherulitic crystalline phase in the absence of any fibrils role as shish. Therefore, batch foaming (solid foaming) of these samples did not represent improvements in their foam properties compared to the neat PLA foams. These findings revealed that not only cell nucleation of polymer and modification of melt elasticity is crucial for improvement in foam properties of a semicrystalline polymer, but also the flexibility of the fillers that can tailor the crystalline phase morphology is determining. It is worth mentioning that an almost similar foam morphology was reported by other researchers<sup>28, 219</sup>.

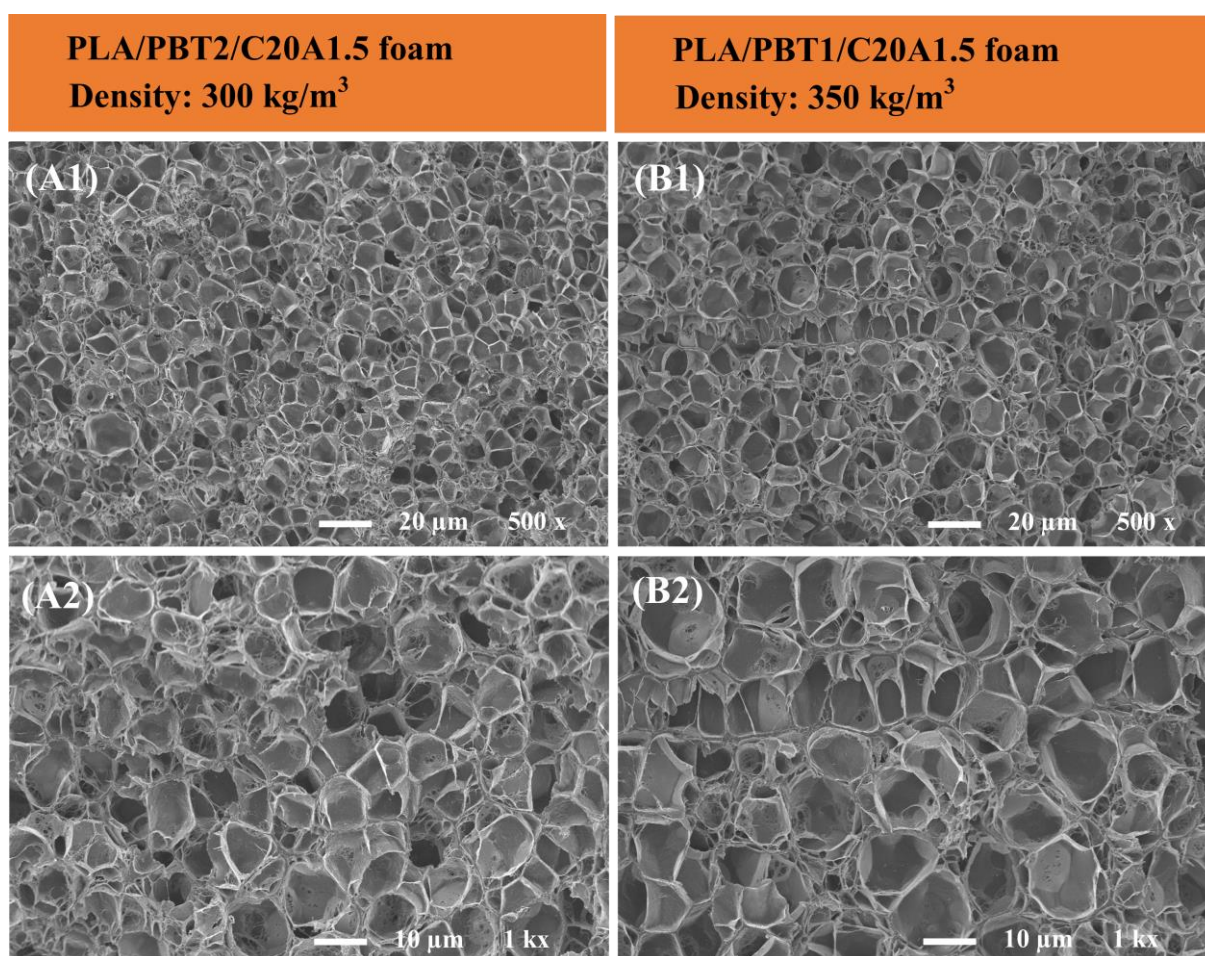


**Figure 5-42.** SEM micrographs of cryogenically fractured surfaces of (A1), (A2) PLA/PBT2/C20A1.5, and (B1), (B2) PLA/PBT1/C20A1.5 foam samples saturated at 116 °C and 180 bar.

## 6 Summary

The final morphology of the immiscible polymer blends has a controlling role in the final properties of the fabrics, therefore the development of morphologies during the blending process has been extensively studied in the past two decades. Melt-spinning process of poly (lactic acid) (PLA)/poly (butylene terephthalate) (PBT) blends containing 1, 3, 5, and 10 wt% of PBT component led to the formation of nanofibrils of the minor phase in the PLA matrix at the optimized processing conditions. The microscopy results showed that the average diameter of the PBT nanofibrils changed from 23 to 51.4 nm due to the varying contents of the PBT, and the aspect ratio of the PBT NFs was over than 500. Observation of ellipsoidal PBT domains oriented along a short die was attributed to a low interfacial tension between the blend constituents and fulfilled melt rheological criteria for fibrillation in a simple shear flow. The stability of the deformed droplets under the shear and elongational flows was studied by comparing the breakup time and residence time in each flow field. It was demonstrated that the deformed droplets (ellipses) with a robust increased interface underwent coalescence through pinch-off in the subsequent elongational flow field and transformed to the nanofibrils with an average diameter comparable to the radius of gyration ( $R_g$ ) of PLA chains.

Although the localization of nanoclay in the PLA matrix was achieved using predefined feeding sequences, the increased matrix elasticity did not improve the drawability of the PBT component in PLA/PBT/nanoclay nanocomposites. This could be attributed to the critical contribution of surface tension between the components in the pinch-off mechanism. The dispersion of nanoclay reduced the matrix polarity, thus reducing steric interactions with the PBT component. Finally, transmission electron microscopy images (TEM) showed that slightly deformed PBT domains were distributed in the PLA/nanoclay nanocomposite.

In the fabricated isotropic in situ nanofibrillar composites (NFCs), random orientation of a 2D nanohybrid shish-kebab (NHSK) superstructure was observed as a result of orthogonal patterning of melt crystallized PLA nanodomains on the PBT NFs surface. The NHSK superstructure established in quiescent bulk through the mechanism of geometric confinement (soft epitaxy) enabled us to tailor the crystalline morphology via annealing temperature. At a constant nanofibril content, increasing the isothermal temperature ( $T_{iso}$ ) up to 114 °C led to an increase in the kebabs' length and interlocking of the adjacent superstructures. A transition to spherulitic crystal morphology was observed due to further temperature increase ( $T_{iso} \geq 117$  °C). The observed transition indicated that at higher  $T_{iso}$ , the fewer raw nuclei, which were initiated

by the soft epitaxy mechanism of PLA chain segments on the PBT NFs at the early stage of nucleation, could conduct self-nucleation and 3D lateral growth. Another transition from the 2D NHSK superstructure to 3D transcrystallinity was observed by increasing the PBT NF content and the nanofibrils bundling. The Avrami model was found to be applicable for interpreting variations of crystallite morphology, crystallization rate, and nucleation mechanisms as a function of PBT NF content and isotherm temperature.

Dynamic mechanical thermal analysis revealed that the NHSK superstructure established on the 3D nanofibrillar network acted as a physical crosslinking agent, resulting in improved heat resistance. The brittle behavior of PLA, which is the main neck for extending its applications, was modified in both amorphous and crystalline states. Tensile test results showed that the tailorable NHSK superstructure via crystallization temperature and PBT NF content significantly affected the mechanical properties of NFCs. Longer interlocked kebabs resulted in a higher tensile modulus, yield strength, strength at break, and strain at break than amorphous PLA.

Dynamic shear rheological studies of the NFCs in the linear viscoelastic region showed that in the presence of only 1 wt% PBT NFs, the storage modulus increased significantly (3 orders of magnitude) at low frequencies; and presented a non-terminal response. A rheologically percolated 3D network of nanofibrils was estimated at a nanofibril content of 0.7 wt% using the Winter-Chambon analysis.

Elongational rheology investigations showed that the inclusion of 1 wt% of PBT NFs caused significant improvements in the PLA's melt strength and strain hardening behavior. Improvements in the rheological properties were attributed to the formation of a three-dimensional network of the entangled PBT NFs. The strain hardening behavior was also observed in PLA/PBT/nanoclay samples, mainly due to strong interactions between the PLA chains and nanoclay platelets. However, nanoclay functioned less effectively than PBT NFs in enhancing the elongational viscosity. This can be due to stress concentration in the matrix by the presence of the platelets.

By comparing the foam density and morphology of PLA and NFCs foams showed that the evolution of cellular structure during the depressurization was strongly dependent on the crystallinity and morphology developed during the saturation time. The NHSK superstructures increased the nanofibrils' roughness, which acted as strong foam nucleating agents, and its random distribution provided uniform morphology of foams. The crystallite morphology of the NFCs at two different foaming conditions contributed to three different structural roles as follows. Embedment of fine flexible NHSK superstructures in the cell walls of the NFC1 resulted in super-light foams with

closed-cell microcellular morphology. In the same sample, at a lower saturation temperature, a thicker yet flexible network of NBSK structures formed a beehive frame during expansion, in which each vessel was filled with interconnected nanocellular foam structures. The formation of rigid transcrystalline PLA phase around the bundles of PBT NFs in NFC3 limited the expansion of highly nucleated samples, thus leading to closed cell nanocellular morphology. Although the nanocellular foams were highly crystalline, relative foam densities of less than 0.5 were achieved, which was attributed to tremendous cell density. Obtaining micro/nanocellular morphology improves the foams' mechanical properties for being used in construction applications. The high percentage crystallinity (providing heat stability) in lightweight PLA nanocellular foams is highly demanded for thermal insulation applications. Polymer foams with large void fractions are required to improve thermal insulation performance because the thermal conductivity of the gas phase is much lower than that of the polymer matrix phase.

Despite the slight strain-hardening behavior observed for PLA/PBT/nanoclay samples and the cell nucleating effect of nanoclay platelets and PBT solid droplets, solid foaming of these samples did not represent improvements in their foam properties compared to the neat PLA foams. The inflexibility of the PBT solid droplets and nanoclay platelets resulted in ruptured cell walls. A similar influence could be considered for the spherulitic crystalline phase. These observations indicate the crucial role of a flexible fibrillar additive with the capability of tailoring the crystalline phase morphology in semicrystalline polymer foam properties.

## 7 Outlook

In the present research, shear rheological studies showed that the rheological percolation threshold of the PBT NFs occurred at 0.7 wt% of the nanofibrils. Therefore, the NFC10 sample is a masterbatch of dispersed nanofibrils in the matrix and can be used in a continuous extrusion foaming process. Considering the cold draw of the PBT NFs during mixing with neat PLA and thus reducing their diameter, the percolation would occur even at lower PBT NF concentrations. Using this approach, the two-step process will change to a one-step process and reduce PLA degradation due to the applied temperature and shear.

Currently, the super toughening of PLA is one of the most important research fields, and different kinds of tougheners and compatibilizers have been developed for this purpose. However, in most investigations with this objective, a dramatic decrease in storage modulus has been frequently reported in exchange for a noticeable increase in elongation at break. The development of a random distributed NHSK superstructure in a toughened system can lead to a super tough system since the crystalline phase increases the modulus without scarifying the deformability. It should be mentioned that as far as the processing temperature does not exceed 200 °C, the nanofibril network and the NHSK superstructure are recyclable. This specification makes the addition of any third component during the next forming process quite possible.

The rheological studies under the scCO<sub>2</sub> pressure in dynamic and/or steady shear flow can obtain useful information about the effect of pressure and shear on the formation of random distributed NHSK superstructures, and thereafter the effect of NHSK superstructure on the melt flow and its viscoelastic properties.

Small-angle X-ray scattering (SAXS) and wide-angle X-ray scattering (WAXS) experiments have been widely used to diagnose the structures in oriented systems. The reported transition of crystallite morphology from the NHSK superstructure to spherulitic in quiescent bulk provides the possibility of extending SAXS applications to explore different crystalline structures in non-oriented polymer composites.

## 8 Bibliography

1. Miller, S. A., Sustainable polymers: opportunities for the next decade. ACS Publications: 2013.
2. Gupta, B.; Revagade, N.; Hilborn, J., Poly (lactic acid) fiber: An overview. *Progress in polymer science* **2007**, *32* (4), 455-482.
3. Standau, T.; Zhao, C.; Murillo Castellón, S.; Bonten, C.; Altstädt, V., Chemical modification and foam processing of polylactide (PLA). *Polymers* **2019**, *11* (2), 306.
4. Auras, R. A.; Lim, L.-T.; Selke, S. E.; Tsuji, H., *Poly (lactic acid): synthesis, structures, properties, processing, and applications*. John Wiley & Sons: 2011; Vol. 10.
5. Singhvi, M.; Gokhale, D., Biomass to biodegradable polymer (PLA). *RSC advances* **2013**, *3* (33), 13558-13568.
6. Vink, E. T.; Davies, S., Life cycle inventory and impact assessment data for 2014 Ingeo™ polylactide production. *Industrial Biotechnology* **2015**, *11* (3), 167-180.
7. Lin, L.; Deng, C.; Lin, G.-P.; Wang, Y.-Z., Super toughened and high heat-resistant poly (lactic acid)(PLA)-based blends by enhancing interfacial bonding and PLA phase crystallization. *Industrial & Engineering Chemistry Research* **2015**, *54* (21), 5643-5655.
8. Wu, S.; Zhou, R.; Zhou, F.; Streubel, P. N.; Chen, S.; Duan, B., Electrospun thymosin Beta-4 loaded PLGA/PLA nanofiber/microfiber hybrid yarns for tendon tissue engineering application. *Materials Science and Engineering: C* **2020**, *106*, 110268.
9. Hassanajili, S.; Karami-Pour, A.; Oryan, A.; Talaei-Khozani, T., Preparation and characterization of PLA/PCL/HA composite scaffolds using indirect 3D printing for bone tissue engineering. *Materials Science and Engineering: C* **2019**, *104*, 109960.
10. Vieira, A.; Medeiros, R.; Guedes, R. M.; Marques, A.; Tita, V. In *Visco-elastic-plastic properties of suture fibers made of PLA-PCL*, Materials Science Forum, Trans Tech Publ: 2013; pp 56-61.
11. Cayla, A.; Rault, F.; Giraud, S.; Salaün, F.; Fierro, V.; Celzard, A., PLA with intumescent system containing lignin and ammonium polyphosphate for flame retardant textile. *Polymers* **2016**, *8* (9), 331.
12. Misra, M.; Drzal, L. T., *Natural fibers, biopolymers, and biocomposites*. Taylor & Francis Milton Park: 2005.
13. Arrieta, M. P.; López, J.; Ferrándiz, S.; Peltzer, M. A., Characterization of PLA-limonene blends for food packaging applications. *Polymer Testing* **2013**, *32* (4), 760-768.
14. Farah, S.; Anderson, D. G.; Langer, R., Physical and mechanical properties of PLA, and their functions in widespread applications—A comprehensive review. *Advanced drug delivery reviews* **2016**, *107*, 367-392.
15. Strong, A. B., *Plastics: materials and processing*, 2006. Upper Saddle River, NJ: Prentice-Hall.
16. Okolieocha, C.; Raps, D.; Subramaniam, K.; Altstädt, V., Microcellular to nanocellular polymer foams: Progress (2004–2015) and future directions—A review. *European Polymer Journal* **2015**, *73*, 500-519.
17. Mooney, D. J.; Baldwin, D. F.; Suh, N. P.; Vacanti, J. P.; Langer, R., Novel approach to fabricate porous sponges of poly (D, L-lactic-co-glycolic acid) without the use of organic solvents. *Biomaterials* **1996**, *17* (14), 1417-1422.
18. Fang, Q.; Hanna, M. A., Functional properties of polylactic acid starch-based loose-fill packaging foams. *Cereal chemistry* **2000**, *77* (6), 779-783.

19. Ramesh, N. S.; Nawaby, A. V.; Amrutiya, N., Polylactic acid foam composition. Google Patents: 2011.
20. Britton, R. N.; Van Doormalen, F. A. H. C.; Noordegraaf, J.; Molenveld, K.; Schennink, G. G. J., Coated particulate expandable polylactic acid. Google Patents: 2012.
21. Lohmann, J.; Sampath, B. D. S.; Gutmann, P.; Künkel, A.; Hahn, K.; Füssi, A., Process for Producing expandable pelletized Material which comprises Polylactic Acid. Google Patents: 2013.
22. Li, B.; Zhao, G.; Wang, G.; Zhang, L.; Gong, J., Fabrication of high-expansion microcellular PLA foams based on pre-isothermal cold crystallization and supercritical CO<sub>2</sub> foaming. *Polymer Degradation and Stability* **2018**, *156*, 75-88.
23. Nofar, M.; Park, C. B., Poly (lactic acid) foaming. *Progress in Polymer Science* **2014**, *39* (10), 1721-1741.
24. Kakroodi, A. R.; Kazemi, Y.; Nofar, M.; Park, C. B., Tailoring poly (lactic acid) for packaging applications via the production of fully bio-based in situ microfibrillar composite films. *Chemical Engineering Journal* **2017**, *308*, 772-782.
25. Kakroodi, A. R.; Kazemi, Y.; Ding, W.; Ameli, A.; Park, C. B., Poly (lactic acid)-based in situ microfibrillar composites with enhanced crystallization kinetics, mechanical properties, rheological behavior, and foaming ability. *Biomacromolecules* **2015**, *16* (12), 3925-3935.
26. Nofar, M., Effects of nano-/micro-sized additives and the corresponding induced crystallinity on the extrusion foaming behavior of PLA using supercritical CO<sub>2</sub>. *Materials & Design* **2016**, *101*, 24-34.
27. Kang, D. J.; Xu, D.; Zhang, Z. X.; Pal, K.; Bang, D. S.; Kim, J. K., Well-Controlled Microcellular Biodegradable PLA/Silk Composite Foams Using Supercritical CO<sub>2</sub>. *Macromolecular Materials and Engineering* **2009**, *294* (9), 620-624.
28. Keshtkar, M.; Nofar, M.; Park, C. B.; Carreau, P., Extruded PLA/clay nanocomposite foams blown with supercritical CO<sub>2</sub>. *Polymer* **2014**, *55* (16), 4077-4090.
29. Lidén, G., The European commission tries to define nanomaterials. *Annals of Occupational Hygiene* **2011**, *55* (1), 1-5.
30. Iijima, S., Helical microtubules of graphitic carbon. *nature* **1991**, *354* (6348), 56-58.
31. Schaefer, D. W.; Justice, R. S., How nano are nanocomposites? *Macromolecules* **2007**, *40* (24), 8501-8517.
32. Fakirov, S., Nano-/microfibrillar polymer-polymer and single polymer composites: The converting instead of adding concept. *Composites Science and Technology* **2013**, *89*, 211-225.
33. Xie, L.; Xu, H.; Niu, B.; Ji, X.; Chen, J.; Li, Z.-M.; Hsiao, B. S.; Zhong, G.-J., Unprecedented access to strong and ductile poly (lactic acid) by introducing in situ nanofibrillar poly (butylene succinate) for green packaging. *Biomacromolecules* **2014**, *15* (11), 4054-4064.
34. Ojijo, V.; Sinha Ray, S.; Sadiku, R., Effect of nanoclay loading on the thermal and mechanical properties of biodegradable polylactide/poly [(butylene succinate)-co-adipate] blend composites. *ACS applied materials & interfaces* **2012**, *4* (5), 2395-2405.
35. Kulinski, Z.; Piorkowska, E.; Gadzinowska, K.; Stasiak, M., Plasticization of poly (L-lactide) with poly (propylene glycol). *Biomacromolecules* **2006**, *7* (7), 2128-2135.
36. Zhang, K.; Mohanty, A. K.; Misra, M., Fully biodegradable and biorenewable ternary blends from polylactide, poly (3-hydroxybutyrate-co-hydroxyvalerate) and poly (butylene succinate) with balanced properties. *ACS applied materials & interfaces* **2012**, *4* (6), 3091-3101.
37. Ojijo, V.; Sinha Ray, S.; Sadiku, R., Role of specific interfacial area in controlling properties of immiscible blends of biodegradable polylactide and poly [(butylene succinate)-co-adipate]. *ACS Applied Materials & Interfaces* **2012**, *4* (12), 6690-6701.



38. Di Lorenzo, M. L.; Rubino, P.; Cocca, M., Miscibility and properties of poly (l-lactic acid)/poly (butylene terephthalate) blends. *European polymer journal* **2013**, *49* (10), 3309-3317.
39. Mishra, R. K.; Thomas, S.; Kalarikkal, N., *Micro and nano fibrillar composites (MFCs and NFCs) from polymer blends*. Elsevier: 2017.
40. Wang, Z.; Macosko, C. W.; Bates, F. S., Fluorine-enriched melt-blown fibers from polymer blends of poly (butylene terephthalate) and a fluorinated multiblock copolyester. *ACS applied materials & interfaces* **2015**, *8* (1), 754-761.
41. Dai, K.; Xu, X.-B.; Li, Z.-M., Electrically conductive carbon black (CB) filled in situ microfibrillar poly (ethylene terephthalate)(PET)/polyethylene (PE) composite with a selective CB distribution. *Polymer* **2007**, *48* (3), 849-859.
42. Jayanarayanan, K.; Thomas, S.; Joseph, K., Morphology, static and dynamic mechanical properties of in situ microfibrillar composites based on polypropylene/poly (ethylene terephthalate) blends. *Composites Part A: Applied Science and Manufacturing* **2008**, *39* (2), 164-175.
43. Lim, L.-T.; Auras, R.; Rubino, M., Processing technologies for poly (lactic acid). *Progress in polymer science* **2008**, *33* (8), 820-852.
44. Evstatiev, M.; Fakirov, S., Microfibrillar reinforcement of polymer blends. *Polymer* **1992**, *33* (4), 877-880.
45. Fakirov, S.; Evstatiev, M.; Petrovich, S., Microfibrillar reinforced composites from binary and ternary blends of polyesters and nylon 6. *Macromolecules* **1993**, *26* (19), 5219-5226.
46. Zhou, S.-Y.; Huang, H.-D.; Ji, X.; Yan, D.-X.; Zhong, G.-J.; Hsiao, B. S.; Li, Z.-M., Super-robust polylactide barrier films by building densely oriented lamellae incorporated with ductile in situ nanofibrils of poly (butylene adipate-co-terephthalate). *ACS Applied Materials & Interfaces* **2016**, *8* (12), 8096-8109.
47. Xie, L.; Xu, H.; Chen, J.-B.; Zhang, Z.-J.; Hsiao, B. S.; Zhong, G.-J.; Chen, J.; Li, Z.-M., From nanofibrillar to nanolaminar poly (butylene succinate): paving the way to robust barrier and mechanical properties for full-biodegradable poly (lactic acid) films. *ACS applied materials & interfaces* **2015**, *7* (15), 8023-8032.
48. Voznyak, Y.; Morawiec, J.; Galeski, A., Ductility of polylactide composites reinforced with poly (butylene succinate) nanofibers. *Composites Part A: Applied Science and Manufacturing* **2016**, *90*, 218-224.
49. Sun, X.; Kharbas, H.; Peng, J.; Turng, L.-S., A novel method of producing lightweight microcellular injection molded parts with improved ductility and toughness. *Polymer* **2015**, *56*, 102-110.
50. Li, Z.; Zhao, X.; Ye, L.; Coates, P.; Caton-Rose, F.; Martyn, M., Fibrillation of chain branched poly (lactic acid) with improved blood compatibility and bionic structure. *Chemical Engineering Journal* **2015**, *279*, 767-776.
51. Ding, W.; Chen, Y.; Liu, Z.; Yang, S., In situ nano-fibrillation of microinjection molded poly (lactic acid)/poly ( $\epsilon$ -caprolactone) blends and comparison with conventional injection molding. *RSC advances* **2015**, *5* (113), 92905-92917.
52. He, Y.; Yang, Z.-t.; Qu, J.-p., Super-toughened poly (lactic acid)/thermoplastic poly (ether) urethane nanofiber composites with in-situ formation of aligned nanofibers prepared by an innovative eccentric rotor extruder. *Composites Science and Technology* **2019**, *169*, 135-141.
53. Hosseinneshad, R.; Vozniak, I.; Morawiec, J.; Galeski, A.; Dutkiewicz, S., In situ generation of sustainable PLA-based nanocomposites by shear induced crystallization of nanofibrillar inclusions. *RSC advances* **2019**, *9* (52), 30370-30380.

- 54.Li, Y.; Han, C.; Yu, Y.; Huang, D., Uniaxial stretching and properties of fully biodegradable poly (lactic acid)/poly (3-hydroxybutyrate-co-4-hydroxybutyrate) blends. *International journal of biological macromolecules* **2019**, *129*, 1-12.
- 55.Liu, T.; Lian, X.; Li, L.; Peng, X.; Kuang, T., Facile fabrication of fully biodegradable and biorenewable poly (lactic acid)/poly (butylene adipate-co-terephthalate) in-situ nanofibrillar composites with high strength, good toughness and excellent heat resistance. *Polymer Degradation and Stability* **2020**, *171*, 109044.
- 56.Kakroodi, A. R.; Kazemi, Y.; Rodrigue, D.; Park, C. B., Facile production of biodegradable PCL/PLA in situ nanofibrillar composites with unprecedented compatibility between the blend components. *Chemical Engineering Journal* **2018**, *351*, 976-984.
- 57.Mahmud, M. B.; Anstey, A.; Shaayegan, V.; Lee, P. C.; Park, C. B., Enhancing the mechanical performance of PA6 based composites by altering their crystallization and rheological behavior via in-situ generated PPS nanofibrils. *Composites Part B: Engineering* **2020**, 108067.
- 58.Rizvi, A.; Park, C. B.; Favis, B. D., Tuning viscoelastic and crystallization properties of polypropylene containing in-situ generated high aspect ratio polyethylene terephthalate fibrils. *Polymer* **2015**, *68*, 83-91.
- 59.Li, Z.-M.; Yang, M.-B.; Lu, A.; Feng, J.-M.; Huang, R., Tensile properties of poly (ethylene terephthalate) and polyethylene in-situ microfiber reinforced composite formed via slit die extrusion and hot-stretching. *Materials letters* **2002**, *56* (5), 756-762.
- 60.Shields, R.; Bhattacharyya, D.; Fakirov, S., Fibrillar polymer-polymer composites: morphology, properties and applications. *Journal of materials science* **2008**, *43* (20), 6758-6770.
- 61.Gupta, V.; Kothari, V., *Manufactured fibre technology*. Springer Science & Business Media: 2012.
- 62.Xing, Q.; Zhu, M.; Wang, Y.; Chen, Y.; Zhang, Y.; Pionteck, J.; Adler, H., In situ gradient nano-scale fibril formation during polypropylene (PP)/polystyrene (PS) composite fine fiber processing. *Polymer* **2005**, *46* (14), 5406-5416.
- 63.Yokohara, T.; Nobukawa, S.; Yamaguchi, M., Rheological properties of polymer composites with flexible fine fibers. *Journal of Rheology* **2011**, *55* (6), 1205-1218.
- 64.Utracki, L. A.; Wilkie, C. A., *Polymer blends handbook*. Springer: 2002; Vol. 1.
- 65.Fakirov, S.; Bhattacharyya, D.; Lin, R.; Fuchs, C.; Friedrich, K., Contribution of coalescence to microfibril formation in polymer blends during cold drawing. *Journal of Macromolecular Science, Part B: Physics* **2007**, *46* (1), 183-194.
- 66.Hajiraissi, R., Linear and nonlinear melt viscoelastic properties of fibrillated blend fiber based on polypropylene/polytrimethylene terephthalate. *Polymer Bulletin* **2019**, 1-20.
- 67.Bigdeli, A.; Nazockdast, H.; Rashidi, A.; Yazdanshenas, M. E., Role of nanoclay in determining microfibrillar morphology development in PP/PBT blend nanocomposite fibers. *Journal of Polymer Research* **2012**, *19* (11), 9990.
- 68.Bigdeli, A.; Nazockdast, H.; Rashidi, A.; Yazdanshenas, M., The Effect of Feeding Method and Compatibilizer on Nanoclay Partitioning and Microfibrillar Morphology Development in PP/PBT/Organoclay Blend Nanocomposite Fibers: This Paper was invited from the PPS Asia/Australia Regional Meeting held on Kish Island, Iran, November 15-17, 2011. *International Polymer Processing* **2013**, *28* (2), 174-179.
- 69.Zhao, C.; Mark, L. H.; Alshrah, M.; Soltani, I.; Lee, P. C.; Park, C. B., Challenge in manufacturing nanofibril composites with low matrix viscosity: Effects of matrix viscosity and fibril content. *European Polymer Journal* **2019**, *121*, 109310.

- 70.Zuo, F.; Tan, D. H.; Wang, Z.; Jeung, S.; Macosko, C. W.; Bates, F. S., Nanofibers from melt blown fiber-in-fiber polymer blends. *ACS Macro Letters* **2013**, *2* (4), 301-305.
- 71.Soltani, I.; Macosko, C. W., Influence of rheology and surface properties on morphology of nanofibers derived from islands-in-the-sea meltblown nonwovens. *Polymer* **2018**, *145*, 21-30.
- 72.Zhu, Z.; He, H.; Xue, B.; Zhan, Z.; Wang, G.; Chen, M., Morphology, Thermal, Mechanical Properties and Rheological Behavior of Biodegradable Poly (butylene succinate)/poly (lactic acid) In-Situ Submicrofibrillar Composites. *Materials* **2018**, *11* (12), 2422.
- 73.Jurczuk, K.; Galeski, A.; Piorkowska, E., All-polymer nanocomposites with nanofibrillar inclusions generated in situ during compounding. *Polymer* **2013**, *54* (17), 4617-4628.
- 74.Ali, M. A. B. M.; Nobukawa, S.; Yamaguchi, M., Morphology development of polytetrafluoroethylene in a polypropylene melt (IUPAC Technical Report). *Pure and Applied Chemistry* **2011**, *83* (10), 1819-1830.
- 75.Rizvi, A.; Tabatabaei, A.; Barzegari, M. R.; Mahmood, S. H.; Park, C. B., In situ fibrillation of CO<sub>2</sub>-philic polymers: Sustainable route to polymer foams in a continuous process. *Polymer* **2013**, *54* (17), 4645-4652.
- 76.Rizvi, A.; Park, C. B., Dispersed polypropylene fibrils improve the foaming ability of a polyethylene matrix. *Polymer* **2014**, *55* (16), 4199-4205.
- 77.Bai, L.; He, S.; Fruehwirth, J. W.; Stein, A.; Macosko, C. W.; Cheng, X., Localizing graphene at the interface of cocontinuous polymer blends: Morphology, rheology, and conductivity of cocontinuous conductive polymer composites. *Journal of Rheology* **2017**, *61* (4), 575-587.
- 78.Utracki, L.; Dumoulin, M. M.; Toma, P., Melt rheology of high density polyethylene/polyamide-6 blends. *Polymer Engineering & Science* **1986**, *26* (1), 34-44.
- 79.Rostami, A.; Nazockdast, H.; Karimi, M., Graphene induced microstructural changes of PLA/MWCNT biodegradable nanocomposites: rheological, morphological, thermal and electrical properties. *RSC Advances* **2016**, *6* (55), 49747-49759.
- 80.Utracki, L.; Kamal, M., The rheology of polymer alloys and blends. *Polymer blends handbook* **2003**, 449-546.
- 81.Shahnooshi, M.; Javadi, A.; Nazockdast, H.; Ottermann, K.; Altstädt, V., Rheological rationalization of in situ nanofibrillar structure development: Tailoring of nanohybrid shish-kebab superstructures of poly (lactic acid) crystalline phase. *Polymer* **2020**, *211*, 123040.
- 82.Janssen, J.; Meijer, H., Droplet breakup mechanisms: Stepwise equilibrium versus transient dispersion. *Journal of Rheology* **1993**, *37* (4), 597-608.
- 83.Grace, H. P., Dispersion phenomena in high viscosity immiscible fluid systems and application of static mixers as dispersion devices in such systems. *Chemical Engineering Communications* **1982**, *14* (3-6), 225-277.
- 84.Wu, S., Formation of dispersed phase in incompatible polymer blends: Interfacial and rheological effects. *Polymer Engineering & Science* **1987**, *27* (5), 335-343.
- 85.Janssen, J.; Meijer, H., Droplet breakup mechanisms: Stepwise equilibrium versus transient dispersion. *Journal of Rheology* **1998**, *37* (4), 597.
- 86.Champagne, M.; Dumoulin, M.; Utracki, L.; Szabo, J., Generation of fibrillar morphology in blends of block copolyetheresteramide and liquid crystal polyester. *Polymer Engineering & Science* **1996**, *36* (12), 1636-1646.
- 87.Cassagnau, P.; Michel, A., New morphologies in immiscible polymer blends generated by a dynamic quenching process. *Polymer* **2001**, *42* (7), 3139-3152.
- 88.Stone, H. A., Dynamics of drop deformation and breakup in viscous fluids. *Annual Review of Fluid Mechanics* **1994**, *26* (1), 65-102.

89. Stegeman, Y. W.; Van De Vosse, F. N.; Meijer, H. E., On the applicability of the Grace curve in practical mixing operations. *The Canadian Journal of Chemical Engineering* **2002**, *80* (4), 1-6.
90. Pesneau, I.; Kadi, A. A.; Bousmina, M.; Cassagnau, P.; Michel, A., From polymer blends to in situ polymer/polymer composites: morphology control and mechanical properties. *Polymer Engineering & Science* **2002**, *42* (10), 1990-2004.
91. Yousfi, M.; Dadouche, T.; Chomat, D.; Samuel, C.; Soulestin, J.; Lacrampe, M.-F.; Krawczak, P., Development of nanofibrillar morphologies in poly (l-lactide)/poly (amide) blends: Role of the matrix elasticity and identification of the critical shear rate for the nodular/fibrillar transition. *RSC advances* **2018**, *8* (39), 22023-22041.
92. Mighri, F.; Aji, A.; Carreau, P., Influence of elastic properties on drop deformation in elongational flow. *Journal of rheology* **1997**, *41* (5), 1183-1201.
93. Sundararaj, U.; Macosko, C., Drop breakup and coalescence in polymer blends: the effects of concentration and compatibilization. *Macromolecules* **1995**, *28* (8), 2647-2657.
94. Astruc, M.; Vervoort, S.; Nouatin, H. O.; Coupez, T.; De Puydt, Y.; Navard, P.; Peuvrel-Disdier, E., Experimental and numerical study of the rotation and the erosion of fillers suspended in viscoelastic fluids under simple shear flow. *Rheologica Acta* **2003**, *42* (5), 421-431.
95. Jašo, V.; Milić, J.; Divjaković, V.; Petrović, Z. S., Novel elastomeric polyurethane fibers modified with polypropylene microfibers. *European Polymer Journal* **2013**, *49* (12), 3947-3955.
96. Cárdenas, M. A.; Perera, R.; Villarreal, N.; Rosales, C.; Pastor, J. M., In situ fiber composites based on metallocene polyethylene matrices. *Journal of applied polymer science* **2007**, *106* (4), 2298-2312.
97. García-Masabet, V.; Santana Pérez, O.; Cailloux, J.; Abt, T.; Sánchez-Soto, M.; Carrasco, F.; MasPOCH, M. L., PLA/PA bio-blends: induced morphology by extrusion. *Polymers* **2020**, *12* (1), 10.
98. Huneault, M.; Champagne, M.; Luciani, A., Polymer blend mixing and dispersion in the kneading section of a twin-screw extruder. *Polymer Engineering & Science* **1996**, *36* (12), 1694-1706.
99. Xing, P.; Bousmina, M.; Rodrigue, D.; Kamal, M., Critical experimental comparison between five techniques for the determination of interfacial tension in polymer blends: model system of polystyrene/polyamide-6. *Macromolecules* **2000**, *33* (21), 8020-8034.
100. Li, Y.; Kröger, M.; Liu, W. K., Nanoparticle geometrical effect on structure, dynamics and anisotropic viscosity of polyethylene nanocomposites. *Macromolecules* **2012**, *45* (4), 2099-2112.
101. Chambon, F.; Winter, H. H., Linear viscoelasticity at the gel point of a crosslinking PDMS with imbalanced stoichiometry. *Journal of Rheology* **1987**, *31* (8), 683-697.
102. Huang, Y.; He, Y.; Ding, W.; Yang, K.; Yu, D.; Xin, C., Improved viscoelastic, thermal, and mechanical properties of in situ microfibrillar polypropylene/polyamide 6, 6 composites via direct extrusion using a triple-screw extruder. *RSC advances* **2017**, *7* (9), 5030-5038.
103. Wang, G.; Zhao, J.; Wang, G.; Zhao, H.; Lin, J.; Zhao, G.; Park, C. B., Strong and super thermally insulating in-situ nanofibrillar PLA/PET composite foam fabricated by high-pressure microcellular injection molding. *Chemical Engineering Journal* **2020**, *390*, 124520.
104. Zhao, J.; Zhao, Q.; Wang, L.; Wang, C.; Guo, B.; Park, C. B.; Wang, G., Development of high thermal insulation and compressive strength BPP foams using mold-opening foam injection molding with in-situ fibrillated PTFE fibers. *European Polymer Journal* **2018**, *98*, 1-10.

105. Zhao, J.; Zhao, Q.; Wang, C.; Guo, B.; Park, C. B.; Wang, G., High thermal insulation and compressive strength polypropylene foams fabricated by high-pressure foam injection molding and mold opening of nano-fibrillar composites. *Materials & Design* **2017**, *131*, 1-11.
106. Sridhar, T.; Acharya, M.; Nguyen, D. A.; Bhattacharjee, P. K., On the extensional rheology of polymer melts and concentrated solutions. *Macromolecules* **2014**, *47* (1), 379-386.
107. Trouton, F. T., On the coefficient of viscous traction and its relation to that of viscosity. *Proceedings of the Royal Society of London. Series A, Containing Papers of a Mathematical and Physical Character* **1906**, *77* (519), 426-440.
108. Münstedt, H., Rheological properties and molecular structure of polymer melts. *Soft Matter* **2011**, *7* (6), 2273-2283.
109. Razavi, M.; Wang, S.-Q., Why is crystalline poly (lactic acid) brittle at room temperature? *Macromolecules* **2019**, *52* (14), 5429-5441.
110. Lu, F.; Yu, H.; Yan, C.; Yao, J., Polylactic acid nanocomposite films with spherical nanocelluloses as efficient nucleation agents: effects on crystallization, mechanical and thermal properties. *RSC Advances* **2016**, *6* (51), 46008-46018.
111. Raquez, J.-M.; Habibi, Y.; Murariu, M.; Dubois, P., Polylactide (PLA)-based nanocomposites. *Progress in Polymer Science* **2013**, *38* (10-11), 1504-1542.
112. Zhang, J.; Duan, Y.; Sato, H.; Tsuji, H.; Noda, I.; Yan, S.; Ozaki, Y., Crystal modifications and thermal behavior of poly (L-lactic acid) revealed by infrared spectroscopy. *Macromolecules* **2005**, *38* (19), 8012-8021.
113. Agüero, A.; Morcillo, M. d. C.; Quiles-Carrillo, L.; Balart, R.; Boronat, T.; Lascano, D.; Torres-Giner, S.; Fenollar, O., Study of the influence of the reprocessing cycles on the final properties of polylactide pieces obtained by injection molding. *Polymers* **2019**, *11* (12), 1908.
114. Yousefzade, O.; Jeddi, J.; Franco, L.; Puiggali, J.; Garmabi, H., Crystallization kinetics of chain extended poly (L-lactide) s having different molecular structures. *Materials Chemistry and Physics* **2020**, *240*, 122217.
115. Rostami, A.; Vahdati, M.; Alimoradi, Y.; Karimi, M.; Nazockdast, H., Rheology provides insight into flow induced nano-structural breakdown and its recovery effect on crystallization of single and hybrid carbon nanofiller filled poly (lactic acid). *Polymer* **2018**, *134*, 143-154.
116. Radano, C. P.; Baker, G. L.; Smith, M. R., Stereoselective polymerization of a racemic monomer with a racemic catalyst: direct preparation of the polylactic acid stereocomplex from racemic lactide. *Journal of the American Chemical Society* **2000**, *122* (7), 1552-1553.
117. Hoogsteen, W.; Postema, A.; Pennings, A.; Ten Brinke, G.; Zugenmaier, P., Crystal structure, conformation and morphology of solution-spun poly (L-lactide) fibers. *Macromolecules* **1990**, *23* (2), 634-642.
118. Cho, T.-Y.; Strobl, G., Temperature dependent variations in the lamellar structure of poly (L-lactide). *Polymer* **2006**, *47* (4), 1036-1043.
119. Zhang, J.; Tashiro, K.; Tsuji, H.; Domb, A. J., Disorder-to-order phase transition and multiple melting behavior of poly (L-lactide) investigated by simultaneous measurements of WAXD and DSC. *Macromolecules* **2008**, *41* (4), 1352-1357.
120. Yan, T.; Zhao, B.; Cong, Y.; Fang, Y.; Cheng, S.; Li, L.; Pan, G.; Wang, Z.; Li, X.; Bian, F., Critical strain for shish-kebab formation. *Macromolecules* **2009**, *43* (2), 602-605.
121. Nie, Y.; Zhao, Y.; Matsuba, G.; Hu, W., Shish-kebab crystallites initiated by shear fracture in bulk polymers. *Macromolecules* **2018**, *51* (2), 480-487.
122. Zhang, Q.; Li, L.; Su, F.; Ji, Y.; Ali, S.; Zhao, H.; Meng, L.; Li, L., From Molecular Entanglement Network to Crystal-Cross-Linked Network and Crystal Scaffold during Film Blowing of Polyethylene: An in Situ Synchrotron Radiation Small-and Wide-Angle X-ray Scattering Study. *Macromolecules* **2018**, *51* (11), 4350-4362.

- 123.Liu, D.; Tian, N.; Cui, K.; Zhou, W.; Li, X.; Li, L., Correlation between flow-induced nucleation morphologies and strain in polyethylene: from uncorrelated oriented point-nuclei, scaffold-network, and microshish to shish. *Macromolecules* **2013**, *46* (9), 3435-3443.
- 124.Shen, B.; Liang, Y.; Kornfield, J. A.; Han, C. C., Mechanism for shish formation under shear flow: An interpretation from an in situ morphological study. *Macromolecules* **2013**, *46* (4), 1528-1542.
- 125.Yang, J.; Wang, C.; Wang, K.; Zhang, Q.; Chen, F.; Du, R.; Fu, Q., Direct formation of nanohybrid shish-kebab in the injection molded bar of polyethylene/multiwalled carbon nanotubes composite. *Macromolecules* **2009**, *42* (18), 7016-7023.
- 126.Patil, N.; Balzano, L.; Portale, G.; Rastogi, S., A study on the chain– particle interaction and aspect ratio of nanoparticles on structure development of a linear polymer. *Macromolecules* **2010**, *43* (16), 6749-6759.
- 127.Balzano, L.; Ma, Z.; Cavallo, D.; van Erp, T. B.; Fernandez-Ballester, L.; Peters, G. W., Molecular aspects of the formation of shish-kebab in isotactic polypropylene. *Macromolecules* **2016**, *49* (10), 3799-3809.
- 128.Zhu, P.-w.; Edward, G., Distribution of shish-kebab structure of isotactic polypropylene under shear in the presence of nucleating agent. *Macromolecules* **2004**, *37* (7), 2658-2660.
- 129.Dukovski, I.; Muthukumar, M., Langevin dynamics simulations of early stage shish-kebab crystallization of polymers in extensional flow. *The Journal of chemical physics* **2003**, *118* (14), 6648-6655.
- 130.Kanaya, T.; Matsuba, G.; Ogino, Y.; Nishida, K.; Shimizu, H. M.; Shinohara, T.; Oku, T.; Suzuki, J.; Otomo, T., Hierarchic structure of shish-kebab by neutron scattering in a wide Q range. *Macromolecules* **2007**, *40* (10), 3650-3654.
- 131.Kmetty, Á.; Bárány, T.; Karger-Kocsis, J., Self-reinforced polymeric materials: A review. *Progress in Polymer Science* **2010**, *35* (10), 1288-1310.
- 132.Ning, N.; Fu, S.; Zhang, W.; Chen, F.; Wang, K.; Deng, H.; Zhang, Q.; Fu, Q., Realizing the enhancement of interfacial interaction in semicrystalline polymer/filler composites via interfacial crystallization. *Progress in polymer science* **2012**, *37* (10), 1425-1455.
- 133.Pan, H.; Cao, Z.; Chen, Y.; Wang, X.; Jia, S.; Yang, H.; Zhang, H.; Dong, L., Effect of molecular stereoregularity on the transcrystallization properties of poly (l-lactide)/basalt fiber composites. *International journal of biological macromolecules* **2019**, *137*, 238-246.
- 134.Dasari, A.; Yu, Z.-Z.; Mai, Y.-W., Interfaces. In *Polymer Nanocomposites*, Springer: 2016; pp 103-131.
- 135.Quan, H.; Li, Z.-M.; Yang, M.-B.; Huang, R., On transcrystallinity in semi-crystalline polymer composites. *Composites Science and Technology* **2005**, *65* (7-8), 999-1021.
- 136.Ning, N.; Zhang, W.; Zhao, Y.; Luo, F.; Fu, Q., Nanohybrid shish kebab structure and its effect on mechanical properties in poly (L-lactide)/carbon nanotube nanocomposite fibers. *Polymer International* **2012**, *61* (11), 1634-1639.
- 137.Folkes, M.; Hardwick, S., The molecular weight dependence of transcrystallinity in fibre reinforced thermoplastics. *Journal of materials science letters* **1984**, *3* (12), 1071-1073.
- 138.Wingstrand, S. L.; Shen, B.; Kornfield, J. A.; Mortensen, K.; Parisi, D.; Vlassopoulos, D.; Hassager, O., Rheological link between polymer melts with a high molecular weight tail and enhanced formation of Shish-Kebabs. *ACS Macro Letters* **2017**, *6* (11), 1268-1273.
- 139.Li, L.; Li, C. Y.; Ni, C., Polymer crystallization-driven, periodic patterning on carbon nanotubes. *Journal of the American Chemical Society* **2006**, *128* (5), 1692-1699.
- 140.Zheng, X.; Xu, Q., Comparison study of morphology and crystallization behavior of polyethylene and poly (ethylene oxide) on single-walled carbon nanotubes. *The Journal of Physical Chemistry B* **2010**, *114* (29), 9435-9444.

141. Park, S. H.; Lee, S. G.; Kim, S. H., Isothermal crystallization behavior and mechanical properties of polylactide/carbon nanotube nanocomposites. *Composites Part A: Applied Science and Manufacturing* **2013**, *46*, 11-18.
142. Yousefzade, O.; Franco, L.; Nami, M.; Puiggali, J.; Garmabi, H., Nanocomposites based on chain extended poly (l-lactic acid)/carboxylated carbon nanotubes: Crystallization kinetics and lamellar morphology. *Journal of Composite Materials* **2019**, *53* (15), 2131-2147.
143. Samthong, C.; Deetum, C.; Yamaguchi, M.; Praserttham, P.; Somwangthanaroj, A., Effects of size and shape of dispersed poly (butylene terephthalate) on isothermal crystallization kinetics and morphology of poly (lactic acid) blends. *Polymer Engineering & Science* **2016**, *56* (3), 258-268.
144. Somani, R. H.; Hsiao, B. S.; Nogales, A.; Srinivas, S.; Tsou, A. H.; Sics, I.; Balta-Calleja, F. J.; Ezquerro, T. A., Structure development during shear flow-induced crystallization of i-PP: in-situ small-angle X-ray scattering study. *Macromolecules* **2000**, *33* (25), 9385-9394.
145. Matsuba, G.; Sakamoto, S.; Ogino, Y.; Nishida, K.; Kanaya, T., Crystallization of polyethylene blends under shear flow. Effects of crystallization temperature and ultrahigh molecular weight component. *Macromolecules* **2007**, *40* (20), 7270-7275.
146. Xu, H.; Xie, L.; Jiang, X.; Hakkarainen, M.; Chen, J.-B.; Zhong, G.-J.; Li, Z.-M., Structural basis for unique hierarchical cylindrites induced by ultrahigh shear gradient in single natural fiber reinforced poly (lactic acid) green composites. *Biomacromolecules* **2014**, *15* (5), 1676-1686.
147. Kalb, B.; Pennings, A., General crystallization behaviour of poly (L-lactic acid). *Polymer* **1980**, *21* (6), 607-612.
148. Xu, H.; Zhong, G.-J.; Fu, Q.; Lei, J.; Jiang, W.; Hsiao, B. S.; Li, Z.-M., Formation of shish-kebabs in injection-molded poly (L-lactic acid) by application of an intense flow field. *ACS applied materials & interfaces* **2012**, *4* (12), 6774-6784.
149. Xu, H.; Xie, L.; Hakkarainen, M., Beyond a model of polymer processing-triggered shear: reconciling shish-kebab formation and control of chain degradation in sheared poly (L-lactic acid). *ACS Sustainable Chemistry & Engineering* **2015**, *3* (7), 1443-1452.
150. Li, C.; Jiang, T.; Wang, J.; Wu, H.; Guo, S.; Zhang, X.; Li, J.; Shen, J.; Chen, R.; Xiong, Y., In situ formation of microfibrillar crystalline superstructure: achieving high-performance polylactide. *ACS applied materials & interfaces* **2017**, *9* (31), 25818-25829.
151. Zhou, S.-Y.; Niu, B.; Xie, X.-L.; Ji, X.; Zhong, G.-J.; Hsiao, B. S.; Li, Z.-M., Interfacial shish-kebabs lengthened by coupling effect of in situ flexible nanofibrils and intense shear flow: achieving hierarchy to conquer the conflicts between strength and toughness of polylactide. *ACS Applied Materials & Interfaces* **2017**, *9* (11), 10148-10159.
152. Li, C.; Guo, J.; Jiang, T.; Zhang, X.; Xia, L.; Wu, H.; Guo, S.; Zhang, X., Extensional flow-induced hybrid crystalline fibrils (shish) in CNT/PLA nanocomposite. *Carbon* **2018**, *129*, 720-729.
153. Fang, H.; Zhang, Y.; Bai, J.; Wang, Z., Shear-induced nucleation and morphological evolution for bimodal long chain branched polylactide. *Macromolecules* **2013**, *46* (16), 6555-6565.
154. Li, Y.; Yang, S.; Li, Y.-K.; Xu, J.-Z.; Ni, H.-W.; Su, Z.-H.; Li, Z.-M., Robust interfacial cylindrites of polylactic acid modulated by an intense shear flow field. *ACS Sustainable Chemistry & Engineering* **2016**, *4* (6), 3558-3566.
155. Xu, H.; Xie, L.; Chen, Y.-H.; Huang, H.-D.; Xu, J.-Z.; Zhong, G.-J.; Hsiao, B. S.; Li, Z.-M., Strong shear flow-driven simultaneous formation of classic shish-kebab, hybrid shish-kebab, and transcrystallinity in poly (lactic acid)/natural fiber biocomposites. *ACS Sustainable Chemistry & Engineering* **2013**, *1* (12), 1619-1629.

- 156.Speranza, V.; De Meo, A.; Pantani, R., Thermal and hydrolytic degradation kinetics of PLA in the molten state. *Polymer degradation and stability* **2014**, *100*, 37-41.
- 157.Mofokeng, J.; Luyt, A., Morphology and thermal degradation studies of melt-mixed poly (lactic acid)(PLA)/poly ( $\epsilon$ -caprolactone)(PCL) biodegradable polymer blend nanocomposites with TiO<sub>2</sub> as filler. *Polymer Testing* **2015**, *45*, 93-100.
- 158.Najafi, N.; Heuzey, M.; Carreau, P.; Wood-Adams, P. M., Control of thermal degradation of polylactide (PLA)-clay nanocomposites using chain extenders. *Polymer Degradation and Stability* **2012**, *97* (4), 554-565.
- 159.Li, L.; Li, B.; Hood, M. A.; Li, C. Y., Carbon nanotube induced polymer crystallization: The formation of nanohybrid shish-kebabs. *Polymer* **2009**, *50* (4), 953-965.
- 160.Ning, N.; Zhang, W.; Yan, J.; Xu, F.; Tang, C.; Fu, Q., Effect of surface "groove" structure of carbon nanotube bundles on the formation of nanohybrid shish kebab. *Journal of Materials Research* **2012**, *27* (21), 2812-2818.
- 161.Hu, X.; An, H.; Li, Z.-M.; Geng, Y.; Li, L.; Yang, C., Origin of carbon nanotubes induced poly (L-lactide) crystallization: surface induced conformational order. *Macromolecules* **2009**, *42* (8), 3215-3218.
- 162.Bai, H.; Zhang, W.; Deng, H.; Zhang, Q.; Fu, Q., Control of crystal morphology in poly (L-lactide) by adding nucleating agent. *Macromolecules* **2011**, *44* (6), 1233-1237.
- 163.Samthong, C.; Seemork, J.; Nobukawa, S.; Yamaguchi, M.; Praserttham, P.; Somwangthanaroj, A., Morphology, structure, and properties of poly (lactic acid) microporous films containing poly (butylene terephthalate) fine fibers fabricated by biaxial stretching. *Journal of Applied Polymer Science* **2015**, *132* (6).
- 164.Bordes, P.; Pollet, E.; Avérous, L., Nano-biocomposites: biodegradable polyester/nanoclay systems. *Progress in Polymer Science* **2009**, *34* (2), 125-155.
- 165.Li, H.; Huneault, M. A., Effect of nucleation and plasticization on the crystallization of poly (lactic acid). *Polymer* **2007**, *48* (23), 6855-6866.
- 166.Nam, J. Y.; Sinha Ray, S.; Okamoto, M., Crystallization behavior and morphology of biodegradable polylactide/layered silicate nanocomposite. *Macromolecules* **2003**, *36* (19), 7126-7131.
- 167.Papageorgiou, G.; Achilias, D.; Nanaki, S.; Beslikas, T.; Bikiaris, D., PLA nanocomposites: effect of filler type on non-isothermal crystallization. *Thermochimica Acta* **2010**, *511* (1-2), 129-139.
- 168.Xu, J.-Z.; Chen, T.; Yang, C.-L.; Li, Z.-M.; Mao, Y.-M.; Zeng, B.-Q.; Hsiao, B. S., Isothermal crystallization of poly (l-lactide) induced by graphene nanosheets and carbon nanotubes: a comparative study. *Macromolecules* **2010**, *43* (11), 5000-5008.
- 169.Nam, J. Y.; Okamoto, M.; Okamoto, H.; Nakano, M.; Usuki, A.; Matsuda, M., Morphology and crystallization kinetics in a mixture of low-molecular weight aliphatic amide and polylactide. *Polymer* **2006**, *47* (4), 1340-1347.
- 170.Valapa, R.; Hussain, S.; Iyer, P. K.; Pugazhenthii, G.; Katiyar, V., Influence of graphene on thermal degradation and crystallization kinetics behaviour of poly (lactic acid). *Journal of Polymer Research* **2015**, *22* (9), 175.
- 171.Xu, T.; Wang, Y.; Han, Q.; He, D.; Li, Q.; Shen, C., Nonisothermal crystallization kinetics of poly (lactic acid) nucleated with a multiamide nucleating agent. *Journal of Macromolecular Science, Part B* **2014**, *53* (10), 1680-1694.
- 172.Borkotoky, S. S.; Chakraborty, G.; Katiyar, V., Thermal degradation behaviour and crystallization kinetics of poly (lactic acid) and cellulose nanocrystals (CNC) based microcellular composite foams. *International journal of biological macromolecules* **2018**, *118*, 1518-1531.



173. Maffezzoli, A.; Kenny, J.; Torre, L., On the physical dimensions of the Avrami constant. *Thermochimica Acta* **1995**, *269*, 185-190.
174. Lorenzo, A. T.; Arnal, M. L.; Albuerno, J.; Müller, A. J., DSC isothermal polymer crystallization kinetics measurements and the use of the Avrami equation to fit the data: Guidelines to avoid common problems. *Polymer testing* **2007**, *26* (2), 222-231.
175. Cai, J.; Liu, M.; Wang, L.; Yao, K.; Li, S.; Xiong, H., Isothermal crystallization kinetics of thermoplastic starch/poly (lactic acid) composites. *Carbohydrate polymers* **2011**, *86* (2), 941-947.
176. Lan, C.-H.; Sun, Y.-M., Influence of the surface properties of nano-silica on the dispersion and isothermal crystallization kinetics of PHB/silica nanocomposites. *Materials Chemistry and Physics* **2017**, *199*, 88-97.
177. Di Lorenzo, M. L.; Rubino, P.; Cocca, M., Isothermal and non-isothermal crystallization of poly (L-lactic acid)/poly (butylene terephthalate) blends. *Journal of Applied Polymer Science* **2014**, *131* (12).
178. Nazockdast, H., *Morphology and structure of polymer blends containing nanofillers*. John Wiley and Sons, Inc New York: 2016.
179. Dil, E. J.; Carreau, P.; Favis, B. D., Morphology, miscibility and continuity development in poly (lactic acid)/poly (butylene adipate-co-terephthalate) blends. *Polymer* **2015**, *68*, 202-212.
180. Wu, S. In *Calculation of interfacial tension in polymer systems*, Journal of Polymer Science Part C: Polymer Symposia, Wiley Online Library: 1971; pp 19-30.
181. Asai, S.; Sakata, K.; Sumita, M.; Miyasaka, K., Effect of interfacial free energy on the heterogeneous distribution of oxidized carbon black in polymer blends. *Polymer journal* **1992**, *24* (5), 415-420.
182. Sumita, M.; Sakata, K.; Asai, S.; Miyasaka, K.; Nakagawa, H., Dispersion of fillers and the electrical conductivity of polymer blends filled with carbon black. *Polymer bulletin* **1991**, *25* (2), 265-271.
183. Gubbels, F.; Jérôme, R.; Vanlathem, E.; Deltour, R.; Blacher, S.; Brouers, F., Kinetic and thermodynamic control of the selective localization of carbon black at the interface of immiscible polymer blends. *Chemistry of materials* **1998**, *10* (5), 1227-1235.
184. Persson, A. L.; Bertilsson, H., Viscosity difference as distributing factor in selective absorption of aluminium borate whiskers in immiscible polymer blends. *Polymer* **1998**, *39* (23), 5633-5642.
185. McClurg, R. B., Design criteria for ideal foam nucleating agents. *Chemical engineering science* **2004**, *59* (24), 5779-5786.
186. Nofar, M.; Zhu, W.; Park, C., Effect of dissolved CO<sub>2</sub> on the crystallization behavior of linear and branched PLA. *Polymer* **2012**, *53* (15), 3341-3353.
187. Sato, Y.; Yurugi, M.; Fujiwara, K.; Takishima, S.; Masuoka, H., Solubilities of carbon dioxide and nitrogen in polystyrene under high temperature and pressure. *Fluid Phase Equilibria* **1996**, *125* (1-2), 129-138.
188. Li, G.; Li, H.; Turng, L.; Gong, S.; Zhang, C., Measurement of gas solubility and diffusivity in polylactide. *Fluid Phase Equilibria* **2006**, *246* (1-2), 158-166.
189. Li, H.; Lee, L. J.; Tomasko, D. L., Effect of carbon dioxide on the interfacial tension of polymer melts. *Industrial & engineering chemistry research* **2004**, *43* (2), 509-514.
190. Mahmood, S.; Keshtkar, M.; Park, C., Determination of carbon dioxide solubility in polylactide acid with accurate PVT properties. *The Journal of Chemical Thermodynamics* **2014**, *70*, 13-23.

- 191.Li, G.; Qi, R.; Lu, J.; Hu, X.; Luo, Y.; Jiang, P., Rheological properties and foam preparation of biodegradable poly (butylene succinate). *Journal of applied polymer science* **2013**, *127* (5), 3586-3594.
- 192.Song, J.; Mi, J.; Zhou, H.; Wang, X.; Zhang, Y., Chain extension of poly (butylene adipate-co-terephthalate) and its microcellular foaming behaviors. *Polymer Degradation and Stability* **2018**, *157*, 143-152.
- 193.Avella, M.; Cocca, M.; Errico, M.; Gentile, G., Biodegradable PVOH-based foams for packaging applications. *Journal of cellular plastics* **2011**, *47* (3), 271-281.
- 194.Ding, W.; Jahani, D.; Chang, E.; Alemdar, A.; Park, C. B.; Sain, M., Development of PLA/cellulosic fiber composite foams using injection molding: Crystallization and foaming behaviors. *Composites Part A: Applied Science and Manufacturing* **2016**, *83*, 130-139.
- 195.Miel, R., With 1 billion pounds of PLA sold, NatureWorks sees rapid growth to 2 billion. *Plastics News* **2014**.
- 196.Standau, T.; Long, H.; Murillo Castellón, S.; Brütting, C.; Bonten, C.; Altstädt, V., Evaluation of the zero shear viscosity, the D-content and processing conditions as foam relevant parameters for autoclave foaming of standard polylactide (PLA). *Materials* **2020**, *13* (6), 1371.
- 197.Wang, J.; Zhu, W.; Zhang, H.; Park, C. B., Continuous processing of low-density, microcellular poly (lactic acid) foams with controlled cell morphology and crystallinity. *Chemical Engineering Science* **2012**, *75*, 390-399.
- 198.Corre, Y.-M.; Maazouz, A.; Duchet, J.; Reignier, J., Batch foaming of chain extended PLA with supercritical CO<sub>2</sub>: Influence of the rheological properties and the process parameters on the cellular structure. *The Journal of Supercritical Fluids* **2011**, *58* (1), 177-188.
- 199.Corneillie, S.; Smet, M., PLA architectures: the role of branching. *Polymer Chemistry* **2015**, *6* (6), 850-867.
- 200.Chen, P.; Wang, W.; Wang, Y.; Yu, K.; Zhou, H.; Wang, X.; Mi, J., Crystallization-induced microcellular foaming of poly (lactic acid) with high volume expansion ratio. *Polymer Degradation and Stability* **2017**, *144*, 231-240.
- 201.Mihai, M.; Huneault, M. A.; Favis, B. D., Crystallinity development in cellular poly (lactic acid) in the presence of supercritical carbon dioxide. *Journal of applied polymer science* **2009**, *113* (5), 2920-2932.
- 202.Mihai, M.; Huneault, M. A.; Favis, B. D., Rheology and extrusion foaming of chain-branched poly (lactic acid). *Polymer Engineering & Science* **2010**, *50* (3), 629-642.
- 203.Saeidlou, S.; Huneault, M. A.; Li, H.; Park, C. B., Poly (lactic acid) crystallization. *Progress in Polymer Science* **2012**, *37* (12), 1657-1677.
- 204.Borkotoky, S. S.; Ghosh, T.; Katiyar, V., Biodegradable Nanocomposite Foams: Processing, Structure, and Properties. In *Advances in Sustainable Polymers*, Springer: 2020; pp 271-288.
- 205.Nofar, M.; Tabatabaei, A.; Sojoudiasli, H.; Park, C.; Carreau, P.; Heuzey, M.-C.; Kamal, M., Mechanical and bead foaming behavior of PLA-PBAT and PLA-PBSA blends with different morphologies. *European Polymer Journal* **2017**, *90*, 231-244.
- 206.Sartore, L.; Inverardi, N.; Pandini, S.; Bignotti, F.; Chiellini, F., PLA/PCL-based foams as scaffolds for tissue engineering applications. *Materials Today: Proceedings* **2019**, *7*, 410-417.
- 207.Zhao, H.; Cui, Z.; Sun, X.; Turng, L.-S.; Peng, X., Morphology and properties of injection molded solid and microcellular polylactic acid/polyhydroxybutyrate-valerate (PLA/PHBV) blends. *Industrial & Engineering Chemistry Research* **2013**, *52* (7), 2569-2581.

208. Ahmed, M. F.; Li, Y.; Yao, Z.; Cao, K.; Zeng, C., TPU/PLA blend foams: Enhanced foamability, structural stability, and implications for shape memory foams. *Journal of Applied Polymer Science* **2019**, *136* (17), 47416.
209. Song, J. J.; Chang, H. H.; Naguib, H. E., Design and characterization of biocompatible shape memory polymer (SMP) blend foams with a dynamic porous structure. *Polymer* **2015**, *56*, 82-92.
210. Yan, Z.; Liao, X.; He, G.; Li, S.; Guo, F.; Li, G., Green method to widen the foaming processing window of PLA by introducing stereocomplex crystallites. *Industrial & Engineering Chemistry Research* **2019**, *58* (47), 21466-21475.
211. Shi, X.; Qin, J.; Wang, L.; Ren, L.; Rong, F.; Li, D.; Wang, R.; Zhang, G., Introduction of stereocomplex crystallites of PLA for the solid and microcellular poly (lactide)/poly (butylene adipate-co-terephthalate) blends. *RSC advances* **2018**, *8* (22), 11850-11861.
212. Wang, J.; Chai, J.; Wang, G.; Zhao, J.; Zhang, D.; Li, B.; Zhao, H.; Zhao, G., Strong and thermally insulating polylactic acid/glass fiber composite foam fabricated by supercritical carbon dioxide foaming. *International journal of biological macromolecules* **2019**, *138*, 144-155.
213. Ameli, A.; Nofar, M.; Jahani, D.; Rizvi, G.; Park, C., Development of high void fraction polylactide composite foams using injection molding: Crystallization and foaming behaviors. *Chemical Engineering Journal* **2015**, *262*, 78-87.
214. Wang, G.; Zhao, G.; Wang, S.; Zhang, L.; Park, C. B., Injection-molded microcellular PLA/graphite nanocomposites with dramatically enhanced mechanical and electrical properties for ultra-efficient EMI shielding applications. *Journal of Materials Chemistry C* **2018**, *6* (25), 6847-6859.
215. Kuang, T.-R.; Mi, H.-Y.; Fu, D.-J.; Jing, X.; Chen, B.-y.; Mou, W.-J.; Peng, X.-F., Fabrication of poly (lactic acid)/graphene oxide foams with highly oriented and elongated cell structure via unidirectional foaming using supercritical carbon dioxide. *Industrial & Engineering Chemistry Research* **2015**, *54* (2), 758-768.
216. Kuang, T.; Chang, L.; Chen, F.; Sheng, Y.; Fu, D.; Peng, X., Facile preparation of lightweight high-strength biodegradable polymer/multi-walled carbon nanotubes nanocomposite foams for electromagnetic interference shielding. *Carbon* **2016**, *105*, 305-313.
217. Wu, D.; Lv, Q.; Feng, S.; Chen, J.; Chen, Y.; Qiu, Y.; Yao, X., Polylactide composite foams containing carbon nanotubes and carbon black: Synergistic effect of filler on electrical conductivity. *Carbon* **2015**, *95*, 380-387.
218. Zhang, X.; Ding, W.; Zhao, N.; Chen, J.; Park, C. B., Effects of compressed CO<sub>2</sub> and cotton fibers on the crystallization and foaming behaviors of polylactide. *Industrial & Engineering Chemistry Research* **2018**, *57* (6), 2094-2104.
219. Ema, Y.; Ikeya, M.; Okamoto, M., Foam processing and cellular structure of polylactide-based nanocomposites. *Polymer* **2006**, *47* (15), 5350-5359.
220. Zhao, J.; Wang, G.; Zhang, L.; Li, B.; Wang, C.; Zhao, G.; Park, C. B., Lightweight and strong fibrillary PTFE reinforced polypropylene composite foams fabricated by foam injection molding. *European Polymer Journal* **2019**, *119*, 22-31.
221. Kuang, T.; Li, K.; Chen, B.; Peng, X., Poly (propylene carbonate)-based in situ nanofibrillar biocomposites with enhanced miscibility, dynamic mechanical properties, rheological behavior and extrusion foaming ability. *Composites Part B: Engineering* **2017**, *123*, 112-123.
222. Peng, X.-F.; Li, K.-C.; Mi, H.-Y.; Jing, X.; Chen, B.-Y., Excellent properties and extrusion foaming behavior of PPC/PS/PTFE composites with an in situ fibrillated PTFE nanofibrillar network. *RSC advances* **2016**, *6* (4), 3176-3185.

223. Jiang, R.; Liu, T.; Xu, Z.; Park, C. B.; Zhao, L., Improving the Continuous Microcellular Extrusion Foaming Ability with Supercritical CO<sub>2</sub> of Thermoplastic Polyether Ester Elastomer through In-Situ Fibrillation of Polytetrafluoroethylene. *Polymers* **2019**, *11* (12), 1983.
224. Wang, G.; Zhao, G.; Zhang, L.; Mu, Y.; Park, C. B., Lightweight and tough nanocellular PP/PTFE nanocomposite foams with defect-free surfaces obtained using in situ nanofibrillation and nanocellular injection molding. *Chemical Engineering Journal* **2018**, *350*, 1-11.
225. Huang, A.; Wang, H.; Peng, X.; Turng, L.-S., Polylactide/thermoplastic polyurethane/polytetrafluoroethylene nanocomposites with in situ fibrillated polytetrafluoroethylene and nanomechanical properties at the interface using atomic force microscopy. *Polymer Testing* **2018**, *67*, 22-30.
226. Shahnooshi, M.; Javadi, A.; Nazockdast, H.; Altstaedt, V., Development of in situ nanofibrillar poly (lactic acid)/poly (butylene terephthalate) composites: Non-isothermal crystallization and crystal morphology. *European Polymer Journal* **2020**, *125*, 109489.
227. Rhim, J.-W.; Hong, S.-I.; Ha, C.-S., Tensile, water vapor barrier and antimicrobial properties of PLA/nanoclay composite films. *LWT-Food Science and Technology* **2009**, *42* (2), 612-617.
228. Koh, H. C.; Park, J. S.; Jeong, M. A.; Hwang, H. Y.; Hong, Y. T.; Ha, S. Y.; Nam, S. Y., Preparation and gas permeation properties of biodegradable polymer/layered silicate nanocomposite membranes. *Desalination* **2008**, *233* (1-3), 201-209.
229. Wu, S., *Polymer interface and adhesion*. M. Dekker New York: 1982; Vol. 188.
230. Hobbs, S.; Dekkers, M.; Watkins, V., Effect of interfacial forces on polymer blend morphologies. *Polymer* **1988**, *29* (9), 1598-1602.
231. Lenk, R., The Hagen-Poiseuille equation and the Rabinowitsch correction. The pressure drop in tapered channels. In *Polymer rheology*, Springer: 1978; pp 75-85.
232. Pillin, I.; Pimbert, S.; Feller, J. F.; Levesque, G., Crystallization kinetics of poly (butylene terephthalate)(PBT): Influence of additives and free carboxylic acid chain ends. *Polymer Engineering & Science* **2001**, *41* (2), 178-191.
233. Rizvi, A.; Andalib, Z. K.; Park, C. B., Fiber-spun polypropylene/polyethylene terephthalate microfibrillar composites with enhanced tensile and rheological properties and foaming ability. *Polymer* **2017**, *110*, 139-148.
234. Chen, Y.; Wan, C.; Liu, T.; Chen, Z.; Qiao, Y.; Lu, J.; Yan, J.; Zhao, L.; Essegir, M., Evaluation of LLDPE/LDPE blend foamability by in situ rheological measurements and bubble growth simulations. *Chemical Engineering Science* **2018**, *192*, 488-498.
235. Xu, Z.; Zhang, Z.; Guan, Y.; Wei, D.; Zheng, A., Investigation of extensional rheological behaviors of polypropylene for foaming. *Journal of Cellular Plastics* **2013**, *49* (4), 317-334.
236. Chou, T.; Prayoonthong, P.; Aitouchen, A.; Libera, M., Nanoscale artifacts in RuO<sub>4</sub>-stained poly (styrene). *Polymer* **2002**, *43* (7), 2085-2088.
237. Kersch, M.; Schmidt, H.-W.; Altstädt, V., Influence of different beta-nucleating agents on the morphology of isotactic polypropylene and their toughening effectiveness. *Polymer* **2016**, *98*, 320-326.
238. Mihai, M.; Huneault, M. A.; Favis, B. D.; Li, H., Extrusion foaming of semi-crystalline PLA and PLA/thermoplastic starch blends. *Macromolecular bioscience* **2007**, *7* (7), 907-920.
239. Oyama, H. T., Super-tough poly (lactic acid) materials: Reactive blending with ethylene copolymer. *Polymer* **2009**, *50* (3), 747-751.
240. Koval'aková, M.; Olčák, D.; Hronský, V.; Vrábek, P.; Fričová, O.; Chodák, I.; Alexy, P.; Sučík, G., Morphology and molecular mobility of plasticized polylactic acid studied using solid-state <sup>13</sup>C- and <sup>1</sup>H-NMR spectroscopy. *Journal of Applied Polymer Science* **2016**, *133* (23).

241. Pan, P.; Zhu, B.; Dong, T.; Yazawa, K.; Shimizu, T.; Tansho, M.; Inoue, Y., Conformational and microstructural characteristics of poly (L-lactide) during glass transition and physical aging. *The Journal of chemical physics* **2008**, *129* (18), 184902.
242. Schmidt, A.; Veeman, W. S.; Litvinov, V. M.; Gabriëlse, W., NMR investigations of in-situ stretched block copolymers of poly (butylene terephthalate) and poly (tetramethylene oxide). *Macromolecules* **1998**, *31* (5), 1652-1660.
243. Jelinski, L. W.; Dumais, J. J.; Engel, A., Multitechnique solid-state NMR approach to assessing molecular motion: poly (butylene terephthalate) and poly (butylene terephthalate)-containing segmented copolymers. IV. *Macromolecules* **1983**, *16* (3), 403-409.
244. Chen, H.; Pyda, M.; Cebe, P., Non-isothermal crystallization of PET/PLA blends. *Thermochimica Acta* **2009**, *492* (1-2), 61-66.
245. Yin, H.; Dittrich, B.; Farooq, M.; Kerling, S.; Wartig, K.-A.; Hofmann, D.; Huth, C.; Okolieocha, C.; Altstädt, V.; Schönhals, A., Carbon-based nanofillers/poly (butylene terephthalate): thermal, dielectric, electrical and rheological properties. *Journal of Polymer Research* **2015**, *22* (7), 140.
246. Shabahang, S.; Kaufman, J.; Deng, D.; Abouraddy, A., Observation of the Plateau-Rayleigh capillary instability in multi-material optical fibers. *Applied Physics Letters* **2011**, *99* (16), 161909.
247. Fang, Y.; Dulaney, A. D.; Gadley, J.; Maia, J. M.; Ellison, C. J., Manipulating characteristic timescales and fiber morphology in simultaneous centrifugal spinning and photopolymerization. *Polymer* **2015**, *73*, 42-51.
248. Denn, M. M., Fibre spinning. In *Computational analysis of polymer processing*, Springer: 1983; pp 179-216.
249. Henson, G.; Cao, D.; Bechtel, S.; Forest, M., A thin-filament melt spinning model with radial resolution of temperature and stress. *Journal of Rheology* **1998**, *42* (2), 329-360.
250. Agassant, J.-F.; Avenas, P.; Carreau, P. J.; Vergnes, B.; Vincent, M., *Polymer processing: principles and modeling*. Carl Hanser Verlag GmbH Co KG: 2017.
251. Middleman, S., *Fundamentals of polymer processing*. McGraw-Hill College: 1977.
252. Pyda, M.; Bopp, R.; Wunderlich, B., Heat capacity of poly (lactic acid). *The Journal of Chemical Thermodynamics* **2004**, *36* (9), 731-742.
253. Stoclet, G.; Seguela, R.; Lefebvre, J.-M., Morphology, thermal behavior and mechanical properties of binary blends of compatible biosourced polymers: Polylactide/polyamide11. *Polymer* **2011**, *52* (6), 1417-1425.
254. Wang, D.; Sun, G., Formation and morphology of cellulose acetate butyrate (CAB)/polyolefin and CAB/polyester in situ microfibrillar and lamellar hybrid blends. *European polymer journal* **2007**, *43* (8), 3587-3596.
255. Köppl, T.; Brehme, S.; Pospiech, D.; Fischer, O.; Wolff-Fabris, F.; Altstädt, V.; Schartel, B.; Döring, M., Influence of polymeric flame retardants based on phosphorus-containing polyesters on morphology and material characteristics of poly (butylene terephthalate). *Journal of Applied Polymer Science* **2013**, *128* (5), 3315-3324.
256. Lee, S.; Kim, M.; Song, H. Y.; Hyun, K., Characterization of the effect of clay on morphological evaluations of PLA/biodegradable polymer blends by FT-Rheology. *Macromolecules* **2019**, *52* (20), 7904-7919.
257. Di Lorenzo, M. L.; Androsch, R., Synthesis, Structure and Properties of Poly (lactic acid). **2018**.
258. Furushima, Y.; Kumazawa, S.; Umetsu, H.; Toda, A.; Zhuravlev, E.; Schick, C., Melting and recrystallization kinetics of poly (butylene terephthalate). *Polymer* **2017**, *109*, 307-314.

259. Tan, S.; Su, A.; Li, W.; Zhou, E., New insight into melting and crystallization behavior in semicrystalline poly (ethylene terephthalate). *Journal of Polymer Science Part B: Polymer Physics* **2000**, *38* (1), 53-60.
260. Standau, T.; Hädelt, B.; Schreier, P.; Altstädt, V., Development of a Bead Foam from an Engineering Polymer with Addition of Chain Extender: Expanded Polybutylene Terephthalate. *Industrial & Engineering Chemistry Research* **2018**, *57* (50), 17170-17176.
261. Li, L.; Yang, Y.; Yang, G.; Chen, X.; Hsiao, B. S.; Chu, B.; Spanier, J. E.; Li, C. Y., Patterning polyethylene oligomers on carbon nanotubes using physical vapor deposition. *Nano letters* **2006**, *6* (5), 1007-1012.
262. Chen, X.; Xu, J.; Lu, H.; Yang, Y., Isothermal crystallization kinetics of poly (butylene terephthalate)/attapulgitite nanocomposites. *Journal of Polymer Science Part B: Polymer Physics* **2006**, *44* (15), 2112-2121.
263. Supaphol, P.; Dangseeyun, N.; Sriraoon, P., Non-isothermal melt crystallization kinetics for poly (trimethylene terephthalate)/poly (butylene terephthalate) blends. *Polymer testing* **2004**, *23* (2), 175-185.
264. Oburoğlu, N.; Ercan, N.; Durmus, A.; Kaşgöz, A., Effects of filler type on the nonisothermal crystallization kinetics of poly (butylene terephthalate)(PBT) composites. *Journal of Applied Polymer Science* **2012**, *123* (1), 77-91.
265. Yin, D.; Mi, J.; Zhou, H.; Wang, X.; Fu, H., Microcellular foaming behaviors of chain extended poly (butylene succinate)/polyhedral oligomeric silsesquioxane composite induced by isothermal crystallization. *Polymer Degradation and Stability* **2019**, *167*, 228-240.
266. Zhang, H.; Wang, S.; Zhang, S.; Ma, R.; Wang, Y.; Cao, W.; Liu, C.; Shen, C., Crystallization behavior of poly (lactic acid) with a self-assembly aryl amide nucleating agent probed by real-time infrared spectroscopy and X-ray diffraction. *Polymer Testing* **2017**, *64*, 12-19.
267. Sperling, L. H., *Introduction to physical polymer science*. John Wiley & Sons: 2005.
268. Hoffman, J. D.; Lauritzen, J., Crystallization of bulk polymers with chain folding-Theory of growth of lamellar spherulites. *Journal of Research of the National Bureau of Standards* **1961**, (4), 297-+.
269. Kalkar, A. K.; Deshpande, V. D.; Vatsaraj, B. S., Poly (butylene terephthalate)/montmorillonite nanocomposites: effect of montmorillonite on the morphology, crystalline structure, isothermal crystallization kinetics and mechanical properties. *Thermochimica acta* **2013**, *568*, 74-94.
270. Sajkiewicz, P., Transient and athermal effects in the crystallization of polymers. I. Isothermal crystallization. *Journal of Polymer Science Part B: Polymer Physics* **2002**, *40* (17), 1835-1849.
271. Sajkiewicz, P., Transient and athermal effects in the crystallization of polymers. II. Nonisothermal crystallization. *Journal of Polymer Science Part B: Polymer Physics* **2003**, *41* (1), 68-79.
272. Sarikhani, K.; Nasser, R.; Lotocki, V.; Thompson, R.; Park, C.; Chen, P., Effect of well-dispersed surface-modified silica nanoparticles on crystallization behavior of poly (lactic acid) under compressed carbon dioxide. *Polymer* **2016**, *98*, 100-109.
273. Kalkar, A.; Deshpande, V.; Kulkarni, M., Isothermal crystallization kinetics of poly (phenylene sulfide)/TLCP composites. *Polymer Engineering & Science* **2009**, *49* (2), 397-417.
274. Cai, J.; Xiong, Z.; Zhou, M.; Tan, J.; Zeng, F.; Lin, S.; Xiong, H., Thermal properties and crystallization behavior of thermoplastic starch/poly ( $\epsilon$ -caprolactone) composites. *Carbohydrate polymers* **2014**, *102*, 746-754.

275. Bai, H.; Huang, C.; Xiu, H.; Gao, Y.; Zhang, Q.; Fu, Q., Toughening of poly (l-lactide) with poly ( $\epsilon$ -caprolactone): Combined effects of matrix crystallization and impact modifier particle size. *Polymer* **2013**, *54* (19), 5257-5266.
276. Cocca, M.; Lorenzo, M. L. D.; Malinconico, M.; Frezza, V., Influence of crystal polymorphism on mechanical and barrier properties of poly( l -lactic acid). *European Polymer Journal* **2011**, *47* (5), 1073-1080.
277. Tábi, T.; Hajba, S.; Kovács, J., Effect of crystalline forms ( $\alpha'$  and  $\alpha$ ) of poly (lactic acid) on its mechanical, thermo-mechanical, heat deflection temperature and creep properties. *European Polymer Journal* **2016**, *82*, 232-243.
278. Aghjeh, M. R.; Asadi, V.; Mehdijabbar, P.; Khonakdar, H. A.; Jafari, S. H., Application of linear rheology in determination of nanoclay localization in PLA/EVA/Clay nanocomposites: correlation with microstructure and thermal properties. *Composites Part B: Engineering* **2016**, *86*, 273-284.
279. Tiwary, P.; Park, C. B.; Kontopoulou, M., Transition from microcellular to nanocellular PLA foams by controlling viscosity, branching and crystallization. *European Polymer Journal* **2017**, *91*, 283-296.
280. Ni, J.; Yu, K.; Zhou, H.; Mi, J.; Chen, S.; Wang, X., Morphological evolution of PLA foam from microcellular to nanocellular induced by cold crystallization assisted by supercritical CO<sub>2</sub>. *The Journal of Supercritical Fluids* **2020**, *158*, 104719.

## Curriculum vitae

<b>Personal data</b>	Mahboobeh Born on September/11/1986, in Isfahan, Iran	Shahnooshi
<b>Nationality</b>	Iranian	
<b>Education</b>	2000-2004	Imam Sadegh High school Diploma in Mathematics & Physics
	2004-2008	Amirkabir University of Technology (Tehran Polytechnic)  B.Sc. of Chemical Engineering, Petrochemical Industries
	2009-2012	Amirkabir University of Technology (Tehran Polytechnic)  M.Sc. of Polymer Engineering, Polymer Industries
	2017 to 2021	University of Bayreuth  Scientific staff member, Polymer Engineering



---

## Publications

### Peer-reviewed Publications:

*M.Shahnooshi, A.Javadi, H.Nazockdast, V.Altstädt*

**Development of in Situ Nanofibrillar Poly (lactic acid) /Poly (butylene terephthalate) Composites: Non-isothermal Crystallization and Crystal Morphology**

European Polymer Journal 125 (2020) 109489

*M.Shahnooshi, A.Javadi, H.Nazockdast, K.Ottermann, V.Altstädt*

**Rheological Rationalization of In Situ Nanofibrillar Structure Development: Tailoring of Nanohybrid Shish-Kebab Superstructures of Poly (lactic acid) Crystalline Phase**

Polymer 211 (2020) 123040